東北大学機関リポジトリ
TOUR
Tohoku University Repository

Development of Screening of Amyloid and Tau Radiotracers using Biomathematical Approach

著者	Nai Ying Hwey
学位授与機関	Tohoku University
学位授与番号	11301甲第17801号
URL	http://hdl.handle.net/10097/00125124

Development of Screening Methodology of Amyloid Radiotracers using Biomathematical Approach

Ying-Hwey Nai

Graduate School of Biomedical Engineering

Tohoku University

A thesis submitted to the Graduate School of Biomedical Engineering in Partial Fulfillment of the Requirements for the Degree of Doctor of Philosophy in Biomedical Engineering

September 2017

Abstract

Alzheimer's disease (AD) is the most common form of dementia, with histopathological hallmarks of amyloid plaques and neurofibrillary tangles. The number of dementia cases is increasing every year worldwide, leading to an increasing cost of care for dementia patients. Early detection of the disease will increase the success rate of treating dementia or slow down the rate of dementia. Although many institutions have tried to develop amyloid and tau-targeting PET radiotracers to assist diagnosis of AD, FDA has only approved three amyloid radiotracers and no tau radiotracer thus far. Conventional radiotracer development process relies on *in vitro* data and preclinical results may not translate well to clinical performance, due to the lack of consideration to the possible *in vivo* kinetics of the radiotracers. Thus, we proposed to develop a screening methodology based on biomathematical modelling with mostly *in silico* inputs to support high-throughput screening of amyloid and tau radiotracers in the early phases of tracer development.

A biomathematical model was developed for predicting the *in vivo* standardised uptake values ratios (*SUVR*s) of amyloid radiotracers using kinetic modelling. A simplified one-tissue-compartment model was chosen to describe the *in vivo* behaviour of a PET radiotracer. The key physicochemical and pharmacological parameters that are linked to the *in vivo* uptake, washout and specific binding of the radiotracers are identified and determined. An *in silico* model was proposed to predict the free fractions in tissue and plasma to support high-throughput screening of compounds by reducing the number of long, tedious experiments. The final amyloid biomathematical model was validated using clinically-applied amyloid radiotracers. The predicted kinetic parameters correlated well with clinically-observed values, hence showing the feasibility of the model in predicting *SUVR* of amyloid radiotracers. For comparison and decision-making in moving candidate radiotracers to clinical applications, a screening methodology was proposed based on the model with noise simulation and population variation, and a common index – clinical usefulness index (*CUI*). The *CUI* ranking of clinically-applied radiotracers coincided with clinical comparison results, hence supporting the use of the screening methodology.

The feasibility of extending the amyloid biomathematical screening methodology for screening tau radiotracers was evaluated by comparing predicted kinetic parameters and *CUI* results of tau radiotracers with clinical results. Despite the greater complexity of tau radiotracers, the screening methodology showed potential in evaluating the clinical usefulness of tau radiotracers.

Acknowledgements

First and foremost, I would like to thank my professor, Hiroshi Watabe, for his patience and support throughout my PhD studies. I would also like to thank Dr Miho Shidahara for allowing me to work on her projects and for her advice and help in completing my PhD project.

I wish to express my gratitude to Dr Chie Seki for teaching me the ultrafiltration procedures and for sharing her experimental results with me. I learnt a lot from our discussion on ultrafiltration and her findings from her experiment.

I would also like to thank Dr Takayuki Ose for providing me materials on my other projects and Mr Shoichi Watanuki and Mr Masayasu Miyake for their help in my other projects.

I thank all my lab mates for their participation and support within the lab and the staff of Cyclotron and Radioisotope Center (CYRIC) at Tohoku university for their help, especially in cases of dealing with Japanese documentation.

Special acknowledgement to Ministry of Education, Culture, Sports, Science and Technology (MEXT), Japanese Government and Asia Japan Alumni (ASJA) International for providing me with the scholarship to study in Japan and experience Japanese culture.

Finally, I would like to thank my family for their continuous support in my life pursue and their company through my tough times.

Contents

Abstract i
Acknowledgements ii
Contents iii
List of Figures vii
List of Tables x
Abbreviations xii
Nomenclature xiv
Chapter 1 1
Introduction 1
1.1 Molecular Imaging 1
1.2 Radiotracer Development 3
1.3 Motivation 5
1.4 Structure of Thesis 7
Chapter 2 9
Pathology & Diagnosis of Alzheimer's Disease 9
2.1 Alzheimer's disease 9
2.1.1 Amyloid-Beta Protein 10
2.1.2 Tau Protein 12
2.1.3 Distributions of Amyloid & Tau 14
2.2 Diagnosis of AD 16
2.2.1 Clinical Diagnosis 16
2.2.2 Biomarkers of AD 18
2.2.3 Clinically-Applied Amyloid & Tau PET radiotracers 20
2.3 Current Issues in Amyloid & Tau PET imaging 22
2.4 Summary 27
Chapter 3 29
Quantification of PET Images & Biomathematical Models 29
3.1 Positron Emission Tomography (PET) 29
3.1.1 Physical Basis of PET 29
3.1.2 Data Acquisition 31
3.1.3 Data Correction 31
3.1.4 Image Reconstruction 33
3.2 Quantitative Analysis of PET 34
3.2.1 Standardised Uptake Values Ratio (*SUVR*) 34

3.2.2 Arterial Blood Sampling 36
3.2.3 Compartmental Models 37
3.3 Properties of Successful PET radiotracers 40
3.4 Biomathematical Models for Radiotracer Development 42
3.4.1 Guo's CNS Model 43
3.4.1.1 Inputs of Biomathematical Model 44
3.4.1.2 Derivation of 1TCM Parameters 45
3.4.1.3 Simulations of the Tissue Time Activity Curves 46
3.4.2 Schafer & Kim's Model 46
3.4.2.1 Input Function Model 47
3.4.2.2 4TCM 47
3.4.2.3 Data Fitting and Simulation 49
3.4.3 Comparison of Biomathematical Models 50
3.5 Summary 51
Chapter 4 53
Determination of Physicochemical & Pharmacological Parameters 53
4.1 Lipophilicity 53
4.1.1 *In Silico* Lipophilicity 54
4.1.2 *In vitro* Lipophilicity 57
4.1.3 Evaluation Methods for Lipophilicity 58
4.1.4 Determination of Representative *In silico* Lipophilicity 63
4.1.5 Summary 66
4.2 Molecular Volume 66
4.3 Free Fractions in Plasma and Tissues 66
4.3.1 Development of *In Silico* f_P-f_{ND} model 67
4.3.2 *In Silico* f_p - f_{ND} Model 70
4.3.3 Evaluation of *In Silico* f_P values by Ultrafiltration 71
4.3.3.1 Issues in Ultrafiltration 71
4.3.3.2 Ultrafiltration 73
4.3.3.3 Determination of f_P 74
4.3.3.4 Comparison with Literature f_P values 75
4.3.4 Summary 77
4.4 Dissociation Constant & Binding Sites Density 77
4.4.1 *In Vitro* Binding Assays 78
4.4.1.1 Saturation Binding Assay 78
4.4.1.2 Competition Binding Assay 80

4.4.1.3 Binding to Multiple Receptor Sites 81
4.4.2 Enzyme-Linked Immuno-Sorbent Assay (ELISA) 82
4.4.3 Concentrations of $A\beta_{1-40}$ & $A\beta_{1-42}$ in Brain 83
4.4.4 Determination of K_D 87
4.4.5 Binding Site Density 88
4.5 Conclusions 90
Chapter 5 91
Development of Biomathematical Model for Amyloid Radiotracers 91
5.1 Choice of *SUVR* as Outcome Parameter of Interest 91
5.2 Clinical Data 93
5.2.1 Clinical *SUVR* 93
5.2.2 Clinical 1TCM Parameters 94
5.3 Determination of Representative Lipophilicity & Validation of *In Silico* f_P-f_{ND} model. 97
5.4 Scaling Factors 100
5.5 Correlation with Three Types of *SUVR* 105
5.6 Choice of Time Window 108
5.7 Input Function 111
5.8 Final Amyloid Biomathematical Model 116
5.9 Evaluation of Amyloid Biomathematical Model 119
5.9.1 Sensitivity Analysis 120
5.9.2 Noise Simulations 123
5.9.3 Effect of Input Functions 126
5.10 Summary 127
Chapter 6 129
Screening Methodology of Amyloid Radiotracers 129
6.1 Existing Evaluation Methods 129
6.1.1 Coefficient of Variance (*COV*) 130
6.1.2 Receiver Operating Characteristics (ROC) 130
6.1.3 Power & Sample Size Analysis 132
6.2 Screening Methodology 133
6.2.1 Simulation with Population Variation & Noise 134
6.2.2 Clinical Usefulness Index (*CUI*) 135
6.2.2.1 Determination of Parameters 136
6.2.2.2 Evaluation of Parameters 137
6.2.3 Overview of Screening Methodology 140
6.3 Screening of Amyloid Radiotracers 142

6.3.1 Screening Results 142
6.3.2 Comparison Data of Clinically-Applied Radiotracers 142
6.3.3 Evaluation of *CUI* 144
6.4 Evaluation of Effects of Input on *CUI* 146
6.4.1 Effect of K_D on *CUI* 147
6.4.2 Effect of Input Function on *CUI* 148
6.4.3 Effect of Time Window on *CUI* 149
6.4.4 Effect of Scaling Factor on *CUI* 150
6.5 Limitations of Screening Methodology with *CUI* 152
6.6 Summary of Use of *CUI* 154
6.7 RSwCUI Software 154
6.8 Summary 158
Chapter 7 159
Extending Screening Methodology to Tau 159
7.1 Tau Radiotracers 159
7.1.1 Issues with Existing Clinically-Applied Tau Radiotracers 159
7.1.2 Chirality and Stereoisomers 160
7.1.3 R-S Enantiomers 162
7.2 *In Vitro* & *In Vivo* Data of Tau Radiotracers 163
7.2.1 *In Vitro* Data of Tau Radiotracers 163
7.2.2 Clinical Data of Tau Radiotracers 167
7.3 Screening of Tau Radiotracers 167
7.3.1 Comparison of 1TCM Kinetic Parameters 169
7.3.2 Comparison of *SUVR* 170
7.3.3 Comparison of TACs and *SUVR* distributions 172
7.3.4 *CUI* Results of Tau Radiotracers 175
7.4 Summary 177
Chapter 8 179
Overall Conclusions and Future Directions 179
Bibliography 181
Conference and Journal Papers 200
Journal Papers 200
International Conference / Symposium Presentations 200
Internal Conference / Symposium Presentations 201

List of Figures

Figure 1.1: Molecular sensitivity and spatial resolution of various imaging modalities.....2
Figure 1.2: Conventional radiotracer development process.....3
Figure 2.1: Amyloid precursor protein and formation of Aβ plaques.....10
Figure 2.2: Various forms of tau protein and neurofibrillary tangles.....13
Figure 2.3: Changes in the magnitude of various biomarkers with AD progression. 19
Figure 2.4: Various dementia diseases involving Aβ and/or Tau. 20
Figure 2.5: Different binding sites (BS) on Aβ protein.....23
Figure 3.1: Image of a PET scan with details of positron-emission annihilation.....30
Figure 3.2: Effects of attenuation, scatter and random. 32
Figure 3.3: Process flow of acquisition, reconstruction and processing of PET Data 35
Figure 3.4: One tissue, two-tissue and three-tissue compartmental models 37
Figure 3.5: Renkin and Crone Model.....40
Figure 3.6: The blood-brain-barrier (BBB).....41
Figure 3.7: Free drug hypothesis.....42
Figure 3.8: Overview of Guo's CNS biomathematical model. 43
Figure 3.9: Overview of Schafer & Kim's 4TCM biomathematical model.....47
Figure 4.1: Chemical structures of 12 clinically-applied amyloid radiotracers. 59
Figure 4.2: Chemical structures of 29 candidate amyloid radiotracers.....60
Figure 4.3: Maurer & Wan: f_{ND} vs. C*LogP* and f_P vs. f_{ND} 68
Figure 4.4: Guo: f_{ND} vs. C*LogD* and f_P vs. f_{ND} 69
Figure 4.5: Summerfield: f_{ND} vs. C*LogP* and f_P vs. f_{ND}.....69
Figure 4.6: Kalvass: f_{ND} vs. X*LogP3* and f_P vs. f_{ND}.....70
Figure 4.7: A typical occupancy curve.....79
Figure 4.8: A typical Scatchard Plot.....80
Figure 4.9: A typical occupancy curve for competition binding assay.....80
Figure 4.10: A Scatchard Plot showing binding to multiple binding sites. 81
Figure 4.11: Procedures for "Sandwich" ELISA 82
Figure 5.1: Quasi-steady-state of time activity curves of target and reference regions.. 92
Figure 5.2: M*LogP* (dproperties): Correlations of predicted & clinically-observed values of K_1, k_2 and BP_{ND} in HC & AD. 98
Figure 5.3: *LogD+S* (MedChem): Correlations of predicted and clinically-observed values of K_1, k_2 and BP_{ND} in HC & AD.....100

Figure 5.4: SF-AD: Correlations between predicted & clinically-observed K_1, k_2 and BP_{ND} in HC & AD.....102
Figure 5.5: SF-HC: Correlations between predicted & clinically-observed K_1, k_2 and BP_{ND} in HC & AD.....103
Figure 5.6: Time activity curves of [^{11}C]PIB simulated using three scaling factors.....104
Figure 5.7: Correlations of predicted *SUVR* with 3 types of clinically-observed *SUVR* 106
Figure 5.8: Correlations of predicted *SUVR* with 3 types of clinically-observed *SUVR* (n = 9).....106
Figure 5.9: Correlations of predicted *SUVR* using SF-AD & SF-Guo.....108
Figure 5.10: Correlations of predicted *SUVR* with clinically-observed *SUVR* of white matter region under HC and AD conditions.....108
Figure 5.11: Ratio of predicted $SUVR_{AD}/SUVR_{HC}$ of 5 different time windows.....109
Figure 5.12: Correlation of predicted *SUVR* generated using 5 different time windows against clinically-observed *SUVR* under AD condition.....111
Figure 5.13: The logarithmic input functions of BF227-HC, BF227-AD, FACT-HC, FACT-AD and FDDAA with time.....112
Figure 5.14: Correlations of clinically-observed *SUVR* with *SUVR* predicted using 5 different input functions.....113
Figure 5.15: Time activity curves of [^{11}C]PIB simulated using the 4 different input functions.....114
Figure 5.16: Simulated time activity curves of the reference region and target regions of HC, MCI and AD of 11 clinically-applied amyloid radiotracers.....115
Figure 5.17: Overview of Final Amyloid Biomathematical Model. 116
Figure 5.18: %*SUVR* difference from reference with ±20% variations in **M*LogP*** only. 121
Figure 5.19: %*SUVR* difference from reference with ±20% variations in $\boldsymbol{V_x}$ only.....121
Figure 5.20: %*SUVR* difference from reference with ±20% variations in $\boldsymbol{f_P}$ only.....121
Figure 5.21: %*SUVR* difference from reference with ±20% variations in $\boldsymbol{f_{ND}}$ only. 122
Figure 5.22: %*SUVR* difference from reference with ±20% variations in $\boldsymbol{B_{avail}}$ only. 122
Figure 5.23: %*SUVR* difference from reference with ±20% variations in $\boldsymbol{K_D}$ only. 122
Figure 5.24: Boxplots of % mean *SUVR* difference generated using BF227-AD, FACT-AD, FACT-HC and FDDAA from that generated using reference input function of BF227-HC under (A) HC, (B) MCI and (C) AD conditions. 127
Figure 6.1: Receiver Operating Characteristic.....131
Figure 6.2: Simulated *SUVR* distributions across HC, MCI and AD conditions for [^{11}C]PIB and [^{18}F]flutemetamol.....135
Figure 6.3: *SUVR* distribution across HC, MCI and AD conditions using poor, average and good radiotracers.....136

Figure 6.4: *Es* (Glass's Delta) Vs. *Es* (Cohen's D) 138
Figure 6.5: Correlations between *Az* and *CL*. 138
Figure 6.6: Relationship between *CL* and *Es* (Cohen's D) 139
Figure 6.7: Overview of screening methodology for amyloid radiotracers 140
Figure 6.8: *CUI* distribution of 31 amyloid radiotracers 143
Figure 6.9: Relationships between Az, Es, Sr and *CUI* 145
Figure 6.10: Relationship of the strengths of *Az*, *Es* and *Sr*. 146
Figure 6.11: *CUI* values generated using original K_D values and ±20% change in K_D values 147
Figure 6.12: %*COV* of *CUI* values generated using 4 different input functions 148
Figure 6.13: *CUI* distributions generated using literature-stated time window and default time window of 40-60 min. 149
Figure 6.14: *CUI* distribution of 31 amyloid radiotracers, simulated using SF-HC SF-Guo 152
Figure 6.15: Logo of RSwCUI software. 154
Figure 6.16: RSwCUI GUI: Overview 155
Figure 6.17: RSwCUI GUI: Results 157
Figure 6.18: RSwCUI GUI: *CUI* distribution 157
Figure 7.1: Classifications of chemical compounds. 161
Figure 7.2: Chemical structures of 22 tau radiotracers. 164
Figure 7.3: Correlation of clinically-observed and predicted *SUVR* using default time window of 40-60 min 171
Figure 7.4: Correlation of clinically-observed and predicted *SUVR* using literature-stated time window 171
Figure 7.5: Simulated TACs from 0–90 min of the reference region and target regions of HC, MCI and AD of 9 clinically-applied tau radiotracers 174
Figure 7.6: Simulated *SUVR* distributions across HC, MCI and AD conditions for [^{18}F]THK523, [^{18}F]THK5117, [^{18}F]T807 and [^{11}C]PBB3. 175
Figure 7.7: *CUI* distributions of 22 tau-related radiotracers 176

List of Tables

Table 2.1: Braak and Braak staging of amyloid and tau 14
Table 2.2: The Delacourte staging of tau distribution 15
Table 2.3: Diagnosis of clinical conditions based on diagnostic criteria 17
Table 3.1: Commonly-applied positron emitting isotopes in PET studies 30
Table 4.1: Overview of 10 different *in silico* lipophilicity models (8 *LogP* and 2 *LogD*) 55
Table 4.2: *In vitro* lipophilicity values of 41 amyloid radiotracers extracted from the literature.....61
Table 4.3: *In silico* lipophilicity values of 41 amyloid radiotracers generated using 10 lipophilicity models 62
Table 4.4: Comparison of 10 *in silico* lipophilicity models 64
Table 4.5: *In silico* and *in vitro LogP* of [^{11}C]PIB and its analogues 65
Table 4.6: Measured f_P of [^{11}C]PIB, [^{18}F]flutemetamol & [^{11}C]MeS-IMPY 75
Table 4.7: Recovery, NSB, ultrafiltrate volume ratio and f_P measured using ultrafiltration 76
Table 4.8: Concentrations of A$\beta_{1\text{-}40}$ and A$\beta_{1\text{-}42}$ (pmol/g of tissue) measured via ELISA.....85
Table 4.9: Compiled K_D or K_i values extracted from literature.....89
Table 5.1: 3 types of clinically-observed *SUVR* of 11 clinically-applied amyloid radiotracers.....95
Table 5.2: Clinically-observed K_1, k_2 and BP_{ND} of 11 clinically-applied amyloid radiotracers.....96
Table 5.3: *In silico* M*LogP* (dproperties) of 11 clinically-applied amyloid radiotracers. 97
Table 5.4: *In silico LogD+S* (MedChem) of 11 clinically-applied amyloid radiotracers. 99
Table 5.5: Ratio of predicted $SUVR_{AD}/SUVR_{HC}$ generated using 5 different time windows.....110
Table 5.6: % difference of predicted *SUVR* from clinically-observed *SUVR* for HC & AD conditions. 110
Table 5.7: Final values of *in silico* M*LogP*, V_x, f_P and f_{ND} of 31 amyloid radiotracers. 119
Table 5.8: %*COV* of *SUVR* generated with noise simulation for 31 amyloid radiotracers under HC, MCI and AD conditions. 125
Table 6.1: Classification of subjects based on diagnostic test results and the actual outcome.....130
Table 6.2: Sensitivity and specificity of five clinically-applied amyloid radiotracers. 132
Table 6.3: Minimum, maximum, spread, mean and standard deviation of the respective parameters, *Az*, *Es*, c*Es*, *Sr*, *Az* x *Es*, *Az* x c*Es*, *Es* x *Sr*, c*Es* x *Sr*, *Az* x *Sr* and *Az* x *Es* x *Sr*. 140
Table 6.4: *Az*, *Es* and *Sr* of conditions-pairs of HC-MCI and MCI-AD and *CUI*.....144
Table 6.5: % difference in *CUI* values generated using default time window from that of literature stated time window. 149
Table 6.6: Averaged *Az*, *Es*, *Sr* and *CUI* calculated from *SUVR* simulated using SF-HC & SF-Guo. 151

Table 7.1: Basic chemical bond symbols 162
Table 7.2: M*LogP*, V_x and K_D values of 22 tau-related radiotracers. 165
Table 7.3: Measured tau concentrations under HC, MCI and AD conditions from the literature. 166
Table 7.4: 3 types of clinically-observed *SUVR* of 8 clinically-applied tau radiotracers 168
Table 7.5: Predicted K_1, k_2, BP_{ND} and *SUVR* of 9 clinically-applied tau radiotracers.....168
Table 7.6: Predicted vs. clinically-observed K_1, k_2 and BP_{ND} of 4 tau radiotracers. 169

Abbreviations

1TCM	1-Tissue-Compartment Model
AD	Alzheimer's Disease
ADL	Activities of Daily Living
ADRDA	Alzheimer's Disease and Related Disorders Association
AIC	Akaike Information Criterion
APP	Amyloid Precursor Protein
AUROC	Area under ROC curve
Aβ	Amyloid-Beta Protein
BACE	β-secretase
BBB	Blood-Brain-Barrier
BP	Binding potential
BS	Binding site
CAA	Cerebral Amyloid Angiopathy
CBF	Cerebral Blood Flow
CDR	Clinical Dementia Rating
CIP	Cahn-Ingold-Prelog
CNS	Central Nervous System
CSF	Cerebrospinal Fluid
CT	Computed Tomography
DSM	Diagnostic and Statistical Manual of Mental Disorders
EIA	Enzyme Immunoassay
ELISA	Enzyme-Linked Immuno-Sorbent Assay
FA	Formic acid
fMRI	Functional MRI
FP	False Positive
FP	False Negative
GUI	Graphical User Interface
HC	Healthy Control
HITP	Heparin-induced tau polymer
IWG	International Working Group
kDa	Kilo-Dalton
keV	Kilo-Electro-Voltage

LOR	Line-Of-Response
MAP	Microtubule-Associated Proteins
MCI	Mild Cognitive Impaired
MMSE	Mini-Mental State Examination
MoCA	Montreal Cognitive Assessment
MRI	Magnetic Resonance Imaging
$MRTM_0$	Original multilinear reference tissue model
NFT	Neurofibrillary tangles
NIA-AA	National Institute on Aging–Alzheimer's Association
NINCDS	National Institute of Neurological and Communicative Disorders and Stroke
NSB	Non-specific binding
PBS	Phosphate Buffer Saline
PCG	Posterior Cingulate Gyrus
PET	Positron Emission Tomography
P-gp	P-glycoprotein
PHF	Paired-Helical Filament
PMT	Photon-Multiplier Tube
PVE	Partial Volume Effect
rCBF	Regional CBF
ROC	Receiver Operating Characteristics
ROI	Region of Interest
SC	Schwarz Criterion
SDS	Sodium Dodecyl Sulfate
SF	Scaling Factor
sMRI	Structural MRI
SNR	Signal-to-Noise Ratio
SP	Senile Plaques
SPECT	Single Photon Emission Computed Tomography
TAC	Time Activity Curve
TN	True Negative
TP	True Positive

Nomenclature

1-β	Power	%
A*LogP*	Ghose-Crippen Atom-based *LogP*	unitless
AUC	Area under curve	varies
Az	Area under ROC	unitless
$B_{avail.A\beta}$	Concentration of free Aβ lesion binding sites	M
$B_{avail.NS}$	Concentration of free non-specific binding sites in brain tissue	M
$B_{avail.\tau}$	Concentration of free τ lesion binding sites	M
B_{max}	Maximum target density	M
$B_{max.A\beta}$	No of binding site on Aβ proteins that can be bound per mole of radiotracer	mol of Aβ/mol of radiotracer
BP_{ND}	Binding potential	unitless
BSA	Body surface area	m^2
BW	Body weight	kg
C_{FT}	Concentration of free ligand in brain tissue compartment	M
CI	Confidence interval	%
C*LogP* / *CLogD*	Calculated *LogP* / *LogD*	unitless
C_{NS}	Concentration of non-specific binding sites occupied by ligand	M
COV	Coefficient of variation	unitless
C_P	Plasma ligand concentration	M
$C_{Reference}$	Radioactivity concentrations in reference region	kBq/mL
$C_{S.\tau}$	Concentration of τ lesion binding sites occupied by ligand	M
$C_{S.A\beta}$	Concentration of Aβ lesion binding sites occupied by ligand	M
C_{Target}	Radioactivity concentrations in target region	kBq/mL
CUI	Clinical usefulness index	unitless
D	Distribution coefficient	unitless
DVR	Distribution volumes ratio	unitless
e_K	Distribution of errors	unitless
Es	Effect size	unitless
f	Fractional occupancy	unitless
f	Perfusion	$mL/cm^3/min$
f_{ND}	Free fraction in tissue	unitless

f_p	Free fraction in plasma	unitless
f_P	Free fraction of ligand in plasma	unitless
IC_{50}	Inhibitory concentration	M
IF	Dynamic metabolite-corrected plasma input function (used in Guo's model)	kBq/mL
K_1	Influx rate constant	mL/cm^3/min
k_2	Efflux rate constant	min^{-1}
K_D	Dissociation constant	M
$K_{D.A\beta}$	Dissociation constant of radiotracer in specific Aβ binding compartment	M
$K_{D.NS}$	Dissociation constant of radiotracer in NSB compartment	M
$K_{D.\tau}$	Dissociation constant of radiotracer in specific tau binding compartment	M
k_{off}	Dissociation rate constant	min^{-1}
K_{on}	Association rate constant	M.min^{-1}
LogD	Logarithmic of Distribution coefficient (*D*)	unitless
LogP	Logarithmic of Partition coefficient (*P*)	unitless
LogP+S* / *LogD+S	*LogP* calculated with Simulations Plus	unitless
Mi*LogP*	Molinspiration *LogP*	unitless
M*LogP*	Moriguchi *LogP*	unitless
NPV	Negative predictive value	unitless
P	Partition coefficient	unitless
P	Permeability	cm/min
PPV	Positive Predictive Value	unitless
PS	Permeability-surface area product	cm^3/min/g
r_1	Association rate constant for non-specific binding in brain tissue	M^{-1}min^{-1}
R^2	Coefficient of determination	unitless
r_2	Dissociation rate constant for non-specific binding in brain tissue	min^{-1}
r_3	Association rate constant for specific binding to Aβ lesions	M^{-1}min^{-1}
r_4	Dissociation rate constant for specific binding to Aβ lesions	min^{-1}
r_5	Association rate constant for specific binding to τ lesions	M^{-1}min^{-1}
r_6	Dissociation rate constant for specific binding to τ lesions	min^{-1}

R_{tran}	Rate constant mediating transfer across the blood–brain barrier	$mL.min^{-1}cm^{-3}$
S	Capillary surface area	cm^2/g of brain
SE	Standard Error	unitless
S_n	Standard deviation of the distribution of errors	unitless
Sr	*SUVR* ratio	unitless
SUV	Standardised uptake value	varies
$SUVR$	Standardised uptake values ratio	unitless
$TPSA$	Topological surface area	$Å^2$
V_{aq_P}	Apparent aqueous volume in plasma	solvent/mL of plasma
V_{aq_T}	Apparent aqueous volume in tissue	solvent/mL of tissue
V_T	Volume of distribution	$mL.cm^{-3}$
V_x	McGowan volume	cm^3/mol/100 or $Å^3$/molecule
α	Significant Level	%
μ	Linear attenuation coefficient	cm^{-1}
σ_{pooled}	Pooled standard deviation	varies

*Molar (M) = moles per liter (mol/L), due to small amount used in measurements, nano-Molar (nM) is commonly applied.

Chapter 1

Introduction

Biomedical imaging techniques such as positron emission tomography (PET) and single photon emission computed tomography (SPECT) have been applied in drug development, diagnosis and treatment of various diseases. However, the diagnosis of diseases using PET or SPECT is limited by the availability of radiopharmaceutical agents or radiotracers.

This chapter provides an overview of molecular imaging and radiotracer development in the diagnosis of dementia, particularly Alzheimer's disease (AD). The motivation and focus of this PhD project will be explained, as well as the structure of this thesis.

1.1 Molecular Imaging

Since the 1960s, biomedical imaging has been applied to provide structural/anatomical or physiological/molecular information in animals and human *in vivo*. These imaging techniques rely on the detection of electromagnetic waves, such as X-rays in computed tomography (CT), radio-waves in magnetic resonance imaging (MRI), visible light in optical imaging and gamma rays in PET and SPECT, and the detection of mechanical waves such as sound waves in ultrasound (US). CT, structural MRI (sMRI) and ultrasound have high spatial resolution and are commonly used to provide *in vivo* structural information. Molecular imaging, on the other hand, provides non-invasive, *in vivo* images of the biochemical or functional processes in the living body at the molecular and cellular level. Molecular imaging technologies include optical imaging, functional MRI (fMRI), ultrasound with microbubbles, PET and SPECT. Molecular imaging modalities have poorer spatial resolution and hence are often used with structural imaging techniques in complementary to each other (Figure 1.1). For example, sMRI provides structural information at high resolution, while PET provides biological information with a radiolabeled chemical compound in a hybrid PET-MR scanner.

Molecular imaging can measure the temporal and spatial distributions of a molecular probe, which can reflect a biological process or target of interest. PET and SPECT rely on the use of a

radiopharmaceutical probe or radiotracer. A radiotracer is a chemical compound in which one or more atoms are replaced with a radioisotope and the detection of its decaying radionuclide allows the tracking of its location. During PET imaging, the radiotracer is injected intravenously into the subject and gamma rays emitted from the radiotracer within the body are detected by dedicated gamma detectors in a PET or SPECT scanner. The ability to detect the radiotracer has allowed the use of PET or SPECT in drug development and the diagnosis of various diseases. During drug development, the candidate drugs are radiolabeled with an isotope, with little or no change in the basic structure of the drug. Biochemical changes in the drugs, in terms of absorption, distribution, metabolism and excretion can be observed and evaluated quantitatively from the dynamic or static PET/SPECT images.

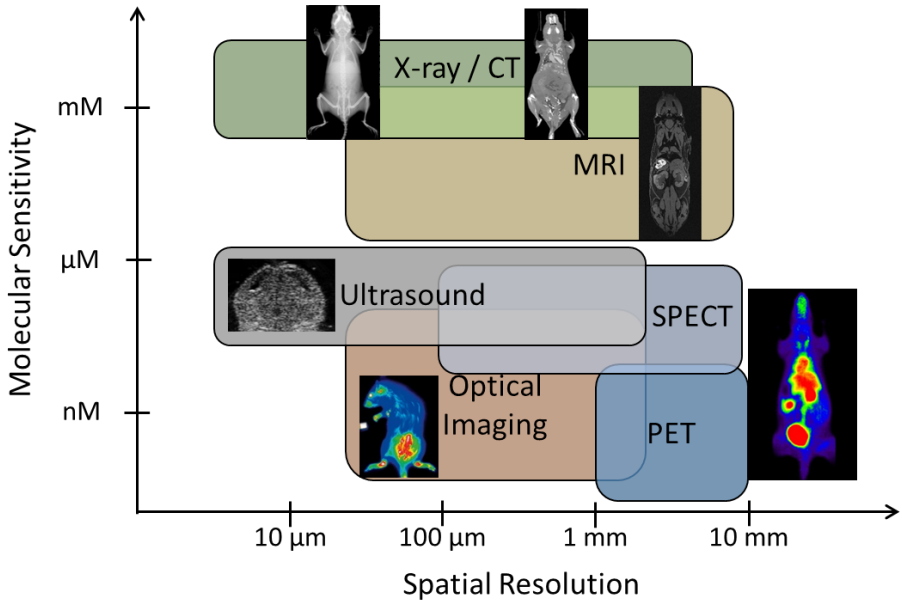

Figure 1.1: Molecular sensitivity and spatial resolution of various imaging modalities: computed tomography (CT), magnetic resonance imaging (MRI), ultrasound, single-photon emission computed tomography (SPECT), positron emission tomography (PET) and optical imaging.

Diagnostic radiotracers are radiolabeled chemical compounds developed to measure a biological function within the body (e.g. blood flow, metabolism) or to measure the concentration and distribution of certain proteins or receptors of interest (e.g. cancer cells, brain receptors). [^{18}F]FDG (fluorodeoxyglucose), a radiolabeled analogue of glucose, is an example of a commonly-applied diagnostic radiotracer that is used to measure glucose metabolism or uptake of glucose within the body. However, unlike glucose, [^{18}F]FDG is missing a hydroxyl group, which prevented it from being further metabolised in the cells. Therefore, it accumulates in tissues

with energy requirement. For example, malignant tumour cells have higher energy consumption compared to normal tissues, and hence [^{18}F]FDG can be used in the diagnosis of cancer. Another example of a diagnostic radiotracer developed to bind to a specific target is [^{11}C]PIB (Pittsburgh compound B), which binds to fibrillary amyloid plaques. Amyloid plaque is a pathological hallmark of Alzheimer's disease (AD) and hence, [^{11}C]PIB can be used to diagnose subjects, who can benefit from anti-Amyloid-beta (Aβ) treatment.

1.2 Radiotracer Development

The development of a new drug or novel radiotracer is a long, tedious and expensive process, typically taking about 10-15 years [Sharma et al., 2010] and 8-10 years [Agdeppa et al., 2009], and cost approximately USD800 million and USD150 million respectively (Figure 1.2). Thousands of chemical compounds may be screened, but only a few get selected for clinical trials, with only one compound making all the way through regulatory approval (Figure 1.2).

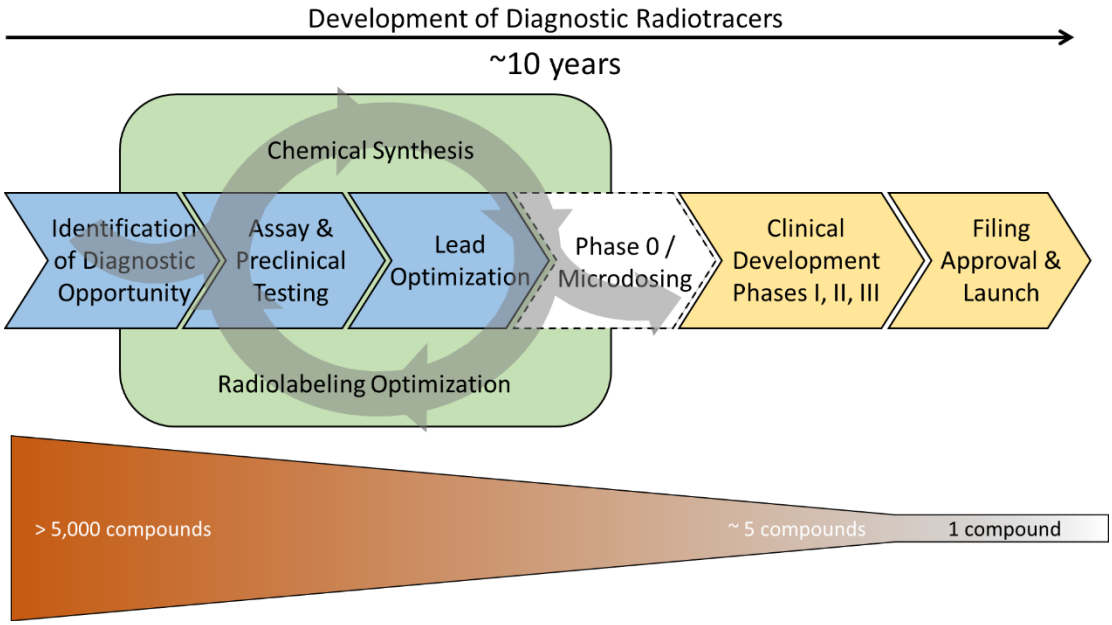

Figure 1.2: Conventional radiotracer development process.

The conventional process of developing a radiotracer (Figure 1.2) starts with identifying the target of interest, after which a large database of chemicals compounds are screened to determine potential chemical structures that can bind to the target of interest. The synthesis and radiolabeling of the candidate chemical compounds are designed and optimized to obtain high chemical yield while minimizing synthesis time and effort, and radioactive exposure to the radiochemists. *In vitro* assessments are performed iteratively to determine the important parameters of the candidate

radiotracers. Preclinical or animal testing are then followed through to determine the pharmacokinetics and pharmacodynamics of the radiotracer or drug in animals. Typically, *in vitro* results are first assessed, from which candidate compounds showing good results get selected for preclinical studies to minimize time and animal sacrifices.

Pharmacokinetics (PK) is the study of what the body does to the drug or radiotracer in terms of absorption, distribution, metabolism and excretion (ADME) as well as the toxicity and efficacy of the drug/radiotracer. Pharmacodynamics (PD) is the study of what the drug does to the body in terms of dose and effect. Biodistribution studies of the drug or radiotracer are important for evaluating the specific and non-specific binding of the drug or radiotracer to the target and non-target sites. *In vitro* assessments and preclinical testing are carried out iteratively until a few lead compounds are identified for further evaluation. In the case of developing a radiotracer, the feasibility and ease of radiolabeling and synthesising the compound are also considered during the development process (Figure 1.2). The procedures of radiolabeling and synthesising are optimized to reduce unnecessary radioactive exposure to radiochemist and to increase the yield of the radiotracer.

Lead compounds showing successful *in vitro* and/or preclinical results are selected and filed for approval for clinical studies. In drug development, phase I is conducted with a small group of healthy subjects (20~100) to evaluate safety and dosage and to identify any side effects. Phase II is carried out in a larger group of subjects (100~300), including patients to determine the efficacy of the drug and to further evaluate the safety of the drug or radiotracer. Phase III is carried in a large group of subjects (300~3000), including both healthy subjects and patients to evaluate the safety, efficacy and effectiveness of the drug or radiotracer. The use of PET and SPECT for evaluating the uptake and binding of the drug/radiotracer *in vivo* has allowed smaller subject groups to be evaluated in each phase, hence speeding up the development process.

However, poor bench-to-bedside translation often results due to the differences between *in vitro* and *in vivo* conditions. Similarly, animal models, especially rodents, are often poor predictors of human physiology and treatment response and have been reported to be incorrect in approximately one out of three cases [Garner et al., 2006]. Although larger animals (e.g. pigs and primates) showed closer physiology to that of human, they are still in-prefect human models and are more costly for high-throughput screening compared to rodents. These issues lead to high attrition rates in drug and radiotracer development.

To address these issue, the Food and Drug Administration (FDA, USA) had initiated a concept known as "Microdosing" using PET or SPECT imaging in 2006. In microdosing, a small group of healthy subjects (<10) is given a dose of no greater than 100 μg (for small molecules) or 1/100 of the No Observed Adverse Effect Level (NOAEL), whichever is the lower [Burt et al., 2016]. Preclinical testing is still required but the number of animals required for clinical approval is reduced, hence reducing the cost. Due to the low exposure of the drug or radiotracer, no gross effect, therapeutic effect, toxic effect or high radiation are expected in the subjects. However, microdosing cannot be used for therapeutic or diagnostic decision making or for safety or efficacy studies as the results may not be linearly related to full dose studies [Burt et al., 2016]. Nevertheless, the results can still be used to support candidate selection and dosage identification in Phase I studies.

The introduction of microdosing has helped to speed up the clinical Phase I studies but phases from compound screening to lead optimisation (Figure 1.2) still continue in the same laborious fashion. Development guides, such as the Rule of Five (Ro5) [Lipinski et al., 2004] provide a list of physicochemical parameters and their associated range of values for increasing the chances of developing successful drugs (e.g. molecular weight < 500 kDa, lipophilicity < 5). However, a compound that meets all the criteria of Ro5 does not guarantee that the compound will be successful [Lipinski et al., 2004]. Computational models have been introduced using different databases of chemical compounds to assist the development of new compounds (section 3.4). However, no standards have been established and only models of known targets are available.

1.3 Motivation

Dementia is a group of brain diseases, with 100 different conditions involving impairments of cognition, function & memory. Dementia patients show clinical symptoms such as memory loss, confusion in time and place etc., and subsequent decline in functional capabilities, such as the ability to eat by themselves or to change their clothes. Among the various types of dementia, Alzheimer's disease (AD) is the most common, accounting for 60~70% of all dementia cases worldwide. The number of dementia cases is increasing every year, which leads to an increasing cost of care for dementia patients. Early detection of the disease will increase the success rate of treating AD or slow down the rate of dementia. Since 2000, many institutions have tried to develop amyloid and tau-targeting radiotracers to assist diagnosis of AD and support AD drug

development. However, up to date, only three amyloid radiotracers and no tau radiotracers had been approved by FDA (section 2.2.3).

The development of a successful diagnostic radiotracer is hampered by the limitations of the conventional radiotracers development process. Firstly, it is a long and iterative process of identifying the right chemical compounds, followed by lead optimisation via iterative processes of conducting multiple *in vitro* experiments and preclinical testing before the radiotracer can be applied clinically. Secondly, *in vitro* and preclinical results may not translate well to clinical performance, due to the lack of consideration to the possible *in vivo* kinetics of the radiotracers. Radiotracers with poor kinetics may not show much differences in the *in vivo* uptake under different subject conditions. Thirdly, the conventional process focuses on a few physicochemical or pharmacological properties (e.g. lipophilicity, selectivity to target sites) to evaluate radiotracer. These properties are often evaluated separately, without considering their interaction effect. Lastly, the noise level of the imaging modality and target variation are either not considered or evaluated separately during radiotracer development.

Biomathematical simulation can complement high-throughput screening by allowing simultaneous and rapid evaluation of many candidate radiotracers. Moreover, the radiotracers can be evaluated by using both physicochemical and pharmacological parameters to simulate their possible *in vivo* kinetics at variable conditions. The statistical evaluation of the radiotracers can also be increased by simulating with noise and population variation. To further support decision-making in moving candidate radiotracers for clinical evaluation, the use of a common index can support comparison of different radiotracers from within and across institutions. As such, biomathematical simulation can help to identify potential compounds from a large number of compounds during the early phrase of drug development, especially before radiolabeling of candidate radiotracers (Figure 1.2). This will help to reduce the number of *in vitro* experiments and radiolabeling procedures and hence speed up the radiotracer development process and reduce radioactive exposures to the radiochemists.

At cyclotron and radioisotope center (CYRIC) in Tohoku University, we are actively developing amyloid and tau radiotracers in hope to support the diagnosis of AD and to assist AD drug treatment. As such, we would like to develop a screening methodology using biomathematical simulations to support the screening process of chemical compounds during the development of amyloid and tau radiotracers, especially during the design of new candidate compounds before

the synthesis and radiolabeling of the candidate compounds (section 1.2). This will help to reduce the radioactive exposure to radiochemists while supporting the screening of thousands of compounds more efficiently with the consideration of the possible *in vivo* kinetics of the radiotracers leading to higher success rate. Thus far, few models for amyloid and tau radiotracers were developed and they were developed using one or a few radiotracers due to the unavailability of many radiotracers. Moreover, the existing amyloid and tau models were not focused on supporting radiotracer development.

We proposed to use the reported clinical data of amyloid radiotracers for the development of an amyloid biomathematical model to predict the *in vivo* kinetic behaviour of candidate amyloid radiotracers in HC and AD. A screening methodology based on the proposed biomathematical model will then be developed to support decision making in moving the candidate radiotracer to clinical application. We then investigate if the screening methodology can be extended to support the development of tau radiotracer.

1.4 Structure of Thesis

Chapter 1 introduces the basics of molecular imaging and the development and uses of radiotracers in drug development and diagnosis of various diseases. The motivation and structure of this thesis are explained. Relevant conferences attended and journal papers submitted during the course of PhD are listed.

Chapters 2 and 3 provide the background in the development of the amyloid biomathematical model. Chapter 2 explains the details of Alzheimer's disease, in particular, the two pathological hallmarks of AD: amyloid and tau proteins. Existing issues in amyloid and tau imaging are discussed, as they are important in supporting the feasibility of the proposed model. Chapter 3 explains the fundamentals of positron emission tomography (PET) and quantitative analysis of PET images. Two existing biomathematical models are then described and the feasibility of extending the model for our model is debated.

Chapters 4 to 6 describe the development of the screening methodology in details. Chapter 4 focuses on determining the physicochemical and pharmacological properties of the radiotracers required in the biomathematical model. The development and evaluation of the amyloid biomathematical model are described in chapter 5. A screening methodology based on the

proposed amyloid biomathematical model is developed in chapter 6. A program written for screening amyloid radiotracers based on the proposed methodology is presented.

In chapter 7, we explore the feasibility of extending the proposed amyloid biomathematical screening methodology for screening tau radiotracers. We then conclude the project and my work done for this PhD project in chapter 8.

Chapter 2

Pathology & Diagnosis of Alzheimer's Disease

Amyloid and tau PET imaging can show the distribution and concentration of amyloid and tau in the subject brain. However, the amyloid and tau proteins have many different structural forms and undergo many post-translational processes, some of which lead to neurotoxic degeneration causing AD, while some do not. In this chapter, the different forms of amyloid and tau proteins are described in details to ensure that the right information is selected for model development. The diagnosis of AD using other biomarkers and classification of subjects based on various diagnostic criteria standards and neuropsychological tests are briefly described followed by two staging methods of AD based on concentration and spatial distribution of amyloid and tau in the brain. Clinically-applied amyloid and tau radiotracers are presented and the existing issues faced in clinical amyloid and tau PET imaging are discussed.

2.1 Alzheimer's disease

Alzheimer's disease (AD) is a progressive neurodegenerative disorder defined by histopathological features such as senile plaques (SP) and neurofibrillary tangles (NFT) [Perrin et al., 2009] and clinical symptoms such as loss of memory, reduced executive functions etc. AD was discovered and named after Alois Alzheimer, a German physician in 1906, who examined a patient exhibiting memory loss, language difficulty and confusion. When the patient died at the age of 51, he carried out post-mortem brain autopsy and observed SP and NFT in her brain tissues. [Stelzmann et al., 1995]. These subsequently became the pathological hallmarks of AD.

In this section, the structure and biological development of SP and NFT from Aβ and tau proteins are described in details, in particular, the i*n vitro* method of identifying Aβ and tau proteins. The spatial and temporal distributions of Aβ and tau proteins in 2 staging methods with AD progression are also explained.

2.1.1 Amyloid-Beta Protein

The component of senile plaques was unknown at the time of discovery by Dr Alzheimer. It was only in 1984 that Aβ was discovered when it was successfully purified from the senile plaques [O'Brien et al., 2011]. Aβ peptide is cleaved from the amyloid precursor protein (APP), which is a transmembrane protein of ~100-130 kDa (kilo-Dalton), with a maximum of 770 amino acids (Figure 2.1A). The APP is located on the plasma membrane, trans-Golgi network, endoplasmic reticulum and endosomal, lysosomal and mitochondrial membrane. As such, Aβ peptide can be found intracellularly and extracellularly. The physiological functions of APP are still unconfirmed but are proposed to relate to cell growth and neuronal plasticity.

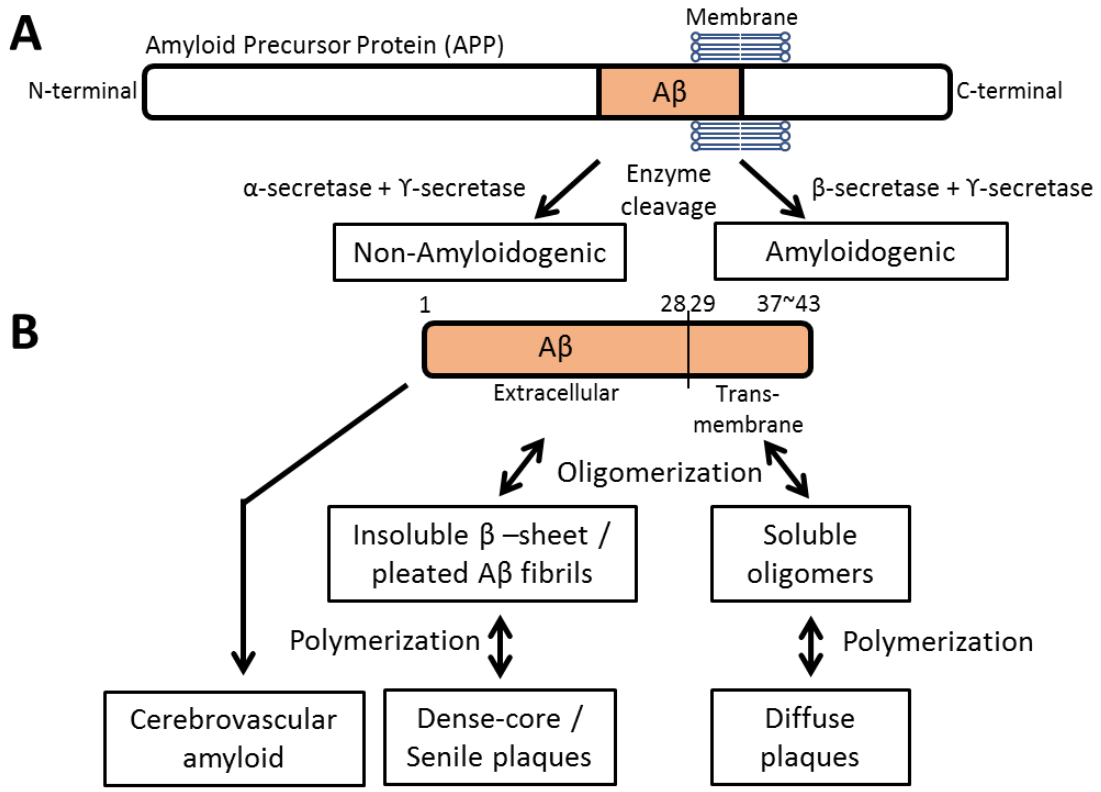

Figure 2.1: (A) Amyloid precursor protein (APP) [O'Brien et al., 2011] and (B) formation of Aβ plaques [Morgan et al., 2004].

Three main proteases are involved in the proteolytic cleavage of APP, namely α-secretase, β-secretase (or BACE) and γ-secretase. They act in pairs to form the amyloidogenic and non-amyloidogenic peptides. Non-amyloidogenic peptides are first cleaved by the α-secretase at the N-terminal, followed by γ-secretase at the C-terminal of APP (Figure 2.1A). The amyloidogenic peptides or Aβ peptide are first cleaved by the β-secretase at the N-terminal, followed by γ-

secretase at the C-terminal (Figure 2.1A).

Aβ is a small peptide of about 4.2 kDa and consists of 37 to 43 amino acids (Figure 2.1B) [O'Brien et al., 2011]. Aβ1-37 to Aβ1-40 are known as the benign forms, while Aβ1-42/43 are known as the toxic forms [Karran et al., 2011]. The most common forms of Aβ peptides are Aβ1-40/42, of which Aβ1-42 was reported to polymerise more readily than Aβ1-40. The different types of Aβ proteins exist in varying degree in different cellular compartments, namely intracellular, extracellular and membrane surface) [Steinerman et al., 2008].

A single Aβ peptide, also known as a monomer, can join together to form longer and more toxic peptides such as dimer, trimer, and tetramer. These peptides undergo oligomerization to form a soluble oligomer or insoluble fibrillary Aβ (Figure 2.1B). Soluble forms are soluble in aqueous solution and remain soluble even after high-speed centrifugation. The concentrations of soluble Aβ and insoluble Aβ peptides are about 6 and at least 100 times respectively higher in AD brains than in normal brains [Morgan et al., 2004]. These oligomers undergo further post-translation modifications (e.g. truncation, racemization, oxidation, polymerization) to form large Aβ deposits.

Three types of amyloid-beta (Aβ) deposits can be found in the human brain, namely senile/neuritic plaques, diffuse plaques and cerebrovascular amyloid (Figure 2.1B) [Morgan et al., 2004]. Senile plaques are large extracellular aggregates of Aβ consisting of a dense central fibrillary Aβ core filled with inflammatory cells and dystrophic neurites or dendrites, containing tau in its periphery [O'Brien et al., 2011]. They are known as the cause of AD. Senile plaques have high concentrations of Aβ1–42, which are subjected to post-translational modifications including oxidation, oligomerization and polymerization. They have pleated β-sheet structure, which is strengthened by hydrogen bonds formed between the Aβ peptides. Senile plaques can be identified by fluorescent dyes, such as Thioflavin-S/T and Congo-Red.

Diffuse plaques are amorphous and non-neuritic amyloid deposits, which are commonly found in the brains of cognitively intact elderly people. They do not β-sheet structure, thus they can only be identified by modified silver methenamine methods. Cerebrovascular amyloid consists of Aβ peptides, mainly Aβ1-39/40/42, deposited in cerebral blood vessels and are spared from post-translational modifications (Figure 2.1B). It forms the main component of cerebral amyloid angiopathy (CAA). The soluble oligomer is said to be the cause of neurotoxic instead of fibrillary senile plaques: the prefibrillar soluble Aβ oligomer may induce toxic effect leading to cell death

or the diffuse plaques may unfold and reorganise into senile plaques, during which toxic is release leading to cell death (Figure 2.1B).

2.1.2 Tau Protein

Tau proteins belong to the microtubule-associated proteins (MAP) family. They are normally present in the axon and plays a part in axonal transportation and stabilisation of the microtubules [Buěe et al., 2000]. The tau structure consists of two domains – projection and microtubule-binding domains (Figure 2.2A) [Buěe et al., 2000]. The projection domain consists of the acidic and basic regions, with the N-terminal (amino terminal). The microtubule-binding region consists of the repeat-domain and neutral regions, with the C-terminal (carboxy-terminal). A total of six isoforms of tau proteins exist. They differ in the number of exons (0, 1, 2) on the acidic region and the number of repeats (3 repeats (3R) or 4R) in the repeat-domain regions (Figure 2.2A). The R1-R2 region exists only in 4R tau (Figure 2.2A) and is the main cause for the 40 times difference in binding affinities to microtubules between 4R and 3R tau [Buěe et al., 2000]. They are made up of about 352~441 amino acids, with a molecular weight ranging from 45 to 65 kDa [Buěe et al., 2000]. The shortest isoform, known as the fetal isoform, is found only in the fetal brain. The rest of the isoforms are known as the adult isoforms. In normal adults, the proportion of 3R and 4R tau is nearly equal, but in AD, the proportion of 4R is much higher than 3R.

Tau proteins undergo many post-translational modifications, of which phosphorylation plays the key role in determining the binding with microtubules (Figure 2.2B). Tau protein undergoes phosphorylation under normal ageing, forming highly soluble phosphorylated tau that does not form filamentous inclusion. However, under abnormal conditions, hyperphosphorylation occurs, yielding intraneuronal filamentous, insoluble inclusions called paired-helical filament (PHF) tau, which consists of a pleated β-sheet structure. A small amount of tau may form other types of ultra-structures, such as straight-like filaments, twisted filaments, randomly coiled filaments or hybrid filament, which has a sharp change from straight to helical structure [Serrano-Pozo et al., 2011].

Further aggregation of PHF-tau results in neurofibrillary tangles (NFT), which consists of 3 morphological stages (Figure 2.2B): (1) Pre-NFT, with a more diffuse structure, (2) Intraneuronal NFT (iNFT), with matured or fibrillary structure, and (3) extraneuronal NFT (eNFT) [Serrano-Pozo et al., 2011]. eNFT is also known as "ghost" tangle, as it results from the death of tangles-containing neurones. It can be identified by the lack of a nucleus and the presence of a stainable

cytoplasm due to the breakdown of the cell membrane [Serrano-Pozo et al., 2011]. Although NFT is said to be toxic, the tau form that leads to neurotoxicity is still being debated. Some have proposed that the soluble tau, which is formed before hyperphosphorylation to form PHF-tau under abnormal conditions, is toxic or both NFT and soluble tau lead to cell death via different routes [Kopeikina et al., 2012].

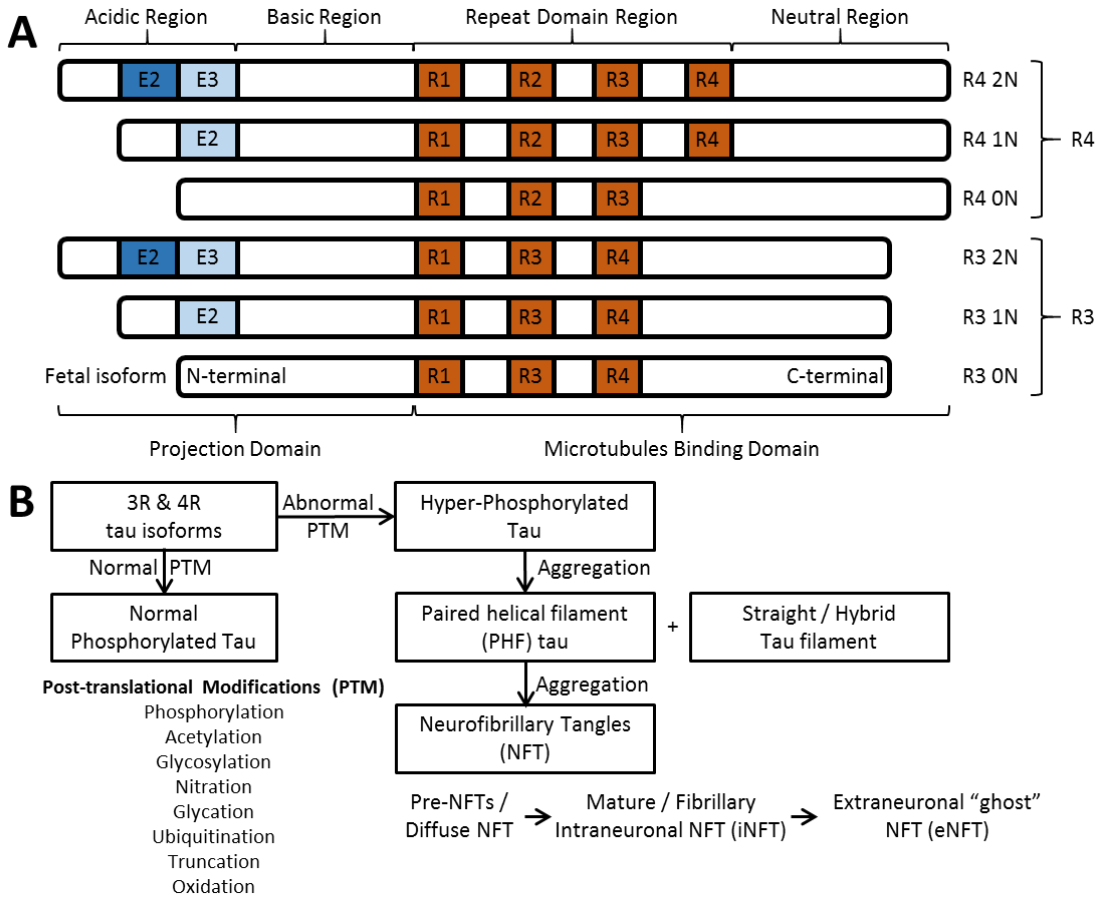

Figure 2.2: Various forms of tau protein: (A) 6 isoforms of tau protein [Ariza et al., 2015], (B) Aggregation of tau protein to neurofibrillary tangles.

NFT are argyrophilic (readily stained by silver salts) and can be identified *in vitro* by silver staining methods (e.g. Gallyas technique) or fluorescent staining or immunostaining using anti-tau antibodies (e.g. AT8 and PHF1 for i/eNFT, MC1 and Alz50 for Pre-NFTs) [Serrano-Pozo et al., 2011]. Fluorescent dyes, such as Thioflavin-S/T and Congo-Red, bind to structures with β-sheet conformation and hence can be used to detect PHF-tau. Apart from NFT in cell bodies, phosphorylated tau can exist as neuropil threads in dystrophic neurites or in the neuropil.

Synthetic heparin-induced tau polymer (HITP) generated *in vitro* composed of 3R and/or 4R tau and does not undergo the same phosphorylation process under *in vitro* conditions [Ariza et al., 2015]. Moreover, synthetic tau phosphorylates to form homogeneous or granular structure instead of fibrillary structure found in human [Buěe et al., 2000; Declercq et al., 2016]. In transgenic mouse model expressing human recombinant tau, only 4R tau isoforms are expressed, but in human AD brains, both 3R and 4R are expressed [Declercq et al., 2016]. As such, *in vitro* and pre-clinical results of tau radiotracers do not translate well into clinical results.

2.1.3 Distributions of Amyloid & Tau

The spatial distributions of amyloid and tau proteins in postmortem brains of healthy and AD subjects have been extensively studied since 1990 especially by Braak and Braak [Braak et al., 1991] and Delacourte [1999]. Both groups have tried to study the spatial and temporal distributions, and changes in the concentrations of amyloid and tau proteins to stage the pathological progression of AD.

Braak et al. staged AD progression based on the histopathological distributions of amyloid and tau proteins separately using 2661 normal and AD brains from 1991 to 1997 [Braak et al., 1997]. Amyloid and tau proteins were identified using silver-pyridine and silver-iodide staining respectively. Braak et al. [1991] managed to stage the amyloid and tau accumulation and distributions into 3 (A-C) and 6 (I-VI) stages accordingly (Table 2.1).

Table 2.1: Braak and Braak staging of amyloid and tau

Amyloid Stages A-C	
Stage A:	Lingual and fusiform gyri (medial and lateral occipito-temporal gyri = basal temporal neocortex)
Stage B	Basal Cortex
Stage C:	Upper portions of the cortex & the primary neocortical areas + Cerebellum
Tau Stages I-VI	
Stage I	Transentrohinal region (Temporal Lobe)
Stage II	+ Entorhinal region
Stage III	+Hippocampal & Temporal preneocortex
Stage IV	+ Adjoining neocortex
Stage V	Spread Superolaterally
Stage VI	Primary Neocortex

Delacourte et al., [1999] on the other hand, staged the disease progression based on the tau

distribution and severity of cognitive impairment evaluated using 2 clinical assessments: Mini-mental state examination (MMSE) and clinical dementia rating (CDR). Aβ was identified using thioflavin-S and antibodies against Aβ. Tau proteins were identified using silver staining (Bielchowski) and antibodies against tau. Delacourte et al [1999] managed to stage AD progression based on tau distribution in ten stages using 130 brains (Table 2.2). However, there was a rare case where an elderly brain with severe cognitive impairment had low concentrations of tau distributed throughout the brain.

Table 2.2: The Delacourte staging of tau distribution

Stages	Regions	No of Subjects	Age (Mean ± Stdev)	Aβ Density (pmol/mg) (Subj No)	Cognitive Status & notes
I	Trans-entorhinal	3	71~83 (77 ± 6)	0	All were Non-Demented
II	+Entorhinal	4	72~95 (86 ± 10)	Low (2)	2 without dementia (incl 95-years-old)
III	+Hippocampus	16	73~95 (84 ± 7)	10 (2), 20 (3)	6 vascular demented, 4 ND
IV	+Anterior temporal cortex	10	69~98 (88 ± 9)	11 (max)	5 ND, 4 MCI; 2pmol/mg Aβ in 98-years-old
V	+Inferior temporal	12	76~98 (89 ± 7)	0 (2), 20 (3), 30 (1)	3 ND, 3 vascular demented
VI	+Mid-temporal	11	71~93 (86 ± 7)	0 (1), 54 (1)	1 ND (88-years-old), rest with moderate Aβ load
VII	+Anterior frontal, superior temporal, inferior parietal	15	84~106 (96 ± 6)	High	1 ND (84-years-old, with low tau conc.), 4 (ND or MCI, low tau conc.)
VIII	+Broca area	5	77~91 (87 ± 6)	88 (2), low~high	All demented
IX	+Motor cortex	19	65~100 (81 ± 8)	10~200	All demented
X	+Occipital areas	27	37~90 (74 ± 13)	-	Highest tau conc. in temporal cortex

From the results of both Braak and Braak [1991 and 1997] and Delacourte [1999], tau was found in the brains of young subjects and in the absence of Aβ. In addition, the hippocampal region was shown to be a vulnerable region to tau degeneration. The deposition of Aβ was more widespread with no consistent pattern except for increasing densities in various regions, while tau deposition is progressive and ordered, following along precise anatomic networks. Although Aβ and tau coexist in late stages of AD, they do not correlate well with each other. Although tau concentrations correlated well with cognitive impairment, there were a few subjects that differed from expectations in Delacourte's results. Moreover, based on Delacourte's staging, all subjects investigated had cognitive impairment only after the late tau stages of VII (Table 2.2). This

showed that tau imaging can also be used as a biomarker for early diagnosis of possible AD conversion apart from amyloid imaging.

2.2 Diagnosis of AD

Early detection of possible AD conversion will help patients benefit from early AD intervention and treatment. As the clinical symptoms of AD overlap with other dementia symptoms, it is important to discriminate the type of dementia in order to treat the patients correctly. AD diagnosis is carried out using clinical assessments and various biomarkers of AD. This section explains the various subject groups based on clinical or other assessments, as well as the biomarkers of AD, in particular, amyloid and tau imaging.

2.2.1 Clinical Diagnosis

Up to date, the only definitive diagnosis of AD is post-mortem autopsy, even then there had been conflicting results with the lack of senile plaques or low concentrations of NFT in subjects showing clinical AD symptoms. Clinical symptoms of dementia can be assessed via neuropsychological assessment, such as mini-mental state examination (MMSE) [Folstein et al., 1975], Montreal cognitive assessment (MoCA) [Nasreddine et al., 2005] and clinical dementia rating (CDR). These assessments evaluate the various cognitive domains, such as attention, memory, language, visuospatial function, and executive function. Risk factors for AD such as family history of dementia, ApoE-4 genotype and female gender are also identified during the clinical assessment.

To standardise the diagnosis of clinical conditions, diagnostic criteria have been established by different working groups. The most commonly used criteria are established by the National Institute of Neurological and Communicative Disorders and Stroke (NINCDS) and the Alzheimer's Disease and Related Disorders Association (ADRDA) (NINCDS-ADRDA) to classify the various conditions, including AD [McKhann et al., 2011], preclinical AD [Sperling et al., 2011] and MCI [Albert et al., 2011]. Other working groups include the Diagnostic and Statistical Manual of Mental Disorders (DSM-5), International Working Group (IWG) and National Institute on Aging–Alzheimer's Association (NIA-AA). Subjects are classified into various groups based on the criteria-stated neuropsychological assessment, risk factors and/or other biomarkers. However, different diagnostic criteria defined and termed the various conditions differently (Table 2.3).

Two common clinical conditions are healthy control (HC), where the subject has no memory or cognitive impairment and AD, where the subject had memory, cognitive and functional impairments. With new information from clinical studies, the terms and criteria used to describe and classify the various subject conditions or states have changed over time. For example, the terms "probable/possible AD dementia" or "dementia due to AD" or "dementia of Alzheimer type (DAT)" are introduced to replace "AD" condition. This is because AD clinical conditions overlap with other dementia conditions and definitive diagnosis of AD can only be confirmed via post-mortem autopsy.

Table 2.3: Diagnosis of clinical conditions based on diagnostic criteria

Clinical Symptoms	NINCDS-ADRDA	DSM-5	IWG	NIA-AA
No / Subtle complaints	Preclinical AD	-	Asymptomatic AD / Presymptomatic AD	Preclinical AD
Cognitive impairment but functionally independence	MCI due to AD	MCI due to AD	Prodromal AD	MCI due to AD
Dementia	Dementia due to AD	Probable AD	AD dementia	Dementia due to AD / Possible AD / Probable AD

The purpose of clinical assessment is to identify subjects that are probably AD to provide correct treatment and those who are likely to convert to AD for early disease intervention. The earlier the intervention, the more effective the treatment and the faster the recovery. As such, the critical diagnosis period between pre-clinical AD and mild cognitive impairment (MCI) are very important for early diagnosis of AD.

Pre-clinical or pre-symptomatic AD condition is the state between HC and MCI, where no clinical symptoms can be observed. Mild cognitive impairment (MCI) is the clinical condition in which memory or other cognitive functions are lower than HC but the daily functioning is not hindered or not severe enough to be classified as AD. MCI can be further classified based on memory impairment (amnestic vs. non-amnestic) and the number of cognitive domains involved (single or multiple domains). Amnestic MCI have memory impairment while non-amnestic MCI do not have memory impairment but suffers from other cognitive impairment (e.g. decision-making, visual perception). As MCI is an evolving diagnostic condition, it has been further classified into

"MCI due to AD", "mild AD" or "mild to moderate AD" and "prodromal AD". Subjects classified as MCI due to AD condition have a high likelihood of converting to AD, with positive Aβ results and/or neuronal injury [Albert et al., 2011].

In our study, mild AD is considered under AD, stage I based on the results by Peterson et al. [1999] (Figure 2.3). Mild AD condition has similar memory performance as MCI conditions but other cognitive domains are more impaired than MCI [Petersen et al., 1999]. Even though some groups have classified prodromal AD as an individual state occurring before MCI, some termed it as clinical assessment of MCI, confirmed with a biomarker such as PET imaging (Table 2.3). Therefore, prodromal AD and MCI are considered under the same clinical diagnosis of MCI in our study.

2.2.2 Biomarkers of AD

Neuropsychological assessments may be limited in discriminating the various subject conditions or types of dementia due to overlapping clinical symptoms and subjective interpretation of assessment questions. Some tests like CDR have small scale range (0-3), while some tests like MMSE have large scale range (0-30). The test differed in sensitivity and specificity, as the cutoff thresholds differ for each group at different centers. Moreover, normal ageing also contributes to poorer test scores and varies with the individual, age and other factors. As such, clinical assessments are often carried out with other biological tests or imaging for more evident classification.

Existing biomarkers for AD either target Aβ deposition, tau deposition or neuronal injury (Figure 2.3). Biomarkers of Aβ deposition includes amyloid PET imaging and decrease Aβ1-42 in cerebrospinal fluid (CSF). Similarly, the biomarkers of tau deposition include tau PET imaging and increase tau in CSF (Figure 2.3). Little or no changes in CSF measurements were obtained during the progression of MCI to AD and the clinical phase of AD. Hence, unlike PET imaging CSF measurements cannot be used for staging of AD or tracking disease progression. This may be due to the sensitivity of measurement methods or due to pathology, where the discharge of amyloid and tau into CSF becomes stable. The extraction of CSF for evaluation requires invasive lumbar puncture and hence is not preferred for diagnosis especially in patient subjects. Moreover, such assessments only measure the concentrations of amyloid and tau but do not provide any spatial information of the amyloid and tau distribution in the brain. Biomarkers of neuronal injury include reduced hippocampal volume or increased rate of brain atrophy measured using MRI or

CT, decreased metabolism with [^{18}F]FDG-PET imaging, and reduced blood flow via fMRI or [^{15}O]H_2O-PET imaging etc. (Figure 2.3). Structural changes in the diseased brain can be evaluated via MRI or CT but changes can be subtle until clinical symptoms set in (Figure 2.3).

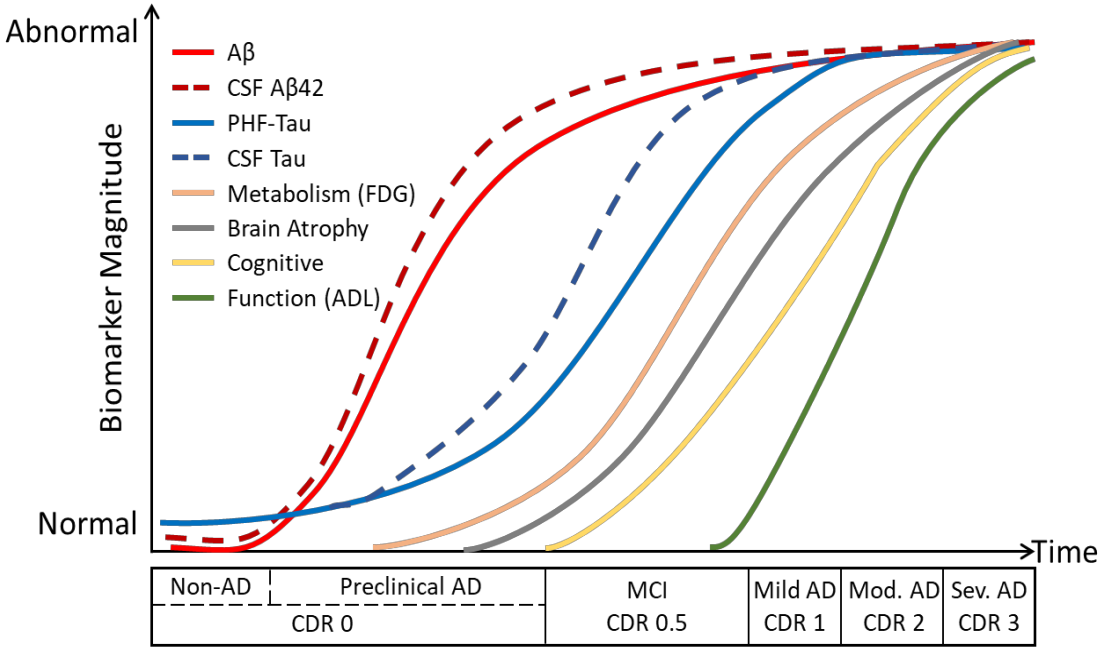

Figure 2.3: Changes in the magnitude of various biomarkers with AD progression.
Aβ = amyloid-beta, NFT = neurofibrillary tangles, CSF = Cerebrospinal fluid, ADL = Activities of daily living, Mod. = Moderate, Sev. = Severe, CDR = Clinical dementia rating.

As Aβ and tau proteins can be found in other types of dementia, amyloid and tau PET imaging can be used for differential diagnosis (Figure 2.4). Differential diagnosis is the process of differentiating two or more diseases or conditions having identical or similar symptoms or target pathologies. A group of neurodegenerative diseases, which pathologically involves tau are called "tauopathies". AD is histopathologically defined by both amyloid and tau proteins only (Figure 2.4). All the other forms of dementia either consists of tau in specific brain regions (e.g. corticobasal degeneration (CBD)) or is also histopathologically defined together with other proteins (Figure 2.4).

Amyloid and tau PET imaging are non-invasive and allows one to measure the *in vivo* spatial distribution of Aβ and tau in the brain quantitatively. As amyloid load shows greater changes in the early stages of AD (Figure 2.3) [Perrin et al., 2009], amyloid imaging allows for early

diagnosis of possible AD conversion and differential diagnosis of various neurodegenerative diseases (Figure 2.4) [Catafau et al., 2015]. However, neuropsychological assessments and amyloid and tau imaging may result in different diagnosis results. Some subjects diagnosed as HC because of the absence of clinical symptoms of dementia may show amyloid uptake similar to that of MCI or AD. As such, in amyloid imaging, the subjects are normally classified into Aβ-positive or Aβ-negative, while subject conditions of HC, MCI and AD are based on neuropsychological assessments.

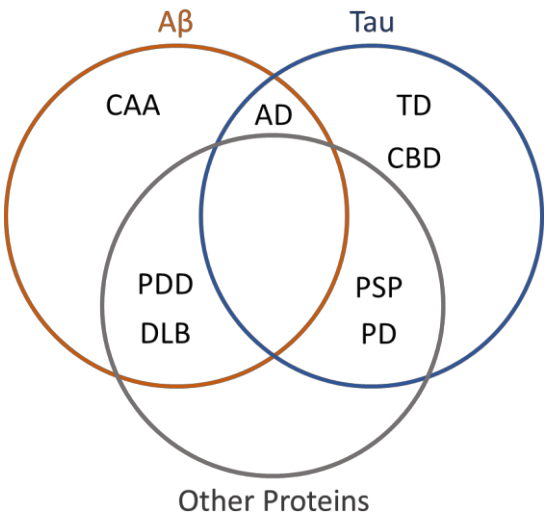

Figure 2.4: Various dementia diseases involving Aβ and/or Tau.
AD = Alzheimer's disease, CAA = Cerebral Amyloid Angiopathy, TD = Tangle-only Dementia, CBD = Cortico-Basal Degeneration, PDD = Parkinson's disease Dementia, DLB = Dementia with Lewy Bodies, PSP = Progressive Supranuclear Palsy, PD = Pick's disease.

For tau imaging, classification of subjects is normally diagnosed together with Aβ-positive/negative results from amyloid imaging. This is because tau was shown to accumulate in the young and in the elderly with normal ageing (section 2.1.3). Using amyloid and tau PET imaging, the concentrations and distributions of Aβ and tau in the brain can be compared with the histopathological staging of AD progression of Braak and Braak or Delacourte (section 2.1.3). This would help to further support diagnosis and progression of clinical conditions especially in the preclinical AD and MCI states.

2.2.3 Clinically-Applied Amyloid & Tau PET radiotracers

Up to date, there are quite a number of amyloid and tau radiotracers that have been developed and

made their way to clinical studies. Yet, only three amyloid radiotracers have been approved by FDA, namely [^{18}F]florbetapir ([^{18}F]AV-45, Amyvid, Eli Lilly & Avid Radiopharmaceuticals, US) [Carpenter et al., 2009], [^{18}F]flutemetamol (GE-067/Vizamyl, GE Healthcare, UK) [Nelissen et al., 2009] and [^{18}F]florbetaben ([^{18}F]AV-1/Neuraceq, Piramal Imaging, Germany) [Rowe et al., 2008], approved in 2012, 2013, 2014 respectively. This section lists some amyloid and tau radiotracers that are applied in human studies.

Amyloid Radiotracers

The first amyloid-targeting radiotracer was [^{18}F]FDDNP developed in 2000. However, it was subsequently found to show binding affinity to PHF-tau, with clinical results showing better correlation to cognitive impairment, similar to that of other tau radiotracers, compared to other amyloid radiotracers. The most well-known amyloid radiotracer was Pittsburg Compound B ([^{11}C]PIB) [Klunk et al., 2004], which is developed by University of Pittsburgh and have been used in research since 2002. However, due to its short half-life of C-11 of 20.4mins, [^{11}C]PIB was only available in hospitals or research centers where there is on-site cyclotron. Thus, the development of ^{18}F-labelled amyloid radiotracers was important to increase the accessibility of PET amyloid imaging for AD diagnosis [Hatashita et al., 2014].

Tohoku university has developed two amyloid-targeting radiotracers, [^{11}C]BF227 [Kikuchi et al., 2010] and [^{18}F]FACT [Furumoto et al., 2013], which had been applied clinically. Other clinically applied amyloid radiotracers included [^{11}C]SB13 [Verhoeff et al., 2004], [^{11}C]AZD2184 [Nyberg et al, 2009], [^{18}F]AV138 [Carpenter et al., 2009], [^{11}C]AZD2995 [Forsberg et al., 2012], [^{18}F]flutafuranol (also known as AZD4694) [Csele´nyi et al., 2012], and [^{18}F]FIBT [Yousefi et al., 2015b]. Radiotracers like [^{11}C]AZD2995 and [^{18}F]AV138 had been applied clinically but were rejected as they were deemed inferior to their respective family radiotracers, [^{11}C]AZD2184, and [^{18}F]florbetapir respectively. There are also other amyloid radiotracers like [^{18}F]MK3328 that have been applied clinically but the results and chemical structures were not reported in the literature.

Tau Radiotracers

Tau radiotracers are developed and applied in clinical studies much later after amyloid radiotracers. The first few tau radiotracers that are applied clinically included a series of THK compounds from Tohoku University: [^{18}F]THK523 [Villemagne et al., 2014], [^{18}F]THK5105 [Okamura et al., 2014], [^{18}F]THK5117 [Harada et al., 2015], [^{18}F]THK5317 [Chiotis et al., 2016]

and [^{18}F]THK5351 [Harada et al., 2016]. Apart from THK compounds, there are three other tau radiotracers that are applied clinically with results reported in literature including [^{18}F]flortaucipir ([^{18}F]T807/[^{18}F]AV-1451, Eli Lilly, US) [Chien et al., 2013] and [^{18}F]T808 (also known as [^{18}F]AV-680) [Chien et al., 2014] developed by Siemens Healthcare (Germany) and [^{11}C]PBB3 developed by National Institute of Radiological Sciences (Japan) [Maruyama et al., 2013]. The ^{18}F-labelled PBB3, [^{18}F]PM-PBB3 (Aprinoia, Japan) has just completed its first in-human studies but the results have yet been reported in the literature. Although there are other tau radiotracers like [^{18}F]MK6420 (Merck, US) that have been applied clinically, the results and chemical structures were not reported in the literature thus far.

2.3 Current Issues in Amyloid & Tau PET imaging

Amyloid and tau PET imaging provides *in vivo* information of the spatial distribution and quantitative concentration of the amyloid and tau load in subjects. However, there are several issues that need to be addressed due to the complex physiology and pathology of amyloid and tau proteins, as well as issues observed in current clinical studies with amyloid and tau radiotracers. In developing a screening methodology for amyloid radiotracers, the availability of *in vitro* data and clinical data need to be considered for model development and validation. In this sub-section, key issues that need to be considered in developing the biomathematical model are discussed.

Different Binding Sites

Amyloid and tau proteins have a few independent binding sites (Figure 2.5), to which different radiotracers bind with different binding affinities. In general, all the evaluated amyloid and tau radiotracers showed high binding affinities to one binding site and low or no binding affinity to others. However, the concentrations of these binding sites on the amyloid and tau proteins are different. High binding affinity to low concentration binding sites will compromise the diagnostic capability of the radiotracer [Lockhart et al., 2005]. Thus far, studies determining the binding affinities of different amyloid radiotracers showed binding to three different binding sites (BS) to both Aβ1-40 and Aβ1-42 proteins (Figure 2.5) [Lockhart et al., 2005; Ni et al., 2013].

BS1 and BS2 are present at high concentrations but BS3 are present at very low concentration (Figure 2.5). Amyloid radiotracers such as [^{18}F]florbetapir, [^{18}F]florbetaben and [^{11}C]BTA-1 showed high binding affinity to BS1 and low binding affinity to BS2, while [^{11}C]BF227 showed high binding affinity to BS3 and low binding affinity to BS1 [Ni et al., 2013]. [^{18}F]FDDNP

showed only binding affinity to BS2. As such, [^{11}C]BF227 might not show high diagnostic capability compared to [^{18}F]florbetapir or [^{18}F]florbetaben due to high binding preference to BS of low concentration. The binding affinities of other amyloid radiotracers to the three different binding sites were not evaluated or reported.

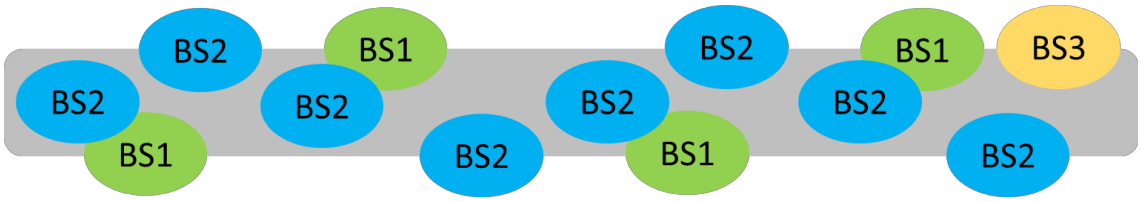

Figure 2.5: Different binding sites (BS) on Aβ protein. [Lockhart et al., 2005]

Tau proteins also showed three possible binding sites [Lemoine et al., 2015] but the concentrations of all binding sites have yet been evaluated. Thus far, only [^{18}F]THK5117 have been evaluated to bind with high binding affinity to one BS and low binding affinity to the second BS, with a possibility of binding to the third BS [Lemoine et al., 2015]. Consideration to the binding preference of the radiotracers to high and low concentration binding sites are preferred but such information is not normally available from the literature. However, the binding affinities of the radiotracers to the types (e.g. Aβ1-40 vs. Aβ1-42) and forms (soluble vs. fibrillary) of amyloid, Aβ) and tau are more important as they are more reflective of the total binding signal in PET measurements. As such, the binding preference of tau radiotracer to Aβ is also important due to the lower concentrations of NFT compared to Aβ plaques.

Differential Binding

In general, the highest concentration of amyloid plaques deposits is found in the frontal cortex [Villemagne et al., 2015]. However, as shown in Braak and Braak's and Delacourte's stagings of AD, amyloid deposition does not follow a consistent spatial pattern (section 2.1.3). In addition, amyloid radiotracers have different affinities ($K_{i2}/K_{i1} > 10$, [Ni et al., 2013]) to different binding sites on both amyloid and tau proteins [Harada et al., 2013].

The highest concentration of PHF-tau deposits is found in temporoparietal cortices [Villemagne et al., 2015]. Although PHF-tau deposition followed a consistent pattern, the tau concentration may vary greatly in subjects regardless of disease severity. Moreover, tau undergoes different post-translational processes in different tauopathies and are present only in certain regions in

different tauopathies (e.g. tau is present in the brainstem in PSP and CBD but not AD) [Villemagne et al., 2015]. The binding of tau radiotracers to non-AD tauopathies have only been evaluated in a few clinically-applied tau radiotracers such as [^{18}F]T807, [^{18}F]THK523 and [^{11}C]PBB3 (Chapter 7). Although [^{18}F]THK523 does not bind to some non-AD tauopathies [Fodero-Tavoletti et al., 2014], and [^{11}C]PBB3 showed distinct selectivity to different tauopathies [Ono et al., 2017], [^{18}F]T807 showed great variation in binding in non-AD tauopathies [Lowe et al., 2016].

PET imaging is unable to discriminate binding to different binding sites on amyloid and tau proteins as it measures all the radioactive signal from the radiolabeled isotope. As such, direct comparison of radiotracers using the same region in the PET image of the same subject is limited. *In vitro* binding information to different binding sites is also limited and measured values vary greatly for low-affinity binding sites. Comparison of radiotracers using measured *in vitro* binding affinity to the highest affinity binding sites might lead to more consistent results than the inclusion of binding affinity to all binding sites.

Binding to Other Proteins

The currently-developed amyloid radiotracers target only fibrillary amyloid plaques, which have β-sheet structures (Figure 2.1B). Likewise, neurofibrillary tangles (Figure 2.2B) and α-synuclein proteins also have β-sheet conformation. As such, specific binding to other targets having similar conformation might arise. Amyloid proteins are much smaller than tau proteins (37~43 vs. 352~441 amino acids), they are present at much higher concentrations of 4~20 times that of tau proteins [Villemagne et al., 2015]. Moreover, amyloid proteins exist in both intracellular and extracellular spaces, in particularly fibrillary amyloid plaques are present in extracellular space, while PHF-tau and α-synuclein proteins are present only in intracellular space. Thus, the quantitative evaluation of amyloid PET images is less affected by specific-binding or NSB to other proteins.

Tau radiotracers, on the other hand, needs to be able to cross the blood-brain-barrier (BBB) and the cell membrane in order to reach the target. On reaching its target, tau radiotracers may bind to amyloid plaques present in the extracellular space. Hence, tau radiotracers require high selectivity of tau over amyloid. A simulation study showed that the selectivity of tau over amyloid needs to be over 20 times in order to accurately discriminate the specific binding to tau from that of amyloid [Schafer et al., 2012].

Off-Target Binding

Candidate radiotracers may bind non-selectively to off-targets [Bittner et al., 2017]. Off-target refers to receptors or enzymes that the radiotracers binds specifically to but are not the target of interest. These off-target sites can be observed if the radiotracer shows uptake in brain regions that are devoid of the target of interest. For example, although tau radiotracers also show binding to amyloid proteins due to similar structural conformation, tau radiotracers also show binding or high uptake in regions devoid of tau and amyloid. These regions are known as off-targets. [^{18}F]T807 was reported to show off-target binding in the midbrain, vessels, iron-associated regions (e.g. basal ganglia), substantia nigra, calcifications in the choroid plexus, and leptomeningeal melanin [Lowe et al., 2016]. Similarly, [^{11}C]PBB3 was reported to accumulate in the venous sinuses [Maruyama et al., 2013] and [^{18}F]THK5351 was reported to accumulate in the basal ganglia [Harada et al., 2016].

Depending on the region of off-target binding, the effects of off-target binding may not limit PET quantification due to little or no anatomical overlap of off-target regions with the target regions of interest (ROIs). Accurate PET quantification is also less affected if the radiotracer has high target selectivity or if the concentrations of off-target binding sites are much lower compared to that of the target [Bittner et al., 2017]. Possible binding to off-targets are difficult to predict and systematic screening is required to determine the binding of the candidate compound to a wide range of proteins. This will increase the time and cost of compound screening.

Cerebellar Binding

Standardised uptake values ratio (*SUVR*) is a semi-quantitative method of PET images and is commonly used for evaluation in amyloid and tau imaging (section 3.2.1). The cerebellum is often used as a reference region using *SUVR* in amyloid PET quantification, due to the low concentration of amyloid in the cerebellum. However, amyloid may accumulate in the cerebellum in the late stages of AD and this may lead to small changes in *SUVR* values in quantitative longitudinal studies. White matter region was reported to lead to more accurate *SUVR* quantification than cerebellum [Landau et al., 2015; Chen et al., 2015], whereby longitudinal increase in *SUVR* was observed using white matter as reference region but not with cerebellum, in MCI and AD [Chen et al., 2015]. The method used for PET quantification is thus important in evaluating the diagnostic capability of the radiotracers.

Reduced Cerebral Blood Flow

Cerebral blood flow (CBF) measurement was proposed as a biomarker for AD in the 1990s as reduced CBF were consistently observed in the temporoparietal regions in AD subjects [Jagust et al., 1997]. However, great variations were observed both within subjects, across the different brain regions, and across different subjects. There were also complications that reduced CBF was due to reduced glucose consumption in the brain. This was later shown to be due to the underlying AD pathological changes, which led to increased oxygen extraction fraction to maintain the cerebral metabolic needs for the brain processes [Nagata et al., 1997]. Yet at the same time, CBF was reported to be preserved despite changes in blood pressure in AD population [van Beek et al., 2012]. Thus far, conflicting changes in CBF and oxygen consumption in early reports and later reports have been reported [Jagust et al., 1997].

Changes in blood flow were reported to affect PET quantification in terms of *SUVR* in longitudinal studies in AD, as the target and reference regions may have different rates of change in CBF [canBerck et al., 2013; Cselenyi et al., 2015]. As such, distribution volume ratio (*DVR*) (section 3.2.3) was proposed as a more consistent method of quantification of PET images than *SUVR*. However, simulation studies showed that the CBF-dependent component in *SUVR* quantification was small and could only explain about 1.5% reduction in longitudinal *SUVR* measurements [Cselenyi et al., 2015]. In these studies, the cerebellum was chosen as the reference region, which might be subjected to changes in amyloid load in dementia subjects. The use of white matter region as the reference region yielded an increase in *SUVR* quantification while cerebellum resulted in a decrease in *SUVR* values in longitudinal studies [Chen et al., 2015]. As such, changes in CBF will not significantly affect PET quantification using *SUVR*.

Non-Specific White Matter Retention

White matter retention led to inaccuracies in cortical *SUVR* measurements [Landau et al., 2014; Villemagne et al., 2012]. The retention was said to occur due to slower white matter clearance compared to gray matter regions [Vandenberghe et al., 2010; Heurling et al., 2015; Villemagne et al., 2012]. Slower washout may be due to the lipophilicity of the radiotracers or due to non-specific binding to myelin sheath [Vandenberghe et al., 2010; Furumoto et al., 2013]. White matter retention was also said to be affected by the spill-over of higher gray matter uptake on neighbouring white matter regions [Landau et al., 2014]. Although some reported higher white matter retention using ^{18}F-labelled radiotracers [Landau et al., 2014; Vandenberghe et al., 2010], others reported no difference in white matter retention from their ^{11}C-equivalent compounds

[Shidahara et al., 2015]. However, some studies have showed that the amount of white matter retention was independent on the amount of amyloid load present in the subjects as supported by the lack of differences in white matter retention between HC and AD [Vandenberghe et al., 2010; Furumoto et al., 2013; Cselenyi et al., 2012; Villemagne et al., 2012].

Studies have also reported that white matter retention did not limit the quantification of cortical uptake of some amyloid PET radiotracer [Vandenberghe et al., 2010; Barthel et al., 2011; Villemagne et al., 2012]. The *SUVR* measurements in the white matter do not correlate with cortical *SUVR* measurements and white matter modifications may be due to normal ageing or other diseases [Nemmi et al., 2014]. Similarly, although PHF-tau is also found in high concentrations in subcortical white matter region in AD [Villemagne et al., 2012], quantification of tau PET images was not shown to be limited.

Metabolites Crossing BBB

The parent radiotracer is metabolised in the body and its resulting metabolites may cross the BBB. In such cases, the presence of metabolites will affect PET quantification if the radioisotope is attached on the metabolite, as the measured PET signal comes from both the parent and the metabolites. Moreover, the binding selectivity and affinity of the metabolite to the target binding sites may be different from that of the parent. Metabolites analysis is thus important for any new radiotracers to ensure accurate quantification of PET signal. Thus far, only the metabolite of one clinically-applied amyloid PET radiotracer, [^{18}F]FDDNP was reported to cross the BBB [Yaqub et al., 2009]. For tau radiotracer, radiolabeled metabolites of [^{11}C]PBB3 [Kimura et al., 2015] was reported to cross the BBB. Although metabolite analysis is important, reliable methods of predicting possible metabolites crossing the BBB has yet been identified or proposed.

2.4 Summary

In this chapter, the basic physiology and pathology of amyloid and tau proteins are explained, followed by spatial distribution of both amyloid and tau proteins with AD progression. The various biomarkers and existing clinical diagnosis of AD conditions are described to discriminate the terms used to define the various subject conditions. Lastly, existing clinically-applied amyloid and tau PET radiotracers are described with a discussion on the key issues observed in clinically-applied amyloid and tau imaging to understand the possible complications in model development. Although overcoming these issues during model development is ideal, there are difficulties in

overcoming some of these issues, especially in predicting metabolites crossing the BBB. To develop an accuracy and precise model in predicting the *in vivo* performance of the radiotracers, careful consideration into the use of various types of *in vitro* and *in silico* parameters is important.

Chapter 3

Quantification of PET Images & Biomathematical Models

Quantification of amyloid and tau PET images is affected by the methods of image processing and analysis. The basics of PET and some methods of quantification of PET images in amyloid and tau imaging are described. A brief description of some properties of successful PET radiotracers that are commonly evaluated during in vitro assay and preclinical phase of radiotracer development process is provided. Various biomathematical models exist but few were developed for the purpose of predicting the in vivo pharmacokinetic behaviour of diagnostic radiotracers. Although there are a few existing biomathematical models related to amyloid radiotracers, they were focused on predicting the changes in amyloid load with AD progression. Two such existing biomathematical models are discussed and compared in this chapter.

3.1 Positron Emission Tomography (PET)

In this section, the fundamentals of PET physics are described in the following order: starting from the physical basis of PET, data acquisition on the PET scanner, correcting the PET data and finally PET image reconstruction.

3.1.1 Physical Basis of PET

A positron (β+) is a positively-charged electron that is emitted from the nucleus of an unstable radioisotope due to the presence of excessive protons and a positive charge. After positron emission, the unstable radioisotope becomes stable by converting the proton to a neutron, hence removing the positive charge. The positron emitted from a radionuclide collides with a nearby electron to produce two photons or gamma rays of 511 keV (kilo-electro-voltage). This process is called annihilation (Figure 3.1). The gamma rays are emitted at approximately 180° to each other and the path that they travelled is called the coincidence line (Figure 3.1). It is the detection of the coincidence events that provide the unique scheme for forming tomographic images using the PET scanner.

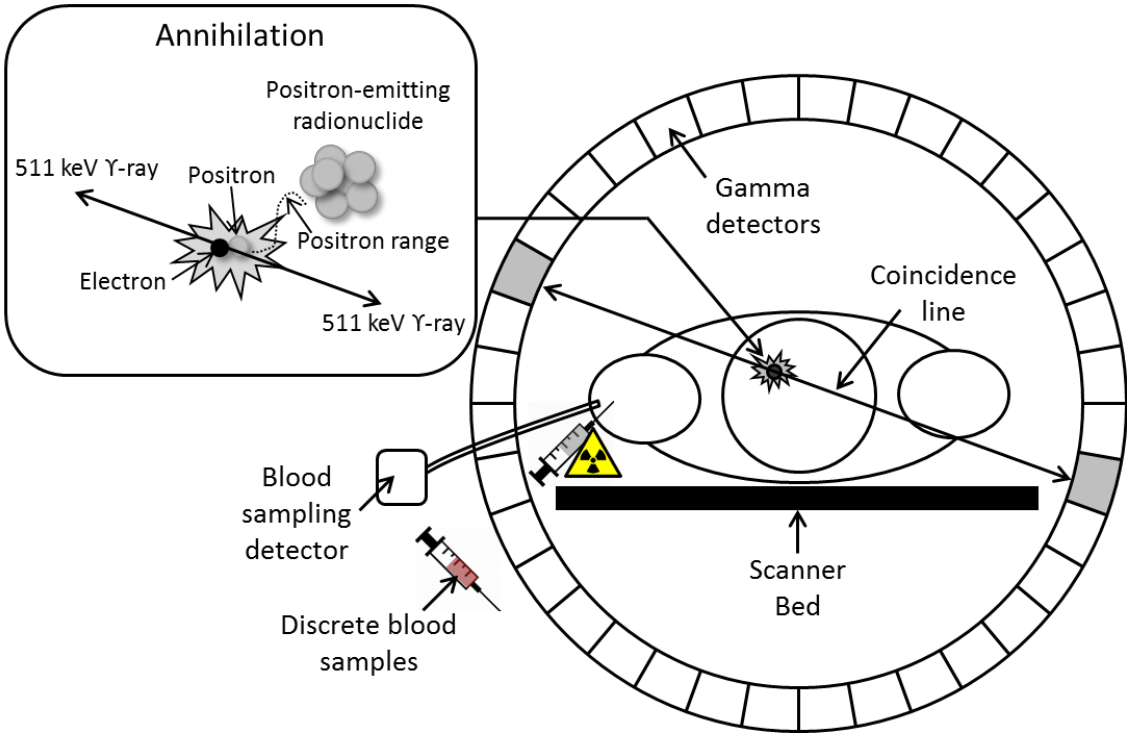

Figure 3.1: Image of a PET scan with details of positron-emission annihilation.

After the positron is emitted from the radionuclide, it travels some distance before colliding with an electron. The distance travelled is known as the positron range (Figure 3.1) and contributes to the uncertainty of the localisation of the decaying radionuclide. The higher the energy of the positron emitted, the larger the positron range. The list of commonly-applied radioisotopes in PET and their respective mean positron ranges and the half-lives of their isotopes are shown in table 3.1. After annihilation, the emitted gamma rays may not travel at exactly 180° to each other. These two factors thus lead to lower spatial resolution of the PET scanner.

Table 3.1: Commonly-applied positron emitting isotopes in PET studies [Valk et al., 2004]

Isotopes	$t_{1/2}$	Mean Positron Range (mm)
^{18}F	109.8 min	0.6
^{11}C	20.4 min	1.1
^{15}O	2.04 min	2.5
^{13}N	9.97 min	1.5
^{64}Cu	12.7 hours	0.56
^{68}Ga	68.1 min	2.9
^{124}I	4.2 days	3.4

3.1.2 Data Acquisition

In a PET scan, the radiolabeled compound is injected intravenously into the subject (radiolabeled syringe in Figure 3.1). The radiolabeled compound then travels throughout the human body into the various organs and undergoes various processes such as metabolism, absorption and excretion. The position of the radioisotope in the body reflects the distribution of the radioisotopes. It can be determined by detecting the photons emitted during the annihilation of positron emitted from radionuclide with a nearby electron in a PET scanner (Figure 3.1).

Each 511 keV gamma-ray emitted is detected by the gamma detectors (Figure 3.1), which then converts the gamma rays into light photons. The light photon is converted into electrons, which then pass through a photon-multiplier tube (PMT) or semiconductor-based photodiodes, where the signal gets amplified and converted into electrical signals. The electrical signals from each detected event are recorded by the PET scanners, in terms of time of acquisition, the energy of each detected photons and the angular and linear positions of detecting an event. A time window is set on the PET scanner to identify coincidence events.

All the coincidence events detected by the PET scanner are stored in either list-mode data format or sinogram data format. The list-mode format stores all coincidence events, while the sinogram format stores the averaged counts within a predefined time window or PET frame. List-mode data are rebinned into sinogram data after the PET scan with the user-defined time window.

3.1.3 Data Correction

Before the sinogram data is reconstructed into PET image, the data needs to be corrected for radioactive decay and effects of attenuation, scatter and random on photons (Figure 3.2). As the correction of the PET data is not the focus of this project, only the sources of error are described.

Radioactive Decay

All radioisotopes will undergo decay and the rate of decay is dependent on the half-life of the radioisotope (Table 3.1). The shorter the half-life, the faster the rate of radioactive decay, where the activity of the radionuclide, with a half-life of $t_{1/2}$, after a time period, t is:

$$A_t = A_0 e^{-\lambda t}, \quad (1)$$

where A_0 is the initial radioactivity and $\lambda = \ln(2)/t_{1/2}$

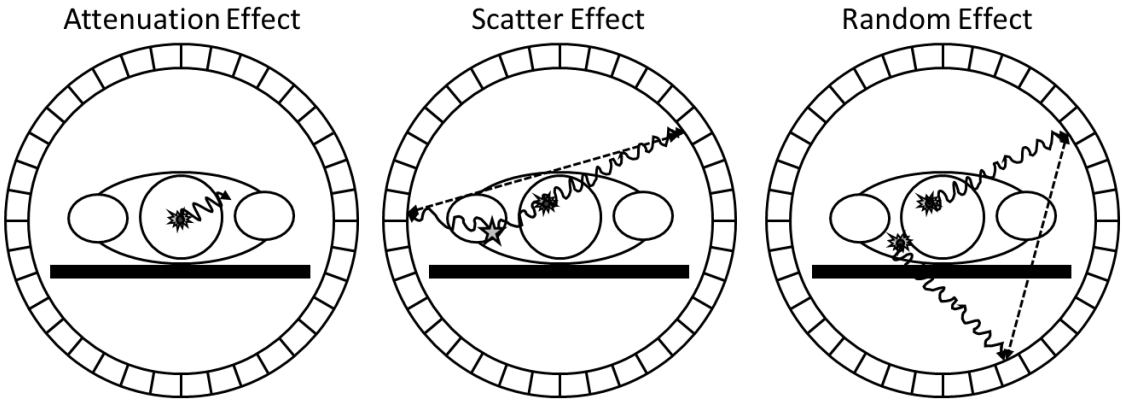

Figure 3.2: Effects of attenuation, scatter and random.

Photon Attenuation

As the emitted gamma rays or photons travel through a medium to reach the detectors, the photons are either absorbed or scattered (Figure 3.2). This leads to a reduction in the number of coincidence photons detected by the PET detectors. The magnitude of photon attenuation is expressed as:

$$\emptyset = \emptyset_0 e^{-\int_s \mu(x,y)ds}, \quad (2)$$

where $\emptyset_0$ and $\emptyset$ are the numbers of incident and transmitted photons per unit area and *ds* is the differential thickness of the medium through which the annihilated photons travel along the path *S*. μ is the linear attenuation coefficient (cm^{-1}), which is the probability that a photon will undergo an interaction when it passes through a unit thickness of tissue. The probability of photon attenuation is dependent on the photon energy, and the density and size of the object or medium through which the photons transverse. Therefore, a medium with a higher density or a greater size will result in a greater amount of photon attenuation.

The attenuation correction (AC) of the PET data involves determining a μ-map, which consists of the spatial information of the μ-values of the object within the field of view (FOV) of the PET scanner [Zaidi et al., 2003]. AC methods can be classified into transmissionless and transmission methods. Transmissionless methods involve the application of a μ-map (1) containing a uniform distribution of specified μ-values within a known volume or (2) determined by the segmentation of the PET emission data [Zaidi et al., 2003]. Transmission methods require transmission imaging with (1) a single-photon source (e.g., ^{137}Cs, ^{57}Co), (2) a coincidence-photon source (e.g., ^{68}Ge-^{68}Ga) or (3) X-ray CT, to determine the μ-map. The attenuation correction of a PET image is normally carried out using a CT image in clinical studies in a hybrid PET-CT scanner. MRI images

have also been used to correct for attenuation of PET images in a hybrid PET-MRI scanner.

Photon Scattering

Apart from attenuation, photons also undergo scattering as they travel through a medium (Figure 3.2). The photons are scattered by Compton scattering, which is the interaction between an incoming photon with a loosely-bound outer shell electron, which resulted in a change in direction of the incoming photon and the ejection of the collided electron from the atom. The photon lost some of its energy to the electron, resulting in energy lower than 511 keV. This effect occurs in the energy range of 100 keV and 2 MeV.

Random Coincidence

The random effect occurs when two events from two different annihilation events are detected by the PET scanner as a coincidence event (Figure 3.2). This effect arises when the coincidence defined timing window is too large such that two temporally close events are detected as coincidence events. This leads to a false coincidence events and normally adds to background counts, hence reducing the signal-to-noise ratio (SNR) of the PET data. The random coincidence is commonly corrected using delayed time window or single count rate methods.

3.1.4 Image Reconstruction

The raw data from the list-mode data or, more commonly from the sinogram data, is reconstructed to form 3D/4D PET images. There are many reconstruction methods, of which filtered-back-projection (FBP) is most commonly applied and is often used as a standard reconstruction method for PET scanner evaluation. Essentially, all the measured activities along each line-of-response (LOR) are back-projected through the image to obtain an approximation of the “true” image. LOR is the straight line connecting the centers of two gamma detectors. The use of back-projection results in star artefacts, which can be reduced by means of a high-pass filter, such as ramp, Hamming, Hanning etc. However, the use of a filter may also introduce additional degradation of the spatial resolution of the scanner (e.g. a filter with a too high cutoff value introduces noise).

Although FBP is commonly applied and results in reliable quantitative PET image, the image is noisy and has poor SNR and hence poor image contrast for quantification of small regions of interest (ROIs). Other reconstruction methods exist, which relies on iterative algorithms such as Order-Subset Expectation Maximization (OSEM) and Maximum Likelihood Expectation Maximisation (MLEM). These reconstruction methods result in images of higher SNR due to

lower noise in the background but can be computationally intensive and time-consuming due to a large number of iterations required until an optimised solution can be obtained.

There are no optimal reconstruction methods and some methods may be preferred over others depending on the SNR, consistency of the evaluated data across subjects, the processing time required, available reconstruction methods on the PET scanner etc. However, it is important to ensure all PET images analysed within a study are reconstructed using the same image reconstruction algorithm for accurate comparison.

3.2 Quantitative Analysis of PET

Quantitative analysis of PET images can be divided into two categories: (1) with plasma input function and (2) without plasma input function. In amyloid and tau imaging, standardised uptake values ratio (*SUVR*) is commonly employed as it does not require any plasma input function. In this section, *SUVR*, arterial blood sampling and analysis with plasma input function using one tissue and two tissues compartmental models are described. The derivation of distribution volumes ratio (*DVR*) and BP_{ND} are also explained.

3.2.1 Standardised Uptake Values Ratio (*SUVR*)

After image reconstruction on the PET scanner, images are transferred from the scanner to other computers for further image processing (Figure 3.3). This includes correcting for patient motion in dynamic 4D PET images, reducing noise and/or partial volume effect (PVE). The PET images are often co-registered to other images for anatomical information (e.g. MRI or CT image). Image processing can be carried out using available software, commercialised (e.g. PMOD), free (e.g. Statistical Parametric Mapping (SPM)) or in-house developed programs.

Regions of interest (ROIs) are then drawn on a 3D or summed 4D PET images, or on anatomical images (e.g. MRI or CT images). ROIs are then applied to the static PET image to obtain the radioactivity concentrations in each ROI, or to the dynamic PET images to generate time activity curves (TACs) for each ROI (Figure 3.3). For PET brain imaging, important brain regions may be small and hence, high spatial resolution MRI images are acquired together with PET imaging to clearly delineate ROIs. ROIs can be generated in three ways: (1) manually drawn by an experienced operator, (2) semi-automatically using predefined small ROIs placed manually by an experienced operator, or (3) automatically using standardised atlas templates normalised to the

subject's MRI image.

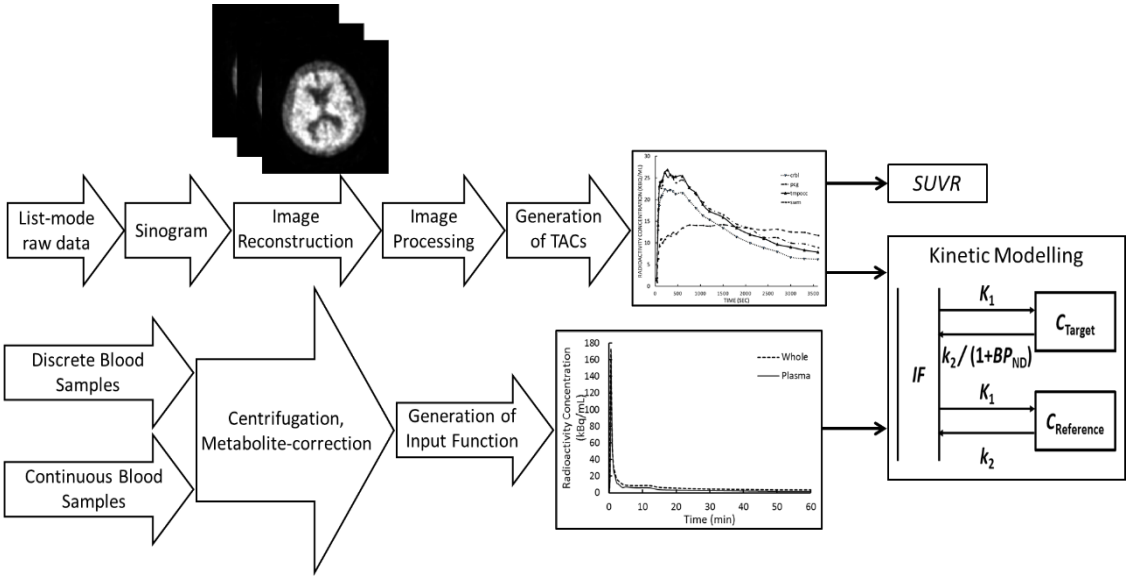

Figure 3.3: Process flow of acquisition, reconstruction and processing of PET Data, with arterial blood sampling to obtain plasma input function for full quantitative PET analysis.

Standardised uptake value (*SUV*) is a semi-quantitative index reflecting the radioactivity uptake in a region or volume of tissues. It is calculated using the measured radioactivity concentration (C_t) in the ROI of the PET image, corrected for injected dose (*ID*, Bq) and normalised by the distribution volume of the tracer, using either body weight (*BW*) or body surface area (*BSA*) [Adams et al., 2010]:

$$SUV_{BW} = \frac{C_{Measured}}{ID \ / \ BW} \tag{3}$$

As *SUV* is subjected to many factors, standardised uptake value ratio (*SUVR*) is often employed by taking the ratio of the *SUV* measured in the target to that of a reference region in a 3D PET image. In a dynamic PET scan, the radioactivity concentrations in an ROI is measured over time to generate the tissue time activity curves (TACs) (Figure 3.3). For some radiotracers, certain brain regions show only non-specific binding or low uptake due to the lack of target expression. These regions can be used as a reference region in *SUVR* evaluation. For example, in amyloid imaging, the cerebellum is often chosen due to the low amount of amyloid found in this region. *SUVR* is determined as the ratio of the area under the TAC curve of the target region to that of the reference region within a specified time window for dynamic 4D PET images.

$$SUVR = \frac{SUV_{Target}}{SUV_{Reference}} = \frac{AUC_{Target}}{AUC_{Reference}} \quad (4)$$

SUVR is a semi-quantitative method and is dependent on many factors such as the choice of time window and reference region. However, it does not require any arterial blood sampling, which it is invasive and painful to subjects. It can also be quantified using PET data acquired within a short period of time, thus reducing the burden on the subject to lie still. Moreover, it can be applied easily, which renders its application popular among physicians for the diagnosis of their patients.

3.2.2 Arterial Blood Sampling

Arterial blood samples are required to determine the input function for compartmental analysis of the PET images (Figure 3.3). An input function describes the concentration of the unchanged radiotracer in the arterial plasma or blood as a function of time. Arterial blood samples are collected either continuously using a blood pump and a gamma counter or discretely using manually drawn samples with a syringe (syringe filled in red colour in Figure 3.1). Continuous arterial blood sampling provides the full whole blood curve with time, while discrete blood sample provides only time-point measurements of the radioactivity concentrations in the blood.

In a PET imaging study that requires arterial blood sampling, both PET data acquisition and arterial blood sampling often start instantaneously together after the intravenous injection of the radiolabeled compound into the subject. Continuous arterial blood sampling is generally preferred to capture the peak of the input function curve. If continuous sampling is not possible, many discrete samples are taken within short time interval at the beginning of the PET scan to capture the peak of the input function curve and few discrete samples are taken with longer time interval afterwards. A combination of both continuous sampling at the beginning of the PET scan and discrete blood sampling can also be applied to reduce the burden on subjects.

A few discrete blood samples are still required to determine the plasma to whole-blood fraction and the parent-metabolite fraction. The plasma is separated from the whole blood from the discrete blood samples by centrifugation. The radioactivity concentration in the plasma is then measured with a gamma counter. The parent-metabolite fraction is then measured by chromatographic methods using the plasma samples. The whole blood radioactivity concentration curve is converted to the plasma radioactivity concentration curve (consists of both parent compound and its metabolites), which is then corrected for metabolites using the parent-

metabolite fraction to obtain the plasma input function of the parent radiotracer.

As arterial blood sampling is both painful and invasive to the subject being scanned, alternatives have been proposed using venous sampling and image-derived input function. These alternatives require correction to match the plasma input function generated using arterial blood sampling. In PET quantification where a reference region exists, blood sampling may not be required and reference kinetic modelling or semi-quantitative methods such as *SUVR* may be applied. However, for full PET quantification when no reference region exists, arterial blood sampling is required.

3.2.3 Compartmental Models

The pharmacokinetics of a radiotracer can be evaluated using compartmental models describing the uptake of the radiotracer from the arterial capillaries into the brain tissues, the washout of the radiotracer from the brain tissues into venous capillaries and the specific and/or non-specific binding to various targets in the brain tissues. Compartments are used to represent a biological space such as the plasma or brain tissues. The tissue compartment can be used to represent three conditions of the radiotracer in the brain tissues: freely-moving (C_F), non-specifically bound (C_{NS}) and specifically-bound (C_S) (Figure 3.4), where C refers to the radioactivity concentration of the radiotracers under these conditions.

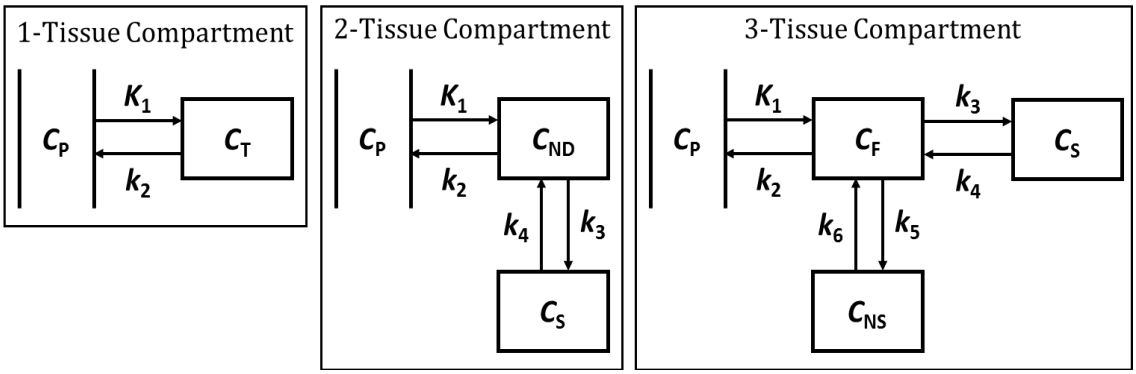

Figure 3.4: One tissue, two-tissue and three-tissue compartmental models

The radioactivity concentration measured from the PET image is a mixture of signals from the radiotracer under these three conditions in the tissue compartment and in the plasma compartment. The three behaviors of the radiotracer in tissues can thus be explained using the three-tissue compartments (3TCM) (Figure 3.4), whereby the radiotracer moves from the plasma compartment (C_P) into the free compartment (C_F) where it then either binds specifically (C_S) or

non-specifically (C_{NS}) to various targets in the brain tissues.

In cases where the free and the non-specifically-bound (NSB) compartments equilibrate very rapidly, it can be difficult to distinguish these compartments. They act as a single compartment, known as the non-displaceable compartment ($C_{ND} = C_{NS} + C_F$). In this case, only two tissue compartment exist and is termed as 2TCM (Figure 3.4). Similarly, when the non-displaceable and specifically-bound compartments equilibrate very quickly, these compartments can be treated as a single compartment ($C_T = C_S + C_{ND}$) in the 1TCM (Figure 3.4). All the compartment models in figure 3.4 show reversible binding, whereby the radiotracer goes back to the compartment that it came from. In this case, equilibrium is achieved within the PET acquisition time.

The transfer of the radiotracer from one compartment to another is represented by micro-parameters, known as the rate constants (Figure 3.4). These rate constants describe the rate of change of the radiotracer concentration or the proportion of radiotracer moving into or out of one compartment per unit time. In PET kinetic models, rate constants are represented by '*k*' and have the units of min^{-1} in the brain tissues. The rate of uptake of the radiotracer from the plasma (C_P) is represented by K_1 and has a unit of (mL of plasma/cm^3 of brain tissues/min) to reflect its relation to the plasma compartment and capitalised to discriminate it from other rate constants.

The 3TCM explains all the possible behaviour of a radiotracer in the tissues and is the ideal model for use. However, these rate constants can be difficult to estimate accurately due to the noise in the PET data. This is particularly so using the 3TCM where there are six rate constants to determine (Figure 3.4). Therefore, the 1TCM and 2TCM are generally used for evaluation. The respective rate of change of radioactivity concentrations of the C_T, C_S and C_{ND} compartments can be described using differential equations and rate constants:

1TCM: $$\frac{dC_T(t)}{dt} = K_1 C_P(t) - k_2 C_T(t) \quad (5)$$

2TCM: $$\frac{dC_S(t)}{dt} = k_3 C_{ND}(t) - k_4 C_S(t) \quad (6)$$

$$\frac{dC_{ND}(t)}{dt} = K_1 C_P(t) - k_2 C_{ND}(t) - k_3 C_{ND}(t) + k_4 C_S(t) \quad (7)$$

The solutions to the above differential equations for 1TCM and 2TCM are as follows:

1TCM: $$C_T = K_1 \cdot e^{-k_2 \times t} \otimes C_P \quad (8)$$

2TCM: $C_{\mathrm{T}} = \mathrm{C_S} + C_{\mathrm{ND}}$

$$C_{\mathrm{T}} = \frac{K_1}{(\beta_2 - \beta_1)}\left[(k_3 + k_4 - \beta_1)e^{-\beta_1 \times t} + (\beta_2 - k_3 - k_4)e^{-\beta_2 \times t}\right] \otimes C_{\mathrm{P}} + V_{\mathrm{B}} C_{\mathrm{P}} \quad (9)$$

where $\beta_{1/2} = \frac{(k_2+k_3+k_4) \mp \sqrt{(k_2+k_3+k_4)^2 - 4k_2k_4}}{2}$, V_{B} = fractional blood volume

In kinetic modelling, the total radioactivity counts in the tissues from PET image (C_{T}) is fitted using an appropriate tissue compartment model (Figure 3.4) with the input function measured from arterial blood sampling (C_{P}). The rate constants are then estimated from the solutions of the differential equations by minimising the residual sum of squared errors using nonlinear least squares. The model that resulted in the best fit to the measured PET data is then determined using selection criteria such as Akaike Information Criterion (AIC), Schwarz Criterion (SC), and F-test.

Due to the huge variations in the estimated rate constants, macro-parameters, such as the volumes of distribution and binding potentials are often estimated to determine the behaviour of the radiotracers. The volume of distribution (V_{T}, mL.cm^{-3}) represents the volume of the radiotracer distributed in a tissue compartment (C_{T}) that is equivalent to the volume of radiotracer distributed in plasma compartment (C_{P}) at equilibrium. It can be derived from using the rate constants from 1TCM and 2TCM respectively:

1TCM: $$V_{\mathrm{T}} = \frac{K_1}{k_2} \quad (10)$$

2TCM: $$V_{\mathrm{T}} = \frac{K_1}{k_2}\left(1 + \frac{k_3}{k_4}\right) \quad (11)$$

For some radiotracers, reference regions exist when there are certain brain regions that do not have the target of interest. The distribution volume ratio (DVR, unitless) can be derived from the ratio of the volume of distribution (V_{T}) in the target region to that of the reference region.

$$DVR = \frac{V_{\mathrm{T,target}}}{V_{\mathrm{T,reference}}} \quad (12)$$

Binding potential (BP) represents the radioactivity concentrations of the specifically-bound compartment to that of a reference compartment. Three forms of BP exist, namely BP_{F}, BP_{P} and BP_{ND}, whereby the subscript represents the reference compartments of the free radiotracer in the tissue compartment, parent radiotracer in plasma (free and plasma protein bound) and non-displaceable compartments. Depending on the target of interest and the type of radiotracer, these

parameters are determined accordingly. BP_{ND} and DVR are macro-parameters that reflect the binding to the target and accounts for changes in blood flow unlike $SUVR$ (section 3.2.1). In amyloid and tau imaging, BP_{ND} is commonly evaluated, which represents the ratio of the radioactivity concentration in the specifically-bound compartment to that of the nondisplaceable compartment. BP_{ND} can also be estimated using DVR, where $DVR = V_T/V_{ND}$ in 2TCM.

$$BP_{ND} = \frac{C_S}{C_{ND}} = \frac{V_S}{V_{ND}} = \frac{V_T - V_{ND}}{V_{ND}} = DVR - 1 \tag{13}$$

3.3 Properties of Successful PET radiotracers

To predict the *in vivo* pharmacokinetics performance of a radiotracer, the key physicochemical and pharmacological parameters of the radiotracer needs to be identified. Properties of successful PET radiotracers commonly evaluated during *in vitro* testing are described in this section.

A successful PET radiotracer must be able to reach the target sites. For target sites within the brain, the radiotracer needs to be able to cross the blood-brain-barrier (BBB). The uptake across the BBB is commonly described by the Renkin and Crone model (Figure 3.5). It describes the relationship between blood flow or perfusion, f and the amount of substance crossing the BBB, as represented by the product of permeability (P) and the capillary surface area (S).

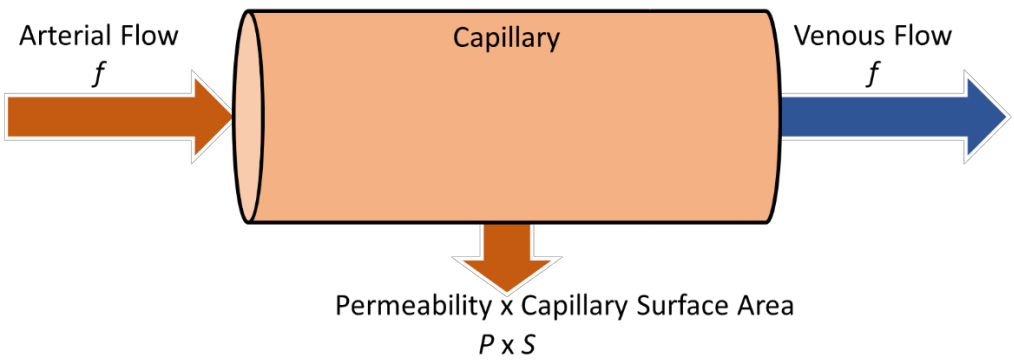

Figure 3.5: Renkin and Crone Model

The most common route of transport from the capillary into the brain tissues across the BBB is by passive diffusion. However, the hydrophilic phosphate head and the hydrophobic tails of the lipid bilayer prevents molecules that are too hydrophobic or too hydrophilic from crossing the BBB (Figure 3.6). Moreover, the tight junction between the endothelial cells and tight packing of the lipid bilayer prevent large molecules from crossing the BBB (Figure 3.6). Thus, permeability

is dependent on the lipophilicity and size of the compound molecule for passive diffusion across the BBB.

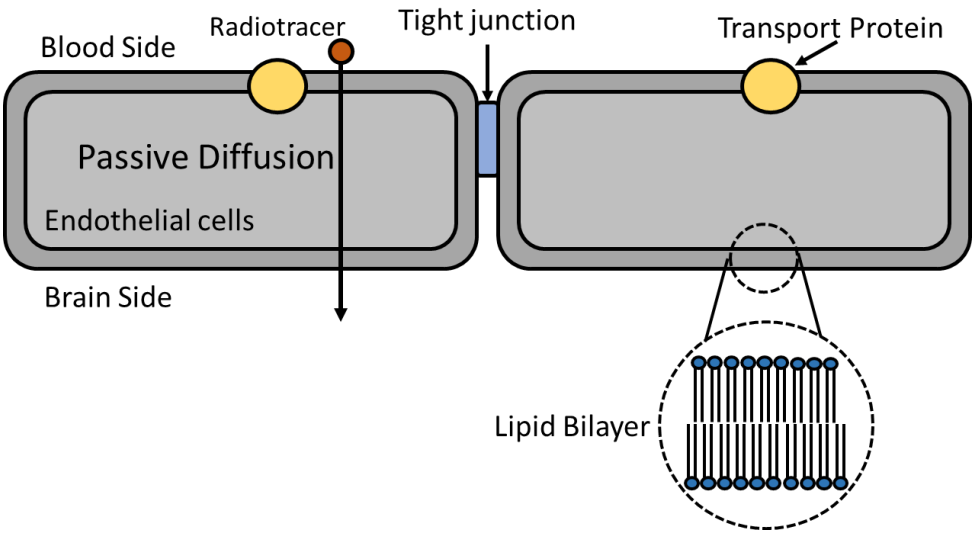

Figure 3.6: The blood-brain-barrier (BBB).

A PET radiotracer must be able to be administered safely at tracer dose without any toxic or side effects. To accurately measure the target of interest, the radiotracer needs to have high selectivity for the target of interest and preferably have high specific to nonspecific binding ratio. The binding affinity of the radiotracers to target sites are normally represented using the dissociation constant, K_D, which is the inverse of binding affinity. The binding of the radiotracers to the target sites is also dependent on the target binding site concentrations, B_{avail}. If there is low target binding site concentration, high amount of binding to non-specific or other specific binding sites will occur. This will lead to inaccurate measurement of the target of interest.

Free fraction in plasma (f_P) and free fraction in tissue (f_{ND}) are important parameters in drug discovery and development since the free drug hypothesis was proposed and accepted. The free drug hypothesis states that only the free or unbound drug is available for distributions and interactions and hence it is the free drug and not the total drug that is able to exert the pharmacological effect at the target region (Figure 3.7) [Wan et al., 2007; Di et al., 2011, Zhang et al., 2012].

Within the blood stream, the radiotracer may bind to the plasma proteins and high protein binding leads to lower amount of radiotracer crossing the BBB (Figure 3.7). The fraction of free radiotracers that can cross the blood-brain-barrier is represented by the free fraction in plasma, f_P.

Similarly, within the tissues, those that free-moving or binding nonspecifically to non-specific sites are represented by the free fraction in tissues, f_{ND} (Figure 3.7). At equilibrium, the ratio of the free drug concentrations will be the same in both tissues and plasma at equilibrium for passively-diffused drugs [Di et al., 2011], which is also equivalent to the rate of uptake to the rate of clearance [Guo et al., 2009].

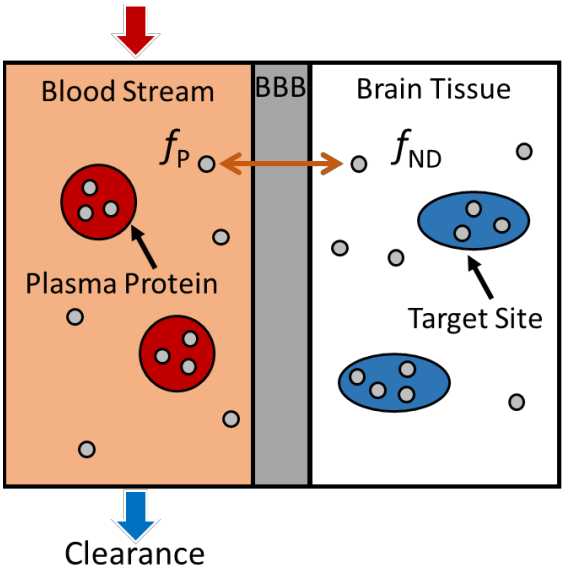

Figure 3.7: Free drug hypothesis showing that only free or unbound drug/radiotracer is available for distributions and interactions, as well as the binding of drug/radiotracers to plasma protein within the blood stream and to target sites within the brain tissues.

Although the free fractions in plasma and tissues are deemed important parameters for evaluation, they are not as commonly measured during *in vitro* and preclinical testing phase. This is because *in vitro* measurements of these two parameters via the gold standard, equilibrium dialysis (section 4.3) are time-consuming and tedious and may be subjected to huge variations in measurements. Dissociation constant, binding sites concentrations and lipophilicity are more commonly reported in literature, compared to free fractions in plasma and tissues.

3.4 Biomathematical Models for Radiotracer Development

The purpose of this project is to develop a biomathematical model to support the development of amyloid and tau radiotracers. Although quite a number of biomathematical model exists, most were either developed to support other types of radiotracer development (e.g. Central Nervous System, CNS) or to predict disease progression. In this section, two biomathematical models are described. The first is a biomathematical model developed to predict the *in vivo* pharmacokinetics

performance of CNS radiotracers in terms of BP_{ND}, using a simplified 1TCM. The second applies 4-tissues-compartmental models to simulate the binding selectivity required for tau radiotracers such that the measured PET data clearly reflects tau binding and not amyloid binding.

The focus of this section is to compare and determine the backbone of a biomathematical model for amyloid radiotracers. Thus, only a brief explanation on the various physicochemical and pharmacological parameters of a radiotracer is provided. Details are provided in the next chapter.

3.4.1 Guo's CNS Model

Guo et al. [2009] developed a biomathematical model (Figure 3.8) to predict the *in vivo* kinetic performance of radiotracers targeting the CNS. The model was based on the simplified 1-tissue-compartment model (1TCM), with a simple uptake and washout from the reference region without any binding, while the target region showed binding to targets with similar uptake and washout as the reference region (Figure 3.8).

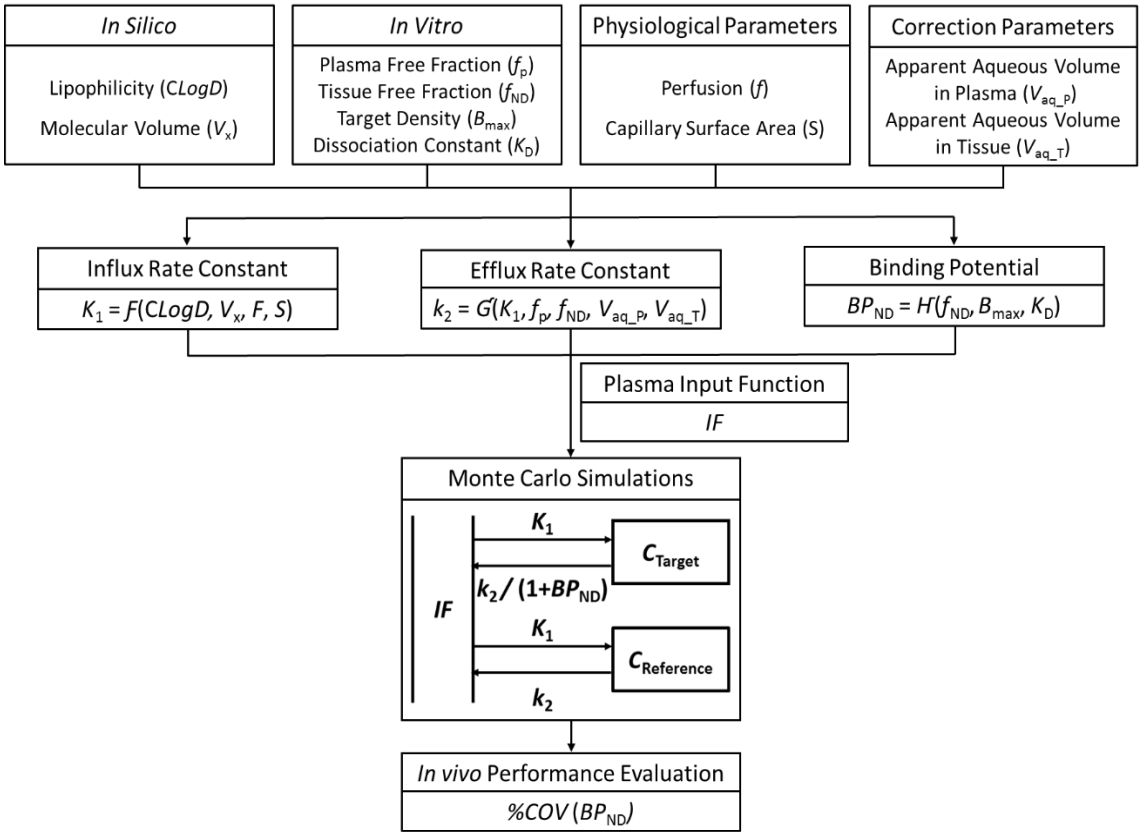

Figure 3.8: Overview of Guo's CNS biomathematical model.

Guo's biomathematical model comprises of three sections starting with the (1) determination of important physicochemical and pharmacological parameters of the radiotracer for (2) prediction of 1TCM kinetic parameters of K_1, k_2 and BP_{ND} to (3) simulate TACs of the target and reference regions using the respective plasma input functions (Figure 3.8). The *in vivo* performance of each radiotracer was assessed using Monte Carlo simulations by varying the predicted K_1 and k_2 values to obtain 1000 estimated BP_{ND} values and determining the coefficient of variance (*COV*) (section 6.1.1).

The basic assumptions underlying compartmental modelling are applied: (1) the radiotracer concentration in the compartment is homogeneous, (2) physiological processes and molecular interactions are constant, (3) all compartments equilibrate quickly, and (4) the radiotracers cross the BBB by passive diffusion [Guo et al., 2009]. A standard plasma input function was applied for simulation, which was shown to have little impact on outcome BP_{ND} values.

3.4.1.1 Inputs of Biomathematical Model

Guo et al. [2009] identified two *in silico* and four *in vitro* physicochemical and pharmacological parameters of a radiotracer that would affect its *in vivo* performance (Figure 3.8) [Guo et al., 2009]. *In silico* data refers to data that are determined via computer simulations. *In vitro* data are determined from experiments measured using microorganisms, cells or tissues, while *in vivo* data are measured within the living subjects by means of medical imaging equipment.

Lipophilicity is represented by calculated *LogD* (C*LogD*, unitless), which is the *in silico* logarithm of the distribution coefficient of all species (neutral and ionized) of a compound between octanol and water at equilibrium (section 4.1). The molecular volume of the radiotracer is represented by McGowan Volume (V_x, cm^3/mol/100). C*LogD* and V_x were generated based on the chemical structure of the CNS radiotracer using GlaxoSmithKline's in-house software [Guo et al., 2009].

Free fraction in plasma (f_P, unitless) and free fraction in tissue or in the non-displaceable compartment (f_{ND}, unitless) were determined via equilibrium dialysis using Yorkshire/Danish Landrace pig blood and brain tissues [Guo et al., 2009]. The equilibrium dissociation constant or the inverse of binding affinity (K_D, nM) was determined from *in vitro* binding assays measured using human or rat brain homogenates. The *in vitro* target density or receptor site concentration (B_{max}, nM) was obtained from the literature, measured using human brain homogenates via saturation binding assays.

The two known physiological parameters, perfusion and capillary surface area, were input as fixed values. Perfusion (f = 0.6 mL/cm^3/min) is the volume flux per tissue volume [Guo et al., 2009; Cumming et al., 2003]. Capillary surface area (S = 150 cm^2/g of the brain) is the luminal area of the brain vascular space [Guo et al., 2009; Summerfield et al., 2007]. Two correction parameters, apparent aqueous volume in plasma (V_{aq_P} = 0.98 solvent/mL of plasma) and tissue (V_{aq_T} = 0.9 solvent/mL of tissue) were included to correct for the differences in volumes of the two chambers in equilibrium dialysis, where V_{aq_P}/V_{aq_T} = 1.08.

3.4.1.2 Derivation of 1TCM Parameters

For each radiotracer, the six *in silico* and *in vitro* physicochemical and pharmacological parameters were used to derive the 1TCM kinetic parameters (Figure 3.8). These parameters were the influx rate constant from arterial capillaries to brain tissue (K_1), efflux rate constant from brain tissue to venous capillary (k_2), and nondisplaceable binding potential of the radiotracer to the target molecules (BP_{ND}).

Influx rate constant (K_1, mL/cm^3/ min) was derived using modified Renkin and Crone equation (section 3.3), with compound-specific permeability (P, cm/min) and fixed values of f and S [Guo et al., 2009].

$$K_1 = f\left(1 - e^{-\frac{PS}{f}}\right) \tag{14}$$

A scaling factor of 3.43 was included to account for the difference between the predicted and *in vivo* K_1 values determined from the PET images of pigs. The permeability (P, cm/min) was then derived from the simplified Lanevskij's permeability model [Lanevskij et al., 2009] using C*LogD* and V_x, with the regression parameters determined using the nonlinear least squares minimization algorithm to yield the best fit between the predicted and experimental data [Guo et al., 2009]:

$$P = 10^{-0.121\left(\mathrm{C}LogD - 2.298\right)^2 - 2.544\log\left(V_x{}^{1/3}\right) - 2.525} \tag{15}$$

The efflux rate constant (k_2, min^{-1}) was derived based on the assumption that the ratio of the free concentrations of the radiotracer in the plasma and tissue compartments were consistent across the BBB at equilibrium. Simplifying the equilibrium model, k_2 can be calculated using K_1, f_p and f_{ND} [Guo et al., 2009]:

$$k_2 = \frac{f_{\mathrm{ND}}}{f_{\mathrm{P}}} \cdot K_1 \cdot \frac{V_{\mathrm{aq_P}}}{V_{\mathrm{aq_T}}} \tag{16}$$

Based on Mintun's equation [Mintun et al., 1984], the *in vivo* nondisplaceable binding potential, (BP_{ND}, unitless) at tracer dose can be derived using $B_{\max}$, f_{ND} and K_{D} [Guo et al., 2009].

$$BP_{\mathrm{ND}} = f_{\mathrm{ND}} \cdot \frac{B_{\max}}{K_{\mathrm{D}}} \tag{17}$$

3.4.1.3 Simulations of the Tissue Time Activity Curves

The predicted 1TCM kinetic parameters, K_1, k_2 and BP_{ND}, were used to simulate the time activity curves (TACs) in the reference (C_{ref}) and target (C_{target}) regions (Figure 3.8). The metabolite-corrected, arterial plasma input functions (*IF*) were measured from pigs injected with the respective radiotracers during PET imaging [Guo et al., 2009].

$$\mathrm{C}_{ref} = K_1 \cdot e^{-k_2 \times t} \otimes IF \tag{18}$$

$$\mathrm{C}_{target} = K_1 \cdot e^{-\frac{k_2}{(1+BP_{\mathrm{ND}})} \times t} \otimes IF \tag{19}$$

3.4.2 Schafer & Kim's Model

Schafer & Kim et al. [2012] developed a 4TCM model and an input function model to determine the selectivity requirements of tau radiotracers to ensure accurate measurements of tau binding. The 4TCM consists of a free compartment (FT), a non-specific (NS) binding compartment, two specific binding compartments to Aβ and NFT (τ) (Figure 3.9). The models developed were based on the assumptions that (1) the radiotracers cross the BBB by passive diffusion, (2) blood flow to and from the capillaries is limited and mediated by transfer rate constant K_{tran}, (3) the radiotracer binds reversibly to specific binding sites on Aβ plaques and NFTs, and to non-specific binding sites homogeneously, (4) radiotracer binds to each binding sites with 1:1 stoichiometry and (5) the occupancy of any given site does not influence binding to others.

Due to the lack of kinetic data for tau radiotracers when the model was being developed in 2012, the data used for development was obtained from the clinical study of 1 AD subject injected with the amyloid radiotracer, [^{11}C]PIB. The rate constants were determined from simulations by (1) fitting the plasma input function with an input function model and (2) fitting the TACs of PET images with the proposed 4TCM.

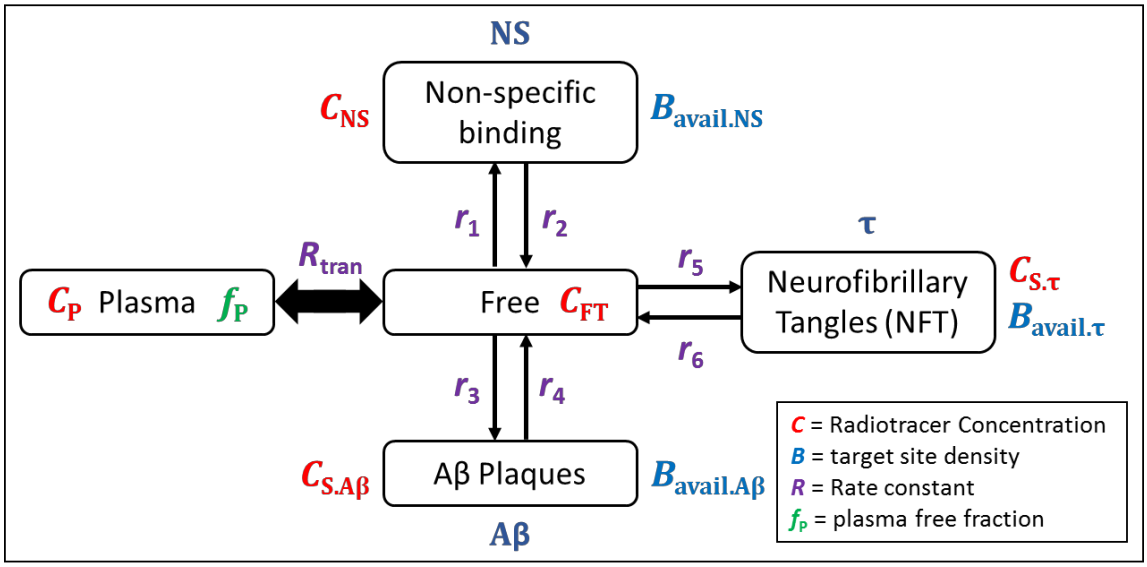

Figure 3.9: Overview of Schafer & Kim's 4TCM biomathematical model.

3.4.2.1 Input Function Model

The arterial plasma radioactivity-time curve following a bolus injection was modelled using a growth function and a tri-exponential decay function respectively to represent the uptake of the radiotracer following bolus injection and washout of the radiotracer from the blood stream [Schafer & Kim et al. 2012]:

$$C_P(t) = \frac{a}{1 + e^{-[\frac{(t-t_i)}{b}]}} \qquad \text{for } t < \tau \qquad (20)$$

$$C_P(t) = \alpha_1 e^{-\beta_1(t-\tau)} + \alpha_2 e^{-\beta_2(t-\tau)} + \alpha_3 e^{-3(t-\tau)} \qquad \text{for } t \geq \tau \qquad (21)$$

where t is the post-injection time (min), t_i is the inflection point corresponding to the time of maximum growth rate, τ is the time to peak activity concentration, a and $\alpha_{1\text{-}3}$ are coefficients and b and $\beta_{1\text{-}3}$ are time coefficients.

3.4.2.2 4TCM

The rates of change in radioactivity concentrations of the radiotracer (C, Molar (M)) in the free (C_{FT}), NSB (C_{NS}) and specific binding to amyloid ($C_{S.A\beta}$) and tau ($C_{S.\tau}$) compartments are represented by differential equations established based on the receptor-ligands interaction [Schafer & Kim et al., 2012]:

$$\frac{d}{dt}(C_{FT}) = R_{tran}(f_P C_P - C_{FT}) - r_1 C_{FT} B_{avail\cdot NS} + r_2 C_{NS} - r_3 C_{FT} B_{avail\cdot A\beta} + r_4 C_{S\cdot A\beta} - r_5 C_{FT} B_{avail\cdot\tau} + r_6 C_{S\cdot\tau} \qquad (22)$$

$$\frac{d}{dt}(C_{\mathrm{NS}}) = r_1 C_{\mathrm{FT}} B_{\mathrm{avail \cdot NS}} + r_2 C_{\mathrm{NS}} \tag{23}$$

$$\frac{d}{dt}(C_{\mathrm{S \cdot A}\beta}) = r_3 C_{\mathrm{FT}} B_{\mathrm{avail \cdot A}\beta} - r_4 C_{\mathrm{S \cdot A}\beta} \tag{24}$$

$$\frac{d}{dt}(C_{\mathrm{S} \cdot \tau}) = r_5 C_{\mathrm{FT}} B_{\mathrm{avail} \cdot \tau} - r_6 C_{\mathrm{S} \cdot \tau} \tag{25}$$

In addition to determining the rate of change in radioactivity concentrations of the radiotracer in the various compartments, the model also included the rates of change in the concentrations of available binding sites (B, Molar (M)) of non-specific targets ($B_{\mathrm{avail.NS}}$), amyloid ($B_{\mathrm{avail.A\beta}}$) and tau ($B_{\mathrm{avail.\tau}}$) [Schafer & Kim et al., 2012]:

$$\frac{d}{dt}(B_{\mathrm{avail \cdot NS}}) = -r_1 C_{\mathrm{FT}} B_{\mathrm{avail \cdot NS}} + r_2 C_{\mathrm{NS}} \tag{26}$$

$$\frac{d}{dt}(B_{\mathrm{avail \cdot A}\beta}) = -r_3 C_{\mathrm{FT}} B_{\mathrm{avail \cdot A}\beta} + r_4 C_{\mathrm{S \cdot A}\beta} \tag{27}$$

$$\frac{d}{dt}(B_{\mathrm{avail} \cdot \tau}) = -r_5 C_{\mathrm{FT}} B_{\mathrm{avail} \cdot \tau} + r_6 C_{\mathrm{S} \cdot \tau} \tag{28}$$

r_1, r_3 and r_5 ($M^{-1}min^{-1}$) are association rate constants of the radiotracer to NSB sites, specific Aβ and tau binding sites respectively. r_2, r_4 and r_6 (min^{-1}) are dissociation rate constants of radiotracer from NSB sites, specific Aβ and tau binding sites respectively. R_{tran} (mL/min/cm^3) is the transfer rate constant for passive bidirectional diffusion of free radiotracer across the blood brain barrier. It can be determined simultaneously with the plasma free fraction (f_{P}, unitless) using the modified Kety-Rekin-Crone equation with fixed cerebral blood flow rate (F = 0.6 mL/min/cm^3) and compound-specific permeability-surface area product (PS, cm^3/min/g of tissue) [Mandula et al., 2006]:

$$R_{\mathrm{tran}} = F(1 - e^{-f_{\mathrm{P}} * PS/F}) \tag{29}$$

$$K_{\mathrm{in}} \approx R_{\mathrm{tran}} * f_{\mathrm{P}} \tag{30}$$

Compound-specific permeability-surface area product (PS) was calculated using the relationship with lipophilicity ($LogP$, unitless) and topological surface area ($TPSA$, Å^2) [Liu et al, 2004]:

$$LogPS = 2.19 - 0.262LogP - 0.0089TPSA \tag{31}$$

mi*LogP* (Molinspiration lipophilicity, section 4.1.1) was used to represent lipophilicity. Both mi*LogP* and *TPSA* were determined using Molinspiration Property Calculation service (Slovak

Republic). The value of F was extracted from literature [Cumming et al., 2003] and was similar to that in Guo's model. K_{in} is the unidirectional brain uptake constant describing the influx of the radiotracer (mL/min/cm^3). Its value was obtained from the K_1 value reported in the literature [Price et al., 2005]. Equation (30) assumes that the association and dissociation of the radiotracer from the plasma protein are sufficiently rapid such that the radiotracer is at equilibrium throughout the entire arteriole and venous capillary beds.

3.4.2.3 Data Fitting and Simulation

Dynamic [^{11}C]PIB PET data of 1 AD subject (AD3: 77 years old, male, MMSE score: 26/30) with the respective plasma input function (C_P) taken from Price et al., [2005]. PET dynamic data was fitted using the 4TCM equations with a local optimisation algorithm simplexSB in Systems Biology Toolbox v.2 and Matlab v.R2011b.

The coefficients of a and $\alpha_{1\text{-}3}$ and time coefficients b and $\beta_{1\text{-}3}$ were determined by fitting the C_P with the input function model using equations (20) and (21). The initial estimates of $B_{avail\cdot NS}$, r_1 and r_2 were determined by fitting the TAC of the reference region, cerebellum [Price et al., 2005], with r_3, r_4, $B_{avail\cdot A\beta}$, r_5, r_6 and $B_{avail\cdot\tau}$ set to 0.

Simulations were carried out by varying the values of $B_{avail\cdot NS}$, r_1, r_2, r_3, r_5 and r_6 to fit the TAC of the target region of posterior cingulate gyrus to predict $C_{S.A\beta}$, $C_{S.\tau}$ and C_{NS} and the final values of these parameters. The initial estimates of $B_{avail\cdot NS}$, r_1, r_2, R_{tran}, f_p and fixed r_4 (0.015 min^{-1}) were applied accordingly. The binding affinities to NSB sites and specific Aβ and tau binding sites were determined from the predicted values of the association and dissociation rate constants and expressed in terms of dissociation constants (K_D, M):

$$K_{D.NS} = r_2/r_1 \tag{31}$$

$$K_{D\cdot A\beta} = r_4/r_3 \tag{32}$$

$$K_{D\cdot\tau} = r_6/r_5 \tag{33}$$

The nondisplaceable binding potential, (BP_{ND}, unitless) was determined from the ratio of Cs and C_{ND} from the TACs of the target (posterior cingulate gyrus) and reference (cerebellum) regions, where Cs consists of both $C_{S.A\beta}$ and Cs.τ, while C_{ND} consists of C_{FT} and C_{NS}.

$$BP_{ND} = C_S/C_{ND} \tag{34}$$

The quality of the fit was estimated from the errors in fitting the clinical data of plasma, reference and target regions using the standard deviation (S_n) of the distribution of errors e_K:

$$S_n = \sqrt{\frac{\sum_{k=1}^{n}(e_K - E)^2}{n-1}} \tag{35}$$

where n is the number of data points within the time period of consideration and E is the empirical mean of the distribution of errors. The time period of consideration was not clearly stated but the dynamic data of a 90 min PET scan was used.

3.4.3 Comparison of Biomathematical Models

Schafer & Kim's model [2012] included the compartments of NSB and specific binding to both Aβ and tau proteins. Their model also included a model to determine the arterial input function specific to each radiotracer. However, their model was developed using clinical data from an AD subject injected with the amyloid radiotracer, [^{11}C]PIB to simulate the performance of tau radiotracer. The behaviour of the amyloid and tau radiotracers might be different and the model required the determination of eight parameters in the input function model and seven rate constants with other inputs (e.g. f_P, K_{in}, TPSA, mi*LogP*) with known data of plasma input function and TACs from dynamic PET images. The rate constants are micro-parameters and thus, are subjected to huge variations.

Although the predicted results appeared to be relatively close to reported values for [^{11}C]PIB [Schafer et al., 2012], the initial estimates were obtained from reported values [Price et al., 2005]. The use of known data of plasma input function and TACs from dynamic PET images limited its use for high-throughput screening. Few physicochemical and pharmacological parameters of the radiotracer were included to fully evaluate the radiotracer. On the whole, although the model considered the various behaviour of the radiotracer, the determination of required parameters is tedious and time-consuming and not feasible for high-throughput screening of radiotracers.

Guo's biomathematical model was focused on using the various key physicochemical and pharmacological parameters of the radiotracer to predict its *in vivo* kinetic performance (section 3.3). Although the model uses 1TCM, the binding of the radiotracer to one target was considered and involved only the prediction of macro-parameters, which were subjected to a less amount of variations. The model worked well in predicting the *in vivo* K_1 and k_2 parameters of CNS radiotracers, even though kinetic evaluation showed that 2TCM yielded better fits to measured

clinical PET data. For amyloid radiotracers, 2TCM was reported to better represent the pharmacokinetics of radiotracer. Regardless, a simpler model with high precision and reasonable accuracy will yield more comparable results. Moreover, there is less concern regarding the specific binding to tau due to the much higher concentration of amyloid plaques in AD brain. Furthermore, the fibrillary amyloid plaques are present extracellularly while NFT is present intracellularly. However, the simplified 1TCM might not accurately predict the *in vivo* kinetic performance of tau radiotracers.

Guo's model did not include the prediction of plasma input function but used existing known input functions of pigs to evaluate the performance of radiotracers. Although Schafer & Kim's model included a model for predicting plasma input function, it also required existing plasma input function to determine the parameters of interest. Moreover, there is no suitable or reliable model available to predict the *in vivo* plasma input function of the radiotracers and hence the possibilities of metabolites crossing the BBB cannot be determined. On the whole, Guo's model is more suitable to fully predict and evaluate the *in vivo* pharmacokinetics performance of amyloid radiotracers based on its physicochemical and pharmacological parameters.

Computational models exist to predict the physicochemical and pharmacological properties of radiotracers and drugs but they were developed using limited compounds with the exclusion of amyloid and tau radiotracers. As such, the *in silico* physicochemical and pharmacological parameters predicted from the various models need to be evaluated with *in vitro* parameters of amyloid and tau radiotracers where applicable to ensure accurate and comparable results. Input parameters required in Guo's model, such as f_P and f_{ND} are not available for clinically-applied amyloid radiotracers, while C*LogD* and B_{max} are predicted using in-house software. Other means of determining these input parameters are required. Further work is required to employ Guo's model for screening of amyloid and tau radiotracers.

3.5 Summary

The basics of PET and common methods of PET quantification in amyloid and tau imaging are explained in details, particularly *SUVR* and the kinetic models. These kinetic models are required to develop the biomathematical model for predicting the *in vivo* kinetic performance of amyloid and tau radiotracers. Two existing biomathematical models for simulating the kinetic performance of radiotracers were described and compared. On the whole, Guo's biomathematical model

showed good potential with good precision and accuracy. However, more work is required to apply the model to the screening of amyloid and tau radiotracers.

Chapter 4

Determination of Physicochemical & Pharmacological Parameters

Guo et al. [2009] used in-house software to determine the values of C*LogD* and V_x, hence other sources to obtain lipophilicity and molecular volume are required. The *in vitro* f_P and f_{ND} values of amyloid radiotracers are not available, hence an *in silico* model is required to determine these values. *In vitro* K_D values can be obtained from the literature but they are measured using different protocols. A selection criterion is thus required to ensure the use of comparable K_D values to yield consistent results. The measured concentrations of the target sites on Aβ varied within and across HC, MCI and AD conditions. Hence, representative concentrations of the target sites on Aβ under HC, MCI and AD conditions need to be determined.

This chapter further describes the six physicochemical and pharmacological parameters: lipophilicity (*LogP*), molecular volume (V_x), free fraction in plasma (f_P), free fraction in tissue (f_{ND}), dissociation constant (K_D) and the concentrations of the target sites on Aβ under HC, MCI and AD conditions (B_{avail}). *In vitro* methods applied to measure f_P, f_{ND}, K_D and B_{avail} are also described. An *in silico* model for predicting f_P and f_{ND} values is developed and validated using f_P values measured via ultrafiltration. This chapter focuses on the determination of representative *in silico* lipophilicity (*LogP*), molecular volume (V_x), free fraction in plasma (f_P), free fraction in tissue (f_{ND}), *in vitro* K_D values from literature with a selection criteria, and representative concentrations of the target sites on Aβ under HC, MCI and AD conditions (B_{avail}) for each amyloid radiotracer.

4.1 Lipophilicity

Lipophilicity is the ability of a chemical compound to dissolve in fats. It affects the kinetic and dynamic behaviour of a radiotracer and/or drug and is commonly evaluated in the conventional development process [Mannhold et al., 2009]. Lipophilicity is commonly represented by the partition coefficient *P*, which is the ratio of the concentrations of a neutral compound in the

organic and aqueous phases at equilibrium [Mannhold et al., 2009]. However, ionizable compounds may be partially ionised at different pH, which will affect its lipophilicity. The distribution coefficient, *D* includes the contributions of both neutral and ionised species of the compound and hence is more representative of the lipophilicity of the compound at the desired pH environment (e.g. blood pH of 7.4). Both coefficients are applied mostly in the logarithmic forms of *LogP* and *LogD*. According to Ro5, the lipophilicity of successful compounds typically have *LogP* < 5 or M*LogP* < 4.15 or 0 < LogD < 3 [Lipinski et al., 2004].

The *in vitro* measurements of lipophilicity are tedious, time-consuming and may suffer from low precision and/or accuracy depending on the measurement methods. Over the years, many *in silico* models have been developed for the cost-effective determination of the lipophilicities of various types of radiotracers and drugs during the development process. Regardless of the types of *in silico* models, they were developed by correlating the *in silico* and *in vitro LogP* or *LogD* values, using mostly CNS drugs. As such, different models led to different *in silico LogP* and *LogD* values, which may not be representative of the lipophilicities of the amyloid radiotracers. Some models are unable to derive lipophilicity values for certain chemical structures. This is due to the limited types of chemical structures included in the model or the limited number of measured lipophilicity values used in the development of the model, especially for *in silico LogD* models.

In this section, 10 different *in silico* lipophilicities (8 *LogP* and 2 *LogD*) from different software are described. Their values are then compared with *in vitro* lipophilicity values from literature to determine the representative *in silico* lipophilicity for amyloid radiotracers. The results are also compared to the comprehensive evaluation results of available *in silico* models by Mannhold et al. [2009].

4.1.1 *In Silico* Lipophilicity

In silico LogP and *LogD* models were developed based on either substructure or physical properties of the compound. Substructure-based methods divide the compounds into atoms or fragments and sum up the respective substructure contributions to derive *LogP* or *LogD* [Mannhold et al., 2009]. Correction factors for possible interactions between the different fragments or types of bonds may be included. Property-based methods identify certain physical properties of a compound and summed up the contributions of these properties to derive *LogP* or *LogD*. However, physical properties (e.g. polarizability, Gibbs energy) of compounds need to be measured and thus property-based models were developed using a smaller number of compounds.

This may lead to lower accuracy compared to substructure-based models with lower feasibility of predicting new compounds. As such, substructure-based models are chosen for predicting the lipophilicity of amyloid radiotracers. This subsection describes the 10 different *in silico* lipophilicity models (8 *LogP* and 2 *LogD*) (Table 4.1).

Table 4.1: Overview of 10 different *in silico* lipophilicity models (8 *LogP* and 2 *LogD*)

LogP/ *LogD*	*In Silico* Model	Software	Substructure / Property	Details	Software Link
LogP	C*LogP*	Biobyte	Substructure	Fragmental	http://www.biobyte.com/index.html
	LogP	ChemBioOffice	Substructure	Atom-based	http://www.cambridgesoft.com/services/documentation/sdk/
	A*LogP*	dproperties	Substructure	Fragmental	http://talete.mi.it/
	M*LogP*	dproperties	Substructure	Atom-based	http://talete.mi.it/
	mi*LogP*	Molinspiration	Substructure	Fragmental	http://www.molinspiration.com/services/logp.html
	LogP	ACD/ ChemSketch	Substructure	Fragmental	http://www.acdlabs.com/resources/freeware/chemsketch/
	M*LogP*	MedChem Designer	Substructure	Fragmental	http://www.simulations-plus.com/software/medchem-designer/
	LogP+S	MedChem Designer	Substructure	Fragmental	http://www.simulations-plus.com/software/medchem-designer/
LogD	C*LogD*	ACD/ ChemSketch	Substructure	Fragmental	http://www.acdlabs.com/resources/freeware/chemsketch/
	LogD+S	MedChem Designer	Substructure	Fragmental	http://www.simulations-plus.com/software/medchem-designer/

(1) C*LogP* (Biobyte, Part of ChemBioOffice, Perkin Elmer, US)

Calculated *LogP* (C*LogP*) is a substructure-based method, which divides a compound into fragments, based on the interaction of carbon atoms with other elements and the associated bonds. The model was developed using 8162 in-house measured *LogP* (also known as Starlist).

(2) *LogP* (ChemBioOffice, Perkin Elmer, US)

LogP is a substructure-based method, which divides a compound into fragments using three methods: 94 atomic contributions evaluated using 830 molecules, 120 atomic contributions evaluated using 893 molecules or 222 atomic contributions calculated using 1868 molecules by least squares analysis. *LogP* values derived using the 1st fragmentation was applied in this study.

(3) A*LogP* (dproperties, Talete, Italy)

Ghose-Crippen-Viswanadhan Approach (A*LogP*) is a substructure-based method using the

hydrophobicity contributions of 115 atom types, without any correction factors [Ghose and Crippen et al., 1986]:

$$ALogP = \sum_{i} n_i a_i \tag{36}$$

where n is the number of the atom of type i and a_i is the corresponding hydrophobicity constant. The model was evaluated using 3,576 molecules with known experimental *LogP* values from NCI Open Database and is only applicable to compounds with C, H, O, N, S, Se, P, B, Si, and halogens atoms [Mauri et al., 2006].

(4) M*LogP* (dproperties, Talete, Italy)

Moriguchi *LogP* is a property-based method using simple topological descriptors developed by Moriguchi et al., [1992]. Moriguchi et al. used 1230 compounds and identified lipophilic atoms and hydrophilic atoms as key parameters affecting lipophilicity and 11 correction parameters to account for the variance [Lipinski et al., 2001]:

(5) mi*LogP* (Molinspiration, Molinspiration Cheminformatics, Slovak Republic)

mi*LogP* is a substructure-based method using group contributions from 35 small basic fragments [Mannhold et al., 2008]. The model was developed by fitting the calculated *LogP* with experimental *LogP* from a training set containing more than twelve thousand compounds, of which most were drug-like molecules.

(6) *LogP* (ChemSketch, Advanced Chemistry Development (ACD), Canada)

ACD/*LogP* is a substructure-based method based on the principle of isolating carbons. *LogP* is derived by summing up the contributions from atoms, structural fragments, and intramolecular interactions. The model was developed using 3601 compounds. [Petrauskas et al., 2000]

(7) M*LogP* (MedChem Designer, Simulation Plus, US)

This model is the same as that of dproperties, but the resulting M*LogP* values were slightly different for the same compound. This may be due to different variable values applied with the use of ions-corrected *LogP* values.

(8) *LogP+S* (MedChem Designer, Simulation Plus, US)

LogP+S is generated using an internal model known as “Simulations Plus”. It is a property-based method that included a diverse range of descriptors, including Morguchi’s. The model was

developed using 12628 compounds selected from the BioByte's StarList of measured ion-corrected *LogP* values.

(9) *CLogD* (ChemSketch, Advanced Chemistry Development (ACD), Canada)
ACD/*LogD* model was developed based on ACD's original models for *LogP* with the acid-ionisation constant to account for ionizable species of the compound at different pH values.

(10) *LogD*+*S* (MedChem Designer, Simulation Plus, US)
LogD+S model was developed based on *LogP*+*S* by accounting for ionizable species at user-specified pH (default 7.4).

4.1.2 *In vitro* Lipophilicity

There are a few methods to measure the lipophilicity of a compound but the two most commonly applied methods for amyloid radiotracers are the shake-flask and reversed-phase high-performance liquid chromatography (RP-HPLC).

Shake-flask
Shake-flask is a classic method for measuring partition coefficient. It uses an organic solvent and an aqueous solution (water) to model the lipid bilayer. Different organic solvents have been utilised, including octanol (amphiphilic), chloroform (proton donors), cyclohexane or dodecane (inert), propylene glycol dipelargonate (PGDP) (proton acceptors) [Rutkowska et al., 2013]. The measured *LogP* values differed with the organic solvent used due to the differences in hydrogen bonding with the solvent. The most common solvent applied is octanol as the chemical structure of octanol is close to that of molecules in the cell membrane and its amphiphilic properties lead to chemical interactions that closely reflects that of the phospholipids.

In the shake-flask procedure, the compound is thoroughly mixed in the organic-aqueous solution and allowed to interact until equilibrium is reached. Ultraviolet–visible spectroscopy (UV/VIS) is then employed to measure the concentrations of the compound in both the organic and aqueous phases [Rutkowska et al., 2013]. The octanol-water partitioning of a compound correlated well with the binding of compounds to serum proteins and, hence was said to resemble the interaction of compounds with the phospholipids [Rutkowska et al., 2013]. As such, the shake-flask method, using octanol-water partitioning, was accepted as a common reference method in measuring the lipophilicity of a compound. However, the procedure is labour intensive, time-consuming and the

results can be affected by the presence of impurities. This method is also unsuitable for measuring partition coefficient of highly lipophilic or hydrophilic compounds [Rutkowska et al., 2013].

RP-HPLC

RP-HPLC is based on the traditional chromatographic method of separating lipophilic and hydrophilic components of the compound into the stationary and mobile phases. The amount of organic solvent is varied to vary the retention of the hydrophilic component of the compound out of the mobile phase. This method applies an indirect mean of measuring partition coefficient and hence, calibration of the equipment is required. This leads to difficulty in ensuring reproducibility of results across the different experiment. However, the method is easy to automate and provides a fast and accurate mean of measuring partition coefficient within a single experiment [Hartmann et al., 2004].

4.1.3 Evaluation Methods for Lipophilicity

To determine the representative *in silico* lipophilicity of amyloid radiotracers, a list of 41 amyloid PET radiotracers (12 clinically-applied, 29 candidates) with either *in vitro LogP* or *LogD* values reported were compiled (Figures 4.1 and 4.2**)**. The *in silico* 8 *LogP* and 2 *LogD* values (Table 4.2) of the list of 41 radiotracers were then compared to their *in vitro* values extracted from the literature (Table 4.3).

The mean, standard deviation (*stdev*), root-mean-squared-error (*RMSE*) and normalised *RMSE* (*NRMSE*) of the *in silico LogP* and *LogD* values from their respective *in vitro* values were calculated. *RMSE* and *NRMSE* were calculated as follows.

$$RMSE = \sqrt{\frac{\sum_i^n (LogP_{\mathrm{C},i} - LogP_{\mathrm{M},i})^2}{n}} \tag{37}$$

$$NRMSE = RMSE \,/\, (LogP_{\mathrm{C,Max}} - LogP_{\mathrm{C,Min}}) \tag{38}$$

where C represents the calculated or *in silico* values, M represents the measured or *in vitro* values obtained from the literature, *n* is the total number of radiotracers.

Linear and orthogonal regressions were carried out between the *in silico* and *in vitro LogP* and *LogD* values of 30 and 13 compounds respectively depending on the availability of the *in vitro LogP* and *LogD* values from the literature. Regressions were carried out using Matlab (Ver. 2014b, The MathWorks, US) and the results were presented using the coefficient of determination, R^2. Orthogonal regression was carried out to account for errors in measured *LogP* and *LogD* values.

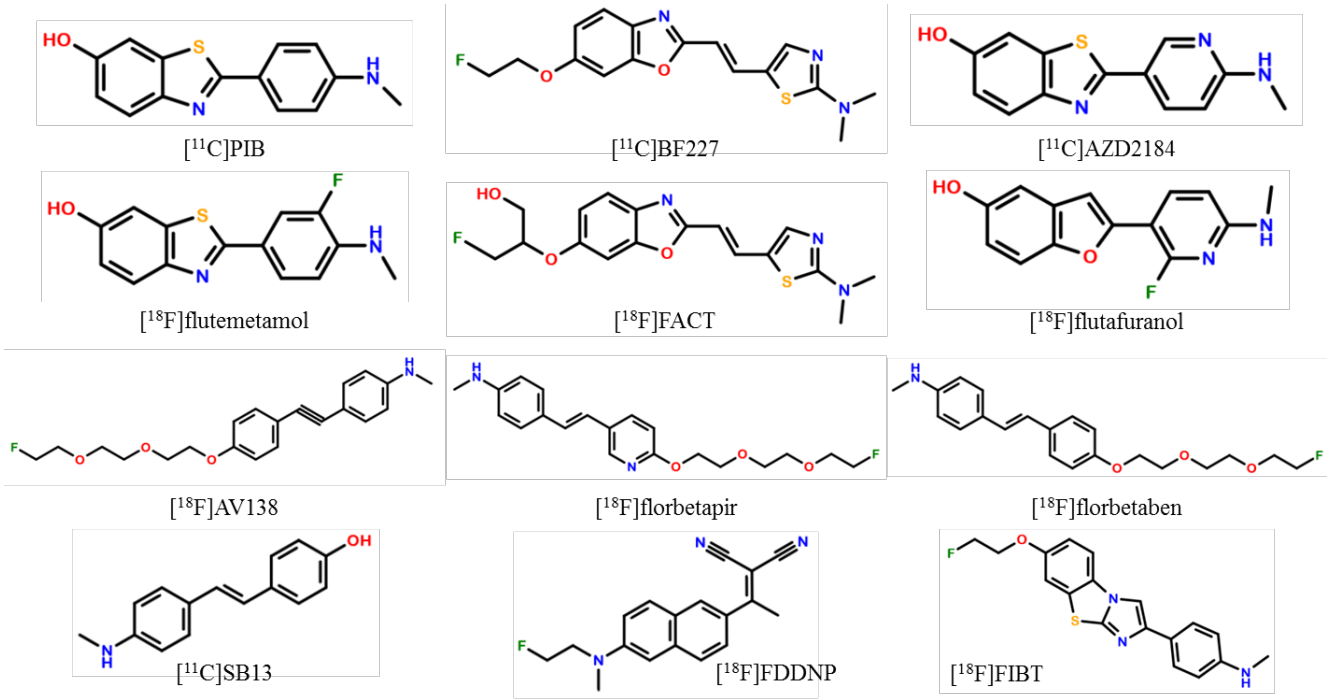

Figure 4.1: Chemical structures of 12 clinically-applied amyloid radiotracers.

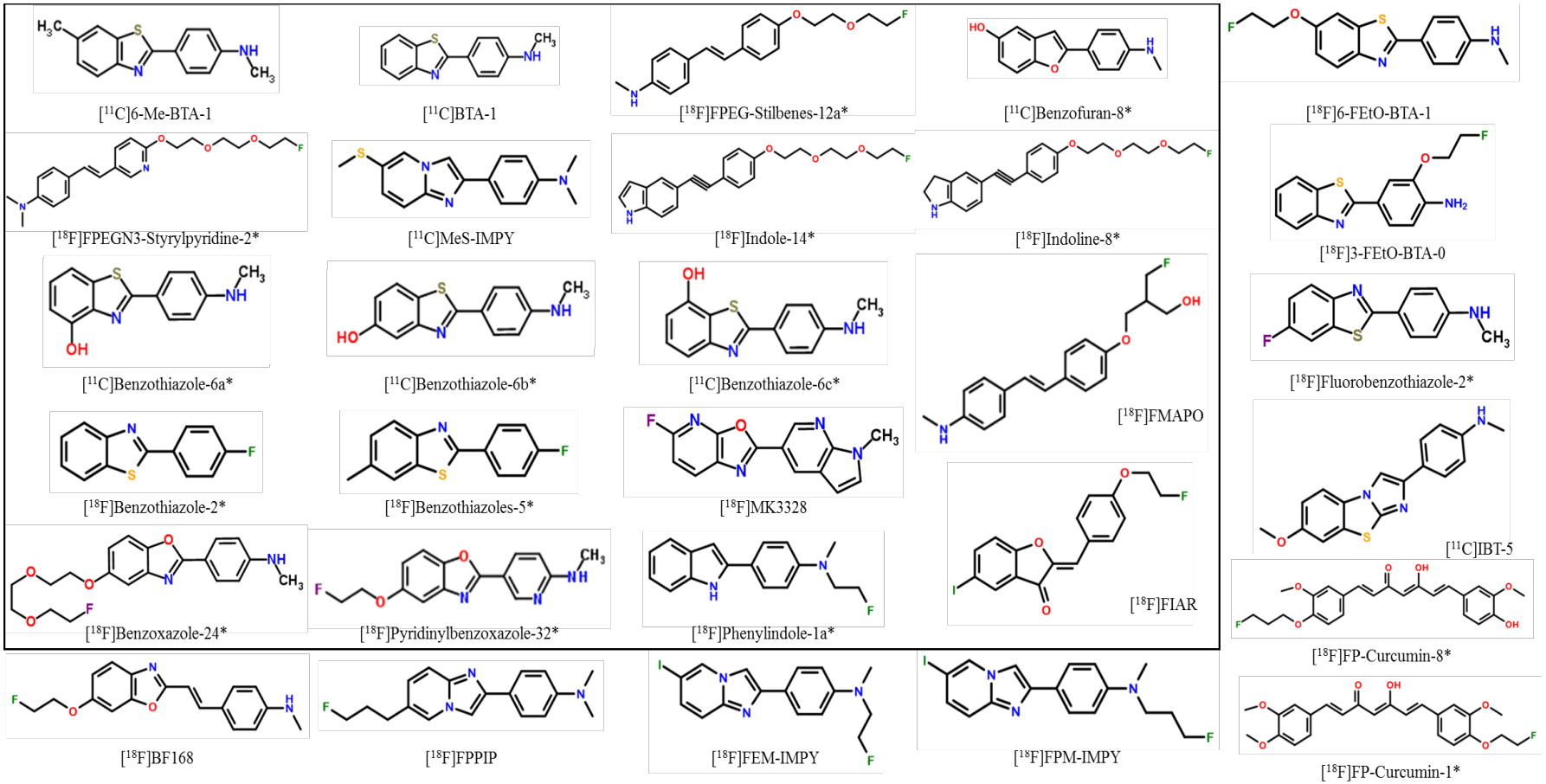

* Simplified name with compound number or alphabet, as reported in literature, used when generic name or institute code name (supplied by the author) was not available.

Figure 4.2: Chemical structures of 29 candidate amyloid radiotracers. Radiotracers highlighted within the box are used for further evaluation.

Table 4.2: *In vitro* lipophilicity values of 41 amyloid radiotracers extracted from the literature.

Radiotracers	*In vitro* lipophilicity measured at pH 7.4		
	LogP	*LogD*	References
[^{11}C]PIB	1.30	2.12$^{\#}$	Mathis et al., 2003, Johnson et al., 2009, Yousefi et al., 2015a, Hostetler et al., 2011
[^{18}F]FDDNP	3.71*	-	Okamura et al., 2013
[^{11}C]SB13	2.36	-	Ono et al., 2003
[^{18}F]florbetaben (Neuraceq)	2.41$^{\$}$	1.58	Koo et al., 2013 Yousefi et al., 2015a
[^{11}C]BF227	2.29$^{\$}$	-	Furumoto et al., 2013
[^{18}F]AV138	3.07	-	Chandra et al., 2007
[^{18}F]flutemetamol (Vizamyl)	-	3.20*	Juréus et al., 2010
[^{18}F]florbetapir (Amyvid)	1.70$^{\$}$	-	Koo et al., 2013
[^{11}C]AZD2184	-	1.8*	Johnson et al., 2009
[^{18}F]flutafuranol	-	2.80*	Juréus et al., 2010
[^{18}F]FACT	1.99$^{\$}$	-	Furumoto et al., 2013
[^{18}F]FIBT	-	1.92	Yousefi et al., 2011b
[^{11}C]6-Me-BTA-1	3.36	-	Klunk et al., 2001
[^{11}C]BTA-1	2.70	-	Mathis et al., 2002
[^{18}F]FMAPO	2.95	-	Zhang et al., 2005
[^{18}F]FPEG-Stilbenes-12a§	2.53	-	Zhang et al., 2005
[^{11}C]Benzofuran-8§	2.36	-	Ono et al., 2006
[^{18}F]FPEGN3-Styrylpyridine-2§	3.22	-	Zhang et al., 2007
[^{11}C]MeS-IMPY	-	4.10$^{\$}$	Seneca et al., 2007
[^{18}F]Indole-14§	2.56	-	Qu et al., 2008
[^{18}F]Indoline-8§	2.95	-	Qu et al., 2008
[^{11}C]Benzothiazole-6a§	3.18*	-	Serdons et., 2009a
[^{11}C]Benzothiazole-6b§	2.48*	-	Serdons et., 2009a
[^{11}C]Benzothiazole-6c§	2.45*	-	Serdons et., 2009a
[^{18}F]F-Benzothiazole-2§	2.86*	-	Serdons et., 2009b
[^{18}F]F-Benzothiazole-5§	2.52*	-	Serdons et., 2009c
[^{18}F]MK3328	-	2.91*	Hostetler et al., 2011
[^{18}F]FIAR	2.45$^{\$}$	-	Watanabe et al., 2011
[^{18}F]F-Benzoxazole-24§	-	3.09	Cui et al., 2012a
[^{18}F]2-Pyridinylbenzoxazole-32§	-	3.52	Cui et al., 2012b
[^{18}F]2-Phenylindole-1a§	-	3.61	Fu et al., 2013
[^{11}C]IBT-5	1.70$^{\$}$	-	Yousefi et al., 2011a
[^{18}F]BF168	1.80	-	Okamura et al., 2005
[^{18}F]FPPIP	2.84	-	Zeng et al., 2006
[^{18}F]FEM-IMPY	-	4.41*	Cai et al., 2004
[^{18}F]FPM-IMPY	-	4.60*	Cai et al., 2004
[^{18}F]FP-Curcumin-8§	1.84*	-	Ryu et al., 2006
[^{18}F]FP-Curcumin-1§	2.40*	-	Lee I. et al., 2011
[^{18}F]6-FEtO-BTA-1	2.40	-	Neumaier et al., 2010
[^{18}F]3-FEtO-BTA-0	2.10	-	Neumaier et al., 2010
[^{18}F]2-Aryl-6-Fluorobenzothiazole-2§	3.20*	-	Lee BC. et al., 2011

§Simplified name with the compound number or alphabet, as reported in the literature.
Values were measured by conventional shake-flask methods unless otherwise stated.
*Measured by HPLC
$^{\#}$Average of (2.8*, 1.5, 2.23*)
$^{\$}$Unknown method of measurement

Table 4.3: *In silico* lipophilicity values of 41 amyloid radiotracers generated using 10 lipophilicity models

Radiotracers	BioByte	ChemBio	dproperties		Molin-spiration	ACD		MedChem		
	C*LogP*	C*LogP*	AL*ogP*	M*LogP*	mi*LogP*	C*LogP*	C*LogD*	M*LogP*	*LogP+S*	*LogD+S*
[^{11}C]PIB	3.99	3.41	3.38	2.40	3.64	3.33	3.19	1.93	3.64	3.64
[^{18}F]FDDNP	3.42	3.95	3.93	2.89	3.61	4.00	4.13	2.89	3.72	3.72
[^{11}C]SB13	3.67	3.57	3.36	3.23	3.87	3.67	3.43	3.23	3.83	3.83
[^{18}F]florbetaben	4.08	3.47	3.75	3.11	4.39	3.63	3.86	3.11	4.22	4.22
[^{11}C]BF227	3.75	3.85	3.58	2.40	3.89	3.02	2.90	1.51	3.49	3.49
[^{18}F]AV138	4.02	3.23	3.87	3.11	3.26	3.54	3.71	3.11	4.01	4.01
[^{18}F]flutemetamol	4.30	3.57	3.59	2.80	3.74	3.50	3.27	2.33	3.98	3.98
[^{18}F]florbetapir	3.48	2.85	3.14	2.52	3.32	3.07	3.18	2.11	3.40	3.40
[^{11}C]AZD2184	3.42	2.79	2.77	1.75	2.92	3.23	2.75	1.27	2.99	2.99
[^{18}F]flutafuranol	3.38	2.49	3.46	2.41	3.09	4.18	3.27	1.93	3.16	3.16
[^{18}F]FACT	2.81	3.31	3.07	1.87	3.25	2.12	-	0.98	2.78	2.78
[^{18}F]FIBT	4.82	4.07	4.72	3.04	4.40	4.09	4.18	2.48	4.21	4.21
[^{11}C]6-Me-BTA-1	4.39	4.29	4.13	3.23	4.57	4.53	4.12	2.76	4.35	4.35
[^{11}C]BTA-1	3.89	3.80	3.65	2.97	4.15	4.07	3.86	2.50	3.97	3.97
[^{18}F]FMAPO	3.75	3.40	3.53	3.47	4.45	4.03	3.30	3.47	3.90	3.90
[^{18}F]FPEG-Stilbenes-12a[§]	4.25	3.63	3.88	3.47	4.60	3.98	4.52	3.47	4.35	4.35
[^{11}C]Benzofuran-8[§]	3.63	2.49	3.49	2.66	3.54	3.52	3.31	2.19	3.96	3.96
[^{18}F]FPEGN3-Styrylpyridine-2[§]	4.15	3.64	3.49	3.74	3.56	4.20	4.19	2.33	4.01	4.01
[^{11}C]MeS-IMPY	4.48	3.72	3.78	3.33	3.46	3.99	3.43	2.58	4.08	4.07
[^{18}F]Indole-14[§]	4.52	3.27	4.36	2.98	3.60	4.09	4.08	2.51	4.60	4.60
[^{18}F]Indoline-8[§]	4.16	3.20	3.95	2.93	3.23	3.57	3.89	2.93	4.19	4.19
[^{11}C]Benzothiazole-6a[§]	3.99	3.41	3.38	2.40	3.88	3.33	2.89	2.44	3.86	3.85
[^{11}C]Benzothiazole-6b[§]	3.99	3.41	3.38	2.40	3.64	3.33	3.12	1.93	3.68	3.67
[^{11}C]Benzothiazole-6c[§]	3.99	3.41	3.38	2.40	3.88	3.33	3.14	1.93	3.76	3.65
[^{18}F]Benzothiazole-2[§]	4.33	4.46	4.04	3.72	4.45	4.48	4.04	3.25	4.28	4.28
[^{18}F]Benzothiazole-5[§]	4.83	4.95	4.53	3.98	4.88	4.94	4.31	3.51	4.69	4.69
[^{18}F]MK3328	1.79	2.15	2.19	2.63	2.79	3.18	2.39	1.27	2.66	2.66
[^{18}F]FIAR	5.39	3.99	4.10	3.66	4.65	4.97	4.19	3.53	4.72	4.72
[^{18}F]Benzoxazole-24[§]	3.33	2.19	3.21	2.41	3.52	3.21	2.89	1.53	3.42	3.42
[^{18}F]Pyridinylbenzoxazole-32[§]	3.19	1.88	2.86	2.42	3.11	3.86	2.77	1.53	2.79	2.79
[^{18}F]Phenylindole-1a[§]	4.65	3.78	4.50	3.84	4.23	4.92	4.38	3.37	4.55	4.55
[^{11}C]IBT-5	4.57	3.88	4.32	2.69	4.10	3.86	4.14	2.31	4.13	4.13
[^{18}F]BF168	4.15	3.29	3.94	3.16	4.54	4.07	3.70	2.29	3.90	3.90
[^{18}F]FPPIP	4.61	4.11	4.35	3.66	4.02	4.42	3.03	3.17	4.31	4.30
[^{18}F]FEM-IMPY	5.17	4.83	4.22	3.93	4.41	4.70	4.03	3.44	4.73	4.73
[^{18}F]FPM-IMPY	5.39	4.93	4.28	4.16	4.68	5.09	4.44	3.67	5.05	5.05
[^{18}F]FP-Curcumin-8[§]	3.90	2.73	4.07	2.49	3.92	3.97	3.18	3.01	4.02	3.37
[^{18}F]FP-Curcumin-1[§]	4.14	2.88	4.26	2.49	3.96	4.27	3.24	3.01	3.95	3.25
[^{18}F]6-FEtO-BTA-1	4.44	3.86	4.03	3.03	4.48	4.21	-	2.56	4.08	4.08
[^{18}F]3-FEtO-BTA-0	3.64	3.56	3.48	2.78	4.06	4.14	-	2.83	3.72	3.72
[^{18}F]Fluorobenzothiazole-2[§]	3.18	1.88	3.85	3.37	4.29	4.12	3.85	2.90	4.26	4.26

[§]Simplified name with the compound number or alphabet, as reported in the literature, used when generic name or institute code name (supplied by the author) was not available.
Note: Some software cannot generate lipophilicity values for certain radiotracers

The accuracy of the various *in silico* models in deriving *LogP* values was shown to (1) decrease linearly with increasing number of non-hydrogen atoms, (2) decrease with greater spread of *LogP* values, (3) decrease with increasing *RMSE*. The optimal *LogP* or *LogD* value was about 2 for most chemical compounds [Rutkowska et al., 2013]. The rankings of the *in silico LogP* and *LogD* models were carried out based on the mean value, *RMSE* and correlations in terms of R^2.

4.1.4 Determination of Representative *In silico* Lipophilicity

The ranking of the various *in silico* lipophilicity models based on R^2 of linear and orthogonal regressions was different. The R^2 values of linear regression were small for all *in silico LogP* and *LogD* with the highest R^2 value of 0.194 obtained using M*LogP* (dproperties), followed by *LogD*+*S* (MedChem) and M*LogP* (MedChem) (Table 4.4). The R^2 values of orthogonal regression were generally high with the highest R^2 of 0.859 obtained using A*LogP* (dproperties). A*LogP* (dproperties), mi*LogP* (Molinspiration), *LogP*+*S* (MedChem), C*LogP* (BioByte), C*LogD* (ACD), *LogD*+*S* (MedChem) and M*LogP* (dproperties) had R^2 values for orthogonal regression of greater than 7.0 (Table 4.4).

Based on *RMSE* and *NRMSE*, M*LogP* (MedChem) was ranked 1st, followed by M*LogP* (dproperties) (Table 4.4). Although *LogD*+*S* (MedChem) and C*LogD* (ACD) were ranked 3rd and 4th based on *RMSE*, they were ranked 5th and 6th based on *NRMSE* (Table 4.4). M*LogP* (MedChem) had the smallest mean value of 2.58, hence resulting in smallest *RMSE* (Table 4.4). On the whole, despite conflicting results, M*LogP* (MedChem), M*LogP* (dproperties), *LogD*+*S* (MedChem) and C*LogD* (ACD) performed generally well. Further evaluation was thus carried out with these 4 lipophilicity models using compounds with nearly-similar chemical structures.

Table 4.5 shows the chemical structures of [^{11}C]PIB and its analogs with the *in silico LogP* values from M*LogP* (dproperties), M*LogP* (MedChem), C*LogD* (ACD) and *LogD*+*S* (MedChem. These four compounds had nearly similar chemical structures and differed only in the positioning of a single –OH group. The measured *LogP* values of the analogues were taken from the same literature [Serdons et al., 2009a] and were different from each other. However, the *in silico* M*LogP* (MedChem), M*LogP* (dproperties) and C*LogD* (ACD) showed the same values for [^{11}C]PIB and all of its analogues. Only *LogD*+*S* (MedChem) resulted in different *LogP* values. The *in silico* M*LogP* values from MedChem and dproperties were also different from each other. M*LogP* (MedChem) resulted in a different value of 2.44 for [^{11}C]Benzothiazole-6a, which was closer to the M*LogP* (dproperties) of 2.40, compared to [^{11}C]PIB and other analogues of 1.93 (Table 4.5).

Table 4.4: Comparison of 10 *in silico* lipophilicity models: *Mean*, standard deviation (*Stdev*), root-mean-squared-error (*RMSE*) and normalised *RMSE* (*NRMSE*) of *in silico LogP* and *LogD* of 41 amyloid radiotracers. The coefficient of determination, R^2 were determined from the linear and orthogonal correlations of *in silico* and *in vitro LogP* and *LogD* using 30 and 13 compounds respectively. The rankings of *in silico LogP* and *LogD* were based on *RMSE* and R^2. The ranking in roman numerals was taken from Mannhold et al. [2008].

	BioByte	ChemBio	Molinspiration	dproperties		ACD		MedChem		
	C*LogP*	C*LogP*	mi*LogP*	A*LogP*	M*LogP*	C*LogP*	C*LogD*	M*LogP*	*LogP+S*	*LogD+S*
RMSE	1.68	1.23	1.62	1.40	0.72	1.49	1.06	0.66	1.57	1.20
NRMSE	0.47	0.40	0.78	0.55	0.30	0.50	0.50	0.24	0.66	0.50
Mean	4.02	3.45	3.90	3.74	2.97	3.90	3.59	2.56	3.94	3.90
Stdev	0.69	0.75	0.54	0.53	0.58	0.61	0.56	0.71	0.54	0.56
COV	0.17	0.22	0.14	0.14	0.20	0.16	0.16	0.28	0.14	0.14
R^2 (Linear)	0.000	0.026	0.003	0.037	0.194	0.104	0.085	0.149	0.105	0.177
R^2 (Ortho)	0.836	0.310	0.845	0.859	0.714	0.517	0.809	0.421	0.843	0.755
Rank (*RMSE*)	10	5	9	6	2	7	3	1	8	4
Rank (R^2, Linear)	10	8	9	7	1	5	6	3	4	2
Rank (R^2, Ortho)	4	10	2	1	7	8	5	9	3	6
Rank*	-	-	II	-	III	I	-	II	I	-

R^2 was determined from the correlations between *in silico* and *in vitro LogP* and *LogD* using 30 and 13 compounds respectively.
* Ranking based on Mannhold et al, 2008

Table 4.5: *In silico* and *in vitro LogP* of [^{11}C]PIB and its analogues with the uptake in normal mice. Data were taken from Serdons et al., 2009a, unless otherwise stated. The *in silico* lipophilicity values were predicted using M*LogP* (dproperties), M*LogP* (MedChem), C*LogD* (ACD) and *LogD+S* (MedChem). %ID/g = % Injected Dose/g of cerebrum tissue. *LogP* is unitless and the *in vitro LogP* values were measured via RP-HPLC.

Radiotracers	Chemical Structures	From [Serdons et al., 2009a]			*In silico*			
		%ID/g of Cerebrum		*LogP*	M*LogP*	M*LogP*	C*LogD*	*LogD+S*
		2 min	60 min	Measured	(dproperties)	MedChem	ACD	MedChem
[^{11}C]PIB	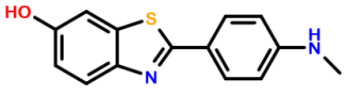	3.60	0.60	1.30*	2.40	1.93	3.33	3.64
[^{11}C]Benzothiazole-6a§	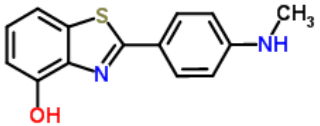	3.80	0.30	3.18	2.40	2.44	3.33	3.85
[^{11}C]Benzothiazole-6b§	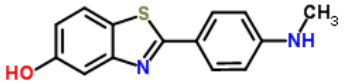	4.30	0.09	2.48	2.40	1.93	3.33	3.67
[^{11}C]Benzothiazole-6c§	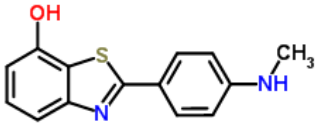	2.60	0.16	2.45	2.40	1.93	3.33	3.65

*Taken from Mathis et al., 2003, measured using the shake-flask method.
§Simplified name with the compound number or alphabet, as reported in the literature, applied when generic name or institute code name (supplied by the author) was not available.

4.1.5 Summary

Measured *LogP* and *LogD* were obtained from the literature and suffered from differences in procedures across institutions and experimental errors within institutions. Hence, *RMSE*, *NRMSE* and R^2 (Linear) might not be suitable for evaluation. Although R^2 (Ortho) was evaluated, the ranking results differed from the other evaluation methods and that of Mannhold [2009]. The *in silico LogP* would be more accurate if their mean values were closer to 2.0 [Rutkowska et al., 2013]. Although M*LogP* (MedChem) had the smallest mean value, the difference in value for only one of [^{11}C]PIB's analogue led to concern about its reliability. The measured *LogP* values differed for [^{11}C]PIB and its analogues and *LogD*+*S* (MedChem) could yield different values. However, the *in silico LogP* values were generally much greater than the measured *LogP* values. Therefore, M*LogP* (dproperties) and *LogD*+*S* (MedChem) were selected for further evaluation to determine the representative *in silico* lipophilicity model that will yield kinetic parameters closer to clinically-observed values in the next chapter.

4.2 Molecular Volume

Apart from the chemical properties of a compound, the size of a compound also plays an important role in determining its solubility, partition behaviour and transport characteristics, such as BBB penetration [Mellors et al., 1985]. Based on Lanevskij's equation of permeability, McGowan volume, V_x is used to represent molecular volume. V_x is the actual volume of a mole when the molecules are not in motion and is applicable to both neutral and ionic compounds [Zhao et al., 2003a]. V_x can be determined from the commercial software, dproperties (Talete, Italy) in the units of Å^3/molecule (Å, molecular radius). It is based on the fragment contributions, using group contributions of each atom and the number of bonds as follows [Zhao et al., 2003a]:

$$V_x = \frac{\sum_i^A w_i - 6.56N_B}{0.602} \tag{39}$$

where w_i is the McGowan's volume atomic contributions [Abraham and McGowan et al., 1987], A is the total number of atoms and N_B is the total number of bonds. It can be converted to cm^3/mol/100 by multiplying by 0.00602 [Zhao et al., 2003a].

4.3 Free Fractions in Plasma and Tissues

Free fraction in plasma (f_P) and free fraction in tissue (f_{ND}) relate to the fraction of free molecules available for distributions and interactions (section 3.3). Equilibrium dialysis is considered the

"gold standard" for measuring f_P and f_{ND} [Zhang et al., 2012; Wang et al., 2013]. However, it is a long and tedious measurement method, which makes it is unsuitable for measuring f_P and f_{ND} of many radiotracers. Less time-consuming techniques, such as ultracentrifugation, gel filtration etc. have been applied but their results do not correlate well with that of equilibrium dialysis [Barre et al., 1985]. Ultrafiltration is another alternative method and the results are reported to correlate well with that of equilibrium dialysis. However, it is only capable of measuring f_P of a compound.

The f_P and f_{ND} values of many amyloid radiotracers are difficult to measure due to the difficulty in getting the radiotracers for measurements. Few reported f_P values can be found from literature (Table 4.6) and none had reported f_{ND} values. The limitations of the *in vitro* methods prompted the need for an *in silico* model to derive f_P and f_{ND} values reliably from the chemical structures of amyloid radiotracers. Currently, no *in silico* f_P-f_{ND} model for amyloid radiotracers exists. This section discusses the development and validation of a simple *in silico* f_P-f_{ND} model.

4.3.1 Development of *In Silico* f_P-f_{ND} model

Wan et al [2007] analysed the relationships between f_{ND} and various structural properties, such as molecular weight, the number of rotatable bonds using 108 CNS drugs. From his results, lipophilicity was the most important component to f_{ND} and f_P, and it correlated well with f_{ND}. Lipophilicity was also reported by others to yield the best correlation with f_{ND} and f_P, and hence was deemed as a dominant factor in tissues binding [Di et al., 2011; Summerfield et al., 2006]. Similarly, f_{ND} and f_P showed good correlation, suggesting that the unbound fractions of a compound in plasma and tissues are governed mostly by non-specific binding [Wan et al., 2007]. Although other parameters like solvent accessible polar surface area, also correlated well with f_{ND}, these parameters also showed good correlations with lipophilicity. This showed a possible link to lipophilicity and hence these parameters were excluded from the *in silico* model.

Relational models were thus developed using lipophilicity, f_{ND} and f_P. The binding in brain tissue is species-independent but binding to plasma protein is species-dependent [Di et al., 2011]. As lipophilicity correlates better with f_{ND} than f_P, the *in silico* f_P-f_{ND} model was developed using lipophilicity as input to derive f_{ND}, which was then used to derive f_P. The lipophilicity, f_P and f_{ND} of various compounds were compiled from four different literature. The relationships between f_P and f_{ND}, and f_{ND} and lipophilicity were determined from the linear regressions of each dataset. All *in vitro* f_P and f_{ND} values were measured via equilibrium dialysis using animal samples. The f_P and f_{ND} values were converted to the logarithmic form to avoid skewed distribution of the data in their

original form.

Wan & Maurer's Dataset

Maurer et al. [2004] measured the f_P and f_{ND} values of 33 CNS drugs using wild type mouse's blood and homogenised brain tissues. Wan et al. [2007] calculated the lipophilicity, C*LogP* of 25 CNS drugs using C-Lab (Dalke Scientific, New Mexico). 24 of the CNS drugs in Wan's dataset were similar to that of Maurer's dataset. Linear regression was carried out using the 24 CNS drugs that were present in both datasets. Good correlations were obtained between f_{ND} vs. C*LogP* and f_P vs. f_{ND}, with R^2 of 0.783 and 0.798 respectively (Figure 4.3).

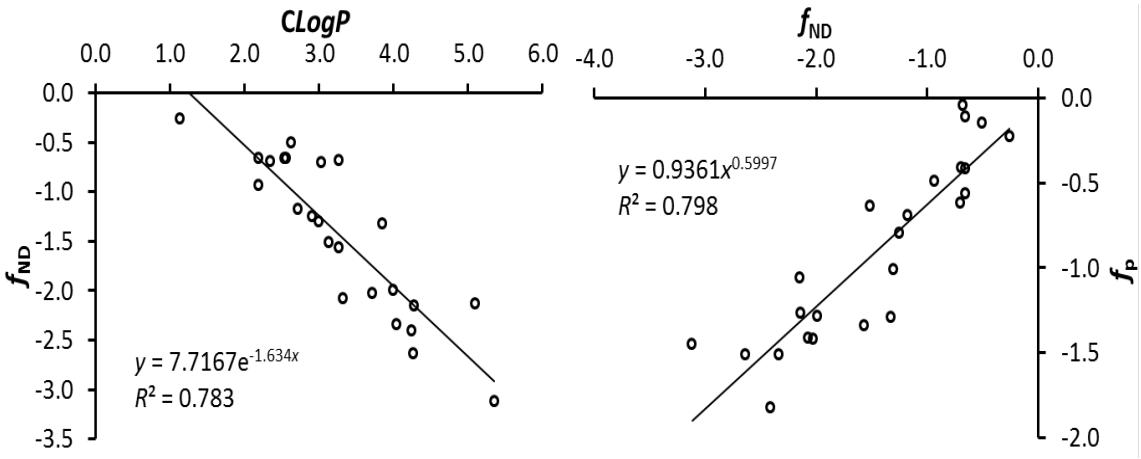

Figure 4.3: Relationships of f_{ND} vs. C*LogP* (Left) and f_P vs. f_{ND} (Right) of 24 CNS drugs, with f_P and f_{ND} measured using mouse's blood and brain tissues by equilibrium dialysis. C*LogP* was calculated using C-Lab. Data was taken from Maurer et al. [2004] and Wan et al. [2007].

Guo's Dataset

Guo et al. [2009] measured the f_P and f_{ND} values of 28 CNS radioligands using pig's blood and homogenised brain tissues. The lipophilicity, C*LogD* of the respective compound was calculated using the in-house software. Reasonably good correlations between f_P vs. f_{ND} (R^2 = 0.548) and poor correlation between f_{ND} and C*LogD* (R^2 = 0.232) were obtained (Figure 4.4). The poor correlation may be due to the inclusion of a few radioligands that are actively transported across the BBB. As it is difficult to distinguish in-house classified compounds that are actively transported across BBB, correlations were carried using all listed compounds.

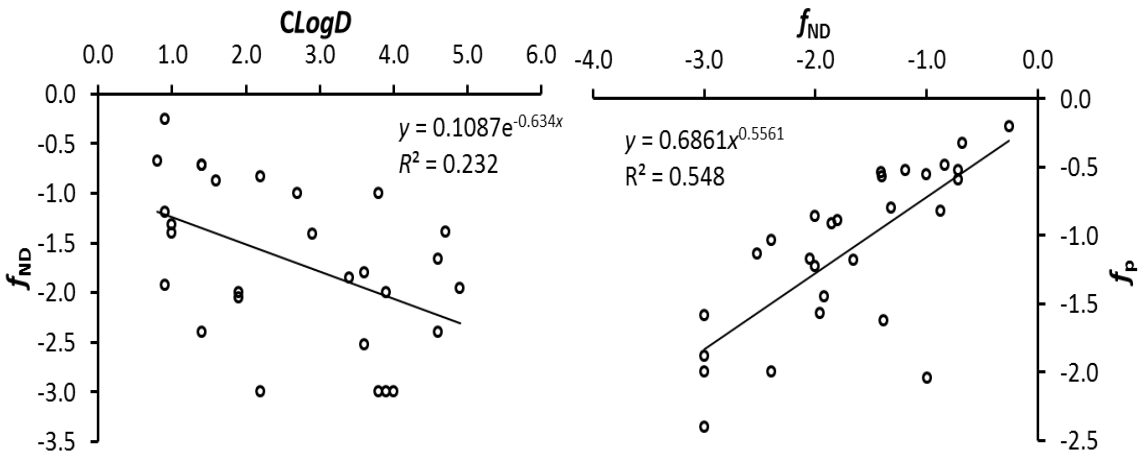

Figure 4.4: Relationships of f_{ND} vs. C*LogD* (Left) and f_P vs. f_{ND} (Right) of 28 CNS radioligands, with f_P and f_{ND} measured using pig's blood and brain tissues by equilibrium dialysis. C*LogD* was calculated using the in-house software. Data was taken from Guo et al. [2009].

Summerfield's Dataset

Summerfield et al. [2006] measured the f_P and f_{ND} values of 43 CNS drugs using rat's blood and homogenised brain tissues. The lipophilicity, C*LogP* was calculated using BioByte (BioByte Corp., US). Reasonably good correlations were obtained between f_{ND} vs. C*LogP* and f_P vs. f_{ND}, with R^2 of 0.601 and 0.664 respectively (Figure 4.5).

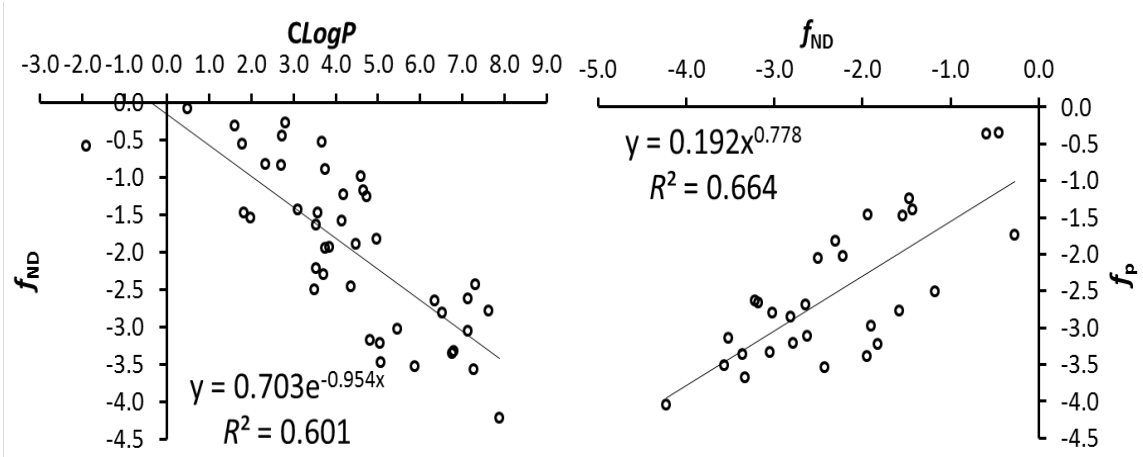

Figure 4.5: Relationships of f_{ND} vs. C*LogP* (Left) and f_P vs. f_{ND} (Right) of 43 CNS drugs, with f_P and f_{ND} measured using rat's blood and brain tissues by equilibrium dialysis. C*LogP* was calculated using BioByte. Data was taken from Summerfield et al. [2006].

Kalvass's Dataset

Kalvass et al. [2007] compiled a list of measured f_P and f_{ND} values of 34 CNS drugs from literature or measured in-house using mouse's blood and homogenised brain tissues. The experimental

lipophilicity, X*LogP3* of the respective compounds were extracted from an online database (ChemSpider, Royal Society of Chemistry). Reasonably good correlations between f_P vs. f_{ND} (R^2 = 0.577) and poor correlation between f_{ND} and X*LogP3* (R^2 = 0.397) respectively were obtained (Figure 4.6). The poor correlations may be due to experimental errors and differences in procedures in measuring f_P, f_{ND} and *LogP*.

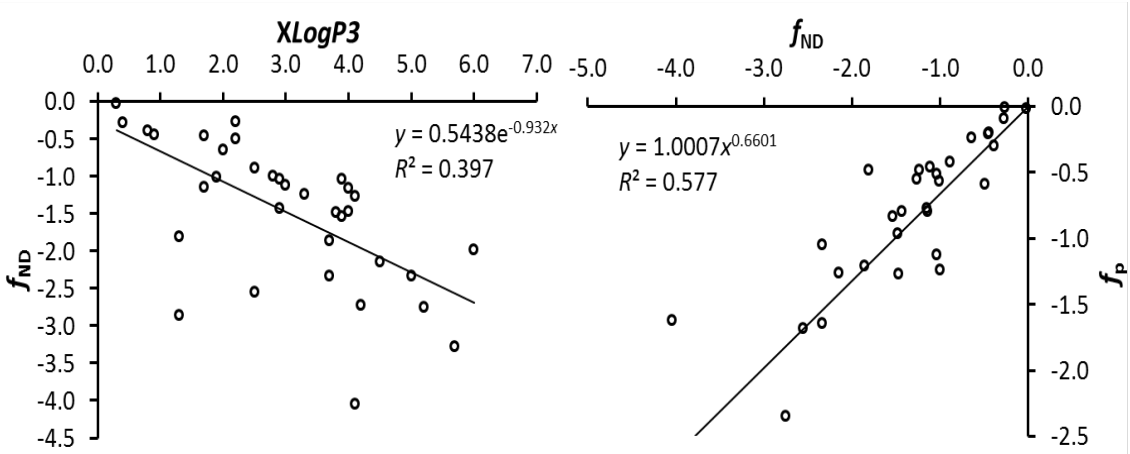

Figure 4.6: Relationships of f_{ND} vs. X*LogP3* (Left) and f_P vs. f_{ND} (Right) of 34 CNS drugs from literature or measured in-house using mouse's blood and homogenised brain tissues by equilibrium dialysis. X*LogP3* was extracted from the online database (ChemSpider). Data was taken from Kalvass et al. [2007].

4.3.2 *In Silico* f_p - f_{ND} Model

Out of the 4 datasets, Wan and Maurer's datasets showed the best correlation between lipophilicity and f_{ND}, as well as f_P and f_{ND}. Summerfield and Guo's dataset contain compounds that are actively transported across the BBB, hence the dataset showed slightly poorer correlations compared to Wan and Maurer's. Kalvass's dataset also had poorer correlations because of experimental errors and differences in procedures from different institutions. Therefore, Wan and Maurer's dataset was used to develop the *in silico* f_P-f_{ND} model to derive f_P and f_{ND} from the lipophilicity of the amyloid radiotracers.

Although C*LogP* (C-Lab) was used to derive the f_P-f_{ND} models, M*LogP* (dproperties) and *LogD+S* (MedChem) will be used as an input for lipophilicity due to the unavailability of C-lab software. The following relationships from Wan [2007] and Maurer [2004] dataset will be applied to determine f_P and f_{ND} values using lipophilicity as input.

$$f_{\mathrm{ND}} = 7.717e^{-1.634 \cdot LogP} \tag{40}$$

$$f_{\mathrm{P}} = 0.936 \cdot {f_{\mathrm{ND}}}^{0.600} \tag{41}$$

This model was developed using CNS drugs that are passively transported cross the BBB, hence it might not be applicable for compounds that are actively transported across the BBB.

4.3.3 Evaluation of *In Silico* f_P values by Ultrafiltration

To evaluate the proposed *in silico* f_P-f_{ND} model, the outcome f_P and f_{ND} values from the model need to be validated. Equilibrium dialysis is the gold standard employed to measure both f_P and f_{ND} values, but it is tedious and long to carry out. Ultrafiltration is a simple and rapid method of separating the free drug from the protein-bound drug using centrifugation to force the mixture through a selectively permeable membrane. Thus, it was applied instead to measure f_P values of the available amyloid radiotracers at our center. This subsection covers the issues in ultrafiltration, followed by the procedures carried out to measure f_P of amyloid radiotracers and the evaluation of the *in silico* f_p values predicted from the proposed f_P-f_{ND} model, using the literature reported f_P values and the f_p values measured via ultrafiltration.

4.3.3.1 Issues in Ultrafiltration

Target Binding Conditions

Compound binding to target sites decreases with increasing temperature [Kwong et al., 1985]. To mimic the *in vivo* conditions, ultrafiltration is normally carried out at 37°C using a temperature-controlled equipment. However, lipolysis of the plasma samples may occur after a long experimental period at 37°C. Therefore, care is needed to ensure that the experiment is conducted within a reasonable time window for consistency in results.

The pH of the plasma may cause ionisation of the compound or the target protein. This affects the interaction between the compound and the target protein. The pH of the plasma is changed when it is mixed with the radioactive compound. Therefore, a neutralising agent may be required to adjust the pH of the mixture. However, pH adjustment takes time and adding neutralising agent may lead to changes in the mixture conditions. Therefore, the pH of the medium was not adjusted in our experiment.

Volume Ratio of Ultrafiltrate

Ultrafiltration utilises a pressure gradient to drive the free compound molecules through a selectively permeable membrane [Kwong et al., 1985; Dong et al., 2013]. As such, a transient decrease in the amount of the compound molecules occurs, causing the initial plasma protein to

compound equilibrium to be broken. This affects the free compound concentration and leads to inaccurate measurement [Kwong et al., 1985; Dong et al., 2013]. To ensure minimum disturbance to the protein-binding equilibrium, the volume ratio of the ultrafiltrate to the sample solution was advised to be kept less than 40% [Kwong et al., 1985, Dow et al., 2006] or if possible, less than 20% [Dong et al; 2013]. However, if the ultrafiltrate volume is too small, accurate measurement may be hindered.

The volume of ultrafiltrate is dependent on the amount and viscosity of the plasma, length of centrifugation time, centrifugal force and the type of rotor etc. Centrifugation using a fixed angle rotor will reduce the sieve effects caused by the polarisation of the plasma proteins and compounds on the filter membrane. However, as a fixed angle rotor is not available, a sliding rotor is used instead. To reduce disturbance to protein-binding equilibrium while ensuring sufficient amount of ultrafiltrate for measurement using a gamma counter, the volume ratio of the ultrafiltrate to the sample solution was kept to less than 20%.

Non-Specific Binding

Ultrafiltration utilises a filter membrane of a specified size to allow unbound compounds and water to freely diffuse through the filter. However, non-specific binding (NSB) of the compound molecules can occur due to the charge property of the filter membrane and the device wall [Wang et al., 2013]. Pre-treatment of the filter membrane can help to reduce binding of the compound to the filter membrane [Lee et al., 2003]. However, NSB should be less than 5% [Dow et al., 2006] without pre-treatment of the filter membrane, or less than 50% with pretreatment to ensure that the f_p values measured by ultrafiltration will correlate with that from equilibrium dialysis [Lee et al., 2003].

NSB is measured using the radiolabelled compound with phosphate buffer saline (PBS). Some suggested that since PBS and plasma have different viscosity properties, they have different NSB behaviours when incubated in the Centrifree tubes [Wang et al., 2013]. As such, NSB values calculated using PBS was said to be a poor representation of that of plasma. However, no reliable methods exist to determine NSB in ultrafiltration. Therefore, NSB was determined using the conventional method with PBS. In addition to NSB, the recovery of the compounds was also determined to evaluate the applicability of ultrafiltration in measuring f_P of amyloid radiotracers.

4.3.3.2 Ultrafiltration

Phosphate Buffer Saline (PBS) solution preparation

PBS (pH 7.4, Wako Pure Chemical Industries, Japan) was diluted with Milli-Q water (Millipore, US) to obtain a 1:10 PBS solution. The solution was stored at about 4°C when not in use.

Plasma Samples Handling and Storage

Human plasma (Common Pool with Heparin, 100 mL) (Cosmo Bio, Japan) was de-froze completely upon receipt, within 80 min at 30°C in a pre-warmed incubator (Taitec, Japan). De-froze plasma samples were then centrifuged using a temperature-controlled centrifugal machine (Kubota 2800, Japan) for 10 min, at 2500 xg at 25°C to remove the triglycerides [Dow et al., 2006]. Triglycerides would be stuck at the bottom of the centrifugal tubes at the end of centrifugation and could be separated from the plasma samples. The samples were then vortexed to ensure even mixing and pipetted into storage tubes (4 mL x 24) for storage at -80°C. Repeated freeze-thaw cycles were kept strictly to two (initial separation and ultrafiltration) to prevent lipolysis and to maintain the integrity of the plasma samples [Dow et al., 2006].

Ultrafiltration

One tube of frozen human plasma sample (4 mL) was de-froze at 37°C for 30 min in a pre-warmed incubator (Taitec, Japan). The presence of triglycerides and plasma pH were checked [Dow et al., 2006]. 4 mL of PBS was pipetted into another storage tube and kept in the incubator for 30 min at the same time. After 30 min of defrosting, 40µL (^{18}F) or 200µL (^{11}C) of the radiolabeled compound was pipetted into both plasma and PBS storage tubes. Both tubes were vortexed and incubated for 30 min at 37°C, with side-to-side tiling to ensure continuous mixing.

1 mL of radioactive plasma and PBS were then pipetted into three Centrifree tubes (10 kDa MWCO, Millipore) each. Centrifugation was carried out with sliding buckets at 2000 xg for 20 min at 37°C, using a temperature-controlled centrifugal machine (Kubota 2800, Japan). The Centrifree tubes of both plasma and PBS and their respective ultrafiltrate containers were weighed before and after centrifugation to obtain the weight of the plasma left in the pipette (W_{pti}) and the ultrafiltrate (W_{pfi}).

Fifteen empty gamma counter tubes were weighed. 100 µL of the plasma in the original storage tubes (C_{pi}), plasma left in the pipette of the Centrifree tubes (C_{pti}) and the respective ultrafiltrate

(C_{pfi}) were pipetted into gamma counter tubes. The radioactivity in each tube was measured in three aliquots using WIZARD2 (2480, Perkin Elmer). The same procedure was repeated for PBS to obtain radioactivity concentration in the original storage tube (C_{bi}), and the PBS ultrafiltrate (C_{bfi}). The filled gamma counter tubes were then weighed.

Ultrafiltration was carried out using three available amyloid radiotracers in CYRIC, Tohoku University – [^{11}C]BF227, [^{11}C]PIB and [^{18}F]florbetapir. For each radiotracer, f_P was measured in three aliquots to determine the variability within each measurement and measurements were carried thrice to determine the reproducibility of measurements.

4.3.3.3 Determination of f_P

Due to NSB issues in ultrafiltration, a few methods were proposed to calculate f_P. The basic method was used as the standard [Dow et al, 2006], but it does not correct for NSB. A "reference" method, using PBS was introduced to correct for NSB [Lee et al., 2003]. However, PBS has different viscosity property from plasma and hence may not be suitable for correcting NSB in plasma [Wang et al., 2013]. Moreover, the accuracy of f_P measurements is dependent on the ultrafiltrate volume ratio. Thus, Wang et al. [2013] introduced a mass-balance method to correct for the differences in measurements due to the differences in volume ratio. The three methods of determining f_P values were explored and compared to literature' values where applicable.

A. Mass-balance Method [Wang et al., 2013]:

The f_P, NSB and recovery were calculated using the mass balance method as follows:

$$\%\ \text{Recovery} = \sum_{i}^{n}\left\{\frac{(C_{pf_i} \times W_{pf_i}) + (C_{pt_i} \times W_{pt_i})}{(C_{p_i} \times W_{p_i})}\right\} \times \frac{100\%}{n} \tag{42}$$

$$\%\ \text{NBS} = \sum_{i}^{n}\left\{1 - \frac{C_{bf_i}}{C_{b_i}}\right\} \times \frac{100\%}{n} \tag{43}$$

$$f_P = \sum_{i}^{n}\left\{\frac{C_{pf_i} \times V_{pf_i}}{(C_{pt_i} \times V_{pt_i}) + (C_{pf_i} \times V_{pf_i})}\right\} \times \frac{100\%}{n} \tag{44}$$

B. Reference Method [Lee et al., 2003]:

$$f_P = \sum_{i}^{n}\left\{\frac{C_{pf_i}/C_{p_i}}{C_{bf_i}/C_{b_i}}\right\} \times \frac{100\%}{n} \tag{45}$$

C. Basic Method [Dow et al, 2006]:

$$f_P = \frac{C_{pf_i}}{C_{p_i}} \times 100\% \quad (46)$$

where *i* refers to the number of samples measured (n = 1 ~ 3), *p* refers to plasma and *b* refers to PBS (buffer), *t* refers to top part or the pipet of the Centrifree tube, *f* refers to the ultrafiltrate, without *t* or *f* refers to the total of both top and filtrate part of Centrifree tube, which is taken from the original storage tube. *C* refers to the radioactive concentration measured using WIZARD and *W* refers to the weight of the sample.

For example, C_{pi} and W_{pi} are the radioactive concentration and the total weight of the plasma sample in the original storage tube, C_{pti} and W_{pti} are the radioactive concentration and weight of the plasma in the pipet of the Centrifree tube, C_{pfi} and W_{pfi} are the radioactive concentration and weight of the ultrafiltrate respectively.

4.3.3.4 Comparison with Literature f_P values

Up to date, there were few values of f_P reported for amyloid radiotracers (Table 4.6), and the methods used to calculate f_P were not discussed. The f_P values extracted from the literature were measured by means of thin layer chromatography or ultrafiltration. Thus far, no f_{ND} values were available from the literature. As binding to plasma protein is species-dependent [Di et al., 2011], human plasma samples were used in our experiment. However, the reported f_P values were measured using animals' plasma samples (e.g. rat and monkey), and hence the direct comparison of f_P values of [^{11}C]PIB was difficult.

Table 4.6: Measured f_P of [^{11}C]PIB, [^{18}F]flutemetamol and [^{11}C]MeS-IMPY reported in literature.

Tracer	f_P (%)	Method of Measurement	Species	References
[^{11}C]PIB	14	Thin-layer Chromatography (60 min)	Rat	Snellman et al., 2012
[^{18}F]flutemetamol	1 (0.9–1.3)#	Ultrafiltration	Rat	Snellman et al., 2012
[^{11}C]MeS-IMPY	0.83 ± 0.17*	Ultrafiltration	Monkey	Seneca et al., 2007

Range of f_P values
* Mean ± Stdev

Table 4.7 shows the recovery, NSB, volume ratio and f_P values, determined using the mass-balanced, reference and basic methods of [^{11}C]PIB, [^{18}F]florbetapir and [^{11}C]BF227. [^{11}C]PIB had the highest NSB to the filter membrane, followed by [^{11}C]BF227 then [^{18}F]florbetapir. The opposite trend was observed in the f_P values calculated using the mass-balance and basic methods.

For the reference method, [^{11}C]BF227 had the highest f_P value, followed by [^{11}C]PIB then [^{18}F]florbetapir. The average volume ratio of the ultrafiltrate was kept less than 20%, with an overall mean of 18.4% and a standard deviation of 0.5% (Table 4.7).

Table 4.7: Recovery, NSB, ultrafiltrate volume ratio and f_P measured using ultrafiltration. Results are presented in *mean* ± *stdev*. *In silico* f_P determined from the model is also displayed.

Radiotracers	Recovery (%)	NSB (%)	Volume Ratio (%)	f_P (%)			
				Mass Balanced	Reference	Basic	*In Silico*
[^{11}C]PIB	82.1±1.3	99.0±0.2	18.7±0.4	0.04±0.02	15.0±4.39	0.13±0.11	30.3
[^{18}F]florbetapir	83.3±0.5	65.6±2.3	16.7±0.8	0.64±0.07	9.28±0.62	3.17±0.19	27.0
[^{11}C]BF227	81.7±1.5	94.7±0.3	18.1±0.5	0.19±0.01	16.2±0.67	0.84±0.03	30.4

Measured values are presented as *Mean* ± *Stdev*.

The mass-balance method can correct for the differences in the ultrafiltrate volume output, which are affected by the centrifugal forces and the length of centrifugation. The reference method corrects for NSB to the filter membrane, by using PBS as a reference. However, the PBS and plasma have different viscosities and hence, the use of PSB to correct for NSB effect should be applied with caution. The basic equation has the advantage of avoiding possible complications of correcting for NSB with PBS, especially for radiotracers with high NSB. However, it has the disadvantage of greater variabilities due to differences in volume ratio, NSB, etc. The three methods resulted in very different f_P values (Table 4.7), hence showing the effect of the calculation methodology on the outcome f_P values. The huge differences might be caused by the high NSB of the amyloid radiotracers to the Centrifree equipment. As such, the reported f_P values measured using ultrafiltration could not be used for validation (Table 4.7).

The measured concentrations varied by less than 5%, within an experiment and between the experiments, for all the radiotracers measured. Therefore, the procedure was well-controlled and optimised for f_P measurements. As only three clinically-applied amyloid radiotracers were available for f_P measurements, it was difficult to use the measured f_P values for validating the *in silico* f_P values. Moreover, due to the binding nature of all the measured amyloid radiotracers, NSB was always greater than 50% and % recovery values were also less than 90% (Table 4.7). Great differences in calculated f_p values across the three calculation methods were observed. Therefore, ultrafiltration was not a suitable method for measuring the f_P of amyloid radiotracers.

Although the results showed that ultrafiltration was not a suitable method for measuring f_P values,

the results obtained showed a similar trend to the performance of clinically-applied radiotracer, whereby [^{11}C]PIB showed higher amyloid binding than [^{18}F]florbetapir. If more clinically-applied radiotracers were available, further evaluation on the possible relationship could be carried out. The literature f_P values that were measured by ultrafiltration were also very small, showing that our measured results were consistent with measured results (Table 4.6). However, as animal's plasma was used in literature, they could not be used for direct validation or comparison with our results.

4.3.4 Summary

An *in silico* f_P-f_{ND} model was developed based on the relationships between lipophilicity, f_P and f_{ND} relationships using data from Wan and Maurer's datasets. We tried to validate the proposed f_P-f_{ND} model using f_P values measured via ultrafiltration. However, high NSB of greater 50% and poor recovery of less than 90% were obtained. Thus, ultrafiltration was not suitable for measuring f_P of amyloid radiotracers. The model needs to be validated by other means. A possible method would be to carry out simulations with the *in silico* f_p and f_{ND} values and to determine if the outcome parameters of interest correlate well with reported clinical results.

4.4 Dissociation Constant & Binding Sites Density

The binding affinity of a radiotracer or drug to the target protein is an important parameter evaluated in the drug/radiotracer development process. It is represented by the inverse of binding affinity, the equilibrium dissociation constant, K_D. K_D is measured via *in vitro* binding assays but can also be determined from *in vivo* measurements via PET or SPECT imaging [Lopresti et al., 2005]. For amyloid radiotracers, K_D or K_i values were commonly measured using synthetic $A\beta_{1-40}$ and $A\beta_{1-42}$ fibrils, or human AD brain homogenates. However, some amyloid radiotracers have been reported to bind to multiple binding sites on the Aβ proteins [Lockhart et al., 2005; Ni et al., 2013] (section 2.3). Reported K_D or K_i values of the various amyloid radiotracers were compiled and compared to understand their binding characteristics. The type and density of various types of Aβ proteins in HC, MCI and AD were surveyed from literature to determine the representative binding sites concentrations.

This section describes the *in vitro* binding assays used to measure K_D and K_i values, as well as the Enzyme-Linked Immuno-Sorbent Assay (ELISA) to measure the concentrations of various types of Aβ proteins in brain homogenates. A selection criterion for selecting K_D and K_i values from

literature to ensure consistency in results for comparison is described. The representative amyloid load concentrations under HC, MCI and AD conditions is also explained.

4.4.1 *In Vitro* Binding Assays

The *in vitro* binding assay is based on the simple 1-to-1 model of the receptor (R) and radiotracer (L) interacting to form a complex (RL) as described by Michaelis and Menten:

$$[\mathrm{L}] + [\mathrm{R}] \rightleftharpoons_{k_{\mathrm{off}}}^{k_{\mathrm{on}}} [\mathrm{RL}] \tag{47}$$

where [L] is the concentration of the free radiotracer (mol/L or M), [R] is the concentration of the receptors (M), and [RL] is the concentration of the bound radiotracer-receptor complex (M). k_{on} is the association rate constant (M/min) and k_{off} is the dissociation rate constant (min^{-1}).

Based on the law of mass action, there is no net change in concentration of the radioligand at equilibrium and the following relationship results:

$$[\mathrm{L}] \cdot [\mathrm{R}] \cdot k_{\mathrm{on}} = [\mathrm{RL}] \cdot k_{\mathrm{off}} \tag{48}$$

Under the law of mass action, it is assumed that (1) all the receptors are equally accessible to all radiotracers, (2) interacting components can diffuse freely within the medium, (3) all receptors are either free or bound, without any partial binding to the radiotracers, (4) the receptor and radiotracers are not altered by interaction, and (5) the binding of radiotracer to the receptor is reversible [Limbird et al., 2011].

In reality, these assumptions are never fully achieved as the radiotracers and receptors are never freely moving in the homogenised tissues or tissue slices or synthetic mixture under *in vitro* conditions. The binding is also dependent on the temperature and pH of the medium and hence the measured K_{D} values are more appropriately referred to as "apparent" values under *in vitro* conditions. Two types of binding assays are commonly employed to determine the binding affinity of a compound, namely saturation and competitive binding assays.

4.4.1.1 Saturation Binding Assay

In a saturation binding assay, increasing concentrations of radiotracer are added to a fixed concentration of receptors. [RL] is measured in the assay while [R] is unknown and needs to be determined. A high concentration of radiotracer is added such that [L] >> [R] and less than 5% of

the radiotracers are bound by either specific binding to the target receptor or non-specific binding to receptors or equipment. In this case, $[L]_{free}$ can be assumed to be equal to the $[L]_{total}$.

The equilibrium dissociation constant (K_D, nmol/L or nM) can be determined from a saturation binding assay. It is defined as the ratio of the dissociation rate constant (k_{off}) and the association rate constant (k_{on}), such that $K_D = k_{off}/k_{on}$. The total receptor concentration, B_{max} is the sum of the free receptor concentration and the bound complex concentration, where B_{max} = [R] + [LR]. By substituting K_D and B_{max} into equation (48):

$$\frac{[\mathrm{RL}]}{B_{\max}} = \frac{[\mathrm{L}]}{K_{\mathrm{D}} + [\mathrm{L}]} \tag{49}$$

Fractional occupancy, f is the ratio of the bound complex concentration to the total receptors concentration, where $f = [RL]/B_{max}$. When the fractional occupancy is 50%, K_D is equal to [L]. The fractional occupancy is plotted against the free radiotracer concentration [L] to obtain the occupancy curve (Figure 4.7) [Limbird et al., 2011].

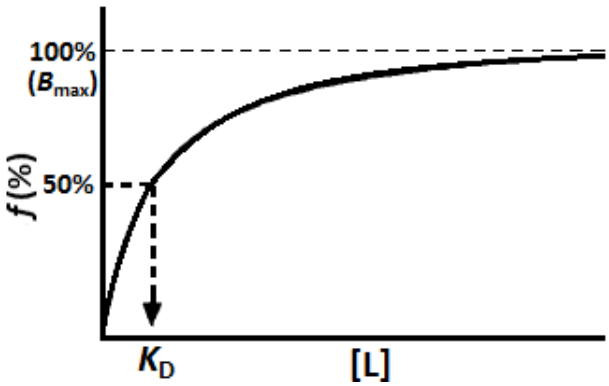

Figure 4.7: A typical occupancy curve.

The accuracy of K_D value is dependent on the choice of the model used to fit the occupancy curve. To avoid the complexity of fitting a sigmoidal curve, a Scatchard plot is commonly employed to derive K_D. This is done by dividing by [L] on both sides of equation (49):

$$\frac{f}{[\mathrm{L}]} = \frac{1}{K_{\mathrm{D}}} - \frac{f}{K_D} \tag{50}$$

A Scatchard plot of f / [L] against f is then linearly fitted whereby the slope yields $-1/K_D$, and the x-intercept gives B_{max} (Figure 4.8).

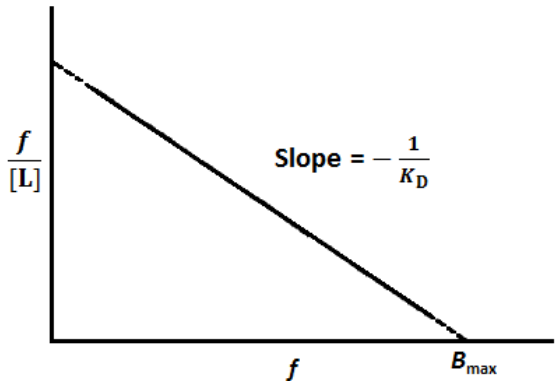

Figure 4.8: A typical Scatchard Plot.

4.4.1.2 Competition Binding Assay

In a competition binding assay, the equilibrium inhibitory constant, K_i of the target compound or unlabeled tracer is determined by using a single concentration of radiolabeled competitor and varying the concentrations of the unlabeled tracer. The radiolabeled competitor and unlabeled tracer should compete for the same target site or receptor. Similar to the saturation binding assay, the concentrations of the radiolabeled competitor and unlabeled tracer are much greater than the receptor concentration, such that the total free concentrations of both the radiolabeled competitor and the unlabeled tracer are equal to the amount added. The fractional occupancy is plotted against the logarithmic concentration of the unlabeled tracer (Figure 4.9) [Limbird et al., 2011].

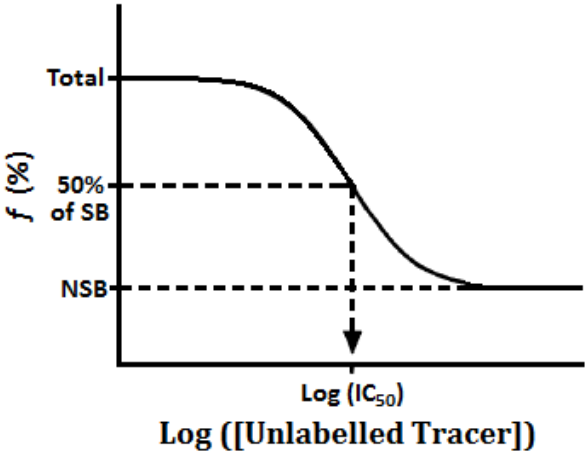

Figure 4.9: A typical occupancy curve for competition binding assay.

When f is 100%, no unlabeled tracer is present. The trough of the curve (Figure 4.9) gives the non-specific binding (NSB), while the difference between the peak and trough gives the specific binding of the radiolabeled competitor. The inhibitory concentration, IC_{50} is defined as the concentration of the unlabeled tracer that results in 50% specific binding of the radiolabeled

competitor. K_i value is determined from IC_{50} using Cheng-Prusoff equation [Limbird et al., 2011].

$$K_i = \frac{IC_{50}}{1 + \frac{[\text{Radioligand}]}{K_D}} \tag{51}$$

K_D value of the radiolabeled competitor must be known and is determined from saturation binding studies. Increasing the concentration of the radiolabeled competitor will increase IC_{50}, but K_i value remains constant. If a radiolabeled competitor with higher affinity (lower K_D) is used, a higher concentration of the unlabeled tracer will be required to compete with the competitor [Limbird et al., 2011]. Longer equilibrium time may lead to inaccurate K_i value of the unlabeled tracer. K_D is only equal to K_i if the radiolabeled competitor and the unlabeled radiotracer are the same compound or have similar binding affinities.

4.4.1.3 Binding to Multiple Receptor Sites

Amyloid radiotracers have been shown to bind with different affinities to multiple independent binding sites of different concentrations on the fibrillar Aβ proteins [Lockhart et al., 2005; Ni et al., 2013]. In such cases, the fractional occupancy of equation (49) is modified as shown:

$$f = \frac{\sum_i^n [\text{RL}_i]}{B_{\max}} = \sum^n \frac{m \cdot n \cdot [\text{L}]}{[\text{L}] + K_{D,n}} \tag{52}$$

where n is the number of binding sites, m is the density of each respective binding site.

The occupancy curve shown in figure 4.7 will become a sum of hyperbolas, which is difficult to be observed by the eye. The occupancy curve is thus converted to Scatchard plot whereby the linear plot in 1-to-1 binding (Figure 4.8) will be observed as a curve in the case of binding to multiple receptor sites (Figure 4.10).

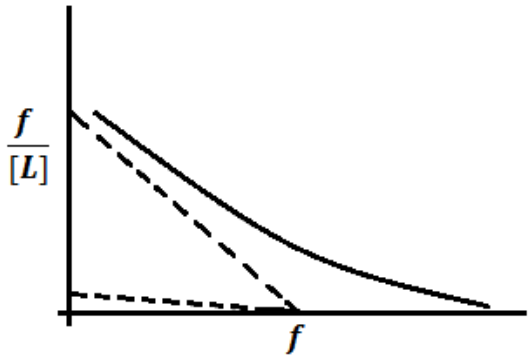

Figure 4.10: A Scatchard Plot showing binding to multiple binding sites. The bold line represents the actual fit through the measured data points. The dashed lines represent the solutions to two possible receptor sites.

4.4.2 Enzyme-Linked Immuno-Sorbent Assay (ELISA)

Enzyme-linked immunosorbent assay (ELISA) or enzyme immunoassay (EIA) are biochemical assays that rely on specific antigen-antibodies binding with chromogenic substrate-enzyme reaction for the detection of very small concentrations of biological molecules such as hormones, peptides and proteins [Gan et al., 2013]. ELISA can be applied only if a known antibody or antigen is available to detect a given antigen or antibody [Gan et al., 2013].

In direct ELISA, the target biological molecules, which are bound to specific antigens, are immobilised in a 96-well microtiter plate (Figure 4.11). The antigen then binds specifically to a capture antibody, which then binds specifically to an enzyme-linked detector antibody. A chromogenic substrate is then added and it interacts with the enzyme to produce a colour change or emit fluorescence. Quantitative measurement of the amount of target biological molecules can be carried out using a colorimetric reading or fluorescence detector. The measured colour intensity correlates directly with the concentrations of the bound antibodies in non-competitive ELISA [Gan et al., 2013].

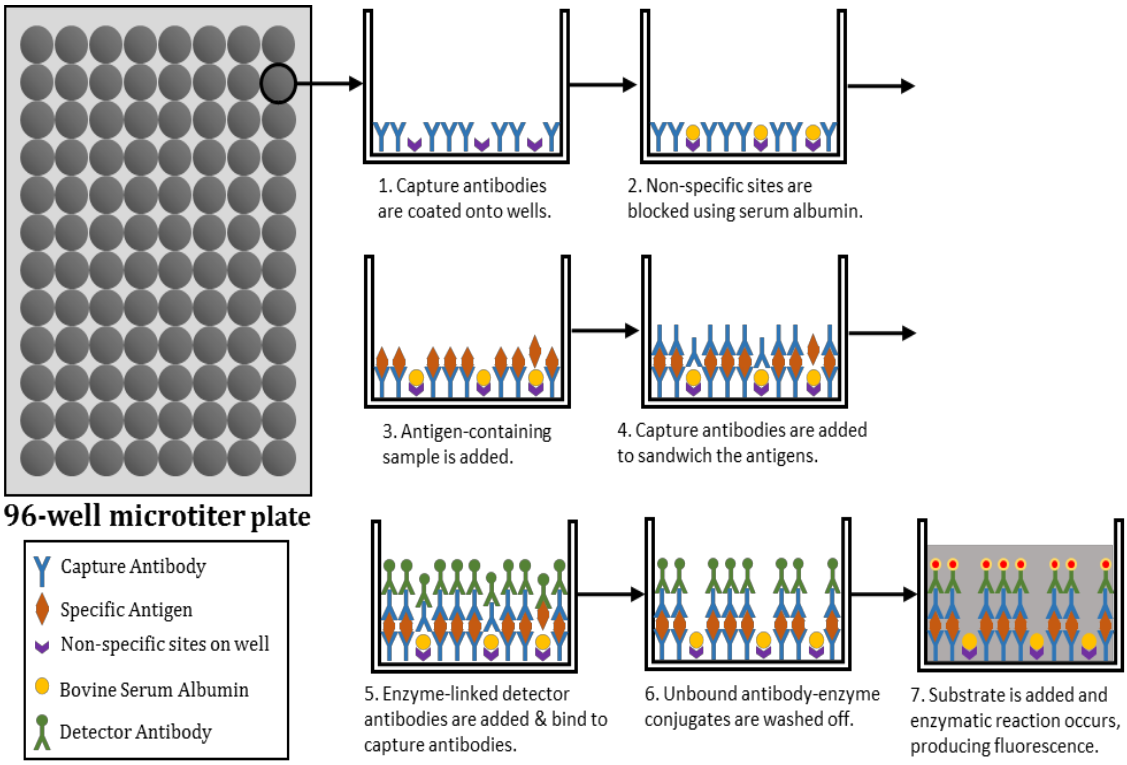

Figure 4.11: Procedures for "Sandwich" ELISA [Gan et al., 2013].

To measure the amount of different types of Aβ in AD brain tissues, "sandwich" ELISA is commonly applied. It is a non-competitive method whereby the antigen is sandwiched between the capture antibodies. This ensures that the target bound antigens are immobilised in the well, hence eliminating the need to purify the mixture from other antigens [Gan et al., 2013]. The general procedure for Sandwich ELISA is shown in figure 4.11.

ELISA is a highly sensitive method for detecting very low concentrations of antigens compared to other technology like spot blotting, immunoblotting, immunohistochemistry etc. However, it also has some limitations, which will affect the accuracy of the measurement. Firstly, the strength of the fluorescence or colour emitted will decrease over a long period, hence reducing the accuracy of measurement. Secondly, the antibodies bind nonspecifically to the walls of the wells or other antigens that may be present in the sample. This NSB may be reduced with the use of bovine serum albumin [Gan et al., 2013] or non-fat dry milk [Naslund et al., 2000]. However, the applicability of milk must be validated as the amount of immunoglobulins or natural antibodies present may affect the measurement. Background correction is also required for each set of measurement to correct for NSB, which is measured with the antigen omitted. Thirdly, ELISA is dependent on the specific antigen-antibodies binding for measuring the target concentrations. Therefore, the accuracy of the detection of the target molecules is dependent on the antigen and the antibodies applied. Lastly, the measurements are affected by the choice of the well, dilution method, the detection method (e.g. colour change, fluorescence). Optimisation of procedures can ensure the reliability and accuracy of the data for comparison and evaluation within an institution but the data cannot be compared directly across institutions.

4.4.3 Concentrations of $A\beta_{1-40}$ & $A\beta_{1-42}$ in Brain

The concentrations of $A\beta_{1-40}$ and $A\beta_{1-42}$ in human brain homogenates can be measured quantitatively using ELISA. The detection of $A\beta_{1-40}$ and $A\beta_{1-42}$ are commonly carried out using immunohistochemistry, western blotting etc. but these methods are unable to measure the concentration of $A\beta_{1-40}$ and $A\beta_{1-42}$ quantitatively. Currently, the available antigen-antibodies employed in ELISA can measure the total concentrations of $A\beta_{1-40}$ and $A\beta_{1-42}$. Compartmental-extraction or biochemical sample method can be applied to differentiate soluble and insoluble, and intracellular and extracellular Aβ using various buffers: Tris (extracellular soluble Aβ), trition (intracellular soluble Aβ), sodium dodecyl sulfate (SDS) (membrane-associated Aβ) and formic acid (FA) (extracellular-insoluble Aβ associated with parenchymal and vascular amyloid deposition) [Steinerman et al., 2008]. However, this method only increases the fractions of the

targeted Aβ proteins. Thus, the samples still suffer from small amounts of contaminations from other forms of Aβ proteins during measurements [Steinerman et al., 2008].

The antibodies for $A\beta_{1-40}$ and $A\beta_{1-42}$ were shown to bind to Aβ oligomers with higher selectivity than that of monomeric Aβ, but the measurements also included a small amount of monomeric Aβ [Klaver et al., 2011]. Moreover, different antibodies with the same affinity to the same target may have different binding kinetics [Klaver et al., 2011]. As PET measures the total signal from the binding of the amyloid radiotracer to fibrillar Aβ in the various brain regions, the total concentrations of $A\beta_{1-40}$ and $A\beta_{1-42}$ in the brain regions measured using ELISA is sufficient for our analysis.

Although there are many studies that measured the concentrations of various Aβ in either synthetic Aβ or human brains using ELISA, few have reported the measured values. The concentrations of $A\beta_{1-40}$ and $A\beta_{1-42}$ in various brain regions of HC and AD subjects measured via ELISA, using different antigen-antibodies pairs, from four different institutions were compared (Table 4.8).

Naslund et al. [2000] used 4G8 (anti-$A\beta_{17-20}$) as the capture antibody and αAβC40 (anti-$A\beta_{40}$) and αAβC42 (anti-Aβ42) as detector antibodies to measure the Aβ concentrations in 38 AD and 24 HC brains. The total concentrations of extracellular soluble and insoluble Aβ were evaluated in 5 different brain regions. Naslund's results showed that the concentrations of $A\beta_{1-42}$ were generally higher than $A\beta_{1-40}$ in both HC and AD (Table 4.8). Moreover, the Tris and FA-extracted $A\beta_{1-40}$ and $A\beta_{1-42}$ correlated with disease severity, and the concentrations of $A\beta_{1-40}$ and $A\beta_{1-42}$ correlated with each other.

Ingelsson et al. [2004] employed BNT77 (anti-$A\beta_{11-28}$) as the capture antibody and BA27 (anti-$A\beta_{40}$) and BC05 (anti-Aβ42) as the detector antibodies to measure the Aβ concentrations in the temporal cortices of 83 AD and 26 HC brains. Ingelsson's results showed that FA-extracted $A\beta_{1-40}$ and $A\beta_{1-42}$ were elevated in AD independent of illness duration and Tris and FA-extracted $A\beta_{1-40}$ are increased in subjects with APOE-ε4 allele.

Table 4.8: Concentrations of $A\beta_{1-40}$ and $A\beta_{1-42}$ (pmol/g of tissue) measured via ELISA in the various brain regions of HC and AD subjects, as reported from four literature. The calculated ratios of the concentrations of $A\beta_{1-42}$ to the total Aβ in HC and AD subjects based on the reported data were also displayed.

References	Biochemical Samples	Brain Regions	Concentrations of Aβ (pmol/g of tissue)				Ratio of $A\beta_{1-42}$/Total	
			HC		AD			
			$A\beta_{1-40}$	$A\beta_{1-42}$	$A\beta_{1-40}$	$A\beta_{1-42}$	HC	AD
Naslund et al., 2000	Tris + FA	Frontal	169 ± 50	478 ± 135	657 ± 116	1924 ± 221	0.7	0.7
		Temporal	63.1 ± 28	161 ± 49	434 ± 99	1199 ± 249	0.7	0.7
		Parietal	141 ± 54	194 ± 63	621 ± 116	1023 ± 172	0.6	0.6
		Entorhinal	54.6 ± 24	303 ± 77	420 ± 169	1765 ± 205	0.8	0.8
		Visual	118 ± 39	254 ± 66	477 ± 113	933 ± 159	0.7	0.7
Ingelsson et al., 2004	Tris	Temporal	160 ± 33	703 ± 263	785 ± 163	6550 ± 641	0.8	0.9
	FA	Temporal	3 ± 1	161 ± 55	156 ± 31	8382 ± 1108	1.0	1.0
Steinerman et al., 2008	Tris	Temporal	0.8 ± 0.4	1.6 ± 3.23	2.7 ± 3.5	14.6 ± 7.5	0.7	0.8
		Cingulate	0.6 ± 0.5	1.1 ± 2.5	1.7 ± 2.4	10.2 ± 7.3	0.7	0.9
	Trition	Temporal	11.9 ± 5.2	4.0 ± 1.6	13.3 ± 9.3	7.0 ± 3.1	0.3	0.3
		Cingulate	11.6 ± 1.5	5.0 ± 1.4	12.4 ± 4.2	8.8 ± 3.0	0.3	0.4
	SDS	Temporal	55.8 ± 34.9	18.6 ± 12.7	55.4 ± 22.1	53.9 ± 27.3	0.3	0.5
		Cingulate	73.6 ± 40.3	17.1 ± 9.1	78.9 ± 28.4	25.6 ± 7.9	0.2	0.2
	FA	Temporal	89.7 ± 52.9	186.3 ± 343.4	555.6 ± 817.2	1240.2 ± 835.1	0.7	0.7
		Cingulate	120.4 ± 70.8	297.5 ± 698.5	389.9 ± 597.6	1088.9 ± 520.9	0.7	0.7
Svedberg et al., 2009	FA	Frontal	38 ± 14	34 ± 7.9	482 ± 98	226 ± 16	0.5	0.3
		Temporal	3.8 ± 1.6	26 ± 7.6	387 ± 103	276 ± 53	0.9	0.4
		Parietal	1.7 ± 1.0	35 ± 12	384 ± 116	138 ± 24	0.9	0.3
		Cerebellum	21 ± 10	4.5 ± 0.9	97 ± 13	6.6 ± 1.6	0.2	0.1

Steinerman et al. [2008] used the same capture and detector antibodies as Ingelsson et al. [2004] to measure the Aβ concentrations in the temporal and cingulate neocortices of 27 AD and 13 HC brains. Steinerman's results showed that Tris and FA-extracted $A\beta_{1-40}$ correlated with illness duration and APOE-ε4 allele. Moreover, Tris and FA-extracted $A\beta_{1-40}$ and $A\beta_{1-42}$ were elevated in AD but only Trition and SDS-extracted $A\beta_{1-42}$ were elevated in AD. Trition and SDS-extracted $A\beta_{1-42}$ correlated with AD progression and SDS-extracted $A\beta_{1-42}$ correlated well with cognitive decline. However, the results of the cingulate cortex differed from that of temporal cortex, and thus were excluded in his evaluation.

Svedberg et al. [2009] used a commercialised ELISA package (Signal Select, Biosource International, USA), with Hu Aβ40 (anti-$A\beta_{40}$) and Hu Aβ42 (anti-Aβ42) as detector antibodies to measure the Aβ concentrations in four regions of 9 AD and 9 HC brains. His results showed that AD had a higher amount of $A\beta_{1-40}$ compared to $A\beta_{1-42}$, which was different from the other studies (Table 4.8). However, Svedberg et al. [2009] concluded that these differences might be due to the inclusion of CAA in AD subjects, where $A\beta_{1-40}$ predominated over $A\beta_{1-42}$.

The measured concentrations of $A\beta_{1-40}$ and $A\beta_{1-42}$ in HC and AD brains showed different results (Table 4.8). The differences may be due to the different immunohistochemical and ELISA protocols, subject/brain inclusion criteria, the use of different brain regions and the methods of analysis across different institutions [Naslund et al., 2000; Steinerman et al., 2008]. As there were few brains available from subjects in the early stages of AD, it was difficult to determine the full disease progression [Naslund et al., 2000]. The binding kinetics and selectivity of the antibodies are different depending on the types of Aβ proteins, the length of the monomeric Aβ proteins (e.g. 40, 42, 43 etc.), and the type of terminals (C or N) after cleavage by β and γ proteases. The folding of the oligomeric and fibrillar Aβ proteins may also have an effect on the total binding.

The reported values of the concentrations of $A\beta_{1-40}$ and $A\beta_{1-42}$ were very different even in the same region with huge amount of variations (Table 4.8). To eliminate the differences caused by the different protocols employed, the ratios of $A\beta_{1-42}$ concentration to total Aβ concentration in HC and AD were determined (Table 4.8). As amyloid radiotracers are targeting extracellular amyloid plaques, only Tris and FA-extracted (extracellular soluble and insoluble) data are considered. Apart from Svedberg's results, which consisted of CAA subjects, the Tris and FA-extracted (extracellular soluble and insoluble) ratios of $A\beta_{1-42}$ to total Aβ concentrations in HC and AD were relatively similar in Naslund's and Steinerman's data. Therefore, the ratio of $A\beta_{1-42}$ to total Aβ

concentrations in HC and AD of 0.7 will be applied as a representative ratio of $A\beta_{1-40}$ and $A\beta_{1-42}$ binding of the radiotracers in amyloid imaging.

4.4.4 Determination of K_D

Reported K_D or K_i values of amyloid radiotracers were measured using either synthetic $A\beta_{1-40}$ fibrils and/or synthetic $A\beta_{1-42}$ fibrils or human AD brain homogenates. In cases where K_D values were not available, the reported K_i values were measured using different competitors such as PIB, IMPY, florbetapir, BTA-1, TZDM and the tracer itself. The K_D or K_i values measured using human AD brain homogenates were said to differ from that measured using synthetic Aβ fibrils [Mathis et al., 2003; Klunk et al., 2005], though some had claimed that there were no differences in the measured values [Klunk et al., 2003]. In addition, the radiotracers also bind with different affinities to different binding sites on the Aβ fibrils [Lockhart et al., 2005; Agdeppa et al., 2009]. Thus, a K_D or K_i selection criteria is required to synchronise the K_D or K_i values extracted from literature to ensure more consistent outcome comparison.

In cases where K_D or K_i values of both synthetic $A\beta_{1-40}$ and $A\beta_{1-42}$ were reported, a model representing the ratio of the concentrations of $A\beta_{1-42}$ to $A\beta_{1-40}$ available in HC and AD brains is applied to obtain a single value of K_D or K_i for input. The ratio of $A\beta_{1-42}$ to total Aβ concentrations in HC and AD of 0.7, determined in the subsection 4.4.3, was employed to combine the K_D values of both synthetic $A\beta_{1-40}$ and $A\beta_{1-42}$ fibrils, as shown:

$$K_D = \left(K_{\mathrm{D,A\beta 1-40}} \times 0.3\right) + \left(K_{\mathrm{D,A\beta 1-42}} \times 0.7\right) \tag{53}$$

K_D was chosen over K_i as K_D is more consistent and representative compared to K_i, which differed greatly depending on the competitor used. The amount, types and distribution of Aβ fibrils in the brain homogenates differed greatly depending on the severity of the AD brain used, thus affecting K_D or K_i measurements. The amounts of $A\beta_{1-40}$, $A\beta_{1-42}$ and/or other proteins (e.g. NFT) in AD brain homogenates are unknown, hence the K_D or K_i values measured may vary depending on the sample homogenates used. On the other hand, the amount of synthetic $A\beta_{1-40}$ and $A\beta_{1-42}$ fibrils used can be controlled in the *in vitro* experiment, which allowed for more accurate comparison. The K_D or K_i values measured using synthetic Aβ fibrils were similar to that of AD brain homogenates [Klunk et al., 2003]. Therefore, K_D or K_i values measured with synthetic amyloid fibrils are preferred over that of AD brain homogenates.

The final K_D or K_i values used for simulations are shown in table 4.9. The K_D or K_i values were chosen in the following preference: (1) modelled value using both synthetic Aβ1-40 and Aβ1-42, (2) synthetic Aβ1-42 only, (3) synthetic Aβ1-40 only, and lastly (4) brain homogenates. For K_i values, only those measured with itself or IMPY as a competitor will be selected. IMPY was chosen due to a large number of K_i values measured with IMPY as a competitor. [^{18}F]florbetaben is the only radiotracer in the list, whereby its K_i value is measured with florbetapir as a competitor. It is included as it is an FDA-approved amyloid radiotracer that has been clinically-applied with clinical data reported in the literature.

Based on the K_D or K_i selection criterion, only radiotracers in figure 4.1 and those highlighted in figure 4.2 are used for further evaluation (Table 4.9). Most candidate radiotracers have K_i values measured with IMPY as a competitor. Those that were excluded, have K_i values measured using other competitors apart from IMPY and itself. Although the K_i value of [^{18}F]FPPIP was measured with IMPY, the value was much higher than the rest of the amyloid radiotracers selected. Therefore, it was excluded for further evaluation. Although [^{18}F]MK3328 had been clinically applied, the clinical data were presented only as posters in conferences. Hence, it was included as a candidate radiotracer instead of a clinically-applied radiotracer.

4.4.5 Binding Site Density

The maximum available binding sites, B_{max} is measured using *in vitro* binding assays, together with K_D or K_i. However, the amount of amyloid fibrils varies greatly for different subject conditions. As such, the amount of available binding sites, B_{avail} is used instead of B_{max}. The representative B_{avail} values for HC, MCI and AD conditions were determined from the *in vitro* autoradiography experiment measured using [^{11}C]PIB in the frontal, parietal and temporal cortical regions of HC, MCI (Braak stage 3) and AD brains.

The amount of [^{11}C]PIB binding is equivalent to B_{avail} and ranged from 1-5 fmol/mg (or nM), 11-34 fmol/mg and 56-62 fmol/mg in HC, MCI and AD respectively [Svedberg et al., 2009]. The B_{avail} in the three regions of the three subject groups were averaged and the resulting B_{avail} values of 4 nM, 20 nM and 50 nM were employed for HC, MCI and AD conditions respectively. Although the mean value of B_{avail} for AD was 60 nM, 50 nM was selected instead to reduce the difference between MCI and AD. The B_{avail} values ranged from 4 ± 80%, 20 ± 35% and 50 ± 25% in HC, MCI and AD conditions using the selected mean values.

Table 4.9: Compiled K_D or K_i values extracted from literature with the final K_D or K_i values used for simulations highlighted in grey. [^{11}C]PIB to [^{18}F]FIBT are clinically applied radiotracers and the rest are candidate radiotracers.

Radiotracers	*In Vitro* K_D (Literature)				
	Aβ1-40	Aβ1-42	Brain Homogenates	K_D for simulations	References
[^{11}C]PIB	2.48$^{\$}$	0.93$^{\$}$		1.40$^{\#}$	Mathis et al., 2003, Klunk et al., 2005 Ikonomovic et al., 2008, Johnson et al., 2009
[^{18}F]FDDNP	0.12	5.52		3.90$^{\#}$	Agdeppa et al., 2001, Harada et al., 2013
[^{11}C]SB13			2.43	2.43	Kung et al., 2004
[^{18}F]florbetaben (Neuraceq)			2.22$^{\&}$	2.22	Choi et al., 2009
[^{11}C]BF227	1.80¶	4.30¶		3.55$^{\#}$	Furumoto et al., 2007
[^{18}F]AV138			1.90*	1.90	Chandra et al., 2007
[^{18}F]flutemetamol (Vizamyl)	1.60			1.60	Jureus et al., 2010
[^{18}F]florbetapir (Amyvid)			3.72	3.72	Choi et al., 2009
[^{11}C]AZD2184	8.40			8.40	Johnson et al., 2009
[^{18}F]flutafuranol	2.30			2.30	Jureus et al., 2010
[^{18}F]FACT	9.40			9.40	Furumoto et al., 2013
[^{18}F]FIBT	2.10†	3.20†	0.70	0.70	Yousefi et al., 2011b, Yousefi et al., 2015a
[^{11}C]6-Me-BTA-1	20.20*			20.20	Klunk et al., 2001
[^{11}C]BTA-1	11.00*			11.00	Mathis et al., 2002
[^{18}F]FMAPO			5.00*	5.00	Zhang et al., 2005a
[^{18}F]FPEG-Stilbenes-12a§			2.90*	2.90	Zhang et al., 2005b
[^{11}C]Benzofuran-8§			0.70*	0.70	Ono et al., 2006
[^{18}F]FPEGN3-Styrylpyridine-2§			2.50*	2.50	Zhang et al., 2007
[^{11}C]MeS-IMPY			8.95*	8.95	Seneca et al., 2007
[^{18}F]Indole-14§			1.50*	1.50	Qu et al., 2008
[^{18}F]Indoline-8§			4.00*	4.00	Qu et al., 2008
[^{11}C]Benzothiazole-6a§			18.80*	18.80	Serdons et al., 2009a
[^{11}C]Benzothiazole-6b§			11.50*	11.50	Serdons et al., 2009a
[^{11}C]Benzothiazole-6c§			11.20*	11.20	Serdons et al., 2009a
[^{18}F]Benzothiazole-2§			9.00*	9.00	Serdons et al., 2009b
[^{18}F]Benzothiazole-5§			5.70*	5.70	Serdons et al., 2009c
[^{18}F]MK3328			9.60	9.60	Harrison et al., 2011
[^{18}F]FIAR		6.81*		6.81	Watanabe et al., 2011
[^{18}F]Benzoxazole-24§		9.30*		9.30	Cui et al., 2012a
[^{18}F]Pyridinylbenzoxazole-32§		8.00*		8.00	Cui et al., 2012b
[^{18}F]Phenylindole-1a§		28.40*		28.40	Fu et al., 2013

$^{\#}K_D$ is derived using K_D values of synthetic $A\beta_{1-40}$ and $A\beta_{1-42}$ using: $K_{D(A\beta1-40)} * 0.3 + K_{D(A\beta1-42)} * 0.7$
$^{\$}K_{D(A\beta1-40)}$ was averaged from 4 literatures (1.02, 0.90, 3.30, 4.70) and $K_{D(A\beta1-42)}$ was averaged from 2 literatures (0.91, 0.95).
*K_i values (with itself or IMPY as competitor)
$^{\&}K_i$ values (with florbetapir as competitor)
$^{\P}K_i$ values (with BF180 as competitor; BF180 exhibits similar binding to IMPY [Furumoto et al., 2007])
†K_i values (with PIB as competitor)
§Simplified name with the compound number or alphabet, as reported in the literature, used when generic name or institute code name (supplied by the author) was not available.

4.5 Conclusions

In this chapter, *in silico* V_x, *in vitro* K_D and fixed values of B_{avail} for HC, MCI and AD conditions were determined. An *in silico* model for predicting the f_P and f_{ND} values of the amyloid radiotracers was proposed. However, due to the limitations of the *in vitro* f_P measured via ultrafiltration, the validation of f_P-f_{ND} model has to be carried out by other means. M*LogP* (dproperties) and *LogD*+*S* (MedChem) showed potential in representing the lipophilicity of the amyloid radiotracers with good performance in *RMSE* and mean values, and good correlations in both linear and orthogonal regressions. Further evaluation by means of model simulation and correlation of predicted kinetic parameters with clinically-observed values is required to determine the representative lipophilicity model and the reliability of the f_P-f_{ND} model in predicting f_P and f_{ND} values for amyloid radiotracers.

Chapter 5

Development of Biomathematical Model for Amyloid Radiotracers

Guo's biomathematical model was developed for CNS radiotracers [Guo et al., 2009], therefore validation is required to ensure that the model is applicable to amyloid radiotracers. Moreover, Guo's model was developed based on pigs' *in vivo* data [Guo et al., 2009], hence adjustment might be required for human data. The two remaining issues from the previous chapter of determining the representative lipophilicity model and validating the proposed f_P-f_{ND} model in predicting the f_P and f_{ND} values for amyloid radiotracers will be addressed in this chapter.

This chapter focuses on the development and evaluation of the final biomathematical model in predicting 1TCM kinetic parameters and the outcome of interest, *SUVR* of amyloid radiotracers in HC, MCI and AD conditions. Firstly, the reason for choosing *SUVR* as the outcome parameter of interest is discussed. Clinical kinetic data and *SUVR* data are compiled for evaluating the outcome parameters of interest of the model. These data are used to determine the representative lipophilicity model by correlating the predicted and clinically-observed K_1 values and to evaluate the *in silico* f_P-f_{ND} model by correlating the predicted and clinically-observed k_2 and BP_{ND} values. As *SUVR* is affected by the input function, shape of the TACs, choice of the time window, these parameters will be optimised for developing the final biomathematical model. The model is evaluated to understand the effect of changing an input on the accuracy of predicting the outcome.

5.1 Choice of *SUVR* as Outcome Parameter of Interest

SUVR is often employed to measure the amyloid load in HC, MCI and AD in clinical amyloid PET imaging studies due to its simplicity in quantification, as no blood sampling is required. However, the measured *SUVR* is dependent on the selected reference region, choice of the time window, and image processing such as partial volume correction. Partial volume effects (PVE) includes spill-in of radioactivity from neighbouring white matter regions into cortical regions resulting in lower cortical measurements, and spill-out from cortical regions to neighbouring

white matter regions, yielding higher radioactivity measurements in white matter regions. To measure the target specific-binding in terms of *SUVR*, the time window chosen should correspond to the phase of quasi-steady-state, where the washout becomes stable in both the target and reference regions. In this state, the ratio of the measured radioactivity in the target region to the reference region or *SUVR* becomes almost constant over time (Figure 5.1).

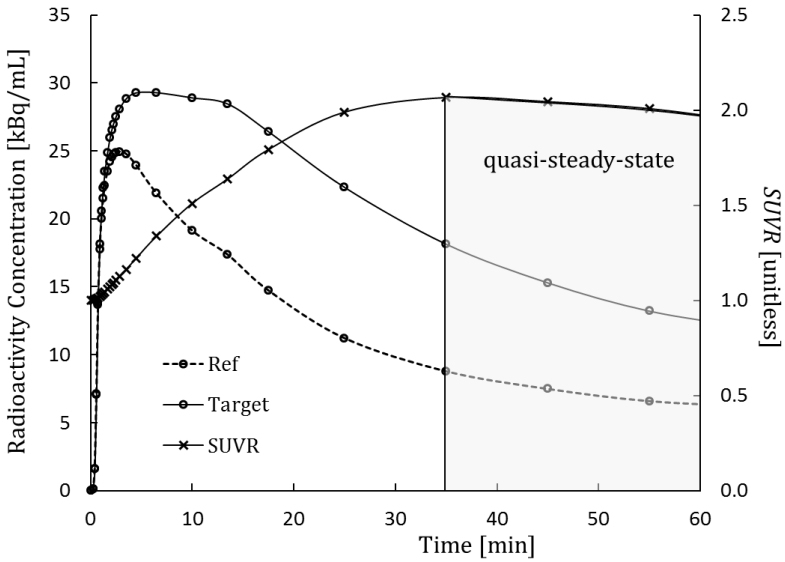

Figure 5.1: Time activity curves of target and reference regions of an amyloid radiotracer (y-axis on the left) and the changes in *SUVR* over time (y-axis on the right). Pale shaded area highlights the quasi-steady-state phase [Cselenyi et al., 2015].

SUVR is shown to correlate well with the distribution volume ratio (*DVR*) for several amyloid radiotracers [Nelissen et al., 2009; Rowe et al., 2008; Hatashita et al., 2014; Cselenyi et al., 2015]. However, changes in the structure (e.g. brain atrophy) and functions (e.g. metabolism, perfusion) of the brain due to normal ageing and disease are shown to affect the definitive diagnosis of AD. As *SUVR* is dependent on the target specific-binding and the regional cerebral blood flow (r*CBF*), changes in *SUVR* values in longitudinal studies may be affected by unequal changes in r*CBF* of the target and reference regions, and/or changes in amyloid load [Cselenyi et al., 2015].

Even though *SUVR* becomes constant over time, the concentration of the radiotracer in plasma is lower than that in tissue. This resulted in a net transport of radiotracer from the tissues into the plasma after the steady-state. In addition, the differences in non-specific binding in the reference and target regions will lead to differences in equilibrium. As a result, *SUVR* is dependent on r*CBF* due to the differences in the equilibrium of the radiotracer distributions between the blood and tissue in the target and reference regions [canBerck et al., 2013]. Although the effect of r*CBF* is

small (~2-5% in *SUVR* of MCI and AD), the variation in *SUVR* was greater than that of *DVR* and other kinetic parameters. The use of *SUVR* will thus confound the measurement of changes in amyloid load in longitudinal studies and hence *DVR* was highly recommended for quantitative PET analysis [canBerck et al., 2013; Cselenyi et al., 2015]. However, the determination of *DVR* requires long dynamic scan time, which may be difficult for patients. As such, many clinical studies are still analysing PET imaging data by means of *SUVR* within an optimal time window.

Cerebellar gray matter or whole cerebellum is generally chosen as the reference region due to its low concentrations of amyloid fibrils [van Berckel at el., 2013; Cselenyi et al., 2015]. White matter dominated regions such as the brain stem [Landau et al., 2014 and 2015] or pons [Leinonen et al., 2014] or sub-cortical white matter [Chen et al., 2015], are also used as reference regions. Although the decrease in r*CBF* may affect longitudinal *SUVR* values, the choice of the reference region also shows an effect on longitudinal *SUVR*. The choice of the pons or cerebellum as the reference region showed both increased and decreased in longitudinal *SUVR* but the choice of subcortical white matter showed a consistent increased in longitudinal *SUVR* [Chen et al., 2015]. Moreover, amyloid was reported to accumulate in the cerebellum in the late stage of Aβ distribution [Jucker et al., 2013]. This might be the cause of reduced longitudinal *SUVR* with the cerebellum as a reference region. Although *DVR* was highly recommended for quantitative evaluation of amyloid PET images, the use of *SUVR* would be less tiring for the patient due to short scan time and ease of quantification. Thus, *SUVR* was chosen as the outcome parameter of interest.

5.2 Clinical Data

Presently, there are about 11 amyloid radiotracers that have been applied clinically-applied, with their clinical *SUVR* data reported in the literature. However, only 9 clinically-applied amyloid radiotracers have been evaluated using kinetic models with their data reported in the literature. Due to the limited number of clinically-applied amyloid radiotracers, the statistical power of our evaluation is low. Yet at the same time, it shows the importance of this project in boosting the development of amyloid radiotracers.

5.2.1 Clinical *SUVR*

The clinically-observed *SUVR* values were measured from different ROIs using different reference regions and different time windows. Although white matter reference region was recommended for longitudinal studies [Chen et al., 2015], most *SUVR* reported from literature

used the cerebellum as the reference region. For consistency, only *SUVR* determined using the cerebellum or cerebellar gray matter was used.

There are three possible types of *SUVR* from the literature that can be used for correlation with the predicted *SUVR*: (1) *SUVR* from the region with greatest clinically-observed *SUVR* in AD, (2) *SUVR* taken from the region with the greatest clinically-observed *SUVR* difference between AD and HC, and (3) *SUVR* taken from the same region across all radiotracers – posterior cingulate gyrus. The posterior cingulate gyrus was chosen as it was commonly reported in many studies. The three types of *SUVR* were compiled for 11 clinically-applied amyloid radiotracers as shown in table 5.1.

5.2.2 Clinical 1TCM Parameters

Although Guo's biomathematical was used to derive the 1TCM parameters - K_1, k_2 and BP_{ND}, 2TCM was reported to result in better fit with the measured clinical data for 8 clinically-applied amyloid radiotracers, [^{11}C]PIB, [^{18}F]florbetaben, [^{11}C]BF227, [^{18}F]flutemetamol, [^{18}F]florbetapir, [^{11}C]AZD2184, [^{18}F]flutafuranol and [^{18}F]FACT. (Table 5.2). Yaqub et al. [2009] showed that the 2 tissue compartment with 1 metabolite (2T1M) resulted in the best fit with measured clinical data for [^{18}F]FDDNP.

As the 2TCM is a representative model of the actual pharmacokinetics of the amyloid radiotracers, K_1, k_2 and BP_{ND} of 2TCM were extracted from the literature for consistency. BP_{ND} values derived from *DVR*-1 were selected instead of k_3/k_4 in 2TCM (Table 5.2). This is because the values of k_3 and k_4 are small and are subjected to huge variations across subjects, while *DVR* is a macro-parameter with smaller variation in the data.

The values of K_1, k_2 and BP_{ND} were taken from the same target region with the highest *SUVR* in AD, which coincided mostly with the region with the greatest *SUVR* difference between HC and AD (Table 5.1). In some cases (e.g. [^{11}C]PIB), kinetic parameters of only one target region were reported, hence they were used for evaluation. Out of the 11 clinically-applied amyloid radiotracers, [^{11}C]SB13 and [^{18}F]FIBT did not have any kinetic data and [^{18}F]florbetapir only had clinically-observed BP_{ND} reported (Table 5.2).

Table 5.1: Three types of clinically-observed *SUVR* of 11 clinically-applied amyloid radiotracers: (1) *SUVR* value of target region with highest *SUVR* in AD, (2) *SUV*R of the target region with the greatest *SUVR* difference between HC and AD and (3) *SUVR* of posterior cingulate gyrus, with *SUVR* of white matter.

Clinically-Applied Radiotracers	Time Window (min)	Highest *SUVR*			Greatest *SUVR* Difference				*SUVR* of PCG		References	*SUVR* of WM		References
		HC	AD	Target Region	HC	AD	HC	AD	HC	AD		HC	AD	
[^{11}C]PIB	40-60	1.32	2.79	PCG	1.32	2.79	1.32	2.79	1.32	2.79	Price et al.,2005	1.65	1.54	Price et al.,2005
[^{18}F]FDDNP	45-55	1.24	1.37	ACG	1.06	1.20	1.10	1.15	1.10	1.15	Tauber et al., 2013	-	-	-
[^{11}C]SB13	40-120	-	1.34	LFC	-	-	-	-	-	-	Verhoeff et al., 2004	-	-	-
[^{18}F]florbetaben	90-120	1.37	2.15	GR	1.27	2.14	1.27	2.14	1.27	2.14	Rowe et al., 2008	1.93	1.89	Rowe et al., 2008
[^{11}C]BF227	40-60	1.32	1.65	TOC	1.32	1.65	1.30	1.58	1.30	1.58	Shidahara et al., 2015	1.73	1.78	Shidahara et al., 2015
[^{18}F]flutemetamol	85-115	1.36	2.16	PC	1.36	2.16	1.40	2.09	1.40	2.09	Hatashita et al., 2014	2.03		Landau et al., 2014
[^{18}F]florbetapir	50-60	1.30	1.85	PC	1.30	1.85	1.31	1.65	1.31	1.65	Wong et al., 2010	1.22	1.56	Nemmi et al., 2014
[^{11}C]AZD2184	40-60	1.24	2.54	PCG	1.24	2.54	1.24	2.54	1.24	2.54	Ito et al., 2014	1.33	1.50	Nyberg et al., 2009
[^{18}F]flutafuranol	51-63	1.15	2.88	PFC	1.15	2.88	1.23	2.73	1.23	2.73	Cselenyi et al., 2012	1.94	2.10	Cselenyi et al., 2012
[^{18}F]FACT	40-60	1.25	1.33	TOC	1.12	1.29	1.24	1.31	1.24	1.31	Shidahara et al., 2015	1.84	1.94	Shidahara et al., 2015
[^{18}F]FIBT	70-90	1.52	1.91	OC	1.52	1.91	-	-	-	-	Yousefi et al., 2015b	-	-	-

PCG = Posterior Cingulate Gyrus, ACG = Anterior Cingulate Gyrus, FC = Frontal Cortex, LFC = Left Frontal Cortex, PFC = Prefrontal Cortex, GR = Gyrus Rectus, OC = Occipital Cortex, TOC = Temporal OC, LTC = Lateral Temporal Cortex, PC = Precuneus, WM = White Matter
Reference regions are either whole cerebellum or cerebellar gray matter

Table 5.2: Clinically-observed K_1, k_2 and BP_{ND} of 11 clinically-applied amyloid radiotracers. [^{11}C]SB13 and [^{18}F]FIBT do not have any 1TCM parameters reported in the literature. [^{18}F]florbetapir does not have any K_1 and k_2 reported in the literature.

Clinically-Applied Radiotracers	K_1		k_2		Target Region	References	BP_{ND}		Target Region	References
	HC	AD	HC	AD			HC	AD		
[^{11}C]PIB	0.291	0.263	0.168	0.123	MPC	McNamee et al., 2009	0.30	1.51	PCG	Price et al.,2005
[^{18}F]FDDNP	0.250	0.360	0.060	0.060	Global*	Yaqub et al., 2009	0.06$^{\$}$	0.07$^{\$}$	Global*	Yaqub et al., 2009
[^{11}C]SB13	-	-	-	-	-	-	-	-	-	-
[^{18}F]florbetaben	0.216	0.187	0.085	0.076	FC	Becker et al., 2013	0.27	0.75	Global$^{\#}$	Becker et al., 2013
[^{11}C]BF227	0.270	0.230	0.130	0.120	TOC	Shidahara et al., 2015	0.25	0.50	TOC	Shidahara et al., 2015
[^{18}F]flutemetamol	0.250	0.230	0.080	0.080	Global¶	Heurling et al., 2015	0.52	0.93	PCG	Nelissen et al., 2009
[^{18}F]florbetapir	-	-	-	-	-	-	0.39	0.60	PU†	Wong et al., 2010
[^{11}C]AZD2184	0.320	0.260	0.520	0.300	PCG	Ito et al., 2014	0.16	1.39	PCG	Ito et al., 2014
[^{18}F]flutafuranol	0.340	0.230	0.300	0.140	PCG	Cselenyi et al., 2012	0.14	1.26	PCG	Cselenyi et al., 2012
[^{18}F]FACT	0.220	0.200	0.230	0.160	TOC	Shidahara et al., 2015	0.23	0.28	TOC	Shidahara et al., 2015
[^{18}F]FIBT	-	-	-	-	-	-	-	-	-	-

Units: K_1 (ml/100 g/min), k_2 (min^{-1}), BP_{ND} (unitless), *SUVR* (unitless), Time Window (min)
All K_1, k_2 were obtained from 2TCM, using the region with the highest *DVR* or *SUVR* differences between HC and AD
BP_{ND} was estimated using *DVR*-1 from 2TCM unless otherwise stated
$^{\$}$ Estimated BP_{ND} from SRTM
† Estimated BP_{ND} (*DVR*-1) from a graphical plot (Zhou's method)

FC = Frontal Cortex, LFC = Left Frontal Cortex, SFC = Superior FC, MIFC = Medial Inferior FC, PFC = Prefrontal Cortex, OFC = Orbital FC, TC = Temporal Cortex, MITC = Medial Inferior TC, STC = Superior TC, PCG = Posterior Cingulate Gyrus, ACG = Anterior Cingulate Gyrus, PU = Putamen, PC = Precuneus, MPC = Middle PC, GR = Gyrus Retus, HIP = Hippocampus, OC = Occipital Cortex, TOC = Temporal OC, PAR = Parietal Cortex, EC = Enthorinal Cortex

* Cortical Regions: OFC, MIFC, ACG, STC, PAR, MITC, SFC, EC and HIP
$^{\#}$ Cortical Regions: FC, LTC, PAR and PCG
¶ Cortical Regions: FC, PAR, ACG, PCG and TC

5.3 Determination of Representative Lipophilicity & Validation of *In Silico* f_P-f_{ND} model

In this section, M*LogP* (dproperties) and *LogD*+*S* (MedChem) were input into Guo's model [2009] to determine the 1TCM kinetic parameters of K_1, k_2 and BP_{ND}. The default values of the physiological and correction parameters in Guo's model were input accordingly. The f_P and f_{ND} values were predicted from the proposed *in silico* f_P-f_{ND} model using equations (40) and (41) with the respective lipophilicity values as input. Fixed B_{avail} values of 4, 20 and 50 nM for HC, MCI and AD conditions (section 4.4.5) were applied, with *in vitro* K_D values extracted from literature (Table 4.9). A fixed input function averaged from six HC subjects injected with [^{11}C]BF227, was used for simulation [Shidahara et al., 2015]. *SUVR* was determined using the literature-stated time window (Table 5.1). The predicted K_1, k_2 and BP_{ND} values were correlated with 8, 8 and 9 clinically-observed values in HC and AD from table 5.2.

Table 5.3 shows the *in silico* M*LogP* (dproperties), with the predicted f_P and f_{ND} values, as well as the predicted K_1, k_2 and BP_{ND} values in HC and AD. The values of K_1 and BP_{ND} were generally greater than the clinically-observed values listed in table 5.2.

Table 5.3: *In silico* M*LogP* (dproperties) of 11 clinically-applied amyloid radiotracers, which were used to predict the f_P and f_{ND} values using the proposed *in silico* f_P-f_{ND} model. These parameters were used to predict the 1TCM parameters of K_1 and k_2 values in general for both HC and AD, and BP_{ND} values in HC and AD.

Clinically-Applied Radiotracers	*In Silico*			Predicted			
	M*LogP*	f_P	f_{ND}	K_1 (ml/100 g/min)	k_2 (min^{-1})	BP_{ND} (unitless)	
						HC	AD
[^{11}C]PIB	2.40	0.303	0.152	0.73	0.40	0.44	5.44
[^{18}F]FDDNP	2.89	0.187	0.068	0.58	0.23	0.07	0.88
[^{11}C]SB13	3.23	0.135	0.040	0.60	0.19	0.07	0.82
[^{18}F]florbetaben	3.11	0.152	0.048	0.47	0.16	0.09	1.09
[^{11}C]BF227	2.40	0.304	0.153	0.63	0.34	0.17	2.16
[^{18}F]flutemetamol	2.80	0.205	0.080	0.69	0.29	0.20	2.49
[^{18}F]florbetapir	2.52	0.270	0.126	0.54	0.28	0.14	1.70
[^{11}C]AZD2184	1.75	0.573	0.441	0.69	0.58	0.21	2.63
[^{18}F]flutafuranol	2.41	0.300	0.150	0.75	0.41	0.26	3.26
[^{18}F]FACT	1.87	0.511	0.365	0.57	0.44	0.16	1.94
[^{18}F]FIBT	3.04	0.162	0.054	0.54	0.19	0.31	3.84

Figure 5.2 shows the correlations between the predicted and clinically-observed K_1, k_2 and BP_{ND} in HC and AD, using M*LogP* (dproperties) as lipophilicity input. Good correlations were obtained in K_1 in both HC and AD, with R^2 of 0.73 and 0.71 respectively. Similarly, good correlations were obtained in k_2 in both HC and AD, with R^2 of 0.81 and 0.83 respectively. A reasonable correlation was obtained in BP_{ND} in AD, with R^2 of 0.63 but a poor correlation was obtained in HC, with R^2 of 0.02. The K_1 value of AD of [^{18}F]FDDNP was excluded for correlation as an outlier. On the whole, good correlations were obtained between the predicted and clinically-observed K_1, k_2 and BP_{ND} with M*LogP* (dproperties) as lipophilicity input.

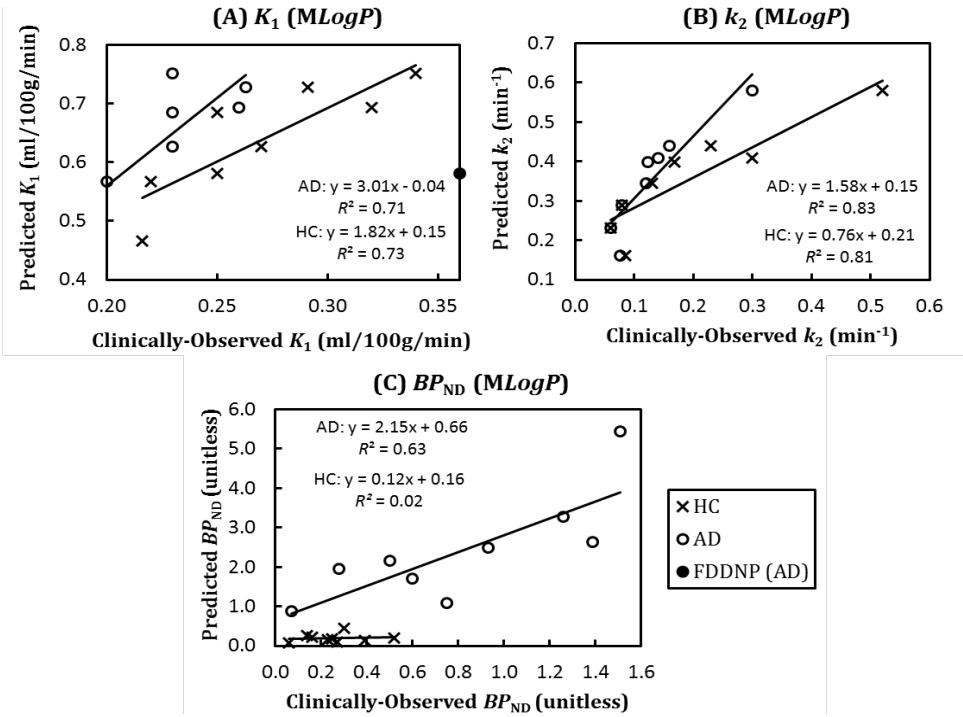

Figure 5.2: Correlations of predicted and clinically-observed values of (A) K_1, (B) k_2 and (C) BP_{ND} in HC and AD. The K_1, k_2 and BP_{ND} values were generated using M*LogP* (dproperties) as lipophilicity input. The K_1 value of [^{18}F]FDDNP in AD was excluded for correlation as an outlier (filled circle).

Table 5.4 shows the *in silico LogD+S* (MedChem), with the predicted f_P and f_{ND} values, as well as the predicted K_1, k_2 and BP_{ND} values in HC and AD. Similar to the case for M*LogP* (dproperties) (Table 5.3), the values of K_1 and BP_{ND} were generally greater than the clinically-observed values listed in table 5.2. Guo's model was developed using pigs' *in vivo* data [Guo et al., 2009], while human clinical data was used in our evaluation. The results showed that the data needs to be rescaled to compensate for the differences in the type of data used for model development.

Table 5.4: *In silico LogD+S* (MedChem) of 11 clinically-applied amyloid radiotracers, which were used to determine f_P and f_{ND} values using the proposed *in silico* f_P-f_{ND} model. These parameters were used to predict the 1TCM parameters of K_1 and k_2 values in general for both HC and AD, and BP_{ND} values in HC and AD.

Clinically-Applied Radiotracers	*In Silico*			Predicted			
	LogD+S	f_p	f_{ND}	K_1 (ml/100 g/min)	k_2 (min^{-1})	BP_{ND} (unitless)	
						HC	AD
[^{11}C]PIB	3.64	0.090	0.020	0.48	0.12	0.06	0.72
[^{18}F]FDDNP	3.72	0.083	0.018	0.39	0.09	0.02	0.23
[^{11}C]SB13	3.83	0.075	0.015	0.42	0.09	0.02	0.30
[^{18}F]florbetaben	4.22	0.051	0.008	0.21	0.04	0.01	0.18
[^{11}C]BF227	3.49	0.104	0.026	0.45	0.12	0.03	0.36
[^{18}F]flutemetamol	3.98	0.064	0.012	0.37	0.07	0.03	0.36
[^{18}F]florbetapir	3.40	0.114	0.030	0.41	0.12	0.03	0.40
[^{11}C]AZD2184	2.99	0.170	0.058	0.67	0.25	0.03	0.35
[^{18}F]flutafuranol	3.16	0.144	0.044	0.64	0.21	0.08	0.96
[^{18}F]FACT	2.78	0.209	0.082	0.56	0.24	0.04	0.44
[^{18}F]FIBT	4.21	0.051	0.008	0.25	0.04	0.04	0.05

Figure 5.3 shows the correlations between the predicted and clinically-observed K_1, k_2 and BP_{ND} in HC and AD using *LogD+S* (MedChem) as lipophilicity input. A reasonable correlation was obtained in K_1 of AD, with R^2 of 0.54, but a poor correlation was obtained in HC, with R^2 of 0.03. The predicted k_2 showed good correlations with clinically-observed k_2 in both HC and AD, with R^2 of 0.72 and 0.66 respectively. Poor correlation was obtained in BP_{ND} in AD, with R^2 of 0.34, but no correlation was obtained in HC, with R^2 of 0.01. The K_1 value of [^{18}F]FDDNP in AD was excluded for correlation as an outlier. On the whole, poorer correlations were obtained using *LogD+S* (MedChem) to predict K_1, k_2 and BP_{ND}.

The predicted K_1, k_2 and BP_{ND} generated using M*LogP* (dproperties) as lipophilicity input showed good correlations with clinically-observed values (Figure 5.2), while those generated using *LogD+S* (MedChem) showed reasonable correlations with clinically-observed values (Figure 5.3). As such, M*LogP* (dproperties) was chosen as the representative lipophilicity input for the biomathematical model for amyloid radiotracers. Poor correlations between predicted and clinically-observed BP_{ND} values in HC were obtained regardless of the lipophilicity inputs. The low concentrations of Aβ load in HC and non-specific binding of the radiotracer might have contributed to the poor correlation in BP_{ND} values in HC. As such, the correlation of BP_{ND} values in HC was excluded for further evaluation.

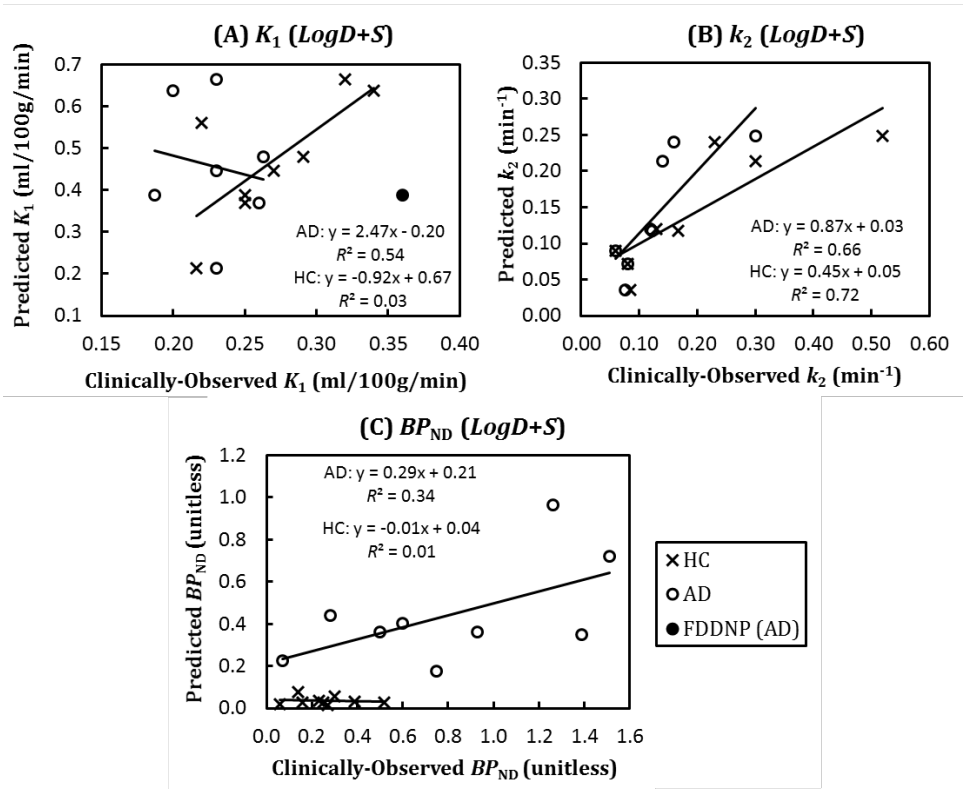

Figure 5.3: Correlations of predicted and clinically-observed values of (A) K_1, (B) k_2 and (C) BP_{ND} in HC and AD. The K_1, k_2 and BP_{ND} values were generated using *LogD+S* (MedChem) as lipophilicity input. The K_1 value of [^{18}F]FDDNP in AD was excluded for correlation as an outlier (filled circle).

The correlations between the predicted and clinically-observed k_2 values in HC and AD were good with k_2 values generated using M*LogP* (dproperties) and *LogD+S* (MedChem). Moreover, relatively good correlation of BP_{ND} values in AD was obtained using M*LogP* (dproperties) as lipophilicity input. This supported the use of the *in silico* f_P-f_{ND} model for deriving f_P and f_{ND} values. However, the predicted K_1 and BP_{ND} values were greater than the clinically-observed values. As such, the scaling factors need to be adjusted or included to account for the differences between predicted and clinically-observed values.

5.4 Scaling Factors

The predicted K_1 and BP_{ND} values were greater than the clinically-observed values (Table 5.2). In Guo's model, a scaling factor of 3.43 was introduced to compensate for the differences between the predicted and *in vivo* K_1 values determined from PET data of pigs [Guo et al., 2009]. In our model, *in vivo* human PET data is used, hence an adjustment to the scaling factor is required. The k_2 and BP_{ND} were predicted using the measured f_P and f_{ND} values obtained from *in vitro*

equilibrium dialysis experiment in Guo's model. The outcome parameter of interest in Guo's model was BP_{ND}. In our model, f_P and f_{ND} values were derived using *in silico* models, based on data of CNS drugs. Therefore, adjustments to both k_2 and BP_{ND} values might be required.

To predict the values of K_1, k_2 and BP_{ND}, the default values of the physiological and correction parameters in Guo's model were input first. The f_P and f_{ND} values were predicted from the proposed *in silico* f_P-f_{ND} model using equations (40) and (41) with M*LogP* (dproperties) as lipophilicity input. Fixed B_{avail} values of 4, 20 and 50 nM for HC, MCI and AD conditions (section 4.4.5) were applied, with *in vitro* K_D values extracted from literature (Table 4.9). A fixed input function averaged from six HC subjects injected with [^{11}C]BF227, was used for simulation [Shidahara et al., 2015]. *SUVR* was determined using the literature-stated time window (Table 5.1). The predicted K_1, k_2 and BP_{ND} values were correlated with 8, 8 and 9 clinically-observed values in HC and AD from table 5.2.

The scaling factors of K_1, k_2 and BP_{ND} can be determined using kinetic data of either HC (SF-HC) or AD (SF-AD). Kinetic data of MCI were not available for most clinically-applied radiotracers and hence could not be applied. The scaling factor of K_1 was first determined by minimising the differences between the predicted and clinically-observed K_1 values. The scaling factor of k_2 was then determined by minimising the differences between the clinically-observed k_2 with the predicted k_2, derived using the newly-scaled K_1 value. The scaling factor of BP_{ND} was then determined by minimising the differences between the clinically-observed BP_{ND} with the predicted BP_{ND}, derived using the newly-scaled K_1 and k_2 values. K_1 of [^{18}F]FDDNP in AD was excluded when adjusting the scaling factors of K_1 due to completely different kinetics from other clinically-applied amyloid tracers [Yaqub et al., 2009]. The same procedure was carried out using the kinetic data of AD and HC individually to determine the scaling factors.

Using the kinetic data of AD, the scaling factor of K_1 was changed from 3.43 to 1.23, and that of k_2 was changed from 1.08 to 1.15. A scaling factor of 0.38 was introduced for BP_{ND}. After the introduction of the new scaling factors, the predicted K_1, k_2 and BP_{ND} values were within the same range as clinically-observed values (Figure 5.4). Changing the scaling factors for predicting K_1, k_2 and BP_{ND} shifted the predicted K_1, k_2 and BP_{ND} values closer to clinically observed values with no changes in the correlations of K_1, k_2 and BP_{ND} as compared to that of Guo's (Figure 5.2).

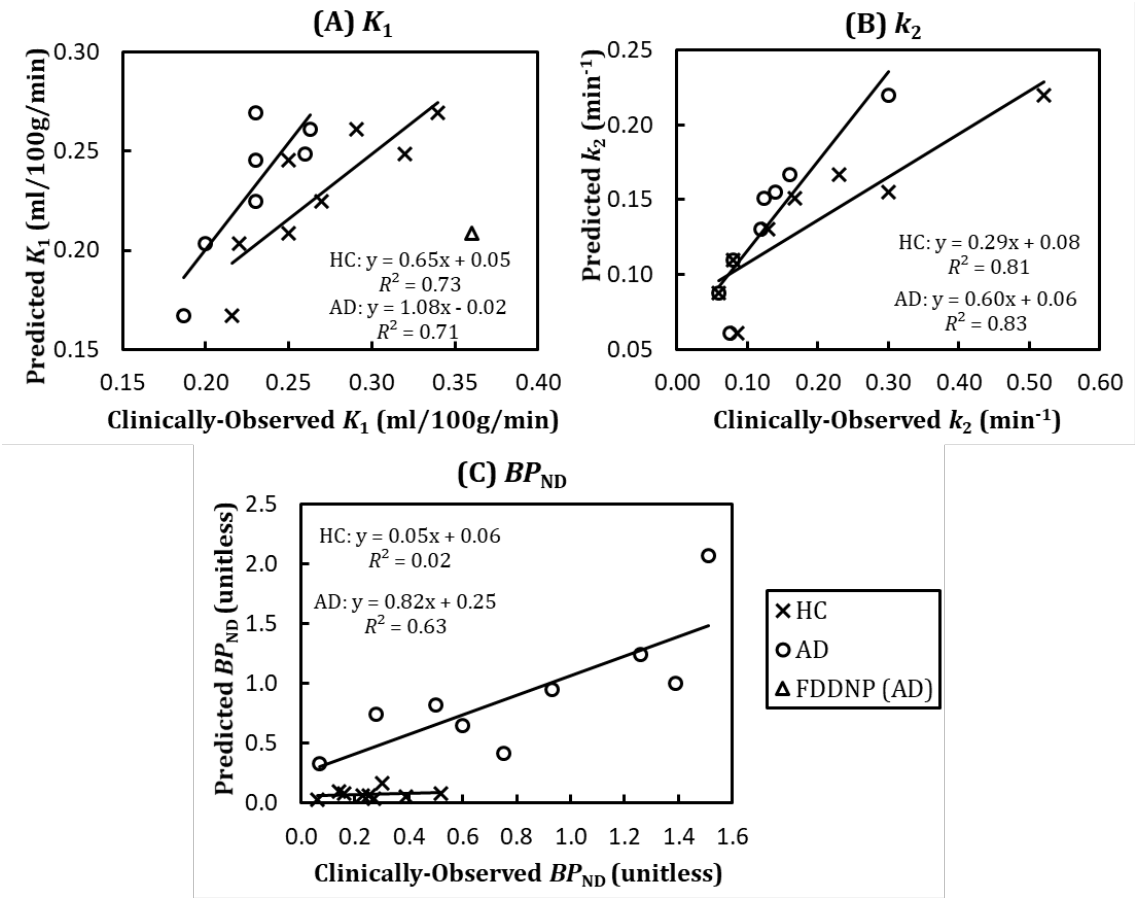

Figure 5.4: Correlations between predicted and clinically-observed (A) K_1, (B) k_2 and (C) BP_{ND} in HC and AD. Predicted values were obtained using scaling factors determined using AD kinetic data.

Using the kinetic data of HC, the scaling factors for K_1, k_2 and BP_{ND} were 1.45, 1.38 and 1.52 respectively. The correlations between the predicted and clinically-observed K_1, k_2 and BP_{ND} of HC and AD were similar using both sets of scaling factors (Figures 5.4 vs 5.5). However, the values of K_1, k_2 and BP_{ND} were generally greater using the scaling factors determined from HC kinetic data, especially for BP_{ND} of AD subjects (Figures 5.4 vs 5.5). The correlation between the predicted and clinically-observed K_1, k_2 and BP_{ND} were similar despite the use of different scaling factors (Figures 5.2, 5.4 and 5.5). The scaling factors determined from AD data were hence more suitable for predicting K_1, k_2 and BP_{ND}.

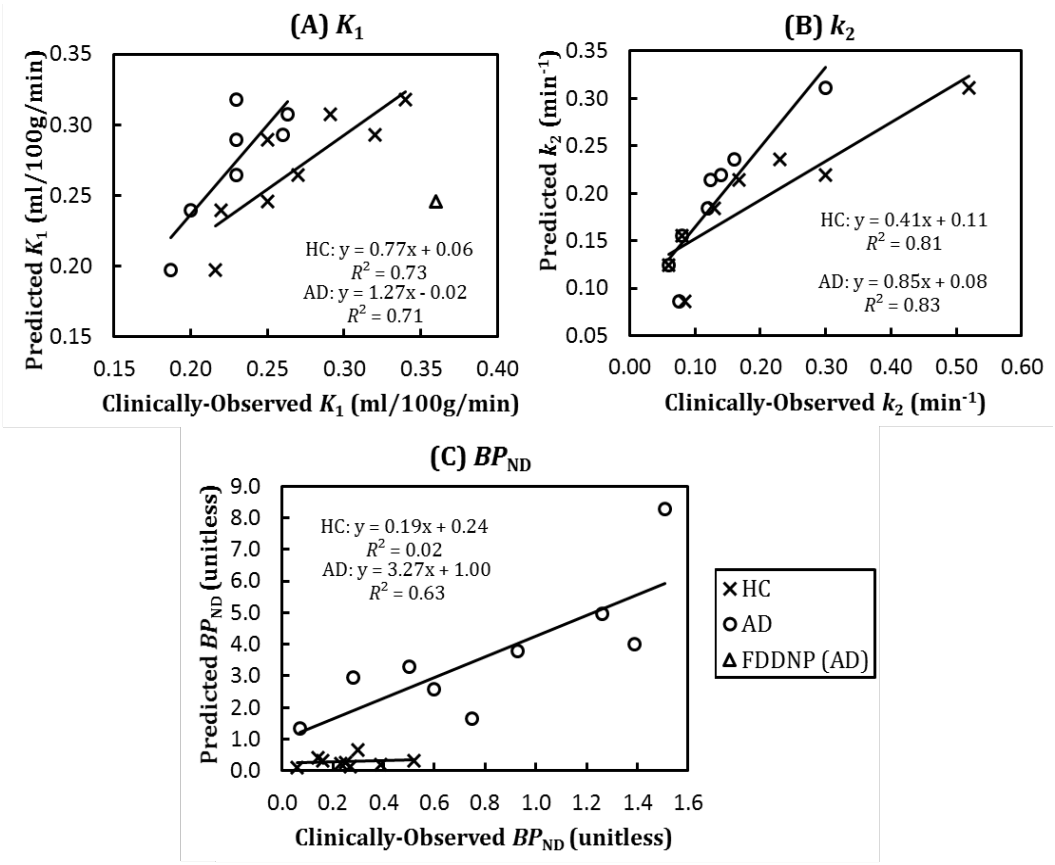

Figure 5.5: Correlations between predicted and clinically-observed (A) K_1, (B) k_2 and (C) BP_{ND} in HC and AD. Predicted values were obtained using scaling factors determined using HC kinetic data.

The TACs of [^{11}C]PIB and [^{18}F]FDDNP were simulated using three different scaling factors (SF-AD, SF-HC and SF-Guo) in the reference and target regions in HC, MCI and AD (Figure 5.6). Within the time window of 40-60 min, the TACs of reference and target regions in HC and MCI were about the same for [^{18}F]FDDNP but were different for the TACs of the target region in AD using the three different scaling factors (Figure 5.6). For [^{11}C]PIB, the TACs of the reference and target regions in HC were about the same but were very different for TACs of the target regions in MCI and AD. [^{11}C]PIB was reported to have greater binding than [^{18}F]FDDNP [Shin et al., 2008], thus the evaluation of higher target binding radiotracers would be more affected by the use of different scaling factors. The shape of the TACs simulated using SF-Guo was different from that of SF-HC and SF-AD, with higher and sharper peak and faster rate of washout (Figure 5.6). The shape of the TACs simulated using SF-AD appeared closer to clinically-observed TACs for [^{11}C]PIB [Price et al., 2005] and [^{18}F]FDDNP [Yaqub et al., 2009]. This supported the use of the new scaling factors derived using the kinetic data of AD.

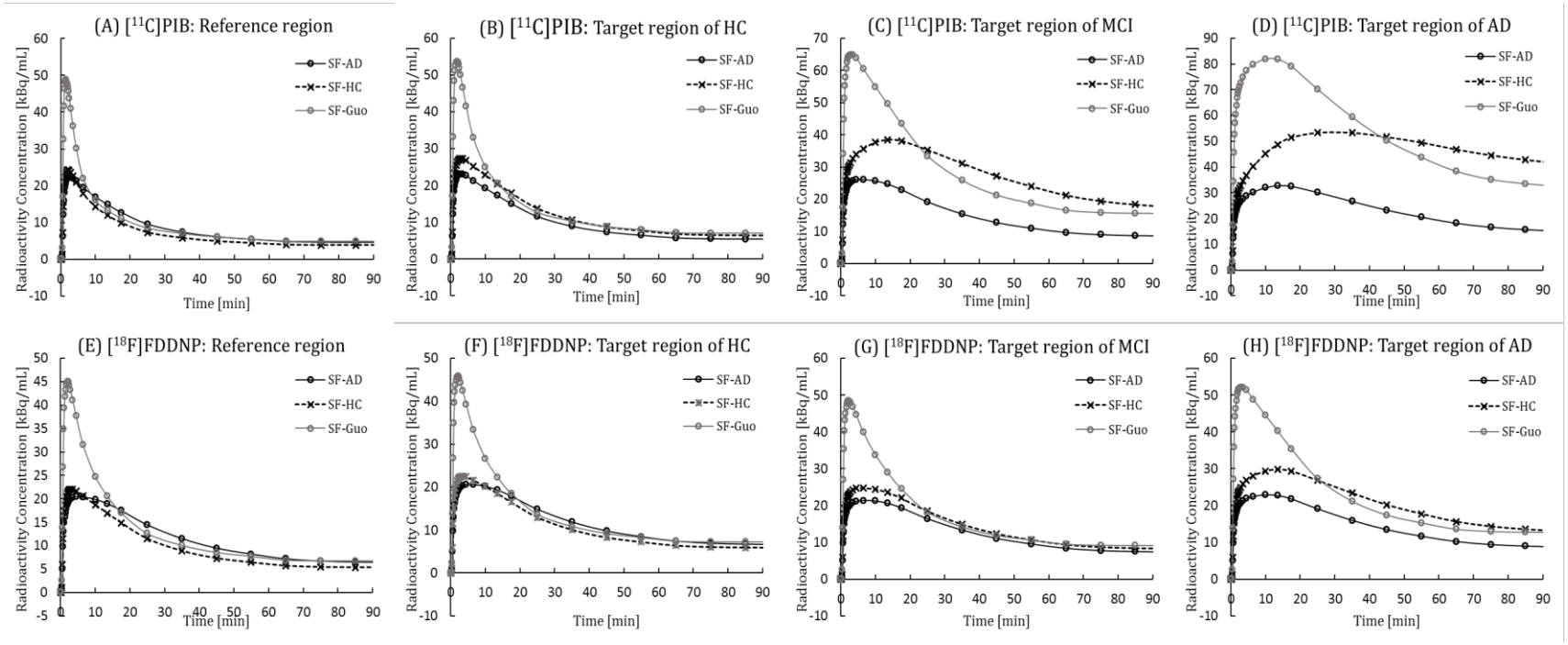

Figure 5.6: Time activity curves of [^{11}C]PIB simulated using three scaling factors (SF-AD, SF-HC and SF-Guo) in the (A) reference, and the target regions in (B) HC, (C) MCI and (D) AD and that of [^{18}F]FDDNP simulated using three scaling factors (SF-AD, SF-HC and SF-Guo) in the (E) reference, and target regions in (F) HC, (G) MCI and (H) AD.

5.5 Correlation with Three Types of *SUVR*

The *SUVR* of the 11 clinically-applied amyloid radiotracers were simulated using the specified time window stated in the literature (Table 5.1). The predicted *SUVR* values were correlated with (1) *SUVR* from the region with the highest *SUVR* in AD, (2) *SUVR* from the region with the greatest *SUVR* difference between HC and AD and (3) *SUVR* of posterior cingulate gyrus (PCG). However, only 9 radiotracers had *SUVR* of PCG reported. For [^{11}C]SB13, only *SUVR* values in AD were reported, hence the region with the greatest *SUVR* difference could not be determined. In this case, only 10 radiotracers were applied. The correlations were also carried out using 9 radiotracers with *SUVR* of PCG reported for all 3 cases for consistency.

To predict the values of K_1, k_2 and BP_{ND}, the following inputs were applied. The f_P and f_{ND} values were predicted from the proposed *in silico* f_P-f_{ND} model using equations (40) and (41) with M*LogP* (dproperties) as lipophilicity input. Fixed B_{avail} values of 4, 20 and 50 nM for HC, MCI and AD conditions (section 4.4.5) were applied, with *in vitro* K_D values extracted from literature (Table 4.9). A fixed input function averaged from 6 HC subjects injected with [^{11}C]BF227, was used for simulation [Shidahara et al., 2015]. *SUVR* was determined using the literature-stated time window (Table 5.1). The new scaling factors determined using AD kinetic data (SF-AD) were applied. Simulations were also carried using Guo's scaling factor (SF-Guo) to determine if the changes in scaling factor would greatly affect the outcome *SUVR*. Correlations of clinically-observed *SUVR* of the white matter region with predicted *SUVR* were also carried out using both HC and AD data.

Averaged correlations were obtained for all three types of *SUVR* with R^2 of 0.46, 0.40 and 0.50 for *SUVR* from the region with the highest *SUVR* in AD, *SUVR* from the region with the greatest *SUVR* difference between HC and AD and *SUVR* of PCG respectively (Figure 5.7). Regardless of the number of radiotracers used for correlation, the *SUVR* of PCG resulted in the best correlation, followed by the *SUVR* from the region with the highest *SUVR* in AD and lastly by the *SUVR* from the region with the greatest *SUVR* difference between HC and AD (Figures 5.7 and 5.8). The difference in R^2 was small using *SUVR* from the region with the highest *SUVR* values in AD and PCG (same region) (Figure 5.8), hence showing that the *SUVR* of PCG were often the highest *SUVR* value (Table 5.1) or close to that of the region with the highest *SUVR*.

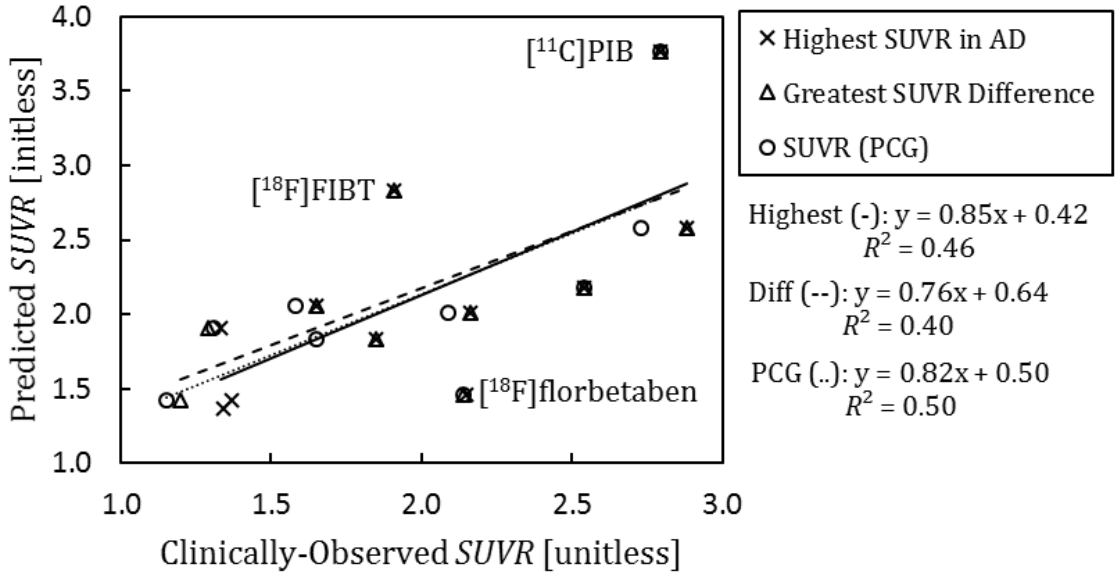

Figure 5.7: Correlations of predicted *SUVR* with clinically-observed *SUVR* of (1) region with the highest *SUVR* in AD (n = 11), (2) region with greatest *SUVR* difference between HC and AD (n =10) and (3) PCG (n = 9).

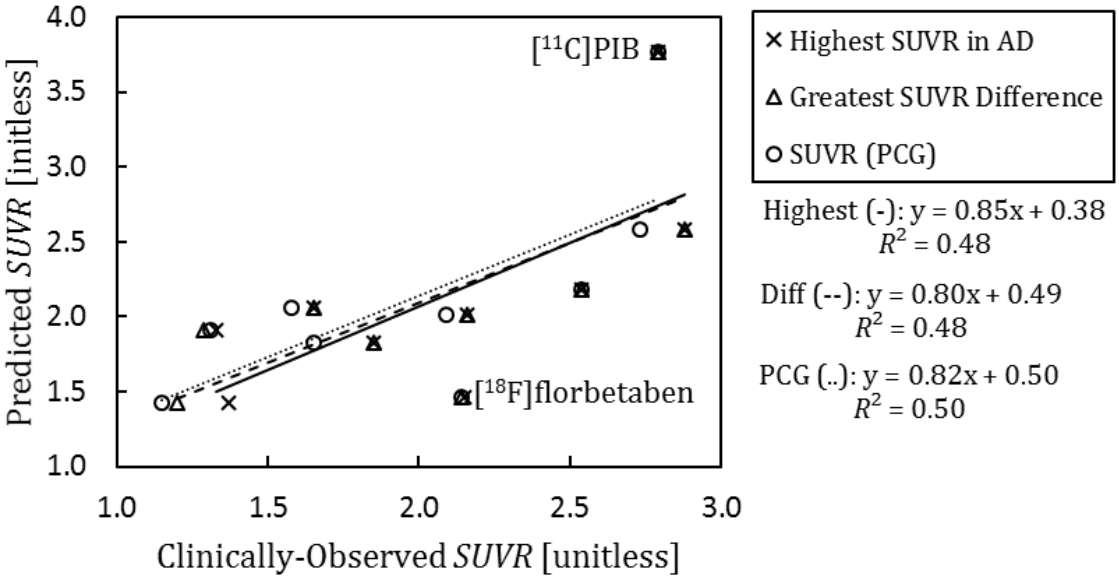

Figure 5.8: Correlations of predicted *SUVR* with clinically-observed *SUVR* of (1) region with the highest *SUVR* in AD, (2) region with greatest *SUVR* difference between HC and AD and (3) PCG of 9 clinically-applied amyloid radiotracers.

The R^2 values for all three correlations were about 5.0 (Figures 5.7 and 5.8). This was probably due to the prediction of *SUVR* values of [^{11}C]PIB, [^{18}F]FIBT and [^{18}F]florbetaben as they appeared as outliers as shown in figures 5.7 and 5.8. The K_D value used for [^{18}F]FIBT was first reported as

K_i values measured using synthetic $A\beta_{1-40}$ and $A\beta_{1-42}$ with PIB as a competitor but was later reported in the later journal as a single K_D value (Table 4.9). As such, the K_D of [^{18}F]FIBT used in our evaluation might not accurate for use. The K_i value used for [^{18}F]florbetaben was measured with florbetapir as a competitor, so it was different from the other clinically-applied radiotracers (Table 4.9). The predicted *SUVR* of [^{11}C]PIB was much greater than the clinically-observed *SUVR*. This may be due to the "ceiling effect" in AD conditions, whereby the rate of Aβ production, aggregation, deposition and clearance reached a steady-state in AD state (Figure 2.3) [Ingelsson et al., 2004]. This would explain the smaller variation in the Aβ concentration in AD subjects and the lack of correlation between Aβ load and disease duration or severity.

Theoretically, *SUVR* values taken from the same region will yield more consistent correlations. This is particularly true in amyloid imaging, especially for regions where the accumulation of the amyloid proteins has reached its peak (no change in amyloid load). In such cases, the *SUVR* values from the region with the highest *SUVR* in AD and the same region will show similar correlation. If the region chosen is the region where amyloid proteins start to accumulate, then *SUVR* values of the region with the greatest *SUVR* difference between HC and AD region should be employed. Since the difference in correlation was small and more clinically-applied radiotracers could be evaluated, *SUVR* from the region with the highest *SUVR* in AD were selected for evaluation.

The *SUVR* correlations in AD were slightly better using the new scaling factor (SF-AD) than Guo's original scaling factor (SF-Guo) (R^2 of 0.46 vs. 0.45) (Figure 5.9). However, the correlations of predicted and clinically-observed *SUVR* in HC were poor regardless of the scaling factor applied with R^2 of less than 0.1 (Figure 5.9). This was probably because of the low amyloid load in HC, and thus other factors such as image processing and white-matter spill-over will greatly affect the measured *SUVR*. The consistency in the correlation between predicted and clinically-observed *SUVR* using both scaling factors supported the use of the new scaling factors to obtain kinetic data and *SUVR* values closer to clinically-observed values.

No correlation was obtained between the predicted *SUVR* and clinically-observed *SUVR* values of the white matter region of both HC and AD subjects of 8 clinically-applied amyloid PET radiotracers (Figure 5.10). This is expected as little or no differences between HC and AD groups were reported [Nemmi et al., 2014] (section 2.3).

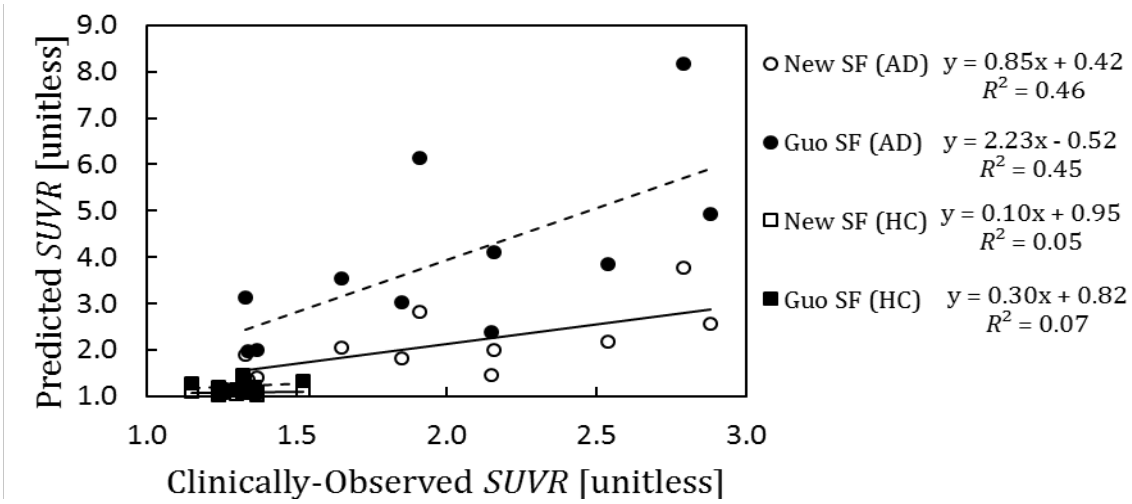

Figure 5.9: Correlations of predicted *SUVR* using new scaling factor (SF-AD) and original Guo's SF (SF-Guo) against clinically-observed *SUVR* in HC (n = 10) and AD (n = 11).

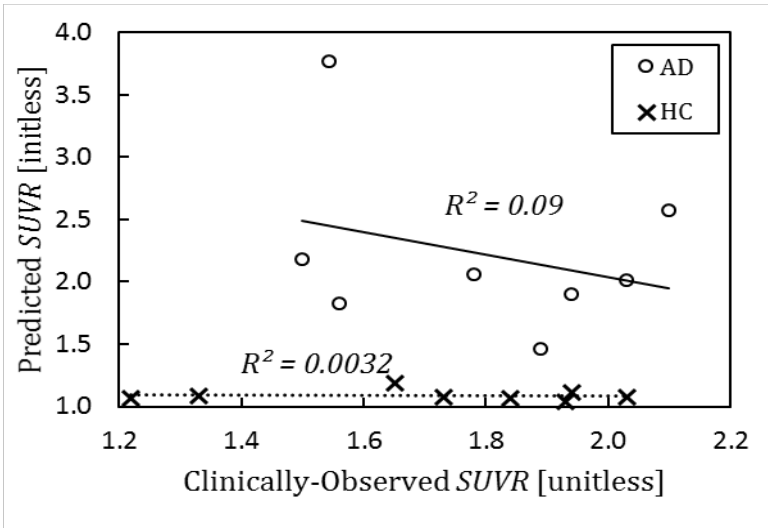

Figure 5.10: Correlations of predicted *SUVR* with clinically-observed *SUVR* of white matter region under HC and AD conditions (n = 8).

5.6 Choice of Time Window

The predicted *SUVR* is affected by the choice of time window. A single time window will be used to predict *SUVR* under HC, MCI and AD conditions for the candidate radiotracers. To determine the optimal time window, *SUVR* under HC and AD conditions of 11 clinically-applied amyloid radiotracers were obtained using time windows of 20-40, 30-50, 40-60, 50-70 and 60-80 min with a 20 min time period of measurement. For each time window, the ratios of the predicted $SUVR_{AD}/SUVR_{HC}$ and the % difference of the predicted *SUVR* from clinically-observed *SUVR* were calculated. The correlations between the predicted *SUVR* of these time windows and

clinically-observed *SUVR* were also evaluated.

The ratios of predicted $SUVR_{AD}/SUVR_{HC}$ plateaued at time windows of 40-60 or 50-70 min for most radiotracers (Figure 5.11, Table 5.5). The quasi-steady-state appeared to have reached around the time window of 40-60 min, as highlighted in table 5.5. The greater the ratio of $SUVR_{AD}/SUVR_{HC}$, the clearer the discrimination between HC and AD conditions. The earliest time window applied clinically was 40-60 min (Table 5.1) and many clinically-applied amyloid radiotracers had optimal time window of 40-60 min (e.g. [^{11}C]PIB, [^{11}C]AZD2184, [^{11}C]BF227 and [^{18}F]FACT) or within the time window of 40 to 60 min (e.g. [^{18}F]FDDNP). The shorter the waiting time, the less tiring it is for the patient. *SUVR* are also less bias and less dependent on blood flow at earlier time window [canBerck et al., 2013]. A default time window of 40-60 min seems to be a good choice.

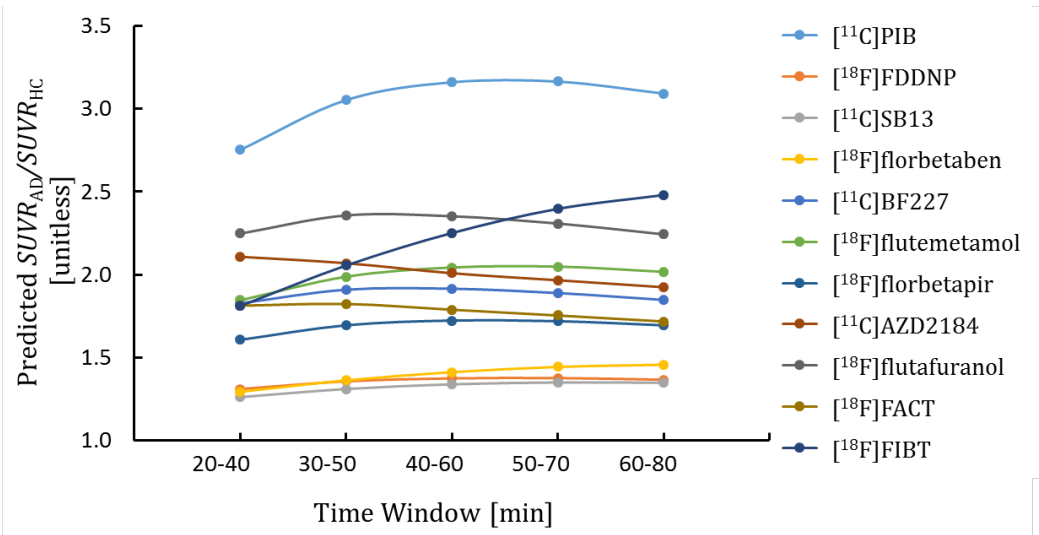

Figure 5.11: Ratio of predicted $SUVR_{AD}/SUVR_{HC}$ of time windows of 20-40, 30-50, 40-60, 50-70 and 60-80 min for 11 clinically-applied amyloid radiotracers.

The best correlation was obtained using time window of 20-40 min, with R^2 of 0.57 (Figure 5.12). The R^2 decreased with late time windows. Although early time window of 20-40 min resulted in the best correlation (Figure 5.12) and the smallest standard deviation (Table 5.6), the average ratio of $SUVR_{AD}/SUVR_{HC}$ was the smallest (Table 5.5). The better correlation obtained using time window of 20-40 min might be caused by the smaller *SUVR* values in AD for [^{11}C]PIB and [^{18}F]FIBT (Table 5.6).

Table 5.5: Ratio of predicted $SUVR_{AD}/SUVR_{HC}$ generated using time windows of 20-40, 30-50, 40-60, 50-70 and 60-80 min of 11 clinically-applied radiotracers. Quasi-steady-state highlighted in gray.

Clinically Applied Radiotracers	Time window (min)				
	20-40	30-50	40-60	50-70	60-80
[^{11}C]PIB	2.75	3.05	3.16	3.17	3.09
[^{18}F]FDDNP	1.31	1.36	1.37	1.38	1.37
[^{11}C]SB13	1.26	1.31	1.34	1.35	1.35
[^{18}F]florbetaben	1.29	1.36	1.41	1.44	1.46
[^{11}C]BF227	1.83	1.91	1.91	1.89	1.85
[^{18}F]flutemetamol	1.85	1.99	2.04	2.05	2.02
[^{18}F]florbetapir	1.61	1.69	1.72	1.72	1.69
[^{11}C]AZD2184	2.11	2.07	2.01	1.97	1.92
[^{18}F]flutafuranol	2.25	2.36	2.35	2.31	2.24
[^{18}F]FACT	1.81	1.82	1.79	1.75	1.72
[^{18}F]FIBT	1.81	2.06	2.25	2.40	2.48
Average	1.81	1.91	1.94	1.95	1.93

Table 5.6: % difference of predicted *SUVR* from clinically-observed *SUVR* for HC and AD conditions. The standard deviation of the % *SUVR* difference of 11 and 8 (excluding [^{11}C]PIB, [^{18}F]FIBT and [^{18}F]florbetaben) clinically-applied amyloid radiotracers are shown.

Clinically-Applied Radiotracers	20-40		30-50		40-60		50-70		60-80	
	HC	AD	HC	AD	HC	AD	HC	AD	HC	AD
[^{11}C]PIB	-8.59	18.8	-8.92	31.4	-9.63	34.9	-10.2	34.2	-10.7	30.4
[^{18}F]FDDNP	-17.0	-1.61	-16.8	2.14	-16.7	3.58	-16.8	3.64	-16.8	2.75
[^{11}C]SB13	-	-3.58	-	0.527	-	2.84	-	3.72	-	3.53
[^{18}F]florbetaben	-24.8	-38.1	-24.4	-34.4	-24.2	-31.8	-24.1	-30.2	-24.1	-29.6
[^{11}C]BF227	-18.2	19.6	-18.2	25.0	-18.4	25.0	-18.6	23.0	-18.8	19.9
[^{18}F]flutemetamol	-19.9	-6.94	-19.6	0.6	-19.7	3.29	-19.9	3.2	-20.2	1.3
[^{18}F]florbetapir	-18.4	-7.92	-18.2	-2.60	-18.2	-1.03	-18.4	-1.44	-18.6	-3.11
[^{11}C]AZD2184	-11.7	-9.15	-12.2	-11.3	-12.4	-14.1	-12.6	-16.1	-12.7	-18.0
[^{18}F]flutafuranol	-2.37	-12.4	-2.70	-8.41	-3.22	-9.10	-3.54	-11.1	-3.86	-13.9
[^{18}F]FACT	-14.2	46.1	-14.5	46.5	-14.7	43.3	-14.9	40.3	-15.0	37.1
[^{18}F]FIBT	-26.6	5.8	-25.4	22.0	-24.8	34.7	-24.7	43.6	-24.9	48.3
Stdev	7.29	21.7	6.88	22.8	6.56	23.4	6.41	24.0	6.33	24.3
Stdev (n = 8)	6.04	20.0	5.81	19.5	5.66	18.7	5.62	18.2	5.59	17.8

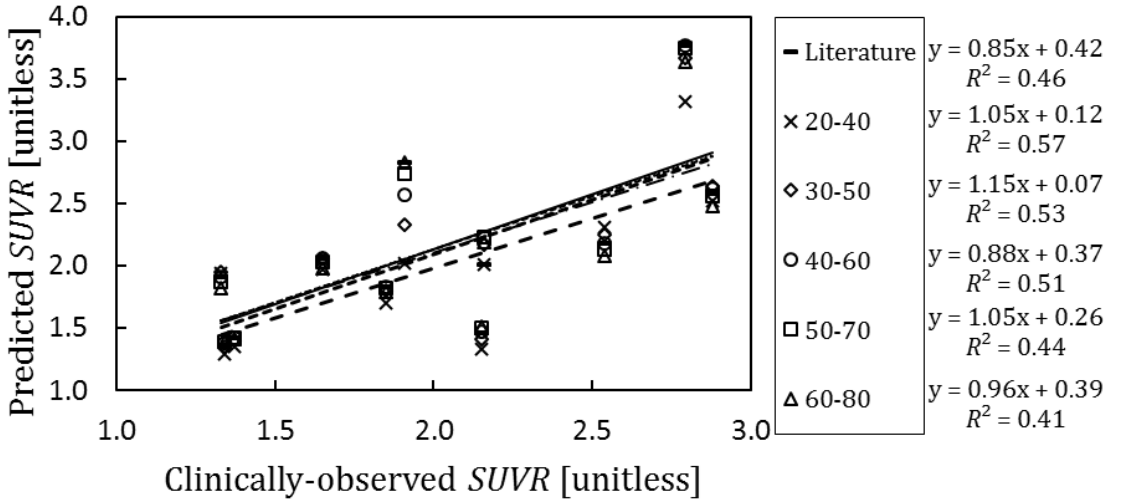

Figure 5.12: Correlation of predicted *SUVR* generated using time windows of literature-stated (-), 20-40 (x), 30-50 (◇), 40-60 (o), 50-70 (□) and 60-80 (Δ) min against clinically-observed *SUVR* under AD condition for 11 clinically-applied amyloid radiotracers.

The standard deviation of the % difference of predicted *SUVR* from clinically-observed *SUVR* in both HC and AD increased with late frame time when all 11 clinically-applied radiotracers were included. When [^{11}C]PIB, [^{18}F]FIBT and [^{18}F]florbetaben were excluded, the % difference decreased with late time window (Table 5.6). This showed that the poor correlation at late time window was due to the greater change in shape of the simulated TACs for radiotracers with high binding affinities such as [^{11}C]PIB and [^{18}F]FIBT. The % *SUVR* difference was small in HC compared to that of AD (Table 5.6).

On the whole, a default time window of 40-60 min proved to be a good choice for screening new candidate amyloid radiotracers. The correlation of the predicted *SUVR* generated using default time window of 40-60 min was better than that generated using literature-stated time window, with R^2 of 0.51 against 0.46 (Figure 5.12). This supported the use of a fixed time window for predicting *SUVR* of amyloid radiotracers.

5.7 Input Function

A fixed plasma input function will be used for screening all candidate compounds. As such, we need to investigate the choice of the input function on the outcome *SUVR*. The input functions of two amyloid radiotracers, [^{11}C]BF227 and [^{18}F]FACT, and one CNS radiotracer, [^{18}F]FDDAA were used for evaluation (Figure 5.13). The input functions of HC and AD subjects might differ and hence their input functions were investigated. The input functions of BF227-HC and BF227-AD were averaged from the metabolite-corrected

plasma input functions of 6 HC and 7 AD subjects injected with [^{11}C]BF227. The input functions of FACT-HC and FACT-AD were averaged from metabolite-corrected plasma input functions of 10 HC and AD subjects injected with [^{18}F]FACT respectively [Shidahara et al., 2015]. The four input functions of BF227-HC, BF227-AD, FACT-HC and FACT-AD have areas under the input function curves of 374, 436, 196 and 279 (kBq/mL).min. The input function of FDDAA was obtained from an HC subject injected with [^{18}F]FDDAA.

The input functions of both HC and AD subjects injected with the amyloid radiotracers, [^{11}C]BF227 and [^{18}F]FACT, showed fast uptake and fast washout with slight differences in the peak magnitude (Figure 5.13). The same trend in input function could be observed for other clinically-applied radiotracers [Price et al., 2005; Heurling et al., 2015; Yaqub et al., 2009; Ito et al., 2014; Csele´nyi et al., 2012]. The input function of [^{18}F]FDDAA was completely different with a higher peak and slower washout compared to that of the amyloid radiotracers.

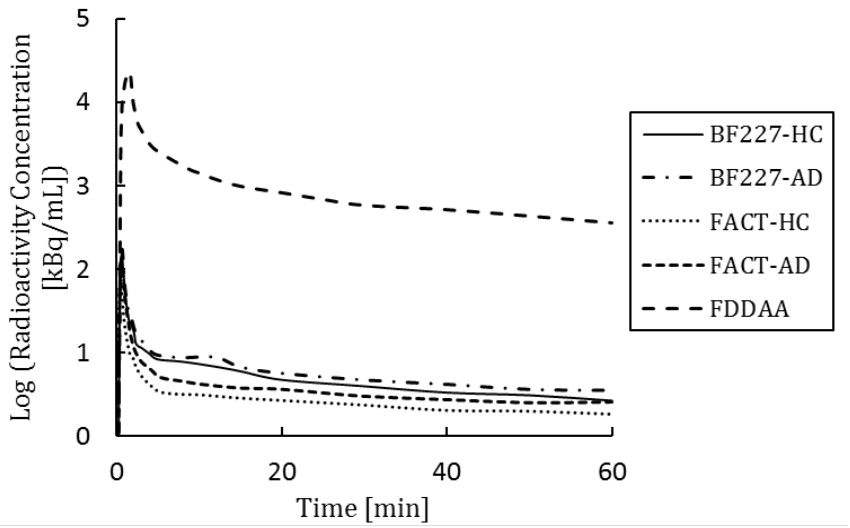

Figure 5.13: The logarithmic input functions of BF227-HC (-), BF227-AD (-.), FACT-HC (..), FACT-AD (--) and FDDAA (- -) with time (min).

The evaluation was carried out by correlating the predicted *SUVR* using the five different input functions (BF227-AD, BF227-HC, FACT-AD, FACT-HC and FDDAA) with clinically observed *SUVR* of 11 clinically-applied amyloid radiotracers. The correlations of the predicted and clinically observed *SUVR* for 11 clinically-applied amyloid radiotracers were relatively similar using the input functions of [^{11}C]BF227 and [^{18}F]FACT, with R^2 of about 0.47 (Figure 5.14). Among the input functions of amyloid radiotracers, FACT-HC with the smallest area under the input function curve (Figure 5.13), resulted in the best

correlation of R^2 = 0.48 (Figure 5.14). The input function of BF227-HC, with the second biggest area under the input function curve (Figure 5.13), resulted in the worse correlation of R^2 = 0.46 (Figure 5.14). The input function of FDDAA was completely different from that of amyloid radiotracer and resulted in poor correlation with R^2 of 0.41 (Figure 5.14). As such, the input function of a different radiotracer should not be used for simulation.

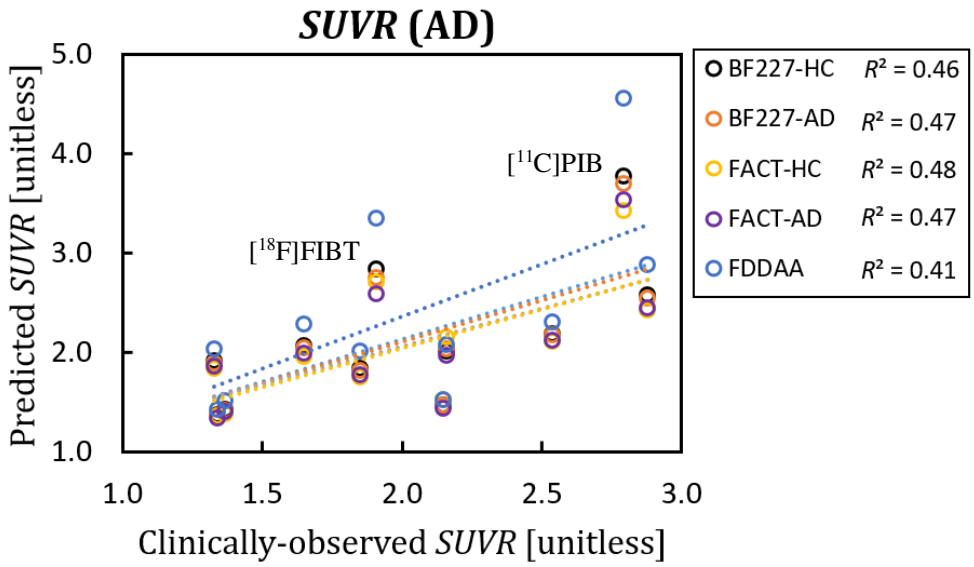

Figure 5.14: Correlations of clinically-observed *SUVR* with *SUVR* predicted using five different input functions (BF227-AD, BF227-HC, FACT-AD, FACT-HC, FDDAA) for 11 clinically-applied radiotracers.

The time activity curves of [^{11}C]PIB were simulated using the four different input functions of BF227-AD, BF227-HC, FACT-AD and FACT-HC, for reference region and target regions of HC, MCI and AD conditions (Figure 5.15). The TACs were simulated for 11 clinically-applied amyloid radiotracers using the five input functions. The simulated TACs of the reference and target regions of HC, MCI and AD conditions using BF227-HC are shown in figure 5.16.

The simulated TACs of [^{11}C]PIB showed similar shape across HC, MCI and AD conditions with fast uptake and steady washout (Figure 5.15). However, the TACs simulated using BF227-HC were different from that using BF227-AD and FACT-HC and FACT-AD under HC condition (Figure 5.15B). The TAC of [^{11}C]PIB simulated using FACT-HC reached the peak and nearly flattened out under AD condition (Figure 5.15D). The clinically-observed TAC for [^{11}C]PIB curved downwards after peak uptake and continued to decrease as observed for simulated TACs of BF227-AD and BF227-HC. [Price et al., 2005]. Thus, the

input functions of [^{18}F]FACT are not suitable for simulations despite slightly better correlations (Figure 5.14).

The input function of HC is more representative as it is less affected by disease progression or the presence of vascular disease (e.g. CAA) [vanBerck et al., 2013]. The correlations between predicted and clinically observed SUVR were about the same for all input functions of [^{11}C]BF227 and [^{18}F]FACT. As such, the input function of BF227-HC was selected for simulation. The TACs simulated using BF227-HC for [^{11}C]PIB, [^{11}C]BF227, [^{18}F]FACT, [^{11}C]AZD2184 and [^{18}F]flutafuranol were relatively similar to that observed clinically (Figure 5.16). Interestingly, the simulated TACs for MCI condition reflected closer to clinically-observed TACs of AD [Price et al., 2005; Shidahara et al., 2015; Ito et al., 2014; Cselenyi et al., 2012], rather than the simulated TACs of AD (Figure 5.16). The simulated TACs of [^{18}F]FIBT and [^{18}F]florbetaben might be affected by the K_D values applied (section 5.5).

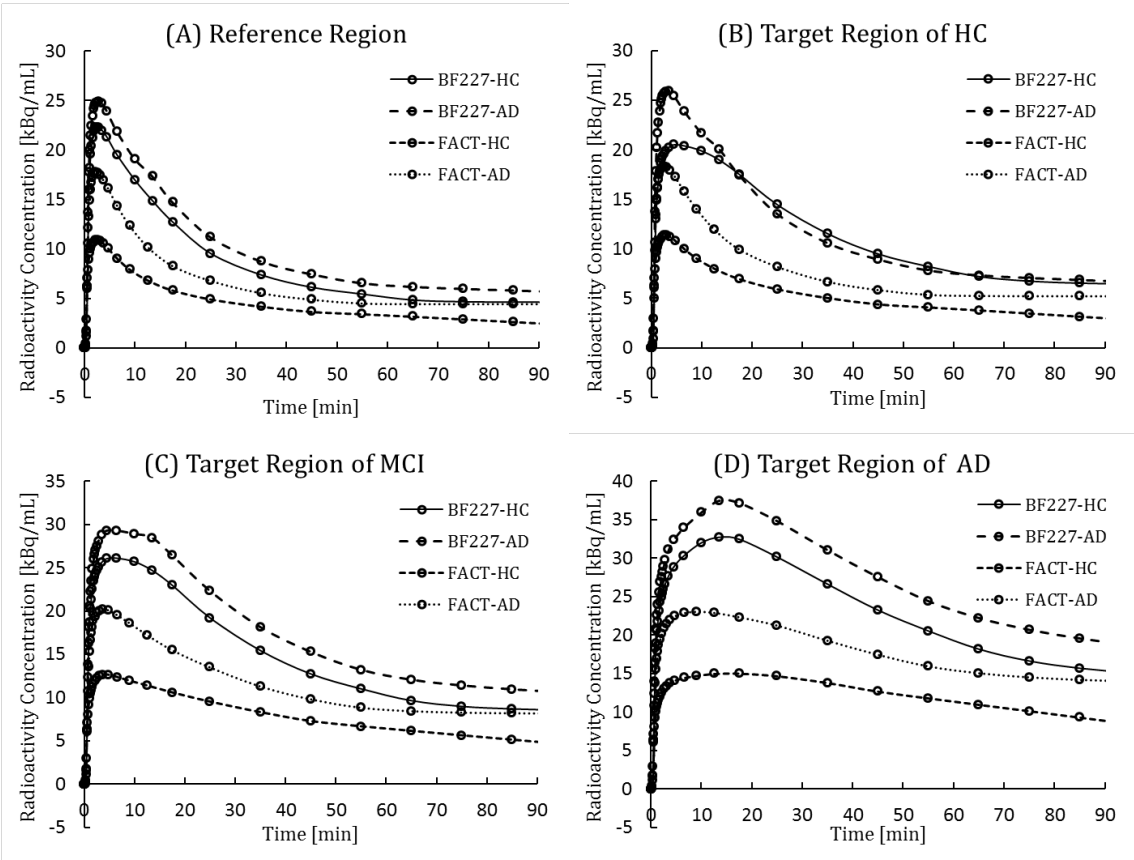

Figure 5.15: Time activity curves of [^{11}C]PIB for the (A) reference region and target regions of (B) HC, (C) MCI and (D) AD, simulated using the input functions of BF227-HC (Default,-), BF227-AD (— —), FACT-HC (..) and FACT-AD (--) respectively.

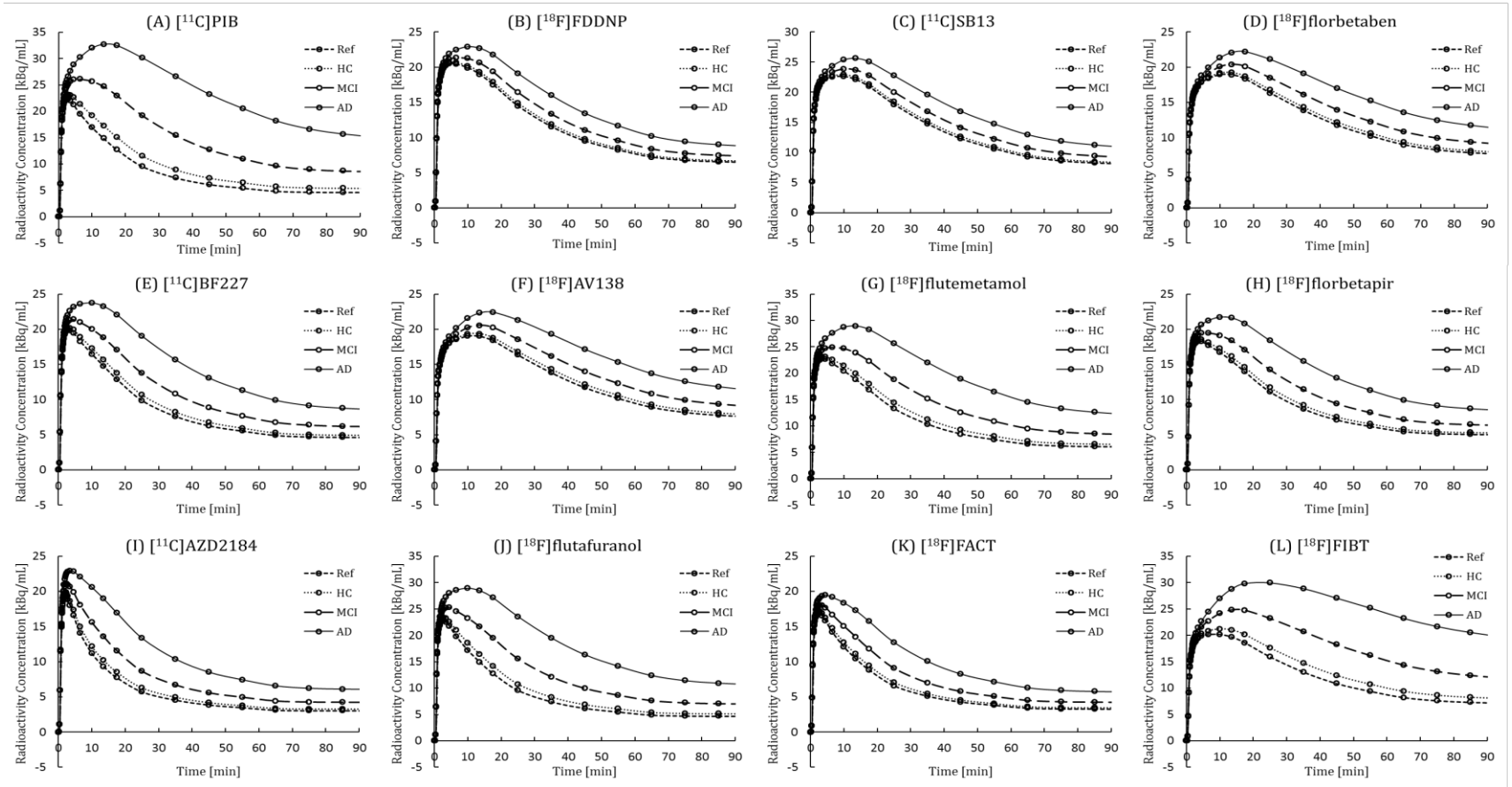

Figure 5.16: Simulated time activity curves from 0–90 min of the reference region and target regions of HC, MCI and AD of 11 clinically-applied amyloid radiotracers: (A) [^{11}C]PIB, (B) [^{18}F]FDDNP, (C) [^{11}C]SB13, (D) [^{18}F]florbetaben, (E) [^{11}C]BF227, (F) [^{18}F]AV138, (G) [^{18}F]flutemetamol, (H) [^{18}F]florbetapir, (I) [^{11}C]AZD2184, [^{18}F]flutafuranol, (K) [^{18}F]FACT and [^{18}F]FIBT.

5.8 Final Amyloid Biomathematical Model

The choice of the basic structure of the biomathematical model was discussed in chapter 3 and the determination of required parameters was discussed in chapter 4. The development of the biomathematical model was described in details in earlier sections of this chapter. This section focuses on providing an overview of the amyloid biomathematical model and summarising all the parts discussed earlier.

The final biomathematical model was based on Guo's simplified 1-tissue-compartment model (1TCM). It involved 3 main steps (Figure 5.17): (1) Generation of physicochemical and pharmacological parameters, (2) Derivation of 1TCM kinetic parameters, and (3) Simulations of TACs and *SUVR*s.

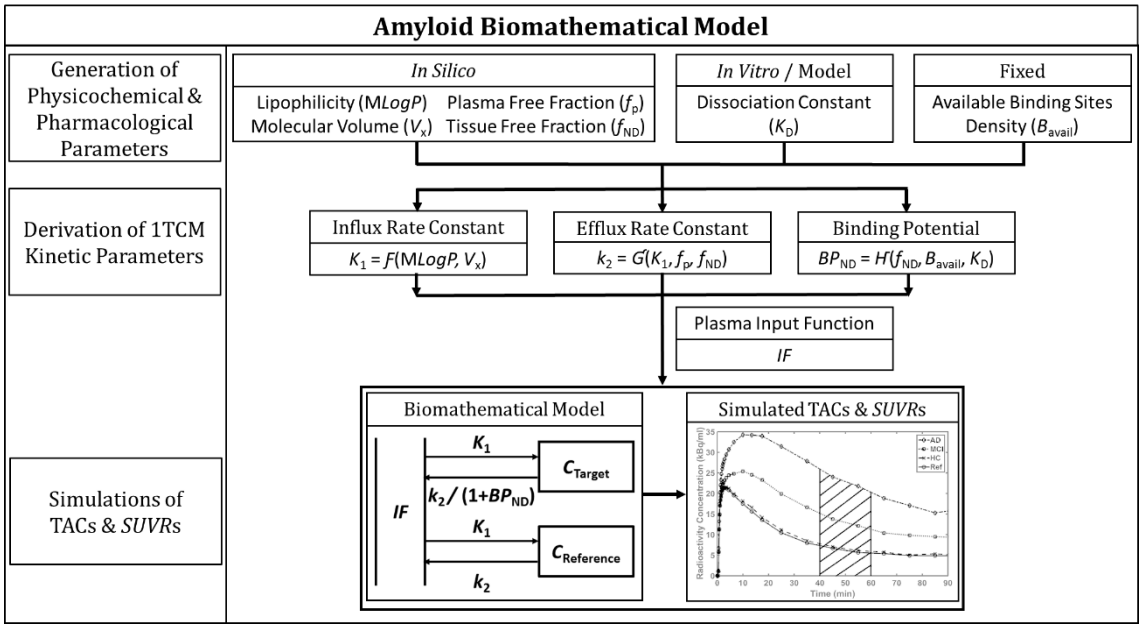

Figure 5.17: Overview of Final Amyloid Biomathematical Model.

Generation of Physicochemical and Pharmacological Parameters

A total of six *in silico*/*in vitro* physicochemical and pharmacological parameters are required as input into the amyloid biomathematical model (Figure 5.17) for each radiotracer. McGowan volume (V_x, cm^3/mol/100) and lipophilicity, represented by Moriguchi *LogP* (M*LogP*, unitless), were generated based on the chemical structure of the amyloid radiotracer using commercial software, dproperties (Talete, Italy). *In silico* free fraction in tissues of the nondisplaceable

compartment (f_{ND}, unitless) and free fraction in plasma (f_P, unitless) were calculated from M*LogP*, using the equations (40) and (41) derived from Wan [2007] and Maurer [2004] datasets.

$$f_{\mathrm{ND}} = 7.717e^{-1.634 \cdot \mathrm{M}LogP} \tag{40}$$

$$f_{\mathrm{P}} = 0.936 \cdot {f_{\mathrm{ND}}}^{0.600} \tag{41}$$

The dissociation constant (K_D, nM) was measured by *in vitro* binding assays using synthetic $A\beta_{1-40}$, synthetic $A\beta_{1-42}$ or human AD brain homogenates (Table 4.9). For accurate comparison of the radiotracers, the same protocol in measuring K_D values should be applied. The *in vitro* binding assays using both synthetic $A\beta_{1-40}$ and $A\beta_{1-42}$ are highly recommended to determine the binding selectivity to $A\beta_{1-40}$ and $A\beta_{1-42}$. In the case where measured K_D values of both synthetic $A\beta_{1-40}$ and $A\beta_{1-42}$ were available, the following model should be applied to obtain the final K_D value:

$$K_{\mathrm{D}} = K_{\mathrm{D}(A\beta 1-40)} \times 0.3 + K_{\mathrm{D}(A\beta 1-42)} \times 0.7 \tag{53}$$

In our evaluation, the K_D or K_i values were selected as previously described in section 4.4.4 with the final K_D values used shown in table 4.9. Fixed available target binding sites (B_{avail}, nM) of 4, 20 and 50 nM were employed to represent the amyloid loads under HC, MCI and AD conditions respectively [Svedberg et al., 2009].

Derivation of 1TCM Kinetic Parameters

The influx rate constant (K_1, mL/cm^3/ min) was derived using the modified Renkin and Crone equation, with compound-specific permeability (P, cm/min) and fixed values of capillary surface area (S = 150 cm^2/cm^3 of brain) and perfusion (f = 0.6 mL/cm^3/min):

$$K_1 = f\left(1 - e^{-\frac{PS}{f}}\right) \tag{14}$$

The compound-specific permeability was derived from the simplified Lanevskij's permeability model [Guo et al., 2009], using M*LogP* and V_x:

$$P = 10^{-0.121\left(\mathrm{M}LogP - 2.298\right)^2 - 2.544\log\left({V_{\mathrm{x}}}^{1/3}\right) - 2.525} \tag{15}$$

At equilibrium, the efflux rate constant (k_2, min^{-1}) can be derived using K_1, f_P and f_{ND}:

$$k_2 = \frac{f_{\mathrm{ND}}}{f_{\mathrm{P}}} \cdot K_1 \tag{16}$$

The *in vivo* non-displaceable binding potential (BP_{ND}, unitless) was derived from Mintun's equation using B_{avail}, f_{ND} and K_D:

$$BP_{\mathrm{ND}} = f_{\mathrm{ND}} \cdot \frac{B_{\mathrm{avail}}}{K_{\mathrm{D}}} \tag{17}$$

Three scaling factors with the values of 1.23, 1.15 and 0.38 were introduced to account for the difference between the predicted and *in vivo* K_1, k_2 and BP_{ND} in equations (14), (16) and (17) respectively. These scaling factors were derived by minimising the differences between the predicted and clinically observed K_1, k_2 and BP_{ND} values of 8, 8 and 9 clinically-applied radiotracers in AD respectively (Table 5.2).

Simulations of TACs and SUVRs

The predicted K_1, k_2 and BP_{ND} were then used to simulate the TACs in the target regions of HC, MCI and AD and a reference region, with a fixed input function (*IF*):

$$C_{\text{Target}}(\text{t}) = K_1 \cdot e^{-\frac{k_2}{(1+BP_{\text{ND}})}\times t} \otimes IF(\text{t}) \tag{18}$$

$$C_{\text{Reference}}(\text{t}) = K_1 \cdot e^{-k_2\times t} \otimes IF(\text{t}) \tag{19}$$

IF was derived by averaging the metabolite-corrected, arterial plasma input functions of 6 HC subjects injected with [^{11}C]BF227 [Shidahara et al., 2015].

The *SUVR* of subject conditions of HC, MCI and AD were determined from the ratio of the areas under the TACs of the target regions in HC, MCI and AD, and that of the reference region within a selected time window. This time window was determined from the literature for clinically-applied amyloid radiotracers (Table 5.1), or otherwise by default of 40 to 60 min. The final list of 31 amyloid radiotracers used for evaluation and their respective *in silico* M*LogP*, V_x, f_P and f_{ND} and *in vitro* K_D are shown in table 5.7.

For the amyloid model developed, the same assumptions made by Guo et al [2009] were applied (Section 3.4.1). For the application of the proposed *in silico* f_P-f_{ND} model, we assumed that the amyloid radiotracers, like CNS radiotracers, displayed consistent plasma to tissue free fractions ratio at equilibrium and that the ratio was consistent in both animals and human [Di et al., 2011]. This is applicable only for radiotracers that cross the BBB by passive diffusion. [^{11}C]PIB has been reported that it was not a substrate of P-glycoprotein (P-gp) [Tournier et al., 2011; Ishiwata et al., 2007] and good correlation between predicted and clinically-observed K_1 was obtained (Figure 5.2). Therefore, we can assume that the clinically-applied amyloid radiotracers listed are transported across the BBB by passive diffusion (Table 5.7).

Table 5.7: Final values of *in silico* M*LogP*, V_x, f_P and f_{ND} of 31 amyloid radiotracers.

Radiotracers	*In Silico*				*In Vitro*
	M*LogP*	V_x	f_P	f_{ND}	K_D
[^{11}C]PIB	2.40	1.88	0.303	0.152	1.40$^{\#}$
[^{18}F]FDDNP	2.89	2.31	0.187	0.068	3.90$^{\#}$
[^{11}C]SB13	3.23	1.86	0.135	0.040	2.43
[^{18}F]florbetaben (Neuraceq)	3.11	2.84	0.152	0.048	2.22
[^{11}C]BF227	2.40	2.33	0.304	0.153	3.55$^{\#}$
[^{18}F]AV138	3.11	2.80	0.152	0.048	1.90
[^{18}F]flutemetamol (Vizamyl)	2.80	1.89	0.205	0.080	1.60
[^{18}F]florbetapir (Amyvid)	2.52	2.80	0.270	0.126	3.72
[^{11}C]AZD2184	1.75	1.84	0.573	0.441	8.40
[^{18}F]flutafuranol	2.41	1.79	0.300	0.150	2.30
[^{18}F]FACT	1.87	2.53	0.511	0.365	9.40
[^{18}F]FIBT	3.04	2.41	0.162	0.054	0.70
[^{11}C]6-Me-BTA-1	3.23	1.96	0.135	0.040	20.2
[^{11}C]BTA-1	2.97	1.82	0.173	0.060	11.0
[^{18}F]FMAPO	3.47	2.50	0.107	0.027	5.00
[^{18}F]FPEG-Stilbenes-12a§	3.47	2.50	0.107	0.027	2.90
[^{11}C]Benzofuran-8§	2.66	1.81	0.236	0.100	0.70
[^{18}F]FPEGN3-Styrylpyridine-2§	3.74	2.94	0.082	0.017	2.50
[^{11}C]MeS-IMPY	3.33	2.20	0.122	0.034	8.95
[^{18}F]Indole-14§	2.98	2.79	0.172	0.060	1.50
[^{18}F]Indoline-8§	2.93	2.83	0.180	0.064	4.00
[^{11}C]Benzothiazole-6a§	2.40	1.88	0.303	0.152	18.8
[^{11}C]Benzothiazole-6b§	2.40	1.88	0.303	0.152	11.5
[^{11}C]Benzothiazole-6c§	2.40	1.88	0.303	0.152	11.2
[^{18}F]Benzothiazole-2§	3.72	1.59	0.083	0.018	9.00
[^{18}F]Benzothiazole-5§	3.98	1.74	0.064	0.012	5.70
[^{18}F]MK3328	2.63	1.78	0.241	0.104	9.60
[^{18}F]FIAR	3.66	2.29	0.088	0.020	6.81
[^{18}F]Benzoxazole-24§	2.41	2.75	0.302	0.152	9.30
[^{18}F]Pyridinylbenzoxazole-32§	2.42	2.03	0.297	0.148	8.00
[^{18}F]Phenylindole-1a§	3.84	2.09	0.074	0.015	28.4

M*LogP* (unitless) and V_x (cm^3/mol/100) were determined using dproperties (Talete, Italy).
f_P (unitless) and f_{ND} (unitless) were extrapolated from relationships of f_P and f_{ND} of CNS tracers.

K_D (nM) was obtained from the literature, measured via in-vitro binding studies using synthetic Aβ1-40, Aβ1-42 or AD brain homogenates.
$^{\#}K_D$ is derived using K_D values measured with synthetic Aβ1-40 and Aβ1-42 using: $K_{D(A\beta 1\text{-}40)} * 0.3 + K_{D(A\beta 1\text{-}42)} * 0.7$

§Simplified name with the compound number or alphabet, as reported in the literature, used when generic name or institute code name (supplied by the author) was not available.

5.9 Evaluation of Amyloid Biomathematical Model

The applicability of a model is dependent on its accuracy and reliability in predicting the outcome parameters of interest. As the measured inputs into a model are subjected to experimental errors, it is important to determine the effect of possible errors on the outcome [Loucks et al., 2005]. Moreover, a model is an imperfect construction of the actual outcome. Hence, it is also important to determine if the assumptions of the model are valid [Loucks et al., 2005]. This section describes

the evaluation of the proposed model via sensitivity analysis and noise simulation, with different input functions on the predicted outcome.

5.9.1 Sensitivity Analysis

Sensitivity analysis is used to evaluate a model of the impact of possible errors in input data on predicted output and to identify the key parameters affecting the predicted outcome [Loucks et al., 2005]. The amyloid biomathematical model requires 6 physicochemical and pharmacological parameters, of which M*LogP*, V_x, f_P and f_{ND} are *in silico* parameters based on the chemical structure of the radiotracer. Fixed values of B_{avail} are used to represent the amount of Aβ load in HC, MCI and AD conditions. K_D is the only *in vitro* parameter measured via binding assay. As such, M*LogP*, V_x, f_P, f_{ND} and B_{avail} would not contribute experimental errors to the outcome parameter. However, to identify the key parameters affecting the predicted outcome, all 6 parameters were evaluated individually.

For each amyloid radiotracer and for each subject condition of HC, MCI and AD, each input parameter was varied by ±20% in 5 steps in each direction (i.e. -20%, -16%, -12%, -8% -4%, 4%, 8%, 12%, 16%, 20%). The predicted *SUVR* were compared with the reference *SUVR* generated without any variations. The % *SUVR* differences from the reference, with respect to the amount of variations (%), in each parameter were investigated for all 6 parameters using the 31 amyloid radiotracers (Table 5.7).

The % *SUVR* differences due to M*LogP,* V_x and f_P were small with less than 1%, 3.5% and 8% in HC, MCI and AD respectively (Figures 5.18-5.20). Therefore, M*LogP*, V_x and f_P will not affect the outcome *SUVR* significantly with small variations in measurements of less than 20%. M*LogP* and V_x affected K_1 and k_2, based on equations (14) to (16), which resulted in irregular patterns (Figures 5.18 and 5.19). All the amyloid radiotracers evaluated had M*LogP* values within the range of 1.5 to 4.15 (Table 5.7), hence these amyloid radiotracers were likely to cross the blood-brain-barrier [Lipinski et al., 2001].

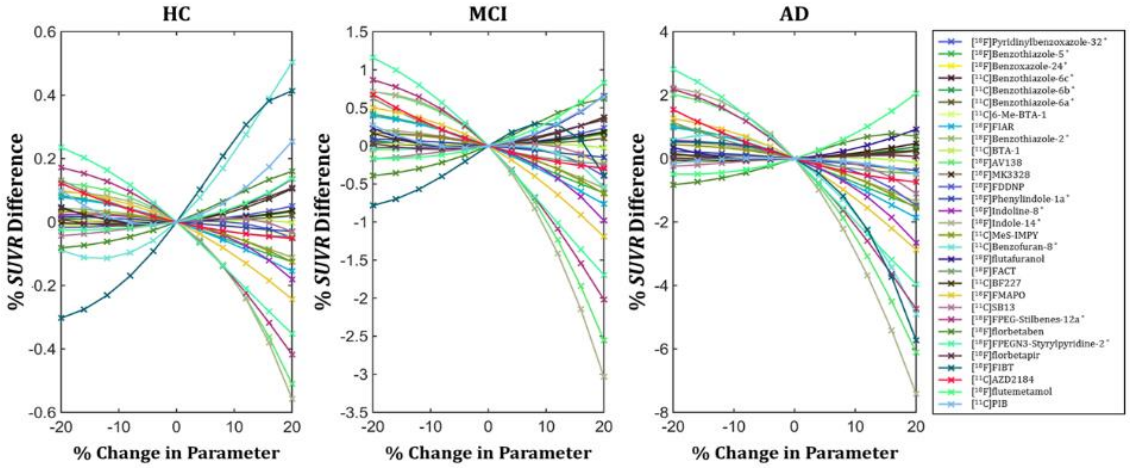

Figure 5.18: %*SUVR* difference from reference with ±20% variations in **M*LogP*** only.

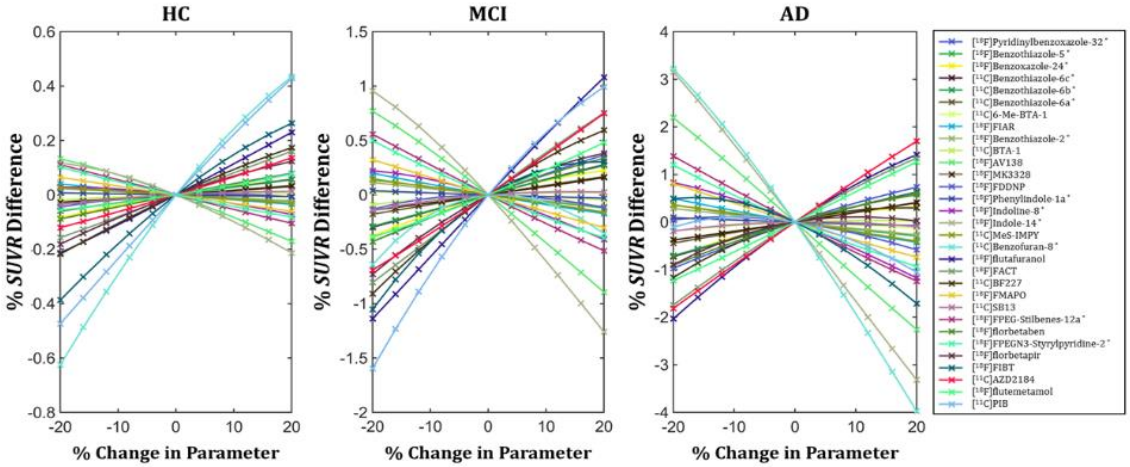

Figure 5.19: %*SUVR* difference from reference with ±20% variations in V_x only.

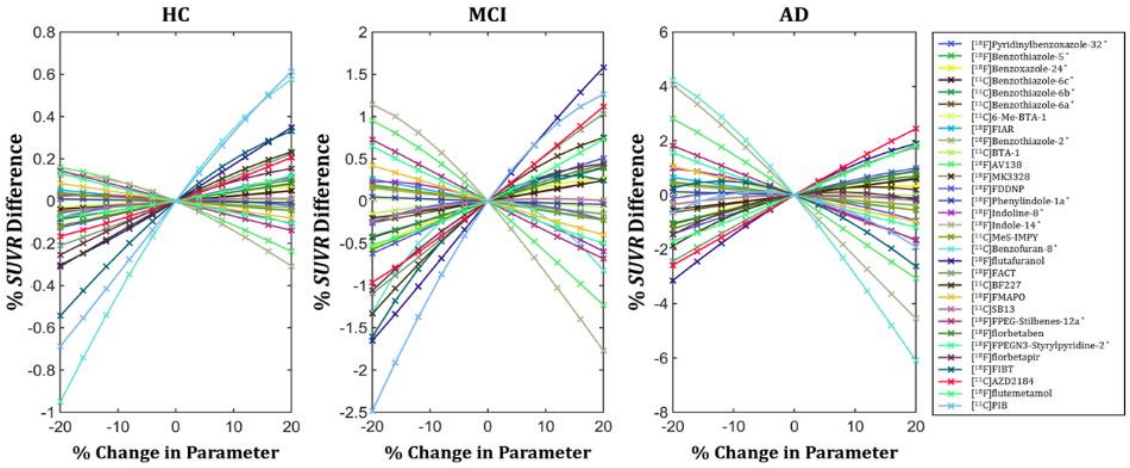

Figure 5.20: %*SUVR* difference from reference with ±20% variations in f_P only.

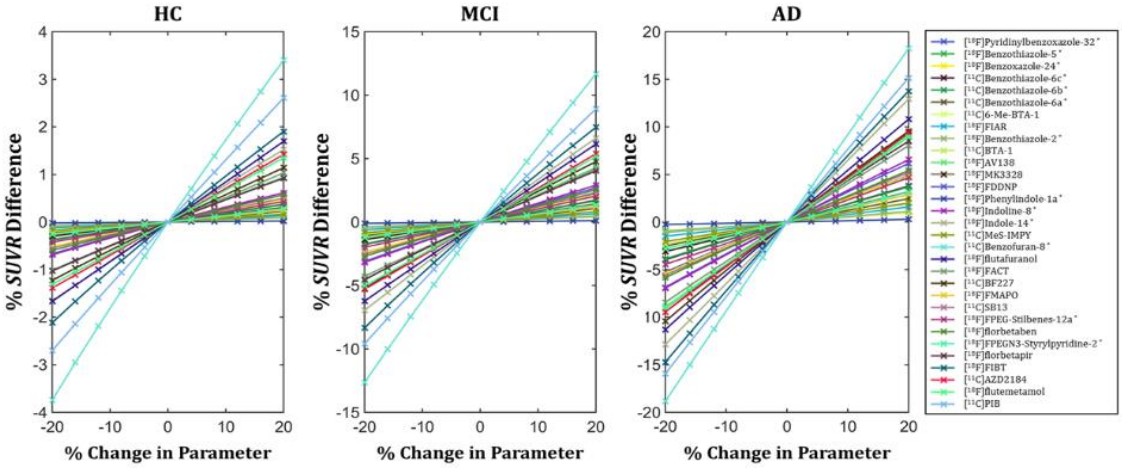

Figure 5.21: %*SUVR* difference from reference with ±20% variations in f_{ND} only.

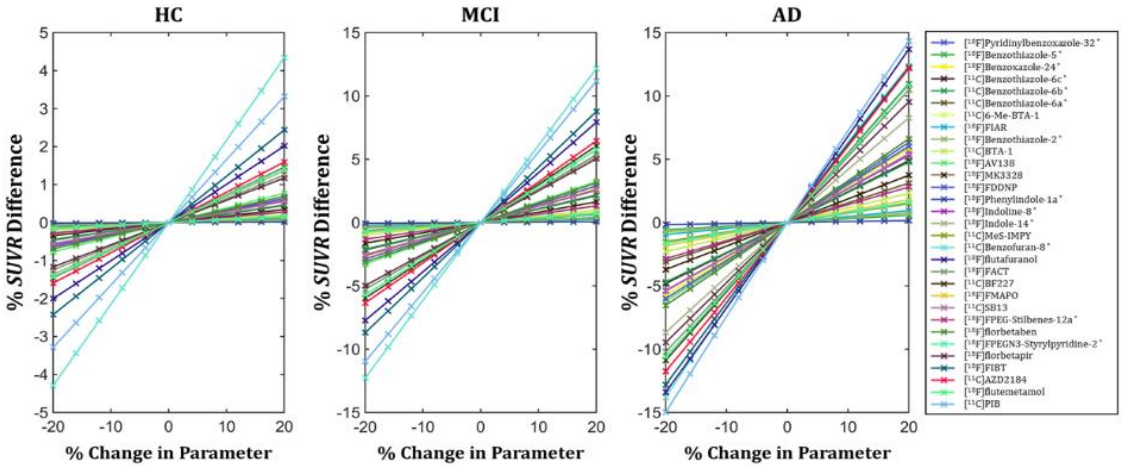

Figure 5.22: %*SUVR* difference from reference with ±20% variations in B_{avail} only.

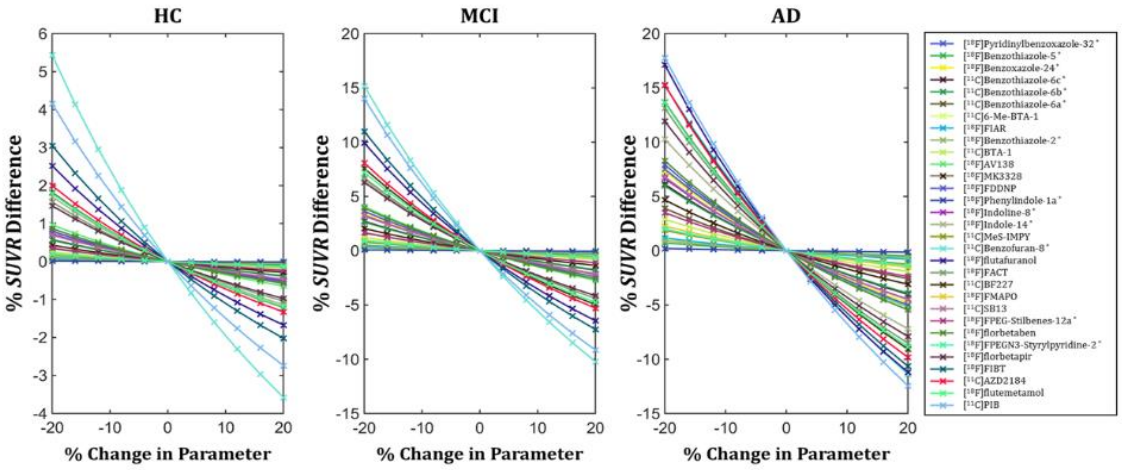

Figure 5.23: %*SUVR* difference from reference with ±20% variations in K_D only.

The % *SUVR* differences were greater in AD compared to HC, with less than 20%, 20% and 15% in AD and less than 4%, 6% and 5% in HC, for f_{ND}, K_D and B_{avail} respectively (Figures 5.21- 5.23). The changes in f_{ND} values resulted in the greatest % *SUVR* differences as it affected both k_2 and BP_{ND} values based on equations (16) and (17). However, in terms of experimental measurement errors, errors in K_D measurement were greater than that of f_{ND}. Increasing f_{ND} and B_{avail} values resulted in greater *SUVR* values (Figures 5.21 and 5.22) while increasing K_D values resulted in smaller *SUVR* values (Figure 5.22). On the whole, variations in K_D led to greatest changes in outcome *SUVR* values, followed closely by f_{ND}, B_{avail}, M*LogP*, f_P then V_x (Figures 5.18- 5.23). Thus, the amyloid biomathematical model is highly sensitive to K_D followed by f_{ND}.

5.9.2 Noise Simulations

The *in vivo SUVR* measured from PET images are subjected to noise due to reduced radioactive counts from decaying radioisotope, scattering of photons etc. (section 3.1). The effects of noise on outcome *SUVR* values was evaluated to determine whether the model is sensitive to noise during the evaluation of the possible clinical performance of candidate radiotracers.

1000 noisy time activity curves were generated using Monte Carlo simulations using equations adopted from Logan [2001]. The random noise simulated at each frame time included the noise effects due to scan durations and radioactive decay of the isotopes:

$$\mathrm{dev(t)} = prn \cdot SF \cdot \sqrt{\frac{e^{-\lambda t} \cdot C_t(t)}{\Delta t}} \tag{54}$$

$$C_t'(t) = C_t(t) + e^{\lambda t} \cdot dev(t) \tag{55}$$

where C_t(t) is the original simulated radioactivity at mid-frame time (t) for each frame, $e^{-\lambda t} \cdot dev(t)$ is the noise contribution at time t, $e^{-\lambda t} \cdot C_t(t)$ is the non-decay corrected radioactivity at time t, λ is the half-life of the isotope, Δt is the duration between two frames, *prn* is the pseudo random number generated from a Gaussian distribution with zero mean and standard deviation of one and, *SF* is the scaling factor to control the level of noise [Ikoma et al., 2008].

The level of noise due to the counting statistics of a PET scanner can be expressed as the inverse square-root of the non-decay-corrected tissue concentration for each frame time. The scaling factor (*SF*) was determined such that the noise level of the time activity curve (TAC) from 8 to 150 min was 3%:

$$N_i = \int_{t_1}^{t_2} C_t(t) \cdot e^{-\lambda t}\, dt \tag{56}$$

$$SD_{mean} \cdot \mathrm{SF} = \sum_{i}^{n} \frac{\sqrt{N_i}}{N_i} \tag{57}$$

N_i represents the area under non-decay corrected TAC from the start of the frame time (t_1) to the end of the frame time (t_2) for the simulated radioactivity ($C_t(t)$) at mid-frame time t.

The TACs were simulated with noise for the reference region and the target regions of each subject conditions of HC, MCI and AD. *SUVR* values were then obtained by dividing the area under the TAC (*AUC*) of the target over the reference region within the stated time window from the literature for clinically-applied radiotracers (Table 5.1) or from 40 to 60 min for candidate radiotracers using equation (4).

$$SUVR = \frac{AUC_{\mathrm{target,t1-t2}}}{AUC_{\mathrm{reference,t1-t2}}} \tag{4}$$

Good amyloid radiotracers will show huge differences in *SUVR* values across the various subject groups, but small variance in *SUVR* values within each subject group to ensure clear differentiation of the subject groups. The coefficient of variance of *SUVR* values simulated by Monte Carlo can be determined from the mean (μ) and standard deviation (σ) of the simulated *SUVR* values:

$$\%COV[SUVR] = \frac{\sigma(SUVR)}{\mu(SUVR)} \times 100\% \tag{58}$$

The %*COV* of predicted *SUVR* values for all 31 amyloid radiotracers across the three subject conditions of HC, MCI and AD were less than 3% indicating that the noise of the PET scanner has very little impact on outcome *SUVR* values (Table 5.8). Moreover, the noise level was approximately the same regardless of the subject conditions for each radiotracer, hence indicating that the simulated TACs were not greatly affected by the increased binding to the higher amyloid load under MCI and AD conditions.

Table 5.8: %*COV* of *SUVR* generated with noise simulation for 31 amyloid radiotracers under HC, MCI and AD conditions.

Radiotracers	%*COV*		
	HC	MCI	AD
[^{11}C]PIB	1.32	1.32	1.27
[^{18}F]FDDNP	2.54	2.55	2.47
[^{11}C]SB13	1.46	1.43	1.38
[^{18}F]florbetaben	2.81	2.73	2.59
[^{11}C]BF227	1.33	1.36	1.30
[^{18}F]AV138	2.16	2.19	2.12
[^{18}F]flutemetamol	2.53	2.42	2.53
[^{18}F]florbetapir	3.02	2.96	2.83
[^{11}C]AZD2184	1.39	1.37	1.29
[^{18}F]flutafuranol	2.94	2.81	2.85
[^{18}F]FACT	2.29	2.32	2.33
[^{18}F]FIBT	2.85	2.75	2.70
[^{11}C]6-Me-BTA-1	1.26	1.26	1.21
[^{11}C]BTA-1	1.26	1.28	1.30
[^{18}F]FMAPO	2.10	2.11	2.06
[^{18}F]FPEG-Stilbenes-12a*	2.12	2.10	2.18
[^{11}C]Benzofuran-8*	1.25	1.23	1.24
[^{18}F]FPEGN3-Styrylpyridine-2*	2.05	2.09	2.04
[^{11}C]MeS-IMPY	1.24	1.24	1.19
[^{18}F]Indole-14*	2.21	2.07	2.12
[^{18}F]Indoline-8*	2.14	2.26	2.21
[^{11}C]Benzothiazole-6a*	1.34	1.35	1.42
[^{11}C]Benzothiazole-6b*	1.34	1.34	1.30
[^{11}C]Benzothiazole-6c*	1.32	1.33	1.30
[^{18}F]Benzothiazole-2*	2.04	2.07	2.07
[^{18}F]Benzothiazole-5*	2.05	2.02	2.03
[^{18}F]MK3328	2.45	2.37	2.46
[^{18}F]FIAR	1.96	1.96	2.00
[^{18}F]Benzoxazole-24*	2.27	2.30	2.24
[^{18}F]Pyridinylbenzoxazole-32*	2.44	2.32	2.42
[^{18}F]Phenylindole-1a*	2.00	2.03	2.00

*Simplified name with the compound number or alphabet, as reported in the literature, used when generic name or institute code name (supplied by the author) was not available.

5.9.3 Effect of Input Functions

The effect of input function on the predicted *SUVR* was evaluated in section 5.7. In this subsection, the effect of input function was further evaluated with noise simulations. The five different input functions obtained from both AD and HC subjects injected with [^{11}C]BF227 and [^{18}F]FACT (BF227-AD, BF227-HC (default), FACT-AD, FACT-HC) and one CNS tracer, [^{18}F]FDDAA were used for evaluation (refer to section 5.7 for details). For each radiotracer, *SUVR* values were simulated 1000 times with noise, as described in section 5.9.2. The mean *SUVR* values were then calculated for each amyloid radiotracer. The % differences of the mean *SUVR* values from that generated using the default input function of BF227-HC were calculated for all 31 amyloid radiotracers (Table 5.7) for subject conditions of HC, MCI and AD.

As BF227-HC has a higher area under the input function curve compared to FACT-HC and FACT-AD (Figure 5.13), the *SUVR* values generated were generally higher than that of FACT-HC and FACT-AD, but smaller than that of BF227-AD and FDDAA, which have larger areas under input function curve. Therefore, the % differences in mean *SUVR* were generally negative for FACT-HC and FACT-AD but positive for BF227-AD and FDDAA (Figure 5.24).

The % differences in mean *SUVR* were less than 1.5%, 7% and 12% under HC, MCI and AD conditions excluding FDDAA. For FDDAA, the % differences in mean *SUVR* were less than 2.5%, 14% and 25% under HC, MCI and AD conditions. This showed that the type of input functions employed will affect the outcome *SUVR* significantly if the input function of a radiotracer with completely different kinetics was used. However, if an input function of a radiotracer with similar kinetics was used, the outcome *SUVR* values would not be greatly affected by more than 12%, regardless of the subject groups used. Hence, the input function of amyloid radiotracers should be used for simulations.

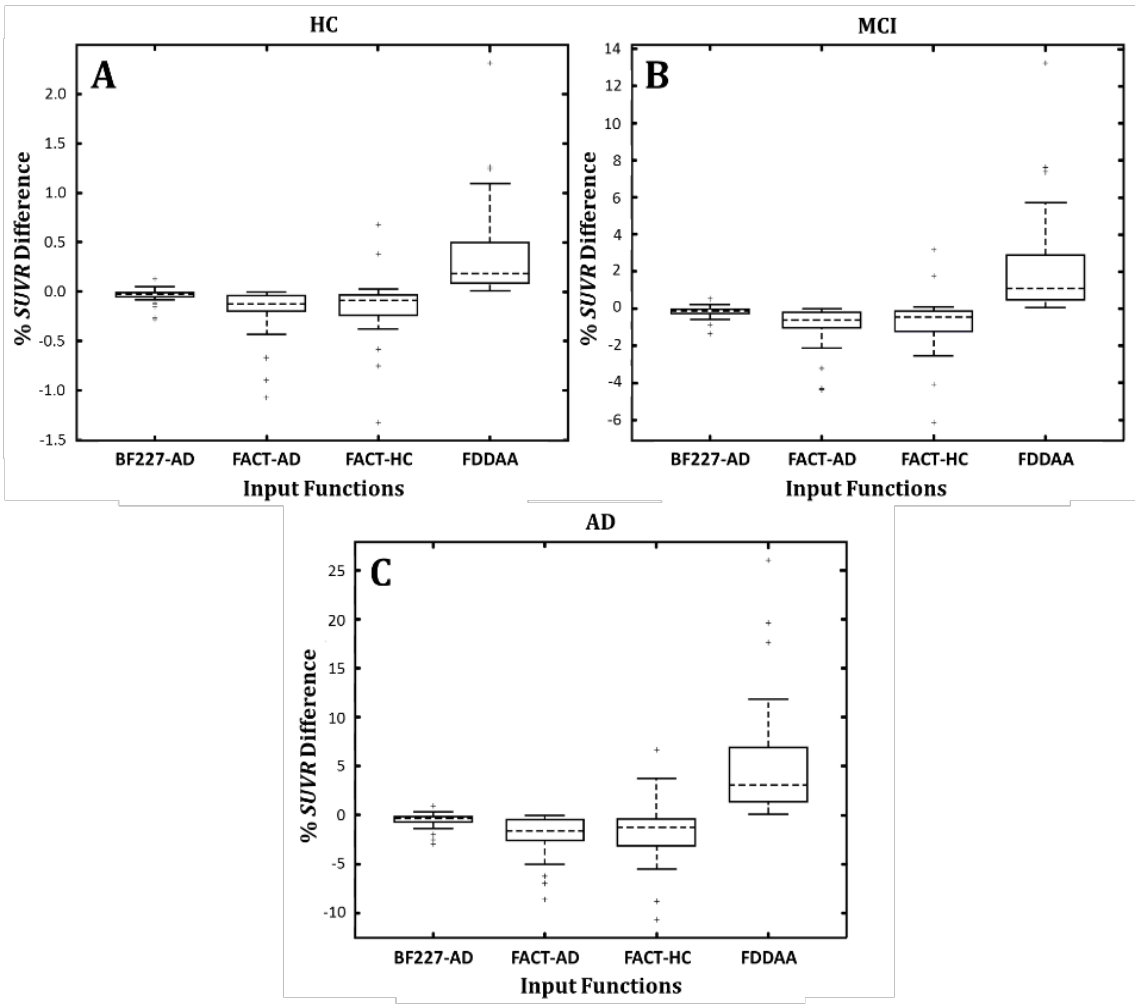

Figure 5.24: Boxplots of % mean *SUVR* difference generated using BF227-AD, FACT-AD, FACT-HC and FDDAA from that generated using reference input function of BF227-HC under (A) HC, (B) MCI and (C) AD conditions.

5.10 Summary

In this chapter, we have developed a biomathematical model for predicting the *SUVR* values under representative HC, MCI and AD conditions with the appropriate scaling factors, choice of the time window and input function. The remaining issue from the previous chapter of determining the representative lipophilicity parameter was resolved by correlating the predicted *SUVR* values with clinically-observed values. M*LogP* was thus chosen as the input parameter for lipophilicity. The *in silico* f_P-f_{ND} model resulted in good correlations between predicted and clinically-observed k_2, BP_{ND} and *SUVR*. This showed the feasibility of the model in predicting f_P and f_{ND} for amyloid radiotracers. The sensitivity analysis of the amyloid biomathematical model showed that K_D was

the key parameter that would greatly affect the outcome *SUVR*, followed by f_{ND}. The outcome *SUVR* would not be greatly affected by the use of a plasma input function of a subject injected with an amyloid radiotracer.

Chapter 6

Screening Methodology of Amyloid Radiotracers

During radiotracer development, the comparison of the amyloid radiotracers is mostly carried out based on K_D or K_i values, which do not reflect the pharmacokinetics of the radiotracers under clinical situations. The developed amyloid biomathematical model helps to predict the possible *in vivo* pharmacokinetics performance of the amyloid radiotracer in terms of *SUVR*. However, to evaluate the diagnostic capability of an amyloid radiotracer, the prediction of *SUVR* values at a single amyloid load under representative HC, MCI and AD conditions would not be sufficient. Moreover, the actual PET data contains noise, which will also affect the measured outcome and the accuracy of the diagnosis. Therefore, to evaluate the diagnostic capability of an amyloid radiotracer in discriminating the subject conditions, simulating variation in population data and noise in PET data are required.

This chapter focuses on the development of a screening methodology to evaluate the diagnostic capability of the amyloid radiotracers in discriminating subject conditions in terms of SUVR. The various existing methods applied to evaluate the diagnostic performance of various radiotracers are also discussed. The feasibility of the screening methodology is evaluated by comparing the ranking results of the radiotracers with comparison results reported in the literature. A total of 31 amyloid radiotracers (12 clinically-applied, 19 candidates) are used for evaluation (Table 5.7).

6.1 Existing Evaluation Methods

There are many existing methods employed to evaluate a treatment effect or the accuracy of a test or diagnosis. These methods measure the different aspects or properties of a treatment or diagnosis and may be sensitive to factors like disease prevalence, the spectrum of the disease etc. However, regardless of the methods applied, they are sensitive to the population being studied and the design of the study [Šimundić et al., 2009]. In this section, three evaluation methods that are commonly applied are described in details.

6.1.1 Coefficient of Variance (*COV*)

The coefficient of variance (*COV*) is a measure of the variability of a set of data, independent of the unit of measurements. Therefore, it can be used to compare the spread of different dataset with different units of measurement. However, it is applicable only if the dataset consists of a real zero. *COV* is commonly determined in % using equation (58):

$$COV(\%) = \frac{stdev}{mean} \times 100\% \tag{58}$$

where *stdev* is the standard deviation of a set of data and *mean* is the average or mean value of the set of data.

COV is used to determine the performance of radiotracer such as CNS. A good CNS radiotracer has small *COV* value which indicates small variation in measured outcome (e.g. BP_{ND}) [Guo et al., 2009]. Small *COV* within a subject condition is desirable. However, *COV* cannot be used to evaluate the performance of the radiotracer in discriminating subject conditions as the variations in *SUVR* differed across the subject conditions and it is used as an index of variability within a subject condition and not across subject conditions.

6.1.2 Receiver Operating Characteristics (ROC)

Receiver operating characteristics (ROC) is commonly applied to judge the diagnostic accuracy of a diagnostic test. It requires a threshold, which is set to discriminate subjects into two groups and involves identifying subjects that are correctly or incorrectly classified. Subjects that are correctly identified as having a disease are termed true-positive (TP), and those correctly identified as not having a disease are termed true negatives (TN). Subjects that are incorrectly identified as having and not having a disease are termed false positive (FP) and false negative (FN) respectively. These 4 cases are summarised in table 6.1.

Table 6.1: Classification of subjects based on diagnostic test results and the actual outcome.

Diagnostic Test Results	Actual Outcomes	
	Positive	Negative
Positive	TP	FP
Negative	FN	TN

The sensitivity of a test is defined as the probability of correctly identifying subjects with the disease and is calculated as TP / (TP+FN). The specificity of a test is defined as the probability of

correctly identifying subjects without the disease and is calculated as TN / (FP+TN) [Bewick et al., 2004]. Positive predictive value (*PPV*) is the probability of having subjects with the disease in the positive diagnostic test results and is calculated as TP / (TP+FP). Negative predictive value (*NPV*) is the probability of having subjects without disease in the negative diagnostic test results and is calculated as TN / (TN+FN) [Bewick et al., 2004].

The receiver operating characteristics (ROC) plot is obtained by varying the thresholds and determining the respective sensitivities and specificities and plotting the sensitivity against the 1-specificity (Figure 6.1). The area under the ROC curve (*AUROC*, *Az*) can be used as a global measure of diagnostic accuracy but it is unable to differentiate test with higher sensitivity from that with higher specificity. The value of *Az* ranges from 0 to 1, whereby the larger the value of *Az*, the higher the diagnostic accuracy.

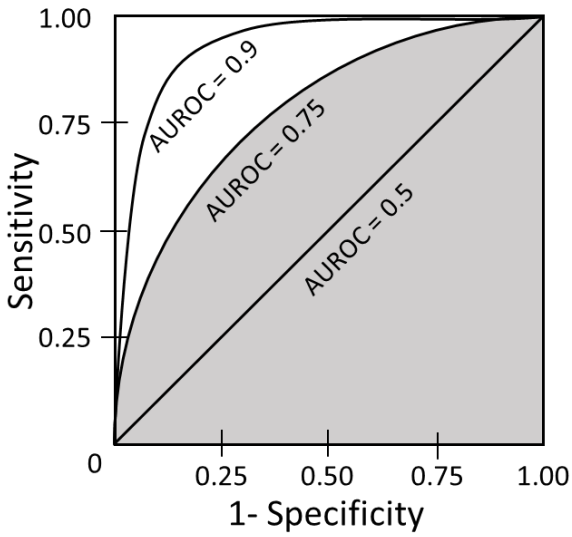

Figure 6.1: Receiver Operating Characteristic plot with three curves of different *Az* values of 0.5, 0.75 and 0.9. The curve with *Az* of 0.75 is coloured in gray.

Az can be determined as a sum of trapezoids (empirical) or by fitting the curve (parametric) [Bewick et al., 2004]. It is often accompanied by the determination of the confidence interval (*CI*) of 95% and a statistics test [Šimundić et al., 2009]. In amyloid imaging, *Az*, sensitivity and specificity are commonly employed to determine the diagnostic accuracy of a radiotracer in classifying the subjects into HC, MCI and AD conditions, as classified by neuropsychological test (Table 6.2). For clinically-applied amyloid radiotracers, the values of sensitivity and specificity are mostly greater than 85% and varied even for the same radiotracers as the sensitivity and specificity depend on the population evaluated.

Table 6.2: Sensitivity and specificity of five clinically-applied amyloid radiotracers.

Radiotracers	ROC		References
	Sensitivity (%)	Specificity (%)	
[^{11}C]PIB	97.2	85.3	Hatashita et al., 2014
[^{11}C]BF227	97.5$^{\#}$	81.7$^{\#}$	Shao et al., 2010; Furumoto et al., 2013
[^{18}F]flutemetamol	95.2*	89.3*	Hatashita et al., 2014; Vandenberghe et al., 2010
[^{18}F]florbetapir	92.7$^{\$}$	95.3$^{\$}$	Clark et al., 2011; Camus et al., 2012
[^{18}F]FACT	90	100	Furumoto et al., 2013

$^{\#}$ Averaged values of Sensitivity (95,100) and of Specificity (92,71.4)
* Averaged values of Sensitivity (97.2,93.1) and of Specificity (85.3,93.3)
$^{\$}$ Averaged values of Sensitivity (93,92.3) and of Specificity (100,90.5)

Sensitivity, specificity, *PPV* and *NPV* are dependent on the thresholds applied and the spectrum of the disease. *Az* is independent on the thresholds set but does not differentiate tests with high specificity or sensitivity. The values of sensitivity, specificity, *PPV*, *NPV* and *Az* range from 0.0 to 1.0. To correctly apply ROC, statistical analysis with CI should be stated to determine the strength of the differences between two treatments or diagnostic test for discriminating two groups of subjects. However, statistical results are dependent on sample size and the disease spectrum in clinical studies.

6.1.3 Power & Sample Size Analysis

Effect size (*Es*) shows the magnitude of the difference between two datasets. It is scale-free (unitless) and hence it is applicable for comparing the relative magnitude effects of different data. There are a few types of formula to determine *Es* and it is dependent on the dataset. The equation used to determine *Es* is similar to that of Z-score or t-value formulae but instead of dividing by the population standard deviation or standard error ($SE = \sigma/\sqrt{n}$) respectively, a specified standard deviation is applied instead. The most common *Es* is the Cohen's D, which can be determined using the means of the two datasets and a pooled standard deviation, σ_{pooled}.

$$Es = \frac{M_2 - M_1}{\sigma_{\text{pooled}}} \tag{59}$$

$$\sigma_{\text{pooled}}\ (\text{Cohen's D}) = \sqrt{\frac{({SD_2}^2 + {SD_1}^2)}{2}} \tag{60}$$

where M_2 is the mean of the sample or dataset 2 and M_1 is the mean of the population or dataset

1. SD_2 is the standard deviation of the sample or dataset 2 and SD_1 is the standard deviation of the population or dataset 1.

However, *Es* (Cohen's D) is applicable only if there is homogeneity in the variance of the datasets such that the results differed due to the sampling variation. If the standard deviations of the two datasets differ greatly, then this assumption will be violated and the standard deviations cannot be pooled together. If the sample sizes of the two datasets differ, σ_{pooled} (Hedges'G) is recommended to weigh the standard deviation by its sample size.

$$\sigma_{\text{pooled}}(\text{Hedges'G}) = \sqrt{\frac{(n_1 - 1) \cdot {SD_1}^2 + (n_2 - 1) \cdot {SD_2}^2}{n_1 + n_2 - 2}} \tag{61}$$

If σ_{pooled} (Hedges'G) is applied, *Es* should be corrected for small positive bias.

$$\text{Corrected } Es \text{ (Hedges'G)} = Es \cdot (1 - \frac{3}{[4(n_1 + n_2) - 9]}) \tag{62}$$

Where n_1 and n_2 are the sample size of dataset 1 and 2 respectively.

If the sample sizes of both datasets are the same but the standard deviations differed, the standard deviation of the control group should be applied instead to determine *Es* (Glass's delta). This is based on the assumption that the measurements of the control group are not biased by the treatment or another external factor.

The use of *Es* is limited to normally-distributed datasets and comparison of one type of measurement at a time. Moreover, *Es* is based on average values, which can differ widely depending on measurement reliability. For normally-distributed datasets with equal variances, *Es* (Cohen's D) can also be converted to a common language effect size (*CL*), also known as *Az* in ROC [McGraw and Wong, 1992]:

$$CL = \emptyset(\frac{\delta}{\sqrt{2}}) \tag{63}$$

where Φ is the cumulative distribution function for a normally-distributed data, δ is the population effect size of datasets with homogeneous variance, similar to *Es* (Cohen's D).

6.2 Screening Methodology

To fully evaluate the diagnostic capability of an amyloid radiotracer, *SUVR* values at variable amyloid load for each subject condition of HC, MCI and AD should be carried out. Moreover, to

mimic actual clinical data, population variation and noise level of scanner modality should be included in the simulations. Screening of radiotracers using population *SUVR* simulations is discussed in this section. The introduction of a common index is also described and evaluated to support objective evaluation of the clinical usefulness of multiple candidate radiotracers simultaneously and rapidly during radiotracer development.

6.2.1 Simulation with Population Variation & Noise

To simulate clinical situations, K_1 and k_2 inputs into the biomathematical model were varied by 10% and 20% respectively [Guo et al., 2012]. B_{avail} was also varied by 80%, 35% and 20% under HC, MCI and AD conditions respectively (section 4.4.5) [Svedberg et al., 2009]. These parameters were varied assuming a normally distributed population. 1000 noisy TACs in both target and reference regions were generated by Monte Carlo simulations. The noise was simulated such that the averaged noise level from 8 to 150 min was 3% using equations (54) to (57) (section 5.9.2) [Logan et al., 2001; Ikoma et al., 2008]. The 1000 TACs simulated for both target and reference regions were used to obtain 1000 *SUVR*s for each subject condition of HC, MCI and AD. *S*imulations were carried out using an in-house software written in Matlab (Ver. R2014b, The MathWorks Inc., US).

SUVR distributions across subject conditions of HC, MCI and AD were different depending on the regions of interest [Vandenberghe et al., 2010]. However, in regions excluding the cerebellum and subcortical white matter, the variations in young HC is the smallest, followed by elderly HC, then AD and lastly MCI [Vandenberghe et al., 2010]. The tails of the boxplot of MCI spreads from the minimum tail in elderly HC to the nearly the mean of AD [Vandenberghe et al., 2010; Hatashita et al., 2014]. The position of the median, box length and whisker length of simulated boxplot were evenly distributed due to the use of 1000 *SUVR* values, which differed from clinical data as the sample size reported were generally smaller. Even for large population datasets, the boxplot is dependent on the population screened. On the whole, the overall spread of simulate *SUVR* distributions across subject conditions of HC, MCI and AD for [^{11}C]PIB and [^{18}F]flutemetamol reflected closely to that observed in clinical data (Figure 6.2), thus showing that the variations in B_{avail} applied were suitable.

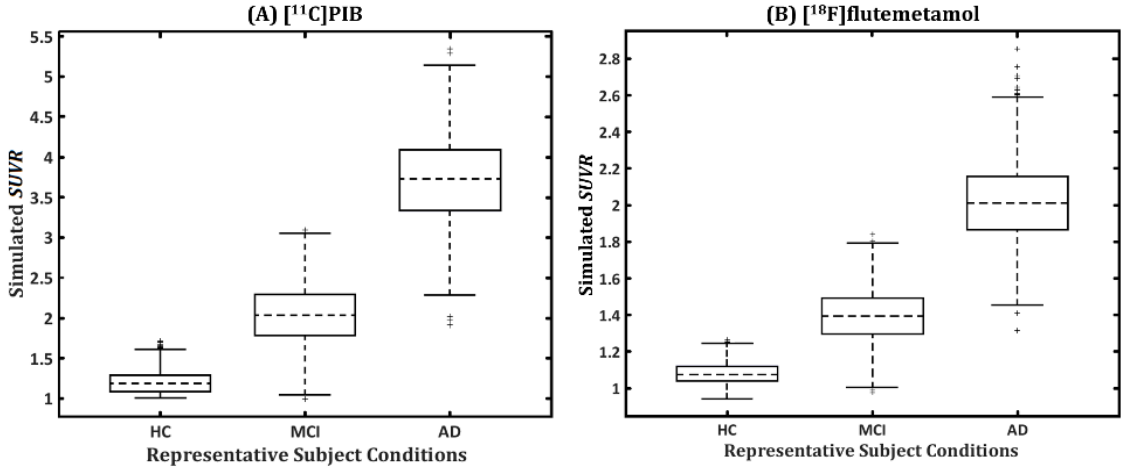

Figure 6.2: Simulated *SUVR* distributions across HC, MCI and AD conditions for (A) [^{11}C]PIB and (B) [^{18}F]flutemetamol.

6.2.2 Clinical Usefulness Index (*CUI*)

The clinical usefulness of a radiotracer reflects its diagnostic capability to differentiate the subject conditions. It is evaluated using methods such as receiver operating characteristics (ROC) and effect size. ROC evaluates the sensitivity and specificity of a radiotracer in diagnosing the subjects' conditions correctly (section 6.1.2) [Fawcett et al., 2006]. Effect size is used to determine the strength of the differences in the measured values between two subject groups (section 6.1.3) [Okamura et al., 2014]. In amyloid imaging, the ratio of *SUVR* of AD to that of HC are often employed [Hatashita et al., 2014, Vandenberghe et al., 2010]. These methods are applied post-imaging and are not evaluated during radiotracer development.

Good amyloid radiotracers show great differences in clinical *SUVR* between subject conditions, thus making it easier to set *SUVR* threshold for diagnosing the subjects with higher accuracy (Figure 6.3). Presently, the comparison of the diagnostic capabilities of clinically-applied radiotracers are carried out by (1) visual comparison of clinical image data based on gray-white matter demarcation [Hatashita et al., 2014; Yousefi et al., 2015a; Carpenter et al., 2009] or (2) white matter retention [Wong et al., 2010; Ito et al., 2014; Cselenyi et al., 2012] or (3) quantitative analysis of *SUVR* differences in gray and white matter regions between HC and AD subjects [Hatashita et al., 2014, Barthel et al., 2011, Price et al., 2005, Becker et al., 2013; Rowe et al., 2008; Shidahara et al., 2015; Heurling et al., 2015; Nelissen et al., 2009; Ito et al., 2014; Carpenter et al., 2009]. However, the comparison of the clinical usefulness of clinically-applied radiotracers was difficult. This was due to issues such as a limited number of subjects and radiotracers

available, variations in subjects' physiology and pathologies (e.g. other dementia), differences in amyloid distributions and densities), and the presence of white matter retention.

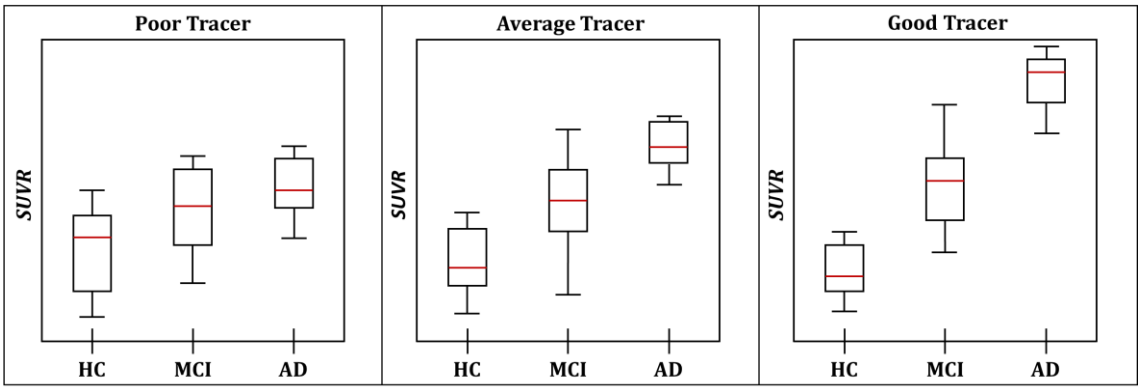

Figure 6.3: *SUVR* distribution across HC, MCI and AD conditions using poor, average and good radiotracers

A clinical usefulness index (*CUI*) was proposed for objective evaluation of the diagnostic power of radiotracer in differentiating the subjects clearly into subject conditions based on its binding capability to the cortical amyloid fibrils, in terms of *SUVR*. Evaluation tests used to evaluate the performance of a radiotracer were selected for the development and evaluation of *CUI*.

6.2.2.1 Determination of Parameters

COV is not suitable for comparing two or more dataset or for evaluating the discrimination power of two sets of data. For ROC analysis, sensitivity, specificity, *PPV* and *NPV* are dependent on the thresholds applied while *Az* is independent on the thresholds set. *Az* was thus selected as a potential parameter for evaluating the diagnostic capability of radiotracers. *Es* can serve as an independent parameter in evaluating the strength of the differences between 2 datasets. However, *Az* and *Es* are related and there are many types of *Es* available, the evaluation of *Az* and *Es* is required. Subject conditions of HC, MCI and AD are then grouped into conditions-pairs of HC-MCI, MCI-AD and HC-AD. The conditions-pairs that can evaluate the diagnostic capability of the radiotracer needs to be determined. The *SUVR* ratios (*Sr*) of HC-MCI, MCI-AD and HC-AD were also included to determine if it was sufficient to evaluate the diagnostic performance of the amyloid radiotracers.

Az was derived from the parametric fitting of the ROC curve using a ROC program written in Matlab (Ver. R2014b, The MathWorks Inc., US). *Es* was calculated from equations (59) and (60) using the means and respective standard deviations of 1000 *SUVR* values for each subject

conditions of HC, MCI and AD. *Sr* was determined by dividing the means of 1000 *SUVR* values for subject conditions of HC, MCI and AD accordingly to obtain $Sr_{MCI/HC}$, $Sr_{AD/MCI}$ and $Sr_{AD/HCI}$ for conditions-pairs of HC-MCI, MCI-AD and HC-AD.

The 1000 *SUVR* values were simulated for all three conditions of HC, MCI and AD, assuming a normally-distributed population. However, the standard deviations of the *SUVR* values simulated across HC, MCI and AD conditions were different, hence their variances were not homogeneous. In this case, σ of a control group should be used (refer to section 6.1.3). The σ_{pooled} (Hedges'G) is not required since the same, large sample size was used for all conditions. As such, *Es* (Cohen's D) and *Es* (Glass's delta) of the 31 amyloid radiotracers were evaluated. The difference between *Az* and *CL* (generated from *Es* (Cohen's D) using equation (63)) was also investigated for conditions-pairs of HC-MCI, MCI-AD and HC-AD.

Az, *Es* and *Sr* of conditions-pairs of HC-MCI and MCI-AD were averaged and combined in pairs or all combined together to form different combinations. The spread and variance of the values of the combinations and the individual averaged parameters were determined. The parameter with the largest spread was evaluated against the other parameters individually using F-Test (ANOVA) on Matlab (Ver. R2014b, The MathWorks Inc., US) to ensure that these parameters are significantly different.

6.2.2.2 Evaluation of Parameters

Es (Glass's Delta) generated using standard deviations of HC and MCI for conditions-pair of HC-MCI were very different, with a range of 0~6.0 and 0~2.5 respectively (Figure 6.4). *Es* (Glass's Delta) generated using standard deviations of MCI for conditions-pair of MCI-AD ranged from 0~4.5. *Es* (Glass's Delta) generated using standard deviations of HC for conditions-pair of HC-AD ranged from 0~18 (Figure 6.4). *Es* (Cohen's D) ranged from 0~3.0, 0~3.5 and 0~6.5 respectively for conditions-pairs of HC-MCI, MCI-AD and HC-AD (Figure 6.4). *Es* (Glass's delta) generated using standard deviations of HC increased with increasing *Es* (Cohen's D) while that of MCI decreased (Figure 6.4).

Es (Glass's Delta) was dependent on the choice of standard deviation used and its range differed greatly between conditions-pairs of HC-MCI, MCI-AD and HC-AD. *Es* (Cohen's D) appeared most consistent with closer ranges for both conditions-pairs of HC-MCI and MCI-AD. Thus, only conditions-pairs of HC-MCI and MCI-AD was selected to evaluate the diagnostic performance

of amyloid radiotracers, while conditions-pair of HC-AD was excluded.

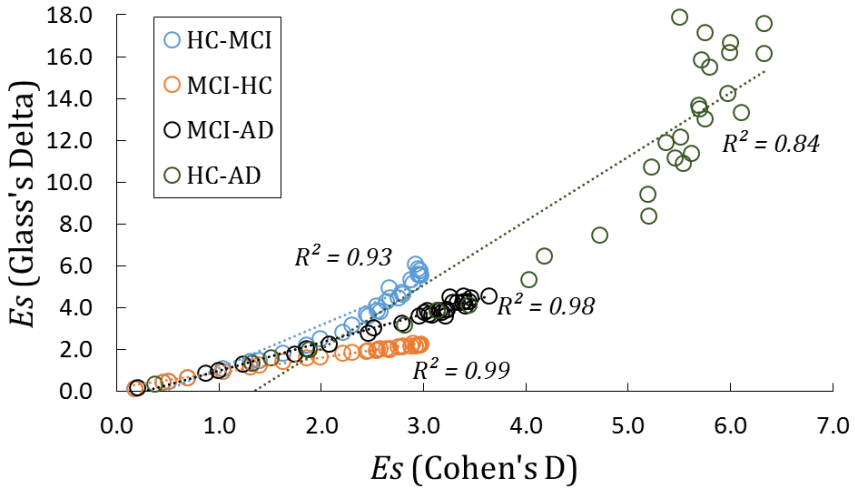

Figure 6.4: *Es* (Glass's Delta) Vs. *Es* (Cohen's D) for conditions-pairs of HC-MCI (Stdev of HC used for Glass's Delta, blue), HC-MCI (Stdev of MCI used for Glass's Delta, orange) and MCI-AD (Stdev of MCI used for Glass's Delta, black) and HC-AD (Stdev of HC used for Glass's Delta, green) of 31 amyloid radiotracers.

The correlations between *Az* and *CL* for conditions-pairs of HC-MCI, MCI-AD and HC-AD were very strong with R^2 of 0.999 (Figure 6.5). The small differences in values between *Az* and *CL* (Figure 6.5) may be due to the fitting of the ROC curve or due to the effects of violating the assumptions applied in using *Es* (Cohen's D). *Az* was assumed to be correct and was used to correct for *Es* (Cohen's D) to determine the differences in *Es* as follows:

$$\text{Corrected } Es\ (cEs) = \frac{Az}{CL} \times Es \tag{64}$$

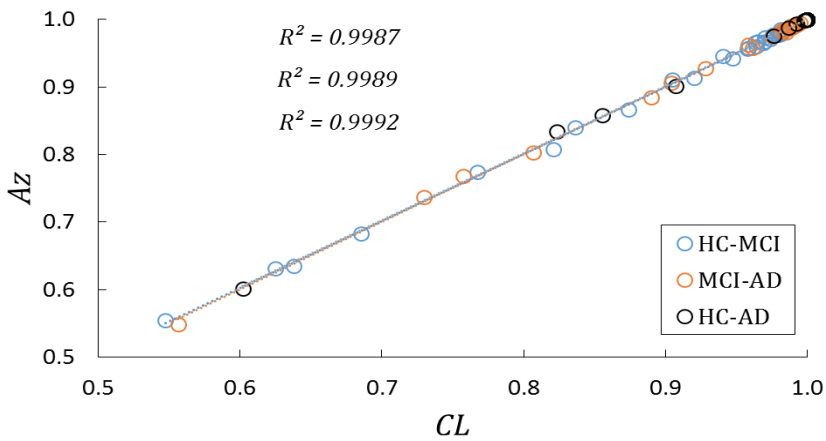

Figure 6.5: Correlations between *Az* and *CL* for conditions-pairs of HC-MCI (blue), MCI-AD (orange) and HC-AD (black) for 31 amyloid radiotracers.

The curve of *CL* vs. *Es* (Cohen's D) followed the cumulative distribution curve, hence showing that *Az* and *Es* evaluated the same properties of the radiotracers but *Es* showed greater differences in values compared to *Az* (Figure 6.6). For conditions-pair of HC-AD, the values of *Az* were similar for most radiotracers, hence *Az* would not be able to discriminate the performance of many amyloid radiotracers between HC and AD conditions. Due to the lack of differences in *Az* and huge differences in *Es* for conditions-pair of HC-AD as compared to conditions-pairs of HC-MCI and MCI-AD, only conditions-pairs of HC-MCI and MCI-AD will be used for further evaluation.

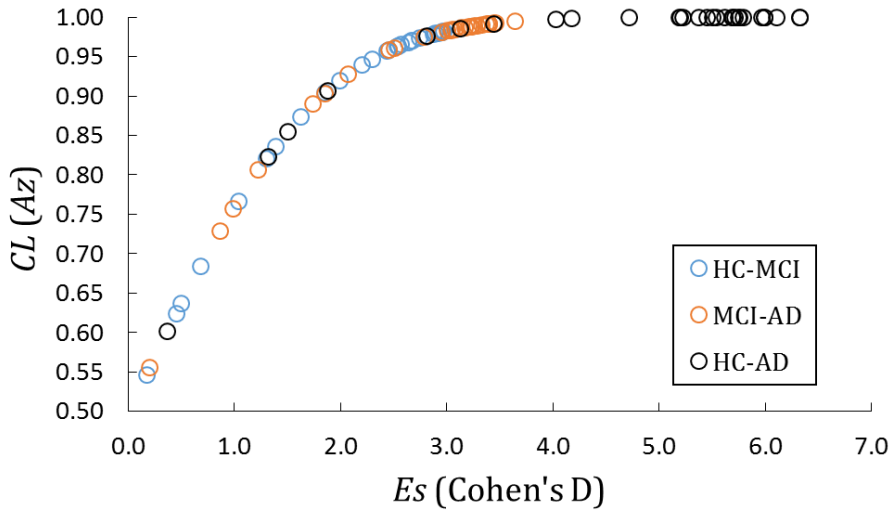

Figure 6.6: Relationship between *CL* and *Es* (Cohen's D) for 31 amyloid radiotracers.

The combination of averaged *Az* x *Es* x *Sr* of conditions-pairs of HC-MCI and MCI-AD yielded the largest spread and variance and hence F-test was determined using this combination as a reference against the other parameters. A small difference was observed between averaged *Es* and c*Es* and between the various combinations using averaged *Es* and c*Es* (Table 6.3). This supported the use of *Es* (Cohen's D) despite inhomogeneous variances across HC, MCI and AD conditions. Although *Az* and *Es* were related via the cumulative distribution function, they were not linearly correlated. As such, the F-value of averaged *Az* x *Es* was different from that of averaged *Es* with respect to averaged *Az* x *Es* x *Sr*.

On the whole, the combination of averaged *Az* x *Es* x *Sr* of conditions-pairs of HC-MCI and MCI-AD showed the greatest discrimination in the performance of the radiotracers. A common index, named clinical usefulness index (*CUI*) was developed using the product of the averaged *Az*, *Es* and *Sr* of conditions-pairs of HC-MCI and MCI-AD.

Table 6.3: Minimum, maximum, spread, mean and standard deviation of the respective parameters, *Az*, *Es*, c*Es*, *Sr*, *Az* x *Es*, *Az* x c*Es*, *Es* x *Sr*, c*Es* x *Sr*, *Az* x *Sr* and *Az* x *Es* x *Sr*. The resulting F-values and p-values from ANOVA with respect to *Az* x *Es* x *Sr* for the various parameters were shown at the bottom of the table.

	Az	*Es*	c*Es*	*Sr*	*Az* x *Es*	*Az* x c*Es*	*Es* x *Sr*	c*Es* x *Sr*	*Az* x *Sr*	*Az* x *Es* x *Sr*
Min	0.55	0.18	0.18	1.00	0.10	0.10	0.18	0.18	0.55	0.10
Max	0.99	3.30	3.29	1.83	3.26	3.25	5.79	5.79	1.80	5.72
Spread (Max-Min)	0.44	3.12	3.11	0.83	3.15	3.15	5.61	5.60	1.25	5.62
Mean	0.92	2.46	2.46	1.22	2.36	2.36	3.11	3.11	1.13	2.99
Stdev	0.11	0.87	0.87	0.22	0.92	0.92	1.42	1.42	0.29	1.47
Variance	0.01	0.75	0.75	0.05	0.86	0.85	2.02	2.01	0.08	2.16
F-value	67	179	180	97	194	194	36279	36746	633	-

6.2.3 Overview of Screening Methodology

In this section, an overview of the proposed screening methodology was described for screening amyloid radiotracers based on their diagnostic capability of discriminating subjects' conditions. The screening methodology involves three main steps (Figure 6.7): (1) Simulating 1000 *SUVR* values, with noise and population variation, for each subject condition of HC, MCI and AD, (2) Determination of AUROC (*Az*), effect size (*Es*) and *SUVR* ratios (*Sr*) for conditions-pairs of HC-MCI and MCI-AD, and (3) Determination of *CUI* from the product of the averaged *Az*, *Es* and *Sr*.

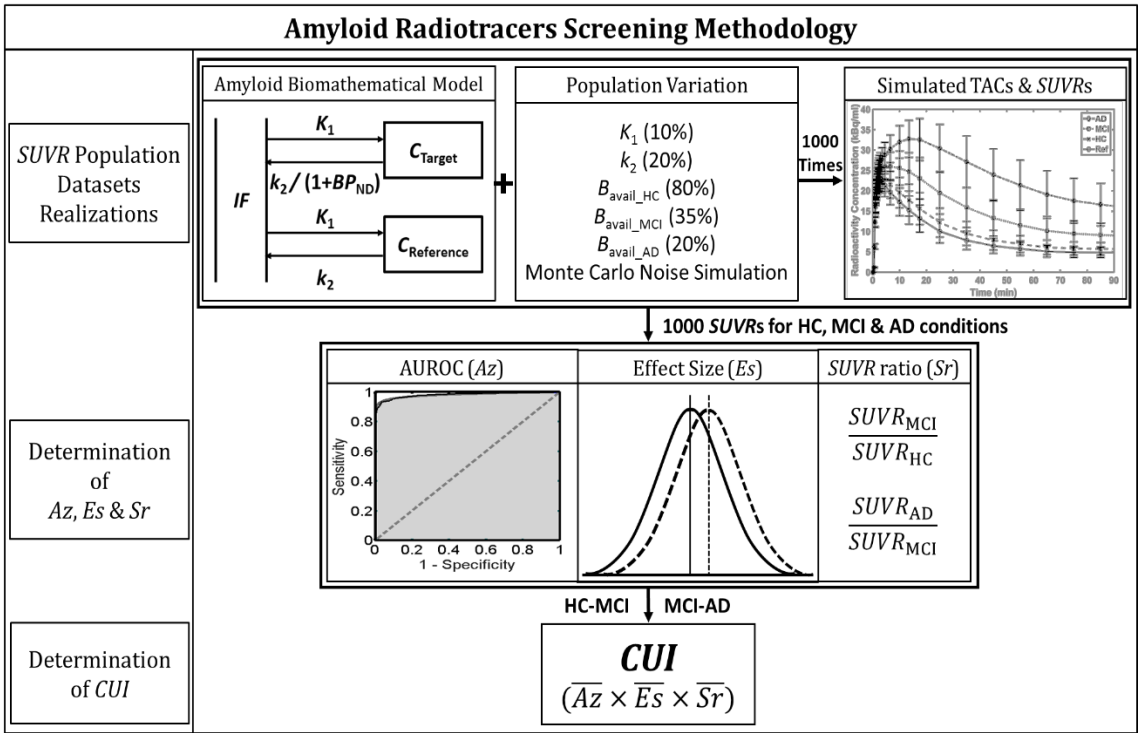

Figure 6.7: Overview of screening methodology for amyloid radiotracers based on the biomathematical model developed.

SUVR Population Datasets Realizations

K_1 and k_2 were varied by 10% and 20% respectively and B_{avail} was also varied by 80%, 35% and 20% under HC, MCI and AD conditions respectively. 1000 noisy TACs in both target and reference regions were generated using the amyloid biomathematical model developed. The noise was simulated such that the averaged noise level from 8 to 150 min was 3%. The 1000 TACs simulated for both target and reference regions were used to obtain 1000 *SUVR*s for each subject condition of HC, MCI and AD. Simulations were carried out using an in-house software written in Matlab (Ver. R2014b, The MathWorks Inc., US).

Determination of Az, Es and Sr

Az, *Es* and *Sr* were determined for each conditions-pair of HC-MCI and MCI-AD using the 1000 *SUVR* values of subject conditions of HC, MCI and AD. *Az* was derived using a ROC program written in Matlab (Ver. R2014b, The MathWorks Inc., US). *Es* was determined using the means (*M*) and standard deviations (*STD*) of 1000 *SUVR* values of subject conditions of HC, MCI and AD, in pairs of HC-MCI and MCI-AD:

$$Es_{1-2} = \frac{(M_2 - M_1)}{\sqrt{({STD_2}^2 + {STD_1}^2)/2}} \tag{65}$$

where 1 = HC and 2 = MCI for conditions-pair of HC-MCI, and 1 = MCI and 2 = AD for conditions-pair of MCI-AD. *Sr* was determined by dividing *M* of 1000 *SUVR* values for subject conditions of HC, MCI and AD accordingly to obtain $Sr_{MCI/HC}$ and $Sr_{AD/MCI}$ for conditions-pairs of HC-MCI and MCI-AD.

Determination of CUI

CUI was obtained from the product of the averaged *Az*, *Es* and *Sr* of conditions-pairs of HC-MCI and MCI-AD as follows:

$$CUI = \frac{1}{2}(Az_{HC-MCI} + Az_{MCI-AD}) \times \frac{1}{2}(Es_{HC-MCI} + Es_{MCI-AD}) \times \frac{1}{2}\left(Sr_{\frac{MCI}{HC}} + Sr_{\frac{AD}{MCI}}\right) \tag{66}$$

$$= \overline{Az} \times \overline{Es} \times \overline{Sr}$$

$\overline{Az}$, $\overline{Es}$ and $\overline{Sr}$ represent the averaged *Az, Es and Sr* of conditions-pairs of HC-MCI and MCI-AD. Conditions-pairs of HC-MCI and MCI-AD were used to represent the conditions of low and high amyloid loads respectively. Equal weightage was applied to both conditions-pairs, indicating that the binding capabilities to low and high amyloid loads were equally important in evaluating the performance of the amyloid radiotracer.

6.3 Screening of Amyloid Radiotracers

The *CUI* values of 31 amyloid PET radiotracers were simulated using the proposed screening methodology and ranked from highest to lowest. The evaluation results of the amyloid radiotracers based on *CUI* were compared with available comparison results of clinically-applied amyloid radiotracers. The relationships among $\overline{Az}$, $\overline{Es}$ and $\overline{Sr}$ and the resulting *CUI* for the listed radiotracers were investigated.

6.3.1 Screening Results

CUI values ranged from 0.10 to 5.72 for the list of 31 amyloid radiotracers evaluated (Table 6.4), with clinically-applied radiotracers having *CUI* values of greater than 3.0. The *CUI* distribution of the 31 amyloid radiotracers shows two slopes (< 3.0, > 3.5) and one flat region (3.0-3.5) (Figure 6.8). Among the clinically-applied amyloid radiotracers, [^{11}C]PIB was ranked first, followed by [^{18}F]FIBT, [^{18}F]flutafuranol, [^{11}C]BF227, [^{11}C]AZD2184, [^{18}F]flutemetamol, [^{18}F]florbetapir, [^{18}F]FACT, [^{11}C]SB13, [^{18}F]florbetaben, [^{18}F]AV138, and lastly [^{18}F]FDDNP.

6.3.2 Comparison Data of Clinically-Applied Radiotracers

The resulting *CUI* values were compared to comparison data of clinically-applied radiotracers from literature. There were few comparison data of clinically-applied radiotracers due to the limited availability of the radiotracers.

<u>[^{18}F]flutafuranol vs. [^{11}C]AZD2184 [Forsberg et al., 2012]:</u>

[^{11}C]AZD2184 (distribution volume ratio (*DVR*) = 1.7) showed relatively similar cortical binding to [^{18}F]flutafuranol (*DVR* = 1.6) in AD subjects. [^{18}F]flutafuranol had a *CUI* value of 4.74 and was ranked 4th, while [^{11}C]AZD2184 had a *CUI* value of 4.32 and was ranked 6th (Table 6.4). [^{18}F]flutafuranol and [^{11}C]AZD2184 showed relatively similar clinical usefulness, which was similar to *DVR* results reported by Forsberg et al.

<u>[^{11}C]BF227 vs. [^{18}F]FACT [Shidahara et al., 2015]:</u>

[^{11}C]BF227 showed greater significant differences in cortical *SUVR* values between HC and AD subjects than [^{18}F]FACT, which allowed for clearer differentiation of subject groups. [^{11}C]BF227 (*CUI* = 4.35, ranked 5th) had higher *CUI* value than [^{18}F]FACT (*CUI* = 3.97, ranked 9th) in our simulations (Table 6.4).

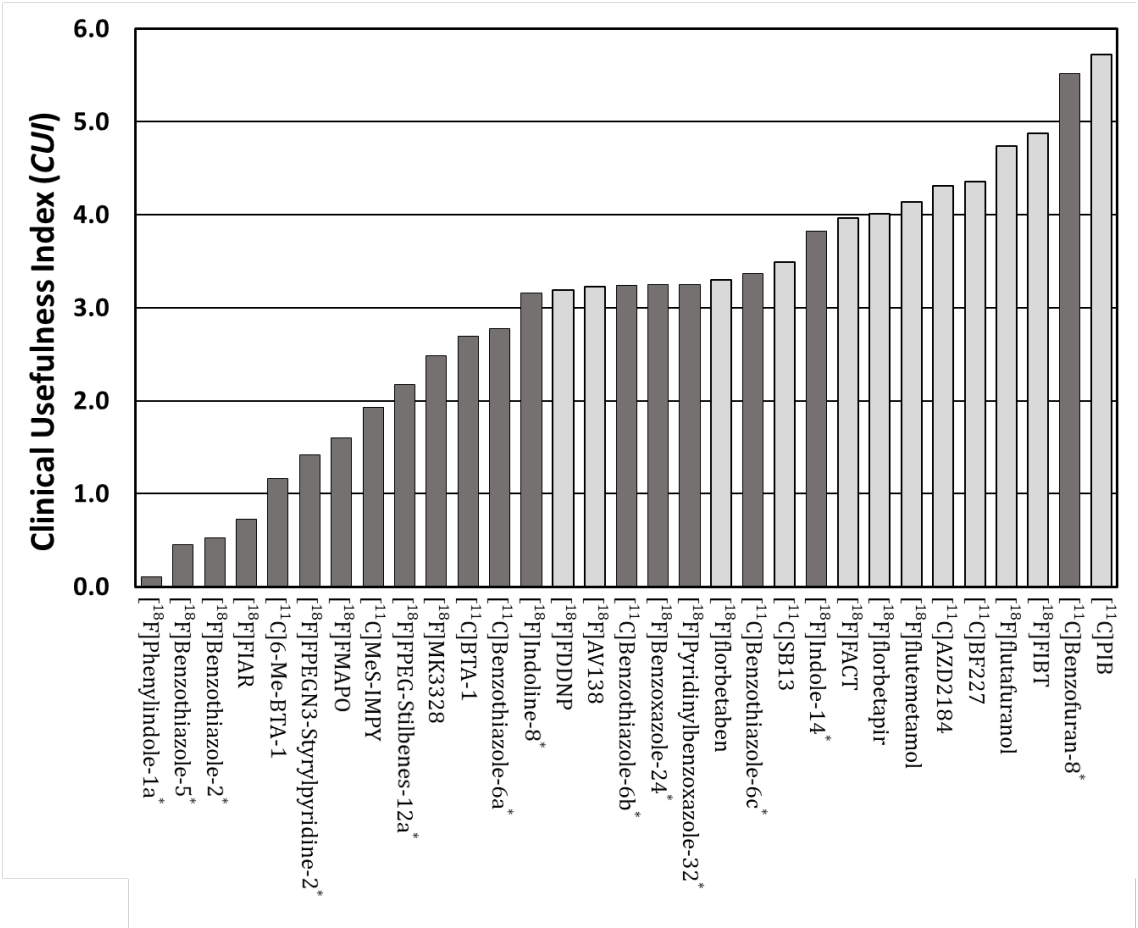

Figure 6.8: *CUI* distribution of 31 amyloid radiotracers. 12 clinically-applied amyloid radiotracers are shaded in light gray.

<u>[^{18}F]florbetapir vs. [^{18}F]AV138 [Carpenter et al., 2009]:</u>

[^{18}F]florbetapir and [^{18}F]AV138 showed similar *SUVR* values in precuneus, but [^{18}F]florbetapir was reported to have better pharmacokinetics and pharmacodynamics compared to [^{18}F]AV138 in the clinical trial**.** [^{18}F]florbetapir (*CUI* = 4.01, ranked 8th) also had higher *CUI* value than [^{18}F]AV138 (*CUI* = 3.22, ranked 17th) in our simulations (Table 6.4).

<u>[^{11}C]PIB vs. [^{18}F]flutemetamol vs. [^{18}F]florbetapir [Landau et al., 2014]:</u>

In terms of clinical cortical uptakes in MCI and AD subjects, [^{11}C]PIB was the highest, followed by [^{18}F]flutemetamol then [^{18}F]florbetapir, without partial volume correction. Likewise, our simulation results showed that [^{11}C]PIB had the highest *CUI* value of 5.72, followed by [^{18}F]flutemetamol (*CUI* = 4.13, ranked 7th) then [^{18}F]florbetapir (*CUI* = 4.01, ranked 8th) (Table 6.4).

The ranking of the *CUI* values of clinically-applied amyloid radiotracers reflected closely to their reported clinical results, attesting to the applicability of the screening methodology and the use of *CUI*, as a common index for evaluating the diagnostic capability of the amyloid radiotracers.

Table 6.4: *Az*, *Es* and *Sr* of conditions-pairs of HC-MCI and MCI-AD and *CUI* of 31 amyloid radiotracers.

Radiotracers	AUROC (*Az*)		Effect Size (*Es*)		*SUVR* ratio (*Sr*)		*CUI*
	HC-MCI	MCI-AD	HC-MCI	MCI-AD	MCI/HC	AD/MCI	
[^{11}C]PIB	0.979	0.995	2.96	3.64	1.68	1.83	5.72
[^{18}F]FDDNP	0.956	0.989	2.44	3.17	1.12	1.21	3.19
[^{11}C]SB13	0.977	0.992	2.79	3.40	1.11	1.19	3.50
[^{18}F]florbetaben	0.968	0.987	2.57	3.13	1.14	1.23	3.30
[^{11}C]BF227	0.981	0.992	2.95	3.46	1.30	1.46	4.35
[^{18}F]AV138	0.964	0.983	2.63	2.95	1.15	1.23	3.22
[^{18}F]flutemetamol	0.977	0.989	2.87	3.28	1.29	1.44	4.13
[^{18}F]florbetapir	0.977	0.993	2.78	3.44	1.23	1.38	4.01
[^{11}C]AZD2184	0.978	0.991	2.94	3.26	1.33	1.50	4.32
[^{18}F]flutafuranol	0.985	0.993	2.94	3.39	1.42	1.61	4.74
[^{18}F]FACT	0.973	0.992	2.66	3.40	1.25	1.42	3.97
[^{18}F]FIBT	0.981	0.991	2.97	3.37	1.49	1.62	4.87
[^{11}C]6-Me-BTA-1	0.774	0.885	1.03	1.74	1.01	1.03	1.17
[^{11}C]BTA-1	0.945	0.981	2.20	3.07	1.04	1.07	2.68
[^{18}F]FMAPO	0.840	0.927	1.39	2.07	1.03	1.06	1.59
[^{18}F]FPEG-Stilbenes-12a*	0.910	0.958	1.85	2.50	1.05	1.10	2.18
[^{11}C]Benzofuran-8*	0.978	0.991	2.91	3.21	1.89	1.78	5.52
[^{18}F]FPEGN3-Styrylpyridine-2*	0.808	0.907	1.30	1.85	1.03	1.05	1.40
[^{11}C]MeS-IMPY	0.866	0.963	1.62	2.45	1.02	1.05	1.93
[^{18}F]Indole-14*	0.977	0.984	2.89	3.00	1.27	1.35	3.77
[^{18}F]Indoline-8*	0.958	0.985	2.45	3.03	1.11	1.19	3.06
[^{11}C]Benzothiazole-6a*	0.943	0.984	2.29	3.05	1.05	1.10	2.77
[^{11}C]Benzothiazole-6b*	0.967	0.988	2.67	3.23	1.09	1.16	3.24
[^{11}C]Benzothiazole-6c*	0.970	0.991	2.74	3.33	1.09	1.17	3.36
[^{18}F]Benzothiazole-2*	0.635	0.768	0.498	0.988	1.01	1.02	0.530
[^{18}F]Benzothiazole-5*	0.631	0.737	0.450	0.865	1.01	1.02	0.456
[^{18}F]MK3328	0.913	0.974	1.99	2.78	1.07	1.12	2.47
[^{18}F]FIAR	0.683	0.803	0.682	1.22	1.01	1.03	0.723
[^{18}F]Benzoxazole-24*	0.960	0.988	2.54	3.22	1.12	1.20	3.25
[^{18}F]Pyridinylbenzoxazole-32*	0.966	0.987	2.53	3.16	1.13	1.22	3.26
[^{18}F]Phenylindole-1a*	0.554	0.548	0.168	0.200	1.00	1.00	0.102

Az, *Es*, *Sr* and *CUI* are unitless.
*Simplified name with the compound number or alphabet, as reported in the literature, used when generic name or institute code name (supplied by the author) was not available.

6.3.3 Evaluation of *CUI*

CUI was derived from the product of $\overline{Az}$, $\overline{Es}$ and $\overline{Sr}$ of conditions-pairs of HC-MCI and MCI-AD using equation (66). The relationships of $\overline{Az}$, $\overline{Es}$ and $\overline{Sr}$ with *CUI* were different (Figures 6.9A to 6.9C), which suggested that the $\overline{Az}$, $\overline{Es}$ and $\overline{Sr}$ assessed different key properties of the

radiotracers. This was also observed from the differences in the ranking of the radiotracers based on $\overline{Az}$, $\overline{Es}$ and $\overline{Sr}$ (Table 6.4). For example, [^{18}F]flutafuranol was ranked the highest based on $\overline{Az}$, while [^{11}C]PIB was ranked the highest based on $\overline{Es}$ and [^{11}C]Benzofuran-8 was ranked as the highest based on $\overline{Sr}$.

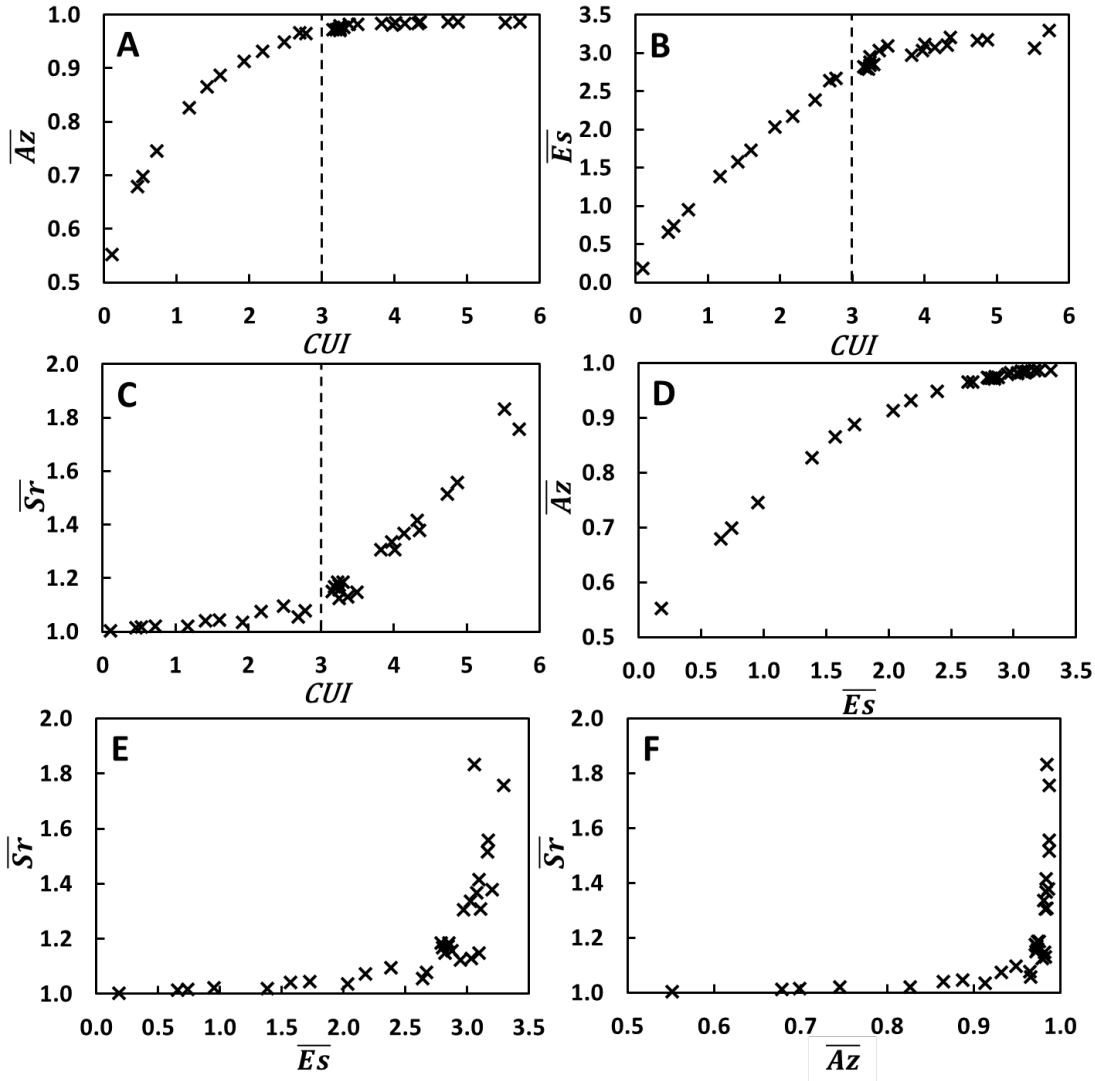

Figure 6.9: Relationships between (A) $\overline{Az}$ vs. *CUI*, (B) $\overline{Es}$ vs. *CUI*, (C) $\overline{Sr}$ vs. *CUI*, (D) $\overline{Az}$ vs. $\overline{Es}$ (E) $\overline{Sr}$ vs. $\overline{Es}$ and (F) $\overline{Sr}$ vs. $\overline{Az}$, of 31 amyloid radiotracers

The rankings of *Az*, *Es* and *Sr* were also different between conditions-pairs of HC-MCI and MCI-AD (Table 6.4). This suggested possible differences in diagnostic capability of amyloid radiotracers at high and low amyloid loads. For instance, comparing [^{11}C]PIB and [^{11}C]Benzofuran-8, [^{11}C]PIB had higher *Az*, *Es* and *Sr* for conditions-pair of MCI-AD, while [^{11}C]Benzofuran-8 had higher *Az*, *Es* and *Sr* for conditions-pair of HC-MCI (Table 6.4). Therefore,

CUI was derived using conditions-pairs of HC-MCI and MCI-AD. The conditions-pair of HC-AD was excluded because of replication of results, and if used individually, it would not be able to differentiate the performance of the radiotracers at low and high amyloid loads.

Individual *Az*, *Es* and *Sr* were unable to evaluate the clinical usefulness of amyloid radiotracers. *Az* had the smallest range of values from 0.548 to 0.995 (Table 6.4), which resulted in many radiotracers having the same $\overline{Az}$ values. Clinical ROC analysis showed that clinically-applied radiotracers were able to diagnose subjects with high sensitivity and specificity (Table 6.2). Similarly, both individual and averaged *Az* calculated were relatively similar for all clinically-applied radiotracers, with high sensitivity and specificity (Table 6.4). As such, *Az* could not be used alone to evaluate the radiotracers. Although the range of values of *Es* of 0.168 to 3.64 was reasonably broad (Table 6.4), it only considered the strength of the differences between the measured outcomes (e.g. *SUVR*) of two conditions with respect to the variations in the measured outcomes. Likewise, *Sr*, which ranged from 1.00 to 1.89, only showed the magnitude of the differences in mean *SUVR* values between 2 conditions (Table 6.4).

The combination of *Az*, *Es* and *Sr* integrated their strengths, including statistical significance (mainly *Es*), sample variability (mainly *Az* and *Es*), and measurement precision (mainly *Az* and *Sr*) (Figure 6.10). Greater spread in $\overline{Az}$ and $\overline{Es}$ were observed when *CUI* was smaller than 3.0, while greater spread in $\overline{Sr}$ was observed when *CUI* was greater than 3.0 (Figure 6.9). The combination of *Az*, *Es* and *Sr* thus complemented each other and resulted in a broader range of *CUI* values of 0.10 to 5.72 (Table 6.4, Figure 6.8). This allowed for clear differentiation of the clinical usefulness of the amyloid radiotracers.

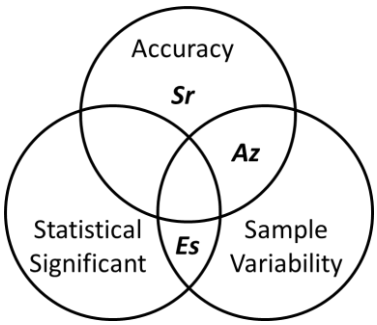

Figure 6.10: Relationship of the strengths of *Az*, *Es* and *Sr*.

6.4 Evaluation of Effects of Input on *CUI*

CUI is dependent on the inputs into the biomathematical model. From the results of sensitivity

analysis of the amyloid biomathematical, the model is highly sensitive to K_D. K_D is also the only *in vitro* input into the model and errors in K_D measurement were the greatest among the 6 physicochemical and pharmacological parameters. The effect of changes in K_D on outcome *CUI* was hence investigated. Effects of the input function, choice of the time window and changes in scaling factor on *CUI* were also investigated.

6.4.1 Effect of K_D on *CUI*

The K_D values for the list of 31 amyloid radiotracers (Table 5.7) were varied by ±20% and input into the amyloid biomathematical screening model (Figure 6.7) to simulate 1000 *SUVR* with noise and population variation. *SUVR* were obtained using the literature-stated time window for clinically-applied amyloid radiotracers and default time window for the candidate radiotracers. The resulting *SUVR* in HC, MCI and AD were then used to determine *Az*, *Es* and *Sr* and *CUI* in conditions-pairs of HC-MCI and MCI-AD.

The distribution of *CUI* values with ±20% change in K_D showed a similar trend to that without any variation (Figure 6.11). However, the ranking of radiotracers based on *CUI* was changed slightly within small groups of radiotracers whose ranking were originally close to each other (Figure 6.11). This showed the small effect of population variation in outcome measurement. Despite the variations, *CUI* still showed reasonable consistency in the ranking results.

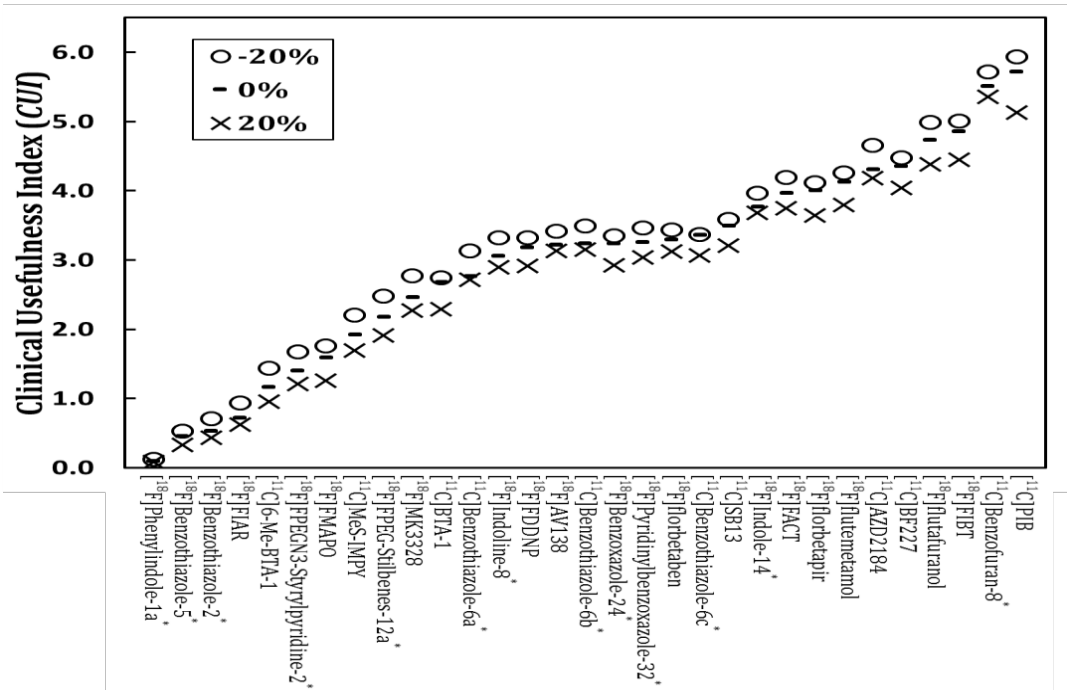

Figure 6.11: *CUI* values generated using original K_D values (0%, '-') and 20% reduction in K_D values (-

20%, ‘o’), and 20% increase in K_D values (+20%, ‘x’).

6.4.2 Effect of Input Function on *CUI*

To determine the effects of input function on *CUI* evaluation of radiotracer, 4 input functions of BF227-HC, BF227-AD, FACT-HC and FACT-AD were input into the amyloid biomathematical screening model. The same values for the 6 physicochemical and pharmacological parameters were applied (Table 5.7). Literature stated time window for clinically-applied amyloid radiotracers and default time window were applied for the candidate radiotracers for the list of 31 amyloid radiotracers. For each radiotracer, the standard deviation and mean of the resulting *CUI* obtained with the four different input functions were used to calculate the %*COV* of the *CUI*.

The %*COV* of the *CUI* values generated using the four input functions were less than 4.5% for all clinically applied radiotracers (Figure 6.12). Poor radiotracer, [^{18}F]FIAR had the largest %*COV* value of 13.4% due to its small *CUI* value (Figure 6.12). Small *CUI* values were not altered significantly despite large %*COV*. On the whole, the ranking of radiotracers would not be altered significantly with the use of different input functions from a subject injected with an amyloid radiotracer.

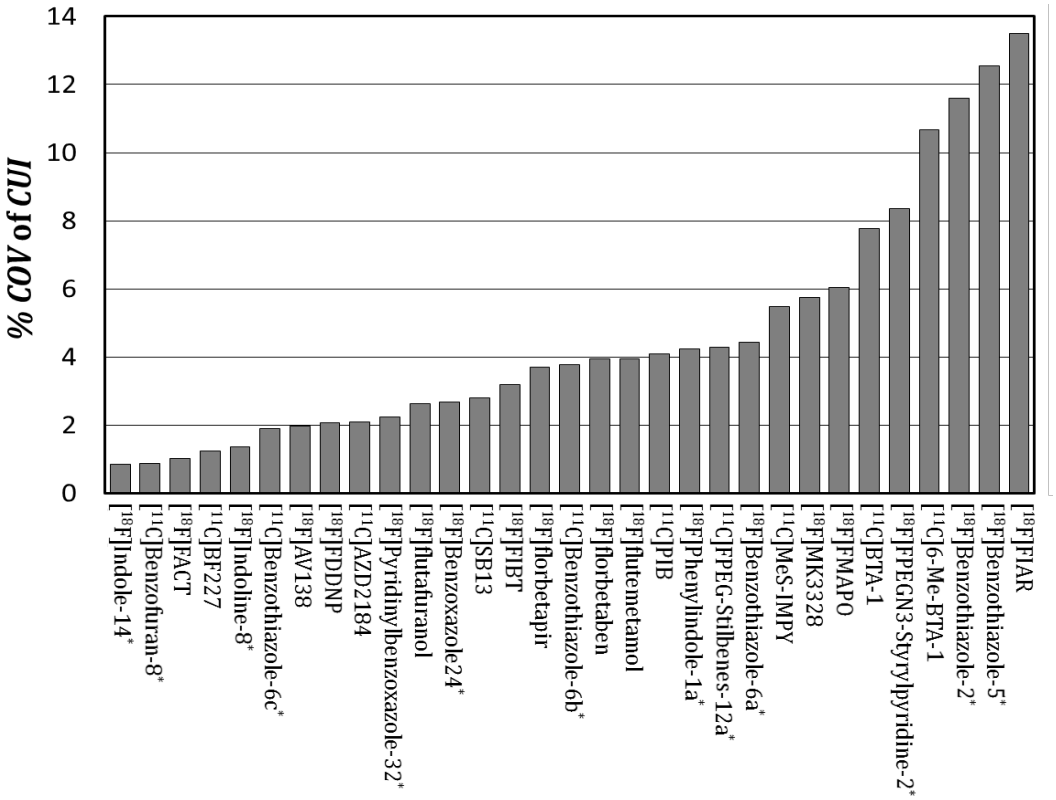

Figure 6.12: %*COV* of *CUI* values generated using BF227-HC, BF227-AD, FACT-HC and FACT-AD input

functions for the list of 31 amyloid radiotracers.

6.4.3 Effect of Time Window on *CUI*

To determine the effect of the use of default time window against literature-stated, optimised time window, *CUI* was simulated using the default time window of 40-60 min and literature-stated time window for 11 clinically-applied radiotracers. The same values for the 6 physicochemical and pharmacological parameters were applied (Table 5.7), with the default input function of BF227-HC. The % difference in *CUI* values determined using the default time window from that of the literature-stated time window was calculated. The *CUI* generated using both time windows are shown in Figure 6.13.

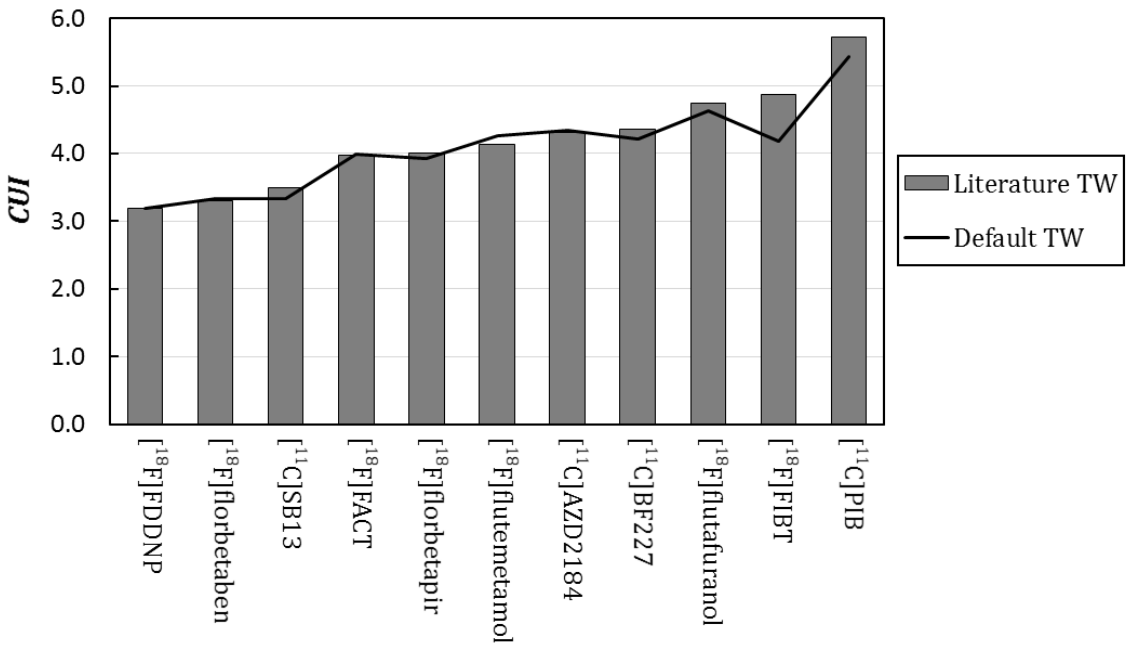

Figure 6.13: *CUI* distributions of 11 clinically-applied amyloid radiotracers, generated using literature-stated time window (box) and default time window of 40-60 min (-).

Table 6.5: % difference in *CUI* values generated using default time window from that of literature stated time window for 7 clinically-applied amyloid radiotracers.

Radiotracers	Time Window (min)	% Difference in *CUI*
[^{18}F]FIBT	70-90	-13.85
[^{11}C]SB13	40-120	-4.60
[^{18}F]flutemetamol	85-115	3.30
[^{18}F]flutafuranol	51-63	-2.45
[^{18}F]florbetapir	50-60	-2.02
[^{18}F]florbetaben	90-120	-1.10
[^{18}F]FDDNP	45-55	0.25

Out of the 11 clinically-applied radiotracers, 7 had *SUVR* values determined using different time window from the default time window of 40-60 min (Table 6.5). These 7 radiotracers had small differences in *CUI* values of less than 5%, except for [^{18}F]FIBT, which had a huge difference in *CUI* value of -13.85% (Table 6.5). This was probably due to the greater change in the shape of the TAC due to its higher binding capability at high amyloid load. However, small differences in *CUI* and in the ranking of *CUI* could also result from population variation. The changes in *CUI* was more prominent for radiotracer with a higher binding capability (Figure 6.13, Table 6.5). Therefore, the % difference in *CUI* was the greatest for [^{18}F]FIBT. On the whole, the % difference in *CUI* was small for the 7 clinically-applied radiotracers, hence the use of default time window of 40-60 min would not affect the evaluation of *CUI* significantly.

6.4.4 Effect of Scaling Factor on *CUI*

The scaling factors of K_1, k_2 and BP_{ND} will change the shape of the TACs, which in turn will affect the outcome *SUVR*. Although similar correlations between the predicted and clinically-observed *SUVR* were obtained using the new scaling factors determined using AD kinetic data (SF-AD), scaling factors determined using HC kinetic data (SF-HC) and original scaling factor determined by Guo et al [2009] (SF-Guo) (Figures 5.4, 5.5 and 5.9), it is also important to determine the effect of scaling factors on *CUI*. *CUI* was simulated using literature-stated time window for 11 clinically-applied radiotracers. The same values for the six physicochemical and pharmacological parameters were applied (Table 5.7*),* with a default input function of BF227-HC. The scaling factors were changed to SF-HC or SF-Guo accordingly.

The ranges of *CUI* using SF-Guo and SF-HC were 0.41~8.01 and 0.59~7.34 (Table 6.6), while that of SF-AD was 0.10~5.72 (Table 6.4). Although the maximum *CUI* were greater using SF-Guo and SF-HC, the differences in *CUI* values were 6.31 and 5.35 respectively (Table 6.6), which were larger slightly greater than that of the original of 5.26 (Table 6.4) if [^{18}F]Phenylindole-1a was removed. The ranges of $\overline{Az}$, $\overline{Es}$ and $\overline{Sr}$ were 0.667~0.989, 0.613~3.25 and 1.01~2.54 respectively using SF-Guo, while they were 0.715~0.988, 0.812~3.25 and 1.02~2.42 respectively using the SF-HC (Table 6.6). The ranges of $\overline{Az}$, $\overline{Es}$ and $\overline{Sr}$ were 0.551~0.989, 0.184~3.30 and 1.00~1.83 using the SF-AD (Table 6.4). The spread of $\overline{Az}$ and $\overline{Es}$ were greater using the SF-AD compared to SF-Guo or SF-HC, while the spread of $\overline{Sr}$ were greater using SF-Guo followed by SF-HC. The contribution of $\overline{Sr}$ to *CUI* was greater using SF-Guo and SF-HC. The range of $\overline{Az}$

was limited from 0~1.0, while $\overline{Es}$ was limited from 0 to about 3.25. The recommended minimum *CUI* was also changed from 3.0 (Table 6.4) to 4.1 and 4.4 using the SF-Guo and SF-HC (Table 6.6). The increase in the values of *CUI* and differences in ranking were probably caused by the increased contribution of $\overline{Sr}$ to *CUI*.

Table 6.6: Averaged *Az*, *Es*, *Sr* and *CUI* calculated from *SUVR* simulated using scaling factors determined using HC kinetic data (SF-HC) and Guo's scaling factors (SF-Guo).

Radiotracers	SF-HC				SF-Guo			
	Az	*Es*	*Sr*	*CUI*	*Az*	*Es*	*Sr*	*CUI*
[^{11}C]PIB	0.985	3.08	2.41	7.34	0.989	3.25	2.36	7.59
[^{18}F]FDDNP	0.984	3.08	1.55	4.69	0.982	3.06	1.37	4.12
[^{11}C]SB13	0.985	3.11	1.50	4.58	0.983	3.09	1.35	4.12
[^{18}F]florbetaben	0.980	2.93	1.55	4.45	0.981	3.06	1.47	4.42
[^{11}C]BF227	0.987	3.22	1.99	6.33	0.983	3.08	1.73	5.23
[^{18}F]AV138	0.982	3.01	1.57	4.64	0.985	3.08	1.48	4.49
[^{18}F]flutemetamol	0.988	3.23	2.02	6.45	0.983	3.06	1.84	5.52
[^{18}F]florbetapir	0.987	3.12	1.84	5.66	0.981	3.02	1.63	4.82
[^{11}C]AZD2184	0.986	3.17	2.14	6.68	0.984	3.05	1.79	5.38
[^{18}F]flutafuranol	0.985	3.25	2.24	7.16	0.984	3.07	1.95	5.88
[^{18}F]FACT	0.981	3.06	1.95	5.86	0.985	3.06	1.65	4.95
[^{18}F]FIBT	0.969	2.80	1.93	5.24	0.987	3.22	2.09	6.64
[^{11}C]6-Me-BTA-1	0.970	2.70	1.08	2.82	0.944	2.31	1.05	2.28
[^{11}C]BTA-1	0.985	3.09	1.20	3.66	0.978	2.96	1.12	3.26
[^{18}F]FMAPO	0.976	2.81	1.18	3.25	0.961	2.71	1.14	2.96
[^{18}F]FPEG-Stilbenes-12a*	0.979	2.86	1.28	3.57	0.979	2.93	1.23	3.52
[^{11}C]Benzofuran-8*	0.974	2.84	2.33	6.44	0.986	3.19	2.54	8.01
[^{18}F]FPEGN3-Styrylpyridine-2*	0.966	2.58	1.17	2.91	0.974	2.84	1.17	3.23
[^{11}C]MeS-IMPY	0.978	2.97	1.14	3.32	0.975	2.78	1.09	2.97
[^{18}F]Indole-14*	0.981	2.98	1.79	5.24	0.981	3.04	1.74	5.20
[^{18}F]Indoline-8*	0.986	3.14	1.49	4.63	0.985	3.09	1.36	4.15
[^{11}C]Benzothiazole-6a*	0.983	3.09	1.27	3.86	0.984	3.07	1.17	3.55
[^{11}C]Benzothiazole-6b*	0.983	3.04	1.42	4.25	0.986	3.13	1.27	3.91
[^{11}C]Benzothiazole-6c*	0.986	3.16	1.43	4.46	0.989	3.19	1.27	4.02
[^{18}F]Benzothiazole-2*	0.937	2.22	1.08	2.24	0.895	1.81	1.05	1.70
[^{18}F]Benzothiazole-5*	0.922	2.03	1.06	1.99	0.899	1.91	1.05	1.81
[^{18}F]MK3328	0.984	3.09	1.37	4.15	0.984	3.08	1.23	3.72
[^{18}F]FIAR	0.962	2.57	1.10	2.71	0.934	2.30	1.08	2.32
[^{18}F]Benzoxazole-24*	0.983	3.10	1.52	4.65	0.982	3.03	1.33	3.96
[^{18}F]Pyridinylbenzoxazole-32*	0.984	3.14	1.57	4.86	0.984	3.12	1.37	4.20
[^{18}F]Phenylindole-1a*	0.715	0.812	1.02	0.59	0.667	0.613	1.01	0.41

*Simplified name with the compound number or alphabet, as reported in the literature, used when generic name or institute code name (supplied by the author) was not available.

The ranking of the radiotracers was different within small groups, such as the flat region (highlighted area of Figure 6.14), poor and good radiotracers. For both sets of scaling factors, [^{18}F]FDDNP showed better performance than [^{11}C]SB13 and for SF-HC, [^{18}F]FDDNP had higher *CUI* than [^{18}F]florbetaben. [^{11}C]Benzofuran-8 and [^{18}F]FIBT had very different *CUI* rankings, which showed that their simulated *SUVR* were very susceptible to changes in the shape of the TACs. The ranking of *CUI* generated using the new scaling factors (SF-AD) was more consistent

with literature-reported results. Moreover, the contributions of *Az*, *Es* and *Sr* to *CUI* were more evenly distributed. However, the different *CUI* results generated using different scaling factors showed that *CUI* was dependent on the model used to derive the outcome parameter of interest.

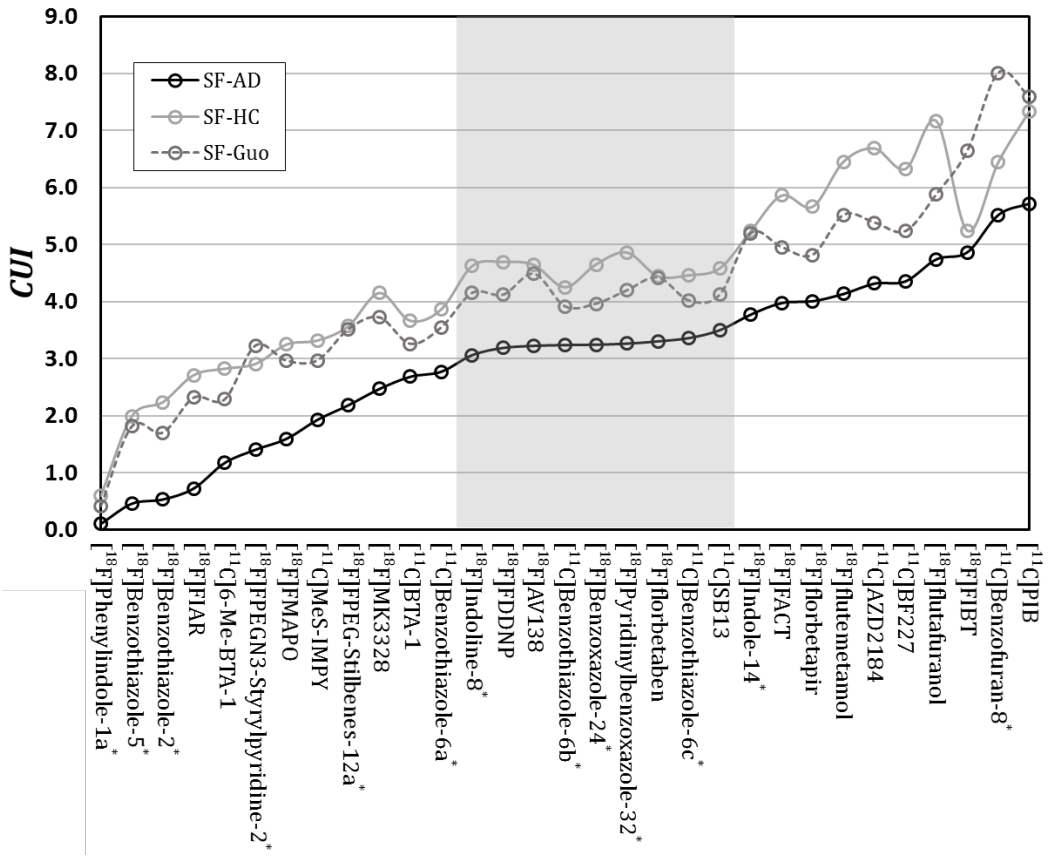

Figure 6.14: *CUI* distribution of 31 amyloid radiotracers, simulated using scaling factors determined using HC kinetic data (SF-HC) and Guo's scaling factors (SF-Guo). The black line represents the *CUI* distribution of the respective radiotracers based on the new scaling factors determined using AD kinetic data (SF-AD). The shaded area highlights the flat region of *CUI* distribution.

6.5 Limitations of Screening Methodology with *CUI*

The amyloid biomathematical model assumes passive diffusion, therefore the model may not work well for amyloid radiotracers that are actively transported across the BBB by transport proteins (e.g. P-glycoprotein (P-gp) substrates) [Guo et al., 2009]. However, the clinically-applied amyloid radiotracers used for the current evaluation showed good correlation between predicted and clinically observed K_1 and k_2 values. This showed that these radiotracers were transported across the BBB by passive diffusion.

CUI was defined to judge the clinical usefulness of a radiotracer, based on its cortical Aβ binding capability. Therefore, the screening methodology with *CUI* could not be used to differentiate radiotracers that showed white matter retention. The screening methodology with *CUI* also could not be used to predict binding to off-target, as observed for THK tau radiotracers. Possible binding to target needs to be known through *in vitro* binding assays. It is impossible to predict binding to off-target during the compound development of both radiotracers and drugs unless the chemical structure of the protein, receptors or any target sites are known and the chemical structure of the candidate compound was known to bind or interact with the target.

The current list of *CUI* values was determined using K_D or K_i values obtained from the various literature. Although K_D is the only *in vitro* input, it is the most sensitive input parameter in the amyloid biomathematical model, followed by f_{ND}, B_{avail}, M*LogP*, f_P then V_x (Figures 5.18-5.23). Changes in 20% in K_D values resulted in less than 6%, 16% and 20% in differences in *SUVR* values in HC, MCI and AD conditions (Figure 5.23) and small changes in *CUI* values (Figure 6.11). The other parameters were *in silico* parameters, hence they will not contribute significant errors to the screening methodology. The K_D or K_i values measured using brain homogenates were said to differ from that measured using synthetic Aβ fibrils [Mathis et al., 2003; Klunk et al., 2005], though some had claimed that there were no differences in measured values [Klunk et al., 2003]. In addition, the radiotracers also bind with different affinities to different binding sites on the Aβ fibrils [Agdeppa et al., 2009, Lockhart et al., 2005]. Despite these issues, reasonable comparison of radiotracers can be achieved by using K_D values measured using the same experimental protocol within an institution.

Amyloid radiotracers such as [^{11}C]PIB, [^{11}C]BF227 and [^{18}F]FDDNP had been reported to bind to neurofibrillary tangles [Harada et al., 2013]. As [^{18}F]FDDNP had a lower binding affinity for amyloid fibrils, it showed lower cortical uptake in AD [Thompson et al., 2009]. The amyloid biomathematical model did not include the effect of tau binding on the binding performance of the amyloid radiotracers. Despite the use of only K_D values of Aβ fibrils, the rankings of *CUI* values of clinically-applied amyloid radiotracers (Figure 6.8, Table 6.4) reflected well with reported clinical results. Therefore, the model showed applicability in evaluating the clinical usefulness of amyloid radiotracers. For proper application of the screening methodology with *CUI*, *in vitro* binding studies to both Aβ fibrils and tau protein, and comparison of *CUI* values with one clinically-applied amyloid radiotracer (e.g. [^{11}C]PIB) are recommended. This ensures accurate and comparable *CUI* values in evaluating the performance of amyloid radiotracers during

radiotracer development.

6.6 Summary of Use of *CUI*

On the whole, *CUI* was most affected by the scaling factors used but was less affected by K_D, choice of the time window and the input function used. This was due to the greater contribution of *Sr* to *CUI* due to the changes in *SUVR* values. Therefore, using the appropriate scaling factors is important in ensuring accurate interpretation of *CUI*. The small changes in *CUI* due to K_D, choice of the time window and the input function used showed consistency and reliability in the use of *CUI* in evaluating the radiotracers. Moreover, *CUI* showed the greatest discrimination power compared to other combinations or evaluation methods in terms of *SUVR*. The ranking of the CUI values of clinically-applied amyloid radiotracers reflected closely to their reported clinical results and hence *CUI* showed potential in radiotracer evaluation. As the predicted kinetic parameters and *SUVR* showed good correlations with clinically-observed values and the ranking of *CUI* was close to literature-reported results, the model was optimised for evaluating amyloid radiotracers.

CUI can be used to screen multiple candidate radiotracers simultaneously and rapidly during radiotracer development. In addition, *CUI* allows for the comparison of candidate radiotracers with clinically-applied radiotracers. This will assist decision-making in moving candidate radiotracers to clinical applications.

6.7 RSwCUI Software

A software written in Matlab was developed based on the proposed biomathematical screening methodology with *CUI*. It comes as a free package with a user manual and a Microsoft excel template for batch processing. The software is named RSwCUI, which is short for Radiotracer Screening with *CUI* (Figure 6.15).

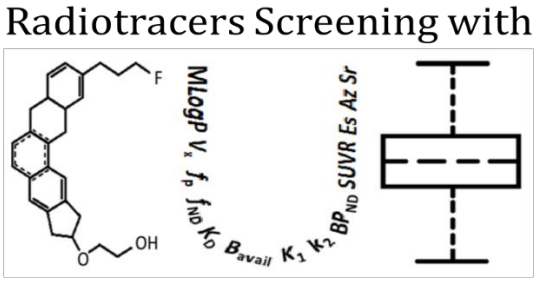

Figure 6.15: Logo of RSwCUI software.

RSwCUI can be run on Matlab by clicking on “RSwCUI.m” followed by “Run”

button or by typing RSwCUI on the Command window if the software folder directory had been added to the program path. A simple graphical user interface (GUI) will be displayed with the default Options settings applied automatically. The GUI consists of 8 parts as shown in Figure 6.16.

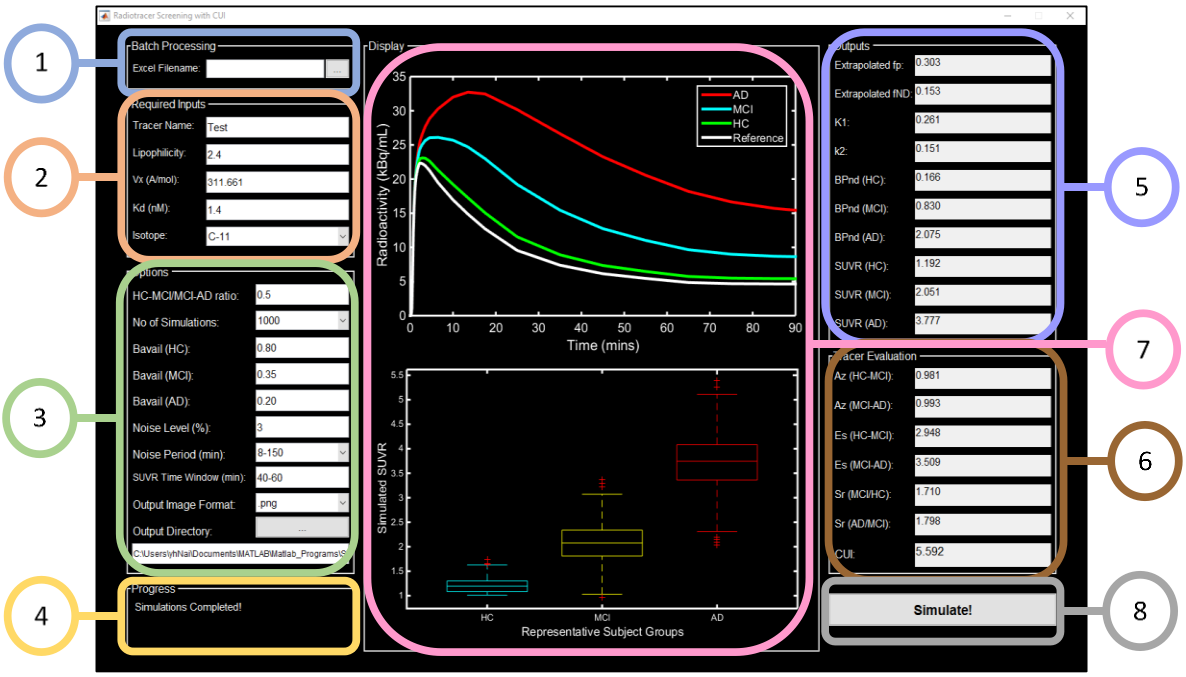

Figure 6.16: RSwCUI GUI: (1) Batch Processing, (2) Required Inputs, (3) Options, (4) Progress panel, (5) Outputs of K_1, k_2, BP_{ND} and *SUVR* at representative amyloid loads for HC, MCI and AD conditions, (6), tracer evaluation results with CUI based on population simulation with noise, (7) Results display and (8) Simulate Button.

(1) Batch Processing

An excel template with the required inputs will be provided with the program. The inputs required are the same as that listed under the “Required Inputs”. The user can click on the […] button and a file directory will prompt the user to select the required excel file.

(2) Required Inputs

The user can choose to evaluate one radiotracer at a time or carry out batch processing by filling in the excel template provided. For each radiotracer, only 5 inputs are required:

(1) Name of the chemical compound for ease of reference, especially in batch processing

(2) Lipophilicity (M*LogP*), determined from dproperties (Talete, Italy).
(3) Molecular volume (V_x), determined from dproperties (Talete, Italy).
(4) Dissociation constant (K_D) as measured by *in vitro* binding assay.
(5) Isotope of the radiotracer (C-11 or F-18)

If the batch processing excel file is selected, the user does not need to fill in the required input. The inputs will be automatically filled in from the excel file. The software will prompt users of any unfilled or incorrect forms of input in the excel file in the "Progress" panel.

(3) Options

The user can choose to change the Options settings depending on the type of radiotracers they want to evaluate. Default settings are recommended if users are uncertain about the amount of population variation etc. The user should select the output directory desired, otherwise it will be automatically saved into the program folder.

(4) Progress Panel

The panel shows the simulation progress and prompts for any errors.

(5) Outputs (K_1, k_2, BP_{ND} and *SUVR*)

The predicted 1TCM kinetic parameters (K_1, k_2, BP_{ND_HC}, BP_{ND_MCI}, BP_{ND_AD}) and *SUVR* values at the representative amyloid loads for HC, MCI and AD conditions will be displayed.

(6) Tracer Evaluation

Az, *Es* and *Sr* for subject-conditions pairs of HC-MCI and MCI-AD and outcome *CUI* will be displayed after 1000 *SUVR* simulations with population variation and noise for each subject conditions of HC, MCI and AD.

(7) Display

The time activity curves at representative amyloid loads for HC, MCI and AD conditions will be displayed (Top of Figure 6.17). After the completion of all simulation for one radiotracer, the *SUVR* distributions across subject conditions of HC, MCI and AD will be displayed (Bottom of Figure 6.17). For batch processing, the same figures will be displayed at the end of each radiotracer. At the end of batch processing, the *CUI* distribution for all radiotracers evaluated will be displayed (Figure 6.18).

(8) Simulate Button

The user only needs to click on the "Simulate" button to begin individual radiotracer evaluation or batch processing.

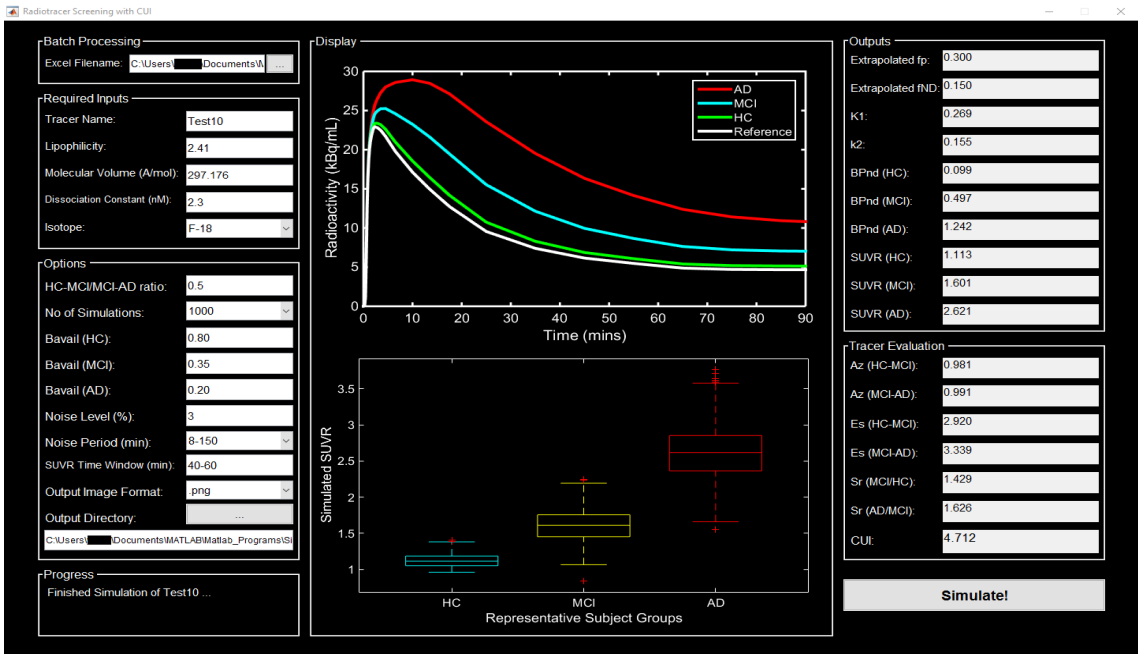

Figure 6.17: RSwCUI GUI: Results displayed at the completion of a single radiotracer evaluation.

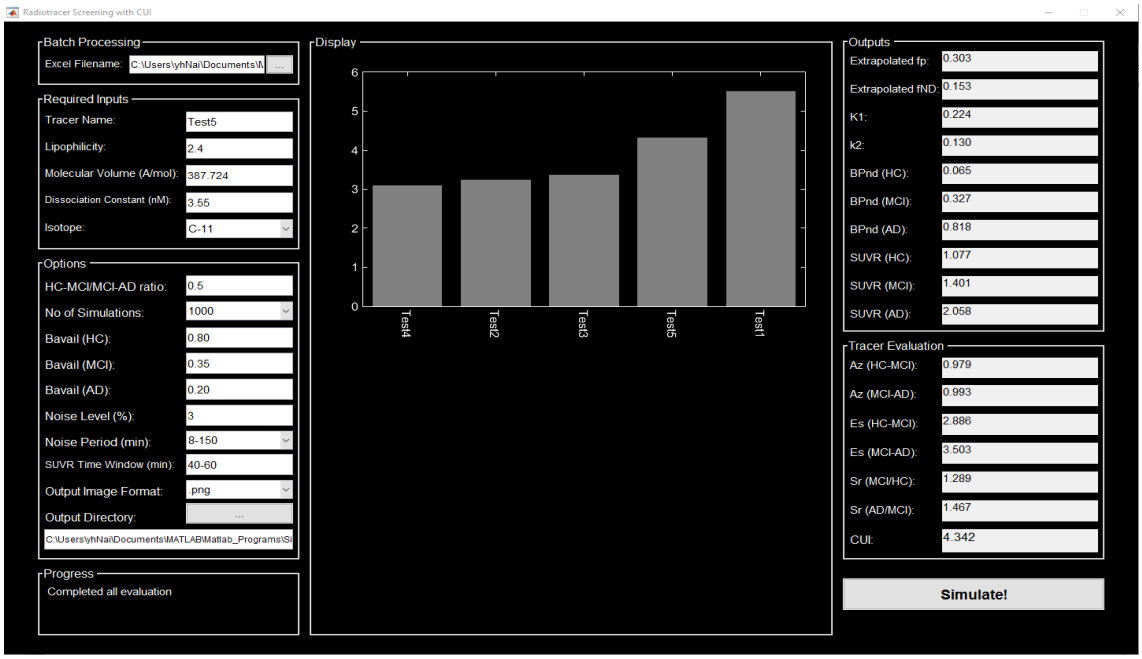

Figure 6.18: RSwCUI GUI: *CUI* distribution of evaluated tracers is displayed at the end of batch processing. The values displayed in the outputs and tracer evaluation column referred to the values of the last radiotracer.

Outputs of the radiotracer evaluation will be saved into folders named after the name of the radiotracer in the selected output directory. The images displayed in “Display” panel will be saved in “.png” format. Outputs listed in the “Output” and “Tracer Evaluation” panels will be compiled together and saved in an excel file.

6.8 Summary

A screening methodology with *CUI* was developed using the proposed amyloid biomathematical model with noise simulation and population variation to evaluate the potential diagnostic capability of an amyloid radiotracer during radiotracer development. The use of biomathematical model helps to predict the possible *in vivo* pharmacokinetics of the radiotracer, while the application of *CUI* serves as a common index to evaluate the diagnostic capability of the radiotracers across subject conditions. *CUI* is defined as the diagnostic capability of a radiotracer to differentiate the subject conditions and is obtained from the product of the averaged *Az*, *Es* and *Sr* of conditions-pairs of HC-MCI and MCI-AD. It showed the greatest differences across subject conditions compared to other combinations or evaluation methods. *CUI* allows for the comparison of multiple candidate radiotracers, as well as clinically-applied radiotracers, which will help to support decision making in moving candidate radiotracers to clinical application. The ranking of the *CUI* of clinically-applied amyloid radiotracers reflected close to their reported clinical results, attesting to the applicability of the screening methodology with *CUI* in screening candidate amyloid radiotracers.

The developed software based on the proposed screening methodology with *CUI* serves as a tool to support the development of amyloid radiotracers especially during the design of compounds in the early phases of radiotracer development. The proposed screening methodology with *CUI* can be extended to other types of radiotracers with similar binding characteristics such as tau radiotracers. However, the extension of the screening methodology with *CUI* to tau radiotracers needs to be further evaluated.

Chapter 7

Extending Screening Methodology to Tau

We have developed a screening methodology with *CUI* for evaluating the diagnostic capability of amyloid radiotracers during radiotracer development. Apart from amyloid radiotracers, tau radiotracers are currently being actively developed to support the diagnosis of AD and other tau-related dementia. Therefore, we would like to determine the feasibility of extending the developed amyloid biomathematical screening methodology in predicting the *in vivo* kinetic parameters and *SUVR* to support the screening of tau radiotracers.

This chapter focuses on evaluating the feasibility of extending the screening methodology with *CUI* in screening the diagnostic capability of tau radiotracers. The chapter starts with the introduction of the current issues faced in tau imaging, followed by the presentation of *in vitro* data of tau radiotracers and clinical data of clinically-applied tau radiotracers. The feasibility of extending the screening methodology to tau radiotracers is investigated using 22 radiotracers: 8 clinically-applied tau-focused, 3 clinically-applied but non-tau-focused and 11 candidates. The predicted kinetic parameters and *SUVR* values were compared with clinically-observed values and the ranking of *CUI* was compared with comparison results of clinically-applied tau radiotracers where applicable.

7.1 Tau Radiotracers

To determine whether a model developed for amyloid radiotracers can be extended to tau radiotracers, the differences between amyloid and tau radiotracers need to be identified. Problems faced in clinical studies with clinically-applied tau radiotracers are discussed in this section with a detailed explanation of the enantiomeric property of chiral chemical compounds, such as Tohoku University's THK tau radiotracers.

7.1.1 Issues with Existing Clinically-Applied Tau Radiotracers

The development of a successful tau radiotracer faces new challenges due to its binding target. In general, a good neuroimaging radiotracer needs to cross the BBB and has high binding affinity to

its target (section 3.3). Tau radiotracers, in addition, need to discriminate PHF-tau from other β-sheet structured aggregates such as Aβ and α-synuclein. Similar to Aβ, tau proteins also have various conformations due to the existence of six (3R and 4R) isoforms, and various post-translational modifications (section 2.1.2). Tau binding sites are present at smaller concentrations compared to Aβ binding sites by 5-20 folds, hence the selectivity of tau over other β-sheet structured aggregates needs to be high to ensure accurate quantification. Moreover, as tau proteins exist intracellularly, tau radiotracers not only need to cross the BBB, they also need to be able to cross the cell membrane.

Existing clinically-applied tau radiotracers showed some limitations. [^{11}C]PBB3 has high binding selectivity to tau over Aβ but it is difficult to synthesise as it is sensitive to photo-isomerization. Moreover, it is rapidly metabolised in the plasma, leading to limited entry into the brain [Hashimoto et al., 2014]. [^{18}F]T808 showed defluorination, which might affect the quantitative analysis of PET images [Declercq et al., 2016]. THK compounds (Tohoku University, Japan) showed differences in uptake due to enantiomeric properties, which need to be carefully prepared to ensure the synthesis of the targeted enantiomer [Tago et al., 2016]. Some THK compounds, [^{11}C]PBB3 and [^{18}F]T807 (also known as [^{18}F]flortaucipir) showed off-target binding [Harada et al., 2016; Maruyama et al., 2013; Lowe et al., 2016]. Subsequently, [^{18}F]THK5351 was showed to also bind to MAO-B enzymes [Ng et al., 2017]. [^{11}C]Astemizole and [^{18}F]Lansoprazole showed binding to tau proteins but are mostly applied in the treatment of allergies and gastrointestinal disorders respectively [Rojo et al., 2010]. [^{18}F]FDDNP was developed as an amyloid radiotracer but also showed some binding to tau proteins. Moreover, its metabolites also entered the BBB, which makes quantification difficult [Luurtsema et al., 2008].

As the enantiomeric property of a chemical compound affects its binding to the target, the next sub-section describe the different forms of a chemical compound and explain the meaning of enantiomeric property. This is important to ensure correct identification of chemical structures of enantiomeric tau radiotracers, especially THK compounds.

7.1.2 Chirality and Stereoisomers

Isomers are different compounds with the same molecular formula. Constitutional isomers are chemical molecules made up of the same atoms but are bonded together in different ways (Figure 7.1). Stereoisomers are compounds with the same molecular formula but differed from each other in structural configuration. They can be further classified as chiral or achiral, depending on the

presence of reflective symmetry element around one or more stereocenters or chiral centers (Figure 7.1). The summary of the different types of chemical compounds is shown in figure 7.1.

A chiral center is single carbon atom surrounded by four different substituents and is typically labelled with an asterisk. Thus, chiral compounds do not have any reflective symmetry elements and exist in pairs as non-superimposable mirror images of each other about the chiral center. Achiral compounds have an internal point or plane of symmetry, hence they are superimposable on its internal mirror image. Samples containing only a single stereoisomer are considered as enantiomerically pure. However, most processes result in a mixture of stereoisomers, known as a racemic mixture, which consists of two enantiomers in equal amount with zero net optical activity.

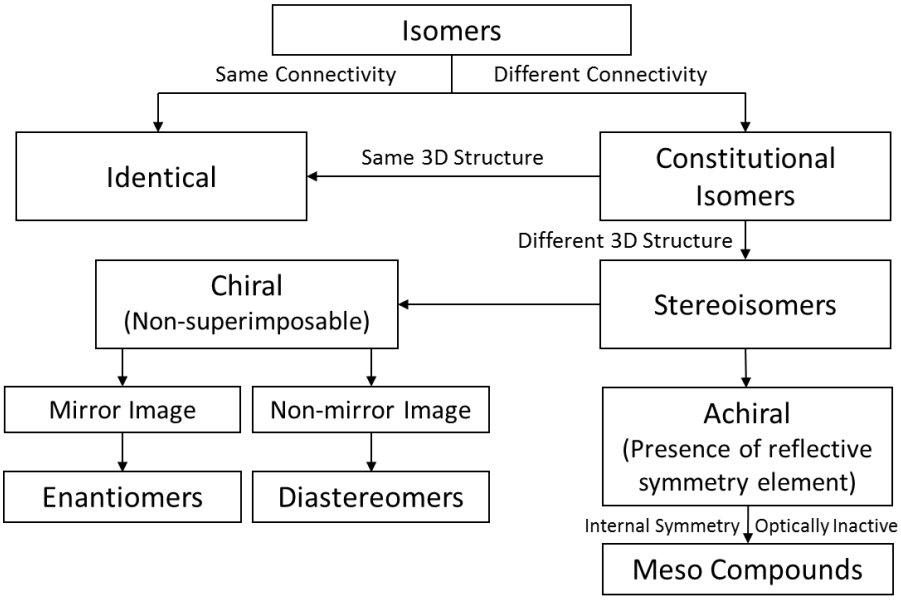

Figure 7.1: Classifications of chemical compounds.

Enantiomers exist as a pair of stereoisomers with the same chemical composition but with a non-superimposable mirror-image relationship. Their asymmetry structure around a chiral center resulted in “R” (+, clockwise, right-handedness) or “S” (-, counter-clockwise, left-handedness) handedness. R-enantiomer and S-enantiomer have the same physical properties (e.g. same melting point and solubility) and have exactly the same kinds of intermolecular attractions.

Stereoisomers that are not enantiomers are called diastereomers. These compounds have two or more chiral centers and are non-superimposable and non-mirror images of each other. They can have different physical properties and reactivity. An achiral form of a stereoisomer is called Meso compound. These compounds have an internal point or plane of symmetry and can be

superimposed on its mirror image. They are optically inactive and have different physical properties and reactivity compared to its equivalent enantiomers and diastereomers.

In cases where only one enantiomer of a pharmaceutical is likely to be therapeutically active or have higher binding affinity to target sites, asymmetric chemical synthesis strategies have been devised for preparing chemical compounds of only one enantiomer. These strategies are: (1) physical separation by temporarily converting the two enantiomers into two diastereomers; (2) physical separation in a chiral chromatographic environment; (3) chemical discrimination in a chiral environment, using enzymes or other chiral platforms as chemical reagents and (4) asymmetric synthesis of one enantiomer in preference to the other.

7.1.3 R-S Enantiomers

Cahn-Ingold-Prelog (CIP) rules, also known as *RS*-rules were instigated by three chemists: R.S. Cahn, C. Ingold, and V. Prelog. The *RS*-rules were used to unambiguously assign the *R* or *S* handedness of a molecule. The 3 basic steps to determine the *RS* configuration are as follows:

Step 1: Order the constituents surrounding the chiral carbon using CIP rules, from 1 (highest priority) to 4 (lowest priority).
CIP rule 1: Isotope substituents with higher atomic mass receives higher priority. (e.g. Br vs. Cl, Br has priority)
CIP rule 2: Molecular substituents with higher molecular mass receives higher priority.
CIP rule 3: Double bonds have higher priority than a single bond and are treated as a chiral carbon bonded to 2 carbons.
Step 2: Rotate the molecule such that substituent, with the least priority, points away from the viewer or is in the back (dashed line, Table 7.1).
Step 3: Draw an arrow from substituent with the highest priority to lowest priority. If the arrow is clockwise, the compound is an *R*-enantiomer; if the arrow moves counter-clockwise, it is an *S*-enantiomer.

Table 7.1: Basic chemical bond symbols

	Solid line indicates that the bond exists **in** the plane of the drawing surface.
	Dashed line indicates that the bond is extending **behind the plane** of the drawing surface.
	Bold-wedged line indicates that the bond is **protruding out** from the plane of the drawing surface.
	Wavy line indicates that the stereochemistry of the bond is **unknown**.
	Dotted line indicates that the bond is only a **partial bond** as in a hydrogen bond or a partially formed or broken bond in a transition state.

7.2 *In Vitro* & *In Vivo* Data of Tau Radiotracers

To determine if the previously developed amyloid biomathematical screening methodology could be extended to support the development of tau radiotracers, comparing the predicted kinetic parameters and *SUVR* values with clinically-observed values and comparing the TACs and *SUVR* distribution with clinically-observed data are important. However, tau clinical studies started in recent years and reported clinical data are limited. As such, the available *in vitro* and *in vivo* data of tau radiotracers are discussed in this section. 22 radiotracers reported to bind to tau proteins were investigated (Figure 7.2). The 8 clinically-applied tau-focused radiotracers include [^{18}F]THK523, [^{18}F]THK5105, [^{18}F]THK5117, [^{18}F]THK5317, [^{18}F]THK5351, [^{18}F]T807, [^{18}F]T808 and [^{11}C]PBB3. The 3 clinically-applied but non-tau-focused radiotracers are [^{11}C]Astemizole, [^{18}F]Lansoprazole and [^{18}F]FDDNP and the remaining are candidates.

7.2.1 *In Vitro* Data of Tau Radiotracers

In silico lipophilicity (M*LogP*) and McGowan volume (V_x) and *in vitro* dissociation constant (K_D) are required as inputs into the developed software, RSwCUI, to predict the outcome 1TCM kinetic parameters and *SUVR* values (Table 7.2). For each tau radiotracer, M*LogP* and V_x were determined using dproperties (Talete, Italy). K_D or K_i values were obtained from the literature, measured using either synthetic heparin-induced tau polymer (HITP) or AD human brain homogenates. However, unlike for amyloid radiotracers, K_D or K_i values measured using AD brain homogenates were selected instead of those measured using HITP. This is because HITP composed of only 3R and/or 4R, and hence may not undergo the same phosphorylation process as human tau [Okamura et al., 2013; Ariza et al., 2015]. As a result, K_D or K_i values differed greatly using synthetic tau and AD brain homogenates (Table 7.2). However, for [^{18}F]Lansoprazol, K_D values measured using synthetic tau was applied instead for comparison with [^{11}C]NML.

The values of B_{avail} set in the amyloid biomathematical model and RSwCUI software were determined using the concentrations of amyloid for HC, MCI and AD conditions. To determine if the values of B_{avail} was suitable for tau radiotracers, the tau concentrations for HC, MCI and AD conditions were extracted from the literature. However, the measurements of tau concentrations using ELISA faced considerable challenges: (1) presence of various post-translational forms of tau and phosphorylated sites (Mukaetova-Ladinska et al., 2015), (2) difficulty in dissolving the insoluble phosphorylated tau for measurement (Hashimoto et al., 1999) and (3) data are regional-dependent due to the progressive distribution of tau with disease progression (Han et al., 2017).

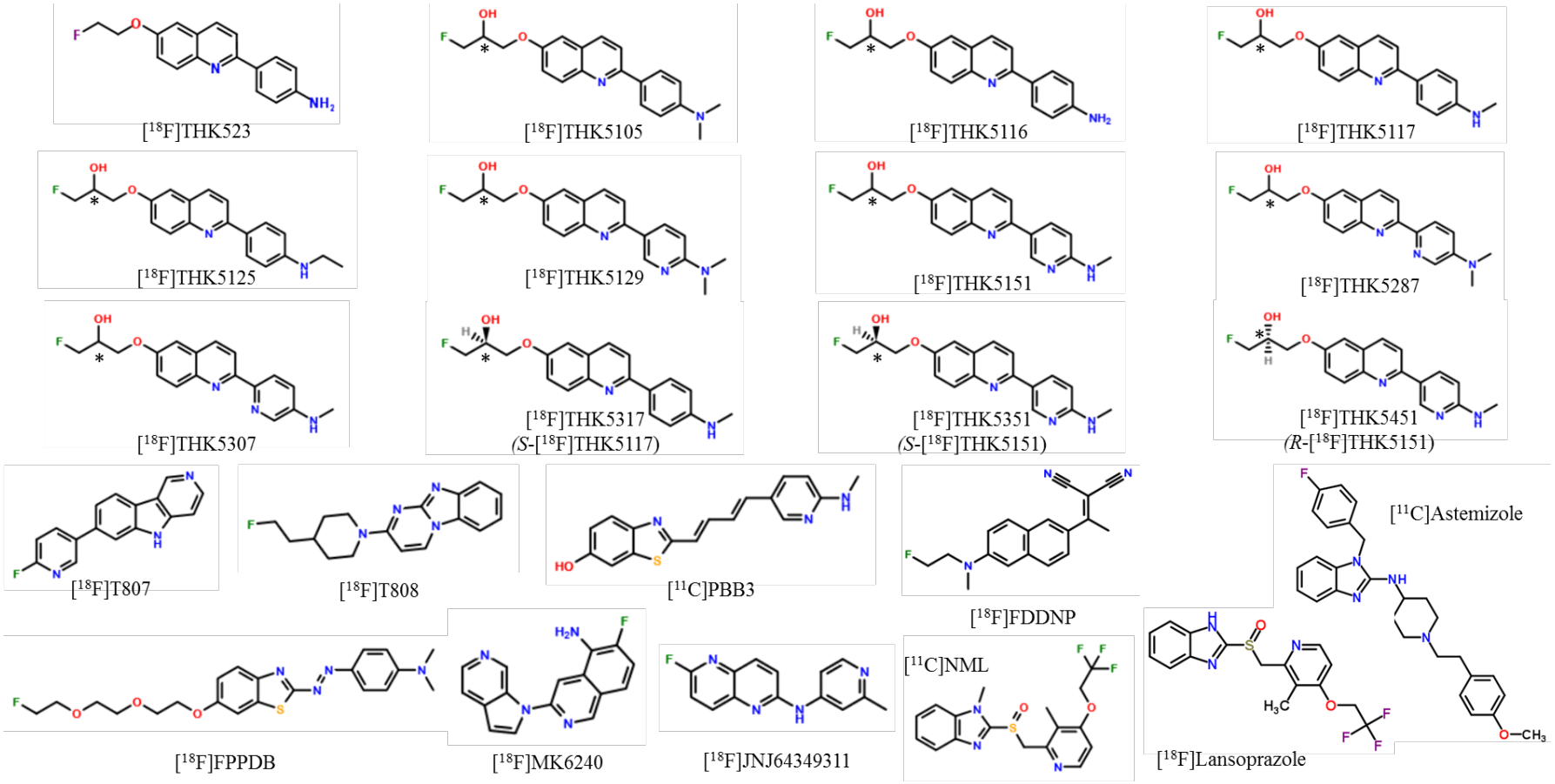

'*' refers to the chiral centers of enantiomeric compounds.

Figure 7.2: Chemical structures of 22 tau radiotracers.

In addition, the reported tau concentrations were mostly measured using the brains of normal aged controls and AD, with very little data on the tau concentrations in MCI. The comparison of ELISA measurements was difficult as different antibodies and technologies were applied since 1999.

Table 7.2: M*LogP*, V_x and K_D values of 22 tau-related radiotracers.

Radiotracers	M*LogP*	V_x	K_D	References for K_D
[^{18}F]THK523	3.19	2.11	1.67$^{\alpha}$	Fodero-Tavoletti et al., 2011
			1.99$^{\alpha}$	Harada et al., 2013
			86.5	Okamura et al., 2013
[^{18}F]THK5105	3.08	2.59	1.45$^{\alpha}$	Okamura et al., 2013
			2.63	
[^{18}F]THK5116	2.62	2.31	106$^{\&}$	Tago et al., 2016
[^{18}F]THK5117	2.85	2.45	2.65$^{\$}$	Lemoine et al., 2015
[^{18}F]THK5125	3.08	2.59	10.2	Tago et al., 2016
[^{18}F]THK5129	2.48	2.55	3.14	Tago et al., 2016
[^{18}F]THK5151	2.25	2.41	7.07	Tago et al., 2016
[^{18}F]THK5287	1.94	2.55	2.60	Tago et al., 2016
[^{18}F]THK5307	1.71	2.41	5.60	Tago et al., 2016
[^{18}F]THK5317	2.85	2.45	9.40$^{\&}$	Tago T., 2016
[^{18}F]THK5351	2.25	2.41	2.90	Harada et al., 2016
[^{18}F]THK5451	2.25	2.41	28.0	Tago et al., 2016
[^{18}F]T807	1.95	1.86	14.6$^{\#}$	Xia et al., 2013
[^{18}F]T808	3.64	2.23	22.0$^{\#}$	Declercq et al., 2016
[^{11}C]PBB3	2.34	2.31	2.50$^{\alpha}$	Kimura et al., 2015
			6.30	Ono et al., 2017
[^{18}F]FDDNP	2.89	2.31	36.7$^{\alpha}$	Harada et al., 2013
[^{18}F]FPPDB	2.87	3.15	44.8	Matsumura et al., 2011
[^{11}C]NML	1.98	2.51	0.700$^{\alpha}$	Fawaz et al., 2014
[^{18}F]Lansoprazol	1.75	2.37	3.30$^{\alpha}$	Fawaz et al., 2014
			>3998$^{\delta}$	Declercq et al., 2016
[^{11}C]Astemizole	4.63	3.56	13.4	Rojo et al., 2010
			1.86$^{\alpha}$	
			>3998$^{\delta}$	Declercq et al., 2016
[^{18}F]MK6240	2.49	1.96	0.260$^{\beta}$	Hostetler et al., 2016
[^{18}F]JNJ64349311 ([^{18}F]JNJ311)	2.07	1.83	7.90$^{\delta}$	Rombouts et al., 2017

Units: M*LogP* (Unitless), V_x (cm^3/mol/100), K_D (nM)
$^{\$}$Averaged K_D values (2.2, 3.1) for tau in AD brain homogenates of temporal and
$^{\beta}$Averaged K_D values 0.14, 0.30, 0.25, 0.24 and 0.38 for tau in AD brain homogenates of frontal and entorhinal cortex of 5 AD.

$^{\alpha}K_D$ values are measured using synthetic tau (K18Δ280K)
$^{\&}K_i$ values measured using AD brain homogenates with THK5105 as competitor
$^{\delta}K_i$ values measured using AD brain homogenates with T808 as competitor
$^{\#}K_D$ values measured using AD brain via autoradiography

The tau concentrations under HC, MCI and AD conditions are measured using ELISA but reported with different units of measurement based on the counting instruments used (Table 7.3). For MCI condition, only soluble tau concentration was reported. However, AD progression is caused by the accumulation of insoluble phosphorylated tau and tau radiotracers binds to insoluble phosphorylated tau in PET imaging. The concentrations of soluble tau under HC, MCI and AD conditions were very different in the frontal and temporal cortices (Table 7.3). Thus, the reported soluble tau concentrations could not be used to determine the values of B_{avail}.

Table 7.3: Measured tau concentrations under HC, MCI and AD conditions from the literature.

References	Biochemical Samples	Brain Regions	Concentrations of Tau			Ratio
			HC	MCI	AD	AD / HC
Herrmann et al., 1999	Phosphorylated tau (ng/ml)	Frontal Cortex	16 ± 2	-	316 ± 50	19.8
		Parietal cortex	14 ± 1	-	374 ± 46	26.7
		Hippocampus	89 ± 39	-	570 ± 35	6.40
		Cerebellum	16 ± 4	-	10 ± 1	0.625
Han et al., 2017	Soluble Tau (ng/mg of protein)	Frontal Cortex	61.96 ± 6.78	42.67 ± 3.28	51.31 ± 2.37	0.8
		Temporal cortex	592.6 ± 57.3	871.0 ± 42.8	874.5 ± 51.34	1.5
Mukaetova-Ladinska et al., 2015	Total Tau (Relative counts)	Frontal Lobe	40 ± 4	-	110 ± 27	2.8
		Temporal Lobe	172 ± 21	-	211 ± 4	1.2
	Phosphorylated Tau (Thr181) (Relative counts)	Frontal Lobe	40.57 ± 2.60	-	37.50 ± 4.91	0.9
		Temporal Lobe	36.87 ± 2.29	-	35.09 ± 2.11	1.0
	Phosphorylated Tau (Ser262) (Relative counts)	Frontal Lobe	7.99 ± 0.61	-	8.11 ± 0.31	1.0
		Temporal Lobe	4.53 ± 0.39	-	10.59 ± 1.89	2.3
	Phosphorylated Tau (Ser202/Thr205) (Relative counts)	Frontal Lobe	0.44 ± 0.04	-	0.65 ± 0.05	1.5
		Temporal Lobe	0.58 ± 0.02	-	0.83 ± 0.13	1.6

Antibodies Thr181, Ser262 and Ser202/Thr205 were used to detect three phosphorylated sites of tau, representing pretangle, matured tau and ghost tangles respectively (Mukaetova-Ladinska et al., 2015). Although the concentrations of more mature tau were higher in AD, the concentrations of pretangles were lower in AD compared to HC. The ratio of tau concentration in AD to that of HC differed with the brain regions and with the type of tau measured (Mukaetova-Ladinska et al., 2015). The results reported by Herrmann et al (1999) showed higher tau concentrations in AD in cortical regions but the AD/HC tau concentrations ratio in the various brain regions were very different from other reported data (Table 7.3). Due to the inconsistent AD/HC tau concentrations ratio, the values of B_{avail} based on tau concentrations could not be determined for simulations of tau radiotracers. As such, the default values of B_{avail} in RSwCUI, which were determined using amyloid concentrations under HC, MCI and AD conditions, are applied.

7.2.2 Clinical Data of Tau Radiotracers

The 1TCM kinetic parameters and *SUVR* values of clinically-applied tau radiotracers in HC and AD subjects were extracted from the literature. For *SUVR* correlations, 3 types of *SUVR* were employed: *SUVR* from the regions with the highest cortical *SUVR* in AD, greatest *SUVR* differences between HC and AD and *SUVR* of the hippocampus (Table 7.4). Thus far, kinetic analysis was carried out for [^{18}F]T807, [^{18}F]THK5317, [^{18}F]THK5351 and [^{11}C]PBB3 only.

For [^{18}F]THK5351, a regional k_2 value of 0.115 min^{-1} was obtained using SRTM [Lockhart et al., 2016]. For [^{18}F]THK5317, the 2TCM or SRTM were said to fit the data well [Jonasson et al., 2016]. K_1 and k_2 values of 0.33 mL/cm^3/min and 0.09 min^{-1} were obtained in the target region using the 2TCM with plasma input function of one subject [Jonasson et al., 2016]. Chiotis et al. [2016] determined *DVR* values using reference Logan graphical method as the arterial blood data was not measured. For our evaluation, a BP_{ND} value (*DVR*-1) of 0.60 was taken from the region with the highest value, Putamen [Chiotis et al., 2016].

For [^{18}F]T807, the averaged cerebellar K_1 and k_2 values of 0.26 mL/cm^3/min and 0.17 min^{-1} respectively were obtained by fitting the measured data to the 2TCM with a variable vascular fraction [Wooten et al. 2016]. For [^{11}C]PBB3, BP_{ND} values of HC and AD of -0.15 and 0.37 were obtained from original multilinear reference tissue model ($MRTM_0$) for our evaluation [Kimura et al., 2015].

7.3 Screening of Tau Radiotracers

Evaluation of the feasibility of extending the amyloid biomathematical model to tau radiotracers was carried out using the *in vitro* and *in vivo* data gathered for 22 tau radiotracers (8 clinically-applied tau-focused, 3 clinically-applied but non-tau-focused and 11 candidates). The three input parameters of M*LogP*, V_x and K_D (Table 7.2) were fed into RSwCUI to generate the predicted *in vivo* 1TCM parameters of K_1, k_2 and BP_{ND}, and *SUVR* under HC, MCI and AD conditions. The predicted *SUVR* was correlated with the three different types of clinically-observed *SUVR* (Table 7.4) using 8 clinically-applied tau radiotracers. The predicted K_1, k_2 and BP_{ND} values were compared with reported values where applicable. The TACs and *SUVR* distributions under HC, MCI and AD conditions were also shown. Finally, the radiotracers were compared using the *CUI* values generated.

Table 7.4: Three types of clinically-observed *SUVR* of 8 clinically-applied tau radiotracers: (1) the highest cortical *SUVR* in AD, (2) greatest *SUVR* differences between HC and AD and (3) *SUVR* of the hippocampus of 8 clinically-applied tau radiotracers.

Clinically-applied Radiotracers	Time Window (min)	Highest Cortical *SUVR*			Greatest *SUVR* Difference			*SUVR* (HIP)		References
		HC	AD	Target Region	HC	AD	Target Region	HC	AD	
[^{18}F]THK523	60-90	0.96	1.81	ITL	0.96	1.81	ITL	0.78	0.97	Villemagne et al., 2014
[^{18}F]THK5105	90-100	1.41	1.52	PU	1.09	1.32	ITL	-	-	Okamura et al., 2014
[^{18}F]THK5117	50-60	1.57	1.77	PU	1.15	1.61	ITL	1.35	1.57	Harada et al, 2015
[^{18}F]THK5351	50-60	2.14	2.98	HIP	1.41	2.27	PAR	2.14	2.98	Harada et al., 2016
[^{18}F]T807	80-100	1.17	2.19	ITL	1.17	2.19	ITL	1.39	1.31	Johnson et al., 2016
[^{18}F]T808	80-100	0.94	1.52	LTL	0.94	1.52	LTL	1.01	1.32	Chien et al., 2014
[^{11}C]PBB3	30-50	0.85	1.42	Global$^{\#}$	0.85	1.42	Global$^{\#}$	-	-	Kimura et al., 2015
[^{18}F]FDDNP	45-55	1.24	1.37	ACG	1.06	1.20	FC	-	-	Tauber et al., 2013

ITL = Inferior Temporal Lobe, LTL = Lateral Temporal Lobe, PU = Putamen, PAR = Parietal Lobe, HIP = Hippocampus
$^{\#}$Global = Cerebral cortex for HC and High binding ROI for AD

Table 7.5: Predicted K_1, k_2, BP_{ND} (HC and AD) and *SUVR* (HC and AD, Literature-stated, default time window of 40-60 min) of 9 clinically-applied tau radiotracers.

Clinically-applied Radiotracers	K_1 (mL/cm^3/ min)	k_2 (min^{-1})	BP_{ND} (unitless)		*SUVR* (unitless)		Time Window (min)	Simulated *SUVR* (Default)	
			HC	AD	HC	AD		HC	AD
[^{18}F]THK523	0.200	0.069	0.035	0.43	1.00	1.01	60-90	1.00	1.01
[^{18}F]THK5105	0.181	0.067	0.053	0.67	1.03	1.41	90-100	1.04	1.43
[^{18}F]THK5117	0.202	0.087	0.042	0.53	1.05	1.67	50-60	1.05	1.66
[^{18}F]THK5317	0.202	0.087	0.012	0.15	1.01	1.17	70-90	1.01	1.18
[^{18}F]THK5351	0.220	0.141	0.10	1.28	1.12	2.67	50-60	1.12	2.68
[^{18}F]T807	0.256	0.199	0.033	0.42	1.03	1.42	80-100	1.04	1.47
[^{18}F]T808	0.151	0.039	0.0010	0.0017	1.00	1.02	80-100	1.00	1.02
[^{11}C]PBB3	0.226	0.136	0.041	0.51	1.05	1.65	30-50	1.05	1.63
[^{18}F]FDDNP	0.209	0.088	0.003	0.036	1.00	1.04	45-55	1.00	1.04

7.3.1 Comparison of 1TCM Kinetic Parameters

For [^{18}F]T807, the predicted K_1 and k_2 of 0.256 and 0.199 were almost similar to the reported averaged cerebellar K_1 and k_2 of 0.26 and 0.17 (Table 7.6). For [^{18}F]THK5351, the predicted k_2 of 0.141 was slightly higher than the clinically-observed k_2 of 0.115 (Table 7.6). This may be due to the differences in binding of the enantiomeric tau radiotracers to plasma proteins [Itoh et al., 1997]. However, the predicted k_2 value of 0.087 of [^{18}F]THK5317, another *S*-enantiomeric compound, was close to the literature reported value of 0.09 (Table 7.6). On the other hand, the predicted K_1 value of 0.202 was smaller than the reported value of 0.33 obtained using 2TCM. The predicted BP_{ND} values of 0.15 and 0.51 were different from clinically-observed values of 0.60 and 0.37 in AD for [^{18}F]THK5317 and [^{11}C]PBB3 respectively (Table 7.6). The great differences in BP_{ND} values may be due the more complicated *in vivo* binding of tau radiotracers in the presence of other similar β-sheet structures (amyloid-β and α-synuclein).

Table 7.6: Predicted vs. clinically-observed K_1, k_2 and BP_{ND} of 4 tau radiotracers.

Radiotracers	Literature Reported Values				Predicted Values	%Diff
	Parameters	Region	Clinically-Observed Values	References		
[^{18}F]T807	K_1	Cerebellum Excluding Vermis	0.26	Wooten et al., 2016	0.256	-1.54
	k_2		0.17		0.199	17.1
[^{18}F]THK5351 (*S*-enantiomer of [^{18}F]THK5151)	k_2[‡]	Cerebellum	0.115	Lockhart et al., 2016	0.141	22.6
[^{18}F]THK5317 (*S*-enantiomer of [^{18}F]THK5117)	K_1	Target[δ]	0.33	Jonasson et al., 2016	0.202	-38.8
	k_2		0.09		0.087	-3.3
	BP_{ND} (AD)	Putamen	0.60*	Chiotis et al., 2016	0.15	-75.0
[^{11}C]PBB3	BP_{ND} (AD)	High-binding cortical regions	0.37[¶]	Kimura et al., 2015	0.51	37.8

#Global: Entorhinal cortex, Fusiform gyrus, Hippocampus, Inferior temporal gyrus, Lingual gyrus, Middle temporal gyrus, Parahippocampal gyrus, Anterior cingulate, Frontal lobe, Occipital lobe, Parietal lobe, Posterior cingulate gyrus, Precuneus, Brainstem, Caudate Nucleus, Cerebral white matter, Pallidum, Putamen, Thalamus, Cerebellar gray.

[δ]Target: Thalamus, putamen, hippocampus, amygdala, parietal cortex, frontal cortex, sensory motor cortex, occipital cortex, midbrain, entorhinal cortex, and temporal cortex.

*BP_{ND} = DVR - 1, where DVR was determined using reference Logan

[¶]BP_{ND} determined using $MRTM_0$

[‡]k_2 determined from SRTM for reference region of cerebellum

We are limited by the small number of reported kinetic parameters to fully determine the limitations of the amyloid biomathematical model. The prediction of K_1 and k_2 values of tau radiotracers appeared to work well in racemic compounds and slightly poor for enantiomeric compounds. However, the model might not be suitable in predicting the BP_{ND} values of tau

radiotracers due to the exclusion of possible binding to other β-sheet structures. Other issues included the use of the default values for population variation and the use of amyloid binding site densities for simulating HC, MCI and AD conditions, which might not be suitable for tau.

7.3.2 Comparison of *SUVR*

The screening of the tau radiotracers was carried out using the default time window of 40-60 min and the literature-stated time window (Table 7.5). The differences in *SUVR* were very small for both HC and AD (Table 7.5). The correlation between predicted and clinically-observed *SUVR* was slightly better, using default time window (Figures 7.3 vs. 7.4). These showed that the use of default time window would not affect the screening outcome.

The best correlation was obtained using clinically-observed *SUVR* of the hippocampus. However, there were a fewer number of reported *SUVR* of the hippocampus (Figures 7.3 and 7.4). To confirm whether the *SUVR* of hippocampus resulted in the best correlation, further correlations were carried out using the highest *SUVR* values in AD from the same radiotracers with available *SUVR* of the hippocampus (n = 5). The correlation using *SUVR* of the hippocampus was still the best with R^2 values of 0.93 (Figures 7.3 and 7.4). The correlation between predicted and clinically-observed *SUVR* from the region with the highest *SUVR* values in AD also resulted in a good correlation with R^2 values of 0.83 and 0.81 (Figures 7.3 and 7.4). As such, the highest *SUVR* in AD were used for evaluation of tau radiotracers.

For amyloid radiotracers, the correlations were almost similar, with R^2 of about 0.50 for 9 radiotracers, using the highest *SUVR* in AD, the *SUVR* from the region with the greatest *SUVR* difference between HC and AD and *SUVR* of posterior cingulate gyrus (Figure 5.7, section 5.5). The three types of *SUVR* reported were very close to each other. This showed that the amyloid binding sites were nearly saturated in AD conditions and that amyloid accumulation progresses drastically from HC to AD conditions. This led to regions with highest *SUVR* in AD and greatest *SUVR* differences between HC and AD having nearly identical *SUVR* values.

For tau radiotracers, correlations were very different using the highest *SUVR* in AD, the *SUVR* from the region with the greatest *SUVR* difference between HC and AD, and *SUVR* of the hippocampus (Figures 7.3 and 7.4). Based on Braak & Braak staging [1991] and Delacourte staging [1999], tau accumulates in the hippocampus after entorhinal cortex in the early stages, yet

the *SUVR* of the hippocampus was not always the highest (Table 7.4). Phosphorylated tau starts to accumulate in small quantities in the early stages of AD and under healthy conditions in normal ageing in certain regions. As such, the *SUVR* of the region with the greatest *SUVR* difference between HC and AD might not correlate well [Braak et al., 1991; Delacourte et al., 1999].

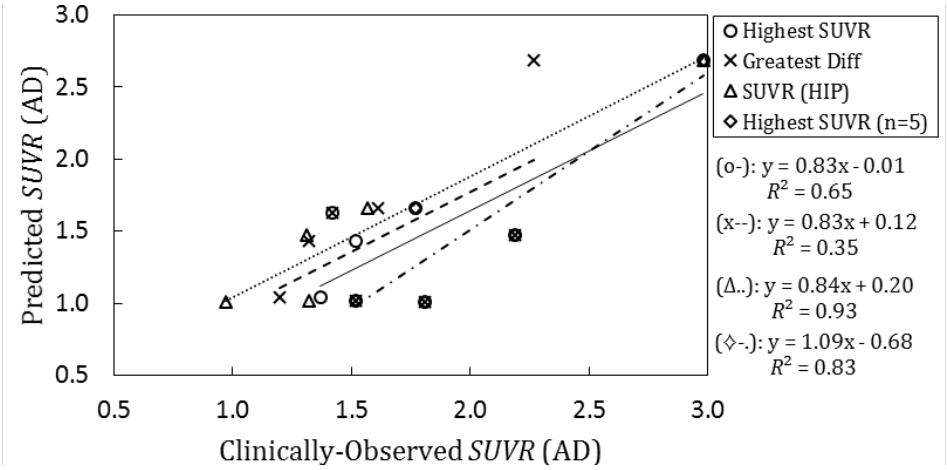

Figure 7.3: Correlation of clinically-observed and predicted *SUVR* using default time window of 40-60 min. Highest *SUVR* value in AD (o-), greatest S*UVR* difference between HC and AD (x--), *SUVR* of the hippocampus (Δ.., n = 5) and highest *SUVR* in AD (n = 5).

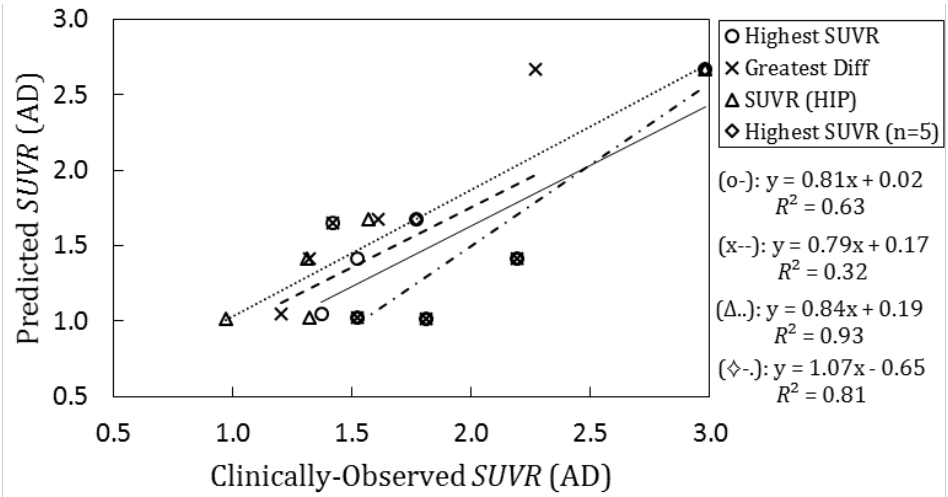

Figure 7.4: Correlation of clinically-observed and predicted *SUVR* using literature-stated time window. Highest *SUVR* value in AD (o-), greatest *SUVR* difference between HC and AD (x--), *SUVR* of the hippocampus (Δ.., n = 5) and highest *SUVR* in AD (n = 5).

Despite the poor prediction of BP_{ND} values (Table 7.6), the predicted *SUVR* correlated well with the highest clinically-observed *SUVR* in AD and *SUVR* of the hippocampus in 9 and 5 clinically-applied tau radiotracers. The clinically-observed *SUVR* distributions across subject groups of HC,

MCI and AD were different depending on the regions of interest [Villemagne et al., 2014; Harada et al., 2015; Chien et al., 2012; Chien et al., 2014; Maruyama et al., 2013]. The lateral/inferior temporal cortex showed clear differences between HC and AD in general, but other regions might not show any differences [Villemagne et al., 2014]. There were also occasional outliers whereby AD subjects with low MMSE scores had *SUVR* values lower than HC in lateral/inferior temporal cortex and other regions [Chien et al., 2014; Maruyama et al., 2013]. The spread of *SUVR* values in HC may also be greater than that of AD in certain regions [Villemagne et al., 2014; Harada et al., 2015]. This may be due to issues like NSB in white matter leading to spill-over in the surrounding cortical regions. NSB issue is more apparent in tau radiotracers with lower tau binding selectivity and higher NSB, such as [^{18}F]THK523 and [^{18}F]THK5117.

7.3.3 Comparison of TACs and *SUVR* distributions

The simulated TACs of [^{18}F]THK523 (Figure 7.5A) had slower washout and overlapping of TACs of HC and AD compared to clinically-observed TACs [Villemagne et al., 2014], which had higher peak in cerebellum region compared to target regions and slightly higher height of the tails of the TACs in AD compared to HC. The simulated TACs of [^{18}F]THK5105 [Okamura et al., 2014] showed faster washout, but with later time to peak compared to clinically-observed TACs (Figure 7.5B). The simulated TACs of [^{18}F]THK5117 [Harada et al., 2015] and [^{18}F]THK5351 [Harada et al., 2016] showed a similar rate of washout to clinically-observed TACs but with later time to peak in the TACs of MCI and AD (Figures 7.5C and E). The clinically-observed TACs of these radiotracers also had higher peaks in the cerebellum than target regions, while the peaks of the simulated TACs of the reference region were always lower than that of the target regions (Figure 7.5). Faster washout was also observed in clinically-observed TACs of the cerebellum compared to that of the target regions in all reported THK tau radiotracers. For [^{18}F]THK5317, the simulated TACs were completely different from clinically-observed TACs. This might be due to the use of K_i and the enantiomeric properties of the compound, which were not included in the amyloid biomathematical model.

The simulated TACs of [^{18}F]T807 (Figure 7.5G) had slightly sharper peaks and faster washout compared to clinically-observed TACs in both HC and AD. Higher peak was observed in the target region than the reference region in simulated TACs, which was similar to that observed in the clinically-observed TACs of posterior cingulate gyrus and the reference region of the cerebellum [Wooten et al., 2016]. The predicted TACs of [^{18}F]T808 of both the reference and target regions of HC, MCI and AD conditions completely overlapped each other (Figure 7.5H).

The clinically-observed TACs of [^{18}F]T808 appeared similar to that of [^{18}F]T807 but with smaller differences between subject conditions [Chien et al., 2014]. The simulated TACs of [^{11}C]PBB3 (Figure 7.5I) were similar to that observed clinically in AD in the nonbinding and low, middle and high binding regions [Kimura et al., 2015]. The differences might be due to the use of K_D values measured using synthetic tau for [^{11}C]PBB3, and K_D values measured via autoradiography for [^{18}F]T807 and [^{18}F]T808.

Thus far, the plots of the arterial input functions of only two clinically-applied tau radiotracers were reported: [^{11}C]PBB3 [Kimura et al.,2015] and [^{18}F]T807 [Wooten et al., 2016]. The arterial input functions of these radiotracers were similar in HC and AD, with fast uptake and fast washout and the shape of the curves was similar to that of BF227-HC used in the simulation. Although the shape of the input functions of these two radiotracers was similar to that of BF227-HC, the shape of the arterial input function might be different for other tau radiotracers. There were also issues with metabolites crossing the BBB (e.g. [^{11}C]PBB3), but the amyloid biomathematical model could not be used to predict the possibilities of metabolites crossing the BBB.

The trend of the simulated *SUVR* population distributions of [^{18}F]THK5117, [^{18}F]T807 and [^{11}C]PBB3 were nearly similar to that observed clinically (Figure 7.6B-D) but not for [^{18}F]THK523 (Figure 7.6A). The lack of differences across subject conditions for [^{18}F]THK523 might be due to the use of K_D value measured using human brain homogenates instead of synthetic tau (Table 7.2). The differences in K_D value measured using human brain homogenates and synthetic tau were much greater in [^{18}F]THK523 than [^{18}F]THK5105 (Table 7.2). On the other hand, the clinically-observed *SUVR* distributions of [^{18}F]THK523 might show greater differences across subject conditions because of binding to other β-sheet proteins (e.g. Aβ) since [^{18}F]THK523 has lower selectivity for tau binding sites. The spread of simulated *SUVR* distributions under HC condition was small compared to that observed clinically (Figure 7.6) [Villemagne et al., 2014; Harada et al., 2015; Chien et al., 2012; Chien et al., 2014; Maruyama et al., 2013].

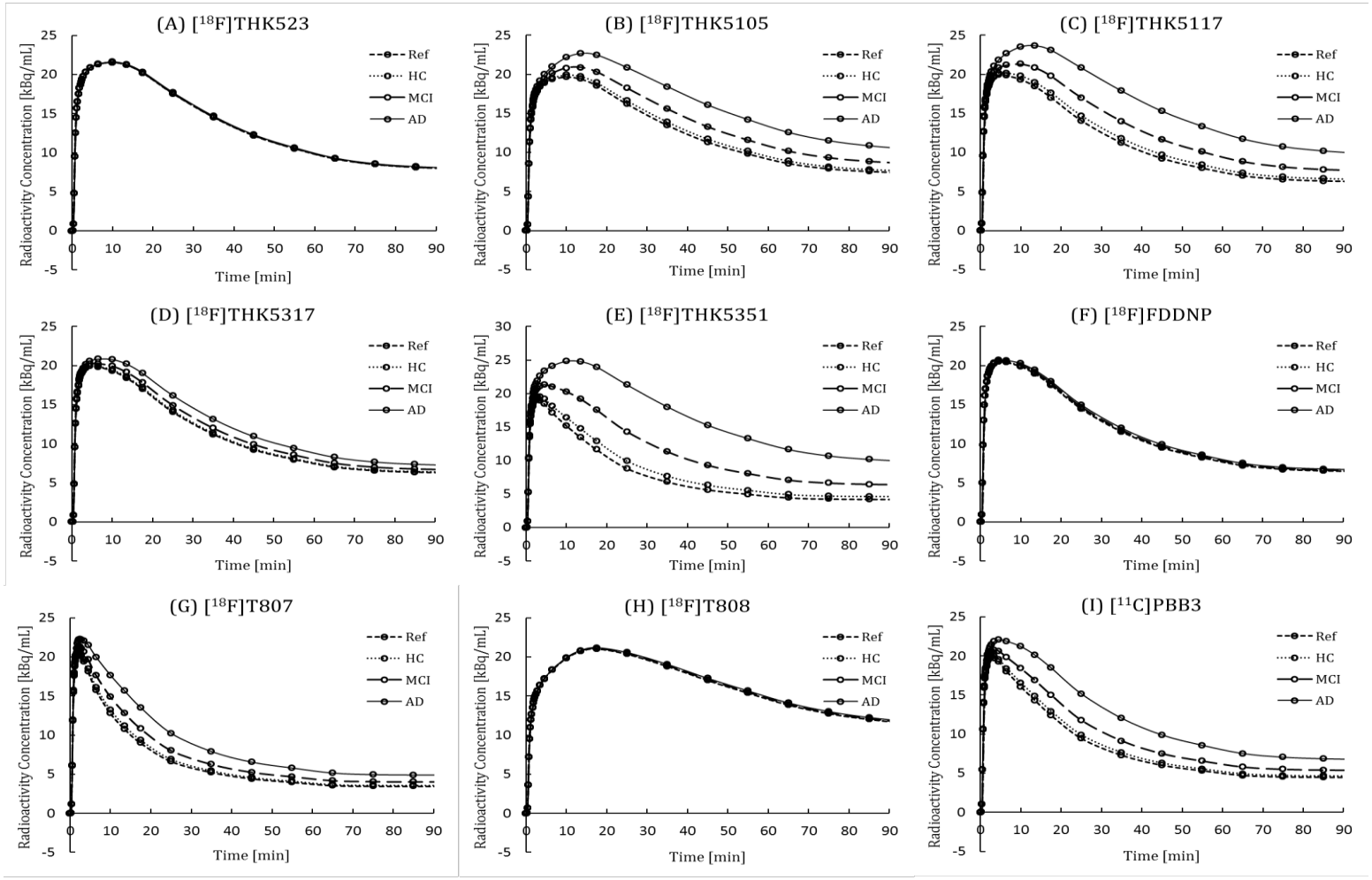

Figure 7.5: Simulated TACs from 0–90 min of the reference region and target regions of HC, MCI and AD of 9 clinically-applied tau radiotracers: (A) [^{18}F]THK523, (B) [^{18}F]THK5105, (C) [^{18}F]THK5117, (D) [^{18}F]THK5317, (E) [^{18}F]THK5351, (F) [^{18}F]FDDNP, (G) [^{18}F]T807, (H) [^{18}F]T808 and (I) [^{11}C]PBB3.

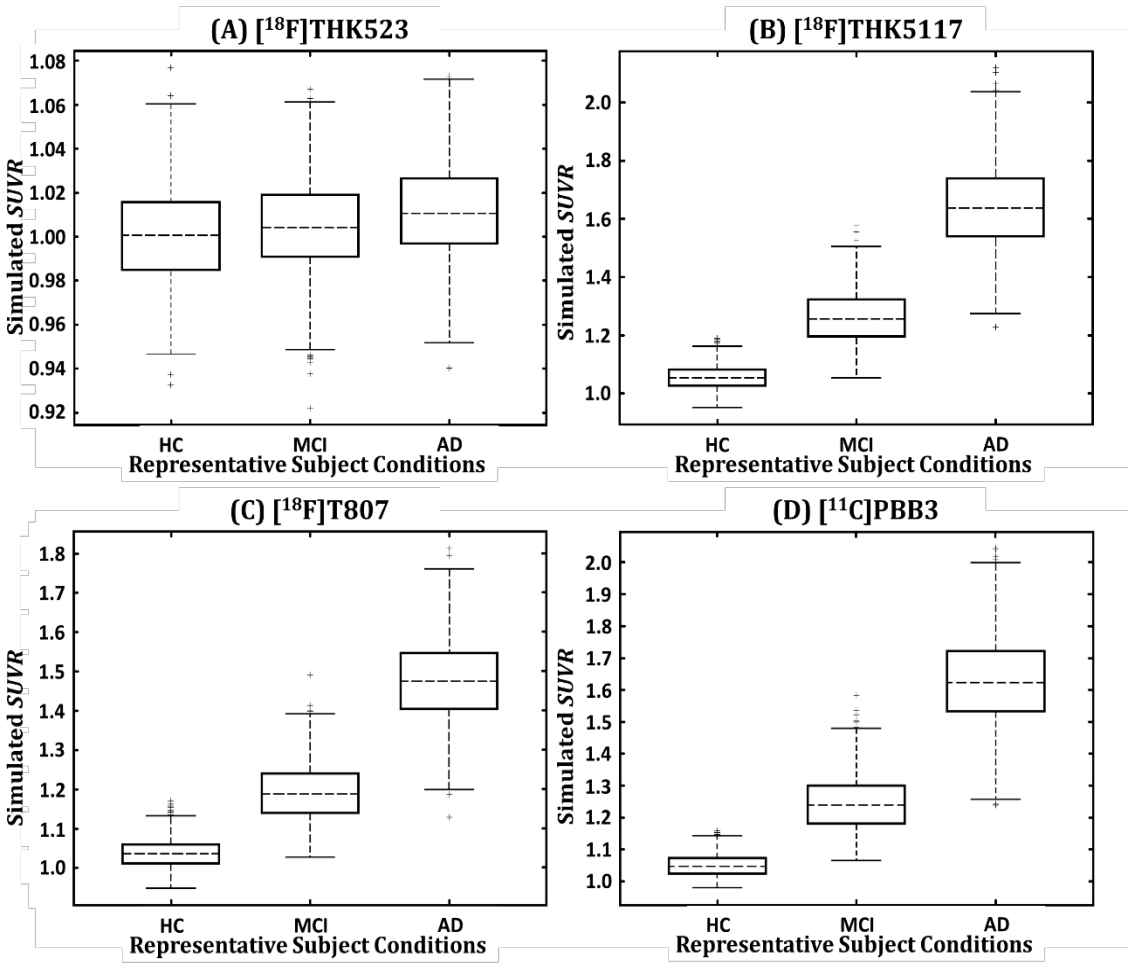

Figure 7.6: Simulated *SUVR* distributions across HC, MCI and AD conditions for clinically-applied tau radiotracers of (A) [^{18}F]THK523, (B) [^{18}F]THK5117, (C) [^{18}F]T807 and (D) [^{11}C]PBB3.

7.3.4 *CUI* Results of Tau Radiotracers

The *CUI* distributions for 22 tau radiotracers are shown in Figure 7.7. Up to date, the comparison of multiple tau radiotracers were carried out by means of *in vitro* competition binding assays in human brain sections or using human AD brain homogenates [Tago et al., 2016; Declercq et al., 2016] or by means of pre-clinical imaging [Chien et al., 2014]. Based on the Declercq's results, [^{18}F]T807 > [^{18}F]T808 > [^{18}F]THK5105 > [^{18}F]Lansoprazole / [^{11}C]Astemizole. Based on Tago's results, [^{18}F]THK5105 > [^{18}F]THK5129 > [^{18}F]THK5287 > [^{18}F]THK5125 > [^{18}F]THK5151 > [^{18}F]THK5307 > [^{18}F]THK523. However, high binding affinity to target does not always yield good *in vivo* pharmacokinetics. Although the K_D values of [^{18}F]T807 was much greater than that of [^{11}C]PBB3, which is greater than [^{18}F]THK5117 (the greater the K_D value, the lower the binding affinity) (Table 7.2), the difference in *SUVR* between HC and AD were greatest in [^{18}F]T807,

followed by [^{18}F]THK5117 then [^{11}C]PBB3 (Table 7.4). Yet, the resulting *CUI* values were about the same for these three radiotracers (Figure 7.7).

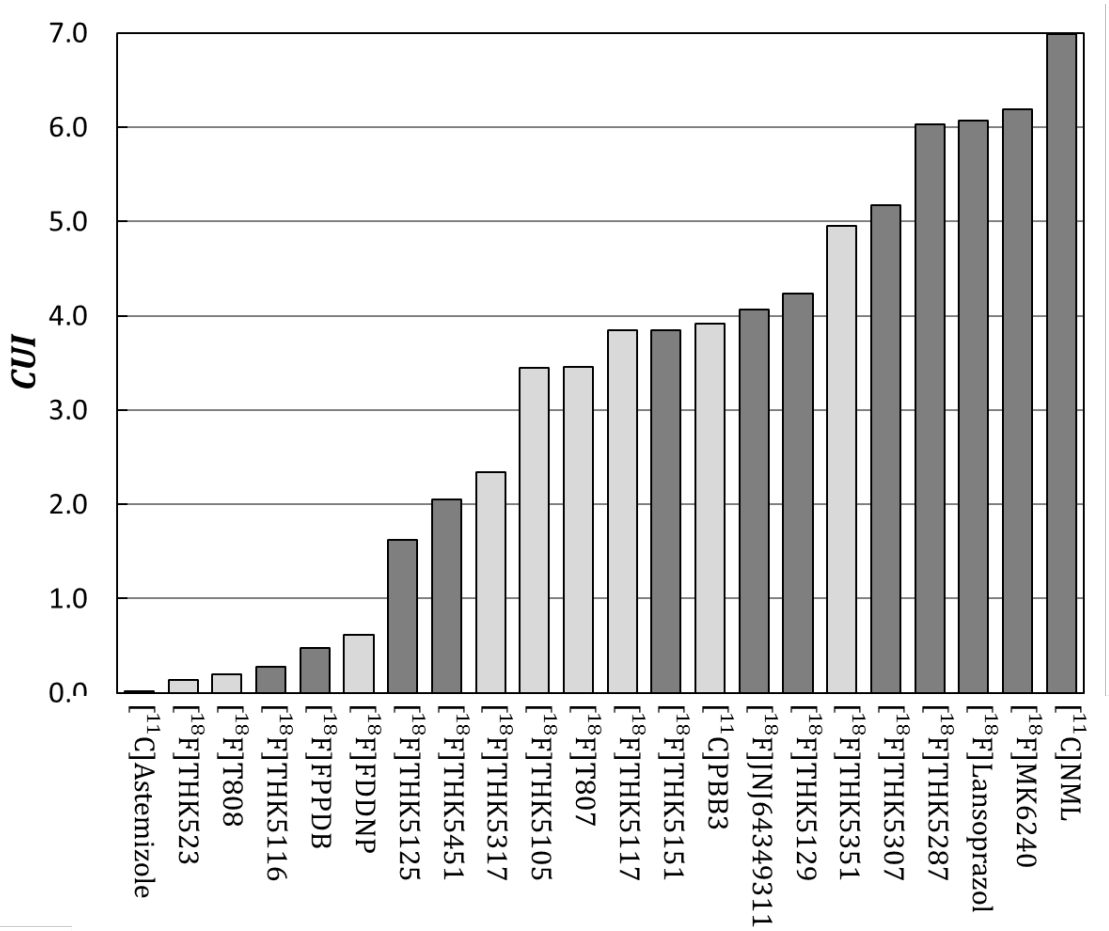

Figure 7.7: *CUI* distributions of 22 tau-related radiotracers. Clinically-applied tau radiotracers are shaded in light gray.

[^{18}F]THK5351 yielded higher clinically-observed *SUVR* than [^{18}F]THK5117 in the same AD patients, with lower white matter binding [Harada et al., 2016]. [^{18}F]THK5351 was also reported to have a higher signal-to-noise ratio (SNR), and lower NSB in white matter than [^{18}F]THK5105 and [^{18}F]THK5117 [Villemagne et al., 2015]. Similarly, *CUI* value of [^{18}F]THK5351 was higher than [^{18}F]THK5105 and [^{18}F]THK5117.

The binding affinity of [^{18}F]T808 to tau was lower than [^{18}F]T807 *in vitro* binding studies using human brain slices (Table 7.2) but showed higher selectivity in competition binding studies using purified tau [Declercq et al., 2016]. In *in vivo* preclinical studies, [^{18}F]T808 displayed lower

uptake but faster pharmacokinetics than [^{18}F]T807 in rodents [Declercq et al., 2016]. The *CUI* value of [^{18}F]T807 was higher than [^{18}F]T808. However, the *CUI* value of [^{18}F]T808 was very small and does not appear to be promising clinical tau radiotracer. Similarly, [^{18}F]THK523 also yielded small *CUI* value, even though clinical studies showed that it can be applied clinically. This is may be due to the use of K_D values measured using human brain via autoradiography instead of the binding assay or due to relatively high selectivity for other β-sheet structures. Therefore, it is important to measure the binding affinity of tau radiotracers to other β-sheet structures such as Aβ and α-synuclein.

[^{18}F]Lansoprazole is used clinically for the treatment of gastrointestinal disorders and hence it is known to have good uptake into the system. The ranking of [^{18}F]Lansoprazole based on *CUI* was high as the K_D value employed was measured using synthetic tau instead of human brain homogenate. The K_D values were very different, hence it was likely that [^{18}F]Lansoprazole has a low binding affinity to human tau. Similarly, [^{11}C]NML yielded high *CUI,* probably due to the use of K_D value measured using synthetic tau. The huge difference in K_D values measured using synthetic tau and human AD brain homogenates (Table 7.2) showed that K_D values measured using human AD brain homogenates should be used for proper evaluation of tau radiotracers.

7.4 Summary

Currently, the screening methodology with *CUI* showed limited potential in evaluating the radiotracers with greater differences observed in the predicted kinetic parameters for enantiomeric radiotracer. Moreover, the evaluation of [^{18}F]THK523 and [^{18}F]T808 were not as expected. This is may be due to differences in K_D values measured synthetic tau, or using human brain via autoradiography and instead of the binding assay, or due to relatively high selectivity for other β-sheet structures. Therefore, it is important to measure binding affinity to other β-sheet structures such as Aβ and α-synuclein. Due to great differences in binding to synthetic tau and human brain homogenates, K_D values should be measured using human brain homogenates in the binding assay.

Thus far, only the arterial input functions of 2 clinically-applied tau radiotracers had been reported. Although the shape of the input functions was relatively similar to that of BF227-HC used for simulation, there were issues with metabolites crossing the BBB (e.g. [^{11}C]PBB3). Moreover, there were limited kinetic data and *SUVR* data of clinically-applied tau radiotracers for a full evaluation of the amyloid biomathematical model. Although predicted and clinically-observed

SUVR showed good correlation, the predicted BP_{ND} of [^{18}F]THK5317 and [^{11}C]PBB3 were very different from that of clinically-observed.

Off-target binding (e.g. [^{18}F]THK5351 also binds to MAO-B enzymes) were observed for some of the clinically-applied tau radiotracers, which further complicates evaluation of the radiotracers. Although ensuring no off-target binding exists for the candidate radiotracer during development is ideal, the process of screening through binding to thousands of possible proteins requires more time and leads to higher costs of evaluation. It would be useful to model possible off-target binding but the inclusion of all possible forms of binding would lead to less accurate and precise models in predicting the binding capability of the radiotracer to the target sites and longer computational time. A balance between accuracy, precision and effort is thus required. In conclusion, more work appears to be required for more accurate and precise screening of tau radiotracers.

Chapter 8

Overall Conclusions and Future Directions

This PhD project is focused on the development of an amyloid biomathematical screening methodology to screen a large number of candidate compounds during the design of the compounds in the early phases of radiotracer development mainly before, but also after optimization of synthesis and radiolabeling procedures. The biomathematical screening methodology is used to predict the possible *in vivo* pharmacokinetic performance and clinical usefulness of multiple radiotracers simultaneously during development. Although some biomathematical models exist, they were either focused on other drugs or radiotracers or, for amyloid radiotracers, they were focused on the progression of amyloid accumulation. Thus far, this study is the first attempt to predict the clinical usefulness of radiotracers during the development phase.

We have successfully developed a biomathematical model to predict the *SUVR* of an amyloid radiotracer, using mostly *in silico* inputs. The free fractions in plasma and tissue can be predicted from the proposed f_P-f_{ND} model using lipophilicity as input. The model can also be used to predict other kinetic parameters such as K_1, k_2 and BP_{ND} and can be extended to other radiotracers with similar binding characteristics as amyloid radiotracers (e.g. tau, alpha-synuclein). A screening methodology based on the proposed biomathematical model and simulations with noise and population variations was developed. A clinical usefulness index (*CUI*) was introduced to support comparison and decision-making of moving candidate radiotracers to clinical applications. It can also be used to compare radiotracers developed within and across institutions with the use of a reference radiotracer.

The feasibility of extending the amyloid screening methodology to the screening of tau radiotracers was evaluated. The prediction of kinetic parameters and *SUVR* values appeared good for a few clinically-applied tau radiotracers. However, tau radiotracers were developed much later than amyloid radiotracers and thus limited clinical pharmacokinetic results were reported. The current screening methodology for amyloid radiotracers could not be adjusted for tau radiotracers. Moreover, more issues were observed in tau imaging due to the tau pathology and hence further

changes to the existing model may be required.

The future work of this project involves the inclusion of a specific binding compartment for amyloid radiotracers and adjustments to f_P-f_{ND} model due to the enantiomeric properties of some tau radiotracers.

Bibliography

Abraham, M. H. & McGowan, J. C. The use of characteristic volumes to measure cavity terms in reversed phase liquid chromatography. *Chromatographia* 23, 243–246 (1987).

Agdeppa, E. D. et al. Binding characteristics of radiofluorinated 6-dialkylamino-2-naphthylethylidene derivatives as positron emission tomography imaging probes for β-amyloid plaques in Alzheimer's disease. *Journal of Neuroscience* 21, RC189–RC189 (2001).

Agdeppa, E. D. & Spilker, M. E. A Review of Imaging Agent Development. *The AAPS Journal* 11, 286–299 (2009).

Albert, M. S. et al. The diagnosis of mild cognitive impairment due to Alzheimer's disease: Recommendations from the National Institute on Aging-Alzheimer's Association workgroups on diagnostic guidelines for Alzheimer's disease. *Alzheimer's & Dementia* 7, 270–279 (2011).

Anton Forsberg. Sensitive and specific amyloid-b PET imaging using the three novel radioligands [18F]AZD4694, [11C]AZD2184 and [11C]AZD2995 in Alzheimer's disease patients. *Journal of Cerebral Blood Flow & Metabolism* 32, S100–S127 (2012).

Ariza, M., Kolb, H. C., Moechars, D., Rombouts, F. & Andrés, J. I. Tau Positron Emission Tomography (PET) Imaging: Past, Present, and Future. *Journal of Medicinal Chemistr*y 58, 4365–4382 (2015).

Barre, J., Chamouard, J. M., Houin, G. & Tillement, J. P. Equilibrium dialysis, ultrafiltration, and ultracentrifugation compared for determining the plasma-protein-binding characteristics of valproic acid. *Clinical chemistry* 31, 60–64 (1985).

Barthel, H. et al. Cerebral amyloid-β PET with florbetaben (18 F) in patients with Alzheimer's disease and healthy controls: a multicentre phase 2 diagnostic study. *The Lancet Neurology* 10, 424–435 (2011).

Becker, G. A. et al. PET Quantification of 18F-Florbetaben Binding to -Amyloid Deposits in

Human Brains. *Journal of Nuclear Medicine* 54, 723–731 (2013).

Bewick, V., Cheek, L. & Ball, J. Statistics review 13: receiver operating characteristic curves. *Critical care 8*, 508 (2004).

Braak, H. & Braak, E. Neuropathological stageing of Alzheimer-related changes. *Acta neuropathologica* 82, 239–259 (1991).

Braak, H. & Braak, E. Frequency of stages of Alzheimer-related lesions in different age categories. *Neurobiology of aging* 18, 351–357 (1997).

Buée, L., Bussière, T., Buée-Scherrer, V., Delacourte, A. & Hof, P. R. Tau protein isoforms, phosphorylation and role in neurodegenerative disorders. *Brain Research*. Rev. 33, 95–130 (2000).

Burt, T. et al. Microdosing and Other Phase 0 Clinical Trials: Facilitating Translation in Drug Development: Microdosing and Phase 0 Trials. *Clinical and Translational Science* 9, 74–88 (2016).

Cai, L. et al. Synthesis and Evaluation of Two 18 F-Labeled 6-Iodo-2-(4‘- N , N - dimethylamino)phenylimidazo[1,2- a]pyridine Derivatives as Prospective Radioligands for β-Amyloid in Alzheimer’s Disease. *Journal of Medicinal Chemistry* 47, 2208–2218 (2004).

Carpenter, A. P., Pontecorvo, M. J., Hefti, F. F. & Skovronsky, D. M. The use of the exploratory IND in the evaluation and development of 18F-PET radiopharmaceuticals for amyloid imaging in the brain: a review of one company’s experience. *The Quarterly Journal of Nuclear Medicine and Molecular Imaging* 53, 387–393 (2009).

Catafau, A. M. & Bullich, S. Amyloid PET imaging: applications beyond Alzheimer’s disease. *Clinical and Translational Imaging* 3, 39–55 (2015).

Chandra, R. et al. New Diphenylacetylenes as Probes for Positron Emission Tomographic Imaging of Amyloid Plaques. *Journal of Medicinal Chemistry* 50, 2415–2423 (2007).

Chen, K. et al. Improved Power for Characterizing Longitudinal Amyloid- PET Changes and Evaluating Amyloid-Modifying Treatments with a Cerebral White Matter Reference Region. *Journal of Nuclear Medicine* 56, 560–566 (2015).

Chien, D. T. et al. Early clinical PET imaging results with the novel PHF-tau radioligand [F-18]-T807. *Journal of Alzheimer's Disease* 34, 457–468 (2013).

Chien, D. T. et al. Early clinical PET imaging results with the novel PHF-tau radioligand [F18]-T808. *Journal of Alzheimer's Disease* 38, 171–184 (2014).

Chiotis, K. et al. Imaging in-vivo tau pathology in Alzheimer's disease with THK5317 PET in a multimodal paradigm. *European Journal of Nuclear Medicine and Molecular Imaging* 43, 1686–1699 (2016).

Choi, S. R. et al. Preclinical Properties of 18F-AV-45: A PET Agent for A Plaques in the Brain. *Journal of Nuclear Medicine* 50, 1887–1894 (2009).

Cselenyi, Z. et al. Clinical Validation of 18F-AZD4694, an Amyloid- -Specific PET Radioligand. *Journal of Nuclear Medicine* 53, 415–424 (2012).

Cselényi, Z. & Farde, L. Quantification of blood flow-dependent component in estimates of beta-amyloid load obtained using quasi-steady-state standardized uptake value ratio. *Journal of Cerebral Blood Flow & Metabolism* 35, 1485–1493 (2015).

Cui, M. et al. Novel 18 F-Labeled Benzoxazole Derivatives as Potential Positron Emission Tomography Probes for Imaging of Cerebral β-Amyloid Plaques in Alzheimer's Disease. *Journal of Medicinal Chemistry* 55, 9136–9145 (2012a).

Cui, M. et al. Synthesis and Evaluation of Novel 18 F Labeled 2-Pyridinylbenzoxazole and 2-Pyridinylbenzothiazole Derivatives as Ligands for Positron Emission Tomography (PET) Imaging of β-Amyloid Plaques. *Journal of Medicinal Chemistry* 55, 9283–9296 (2012b).

Cumming, P. et al. Effects of acute nicotine on hemodynamics and binding of [11C]raclopride to dopamine D2,3 receptors in pig brain. *NeuroImage* 19, 1127–1136 (2003).

Declercq, L. et al. Comparison of New Tau PET-Tracer Candidates With [18 F]T808 and [18 F]T807. *Molecular Imaging* 15, 153601211562492 (2016).

Delacourte, A. et al. The biochemical pathway of neurofibrillary degeneration in aging and Alzheimer's disease. *Neurology* 52, 1158–1158 (1999).

Di, L. et al. Species Independence in Brain Tissue Binding Using Brain Homogenates. *Drug Metabolism and Disposition* 39, 1270–1277 (2011).

Dong, W., Zhang, Z., Jiang, X., Sun, Y. & Jiang, Y. Effect of volume ratio of ultrafiltrate to sample solution on the analysis of free drug and measurement of free carbamazepine in clinical drug monitoring. *European Journal of Pharmaceutical Sciences* 48, 332–338 (2013).

Dow, N. Determination of compound binding to plasma proteins. *Current protocols in Pharmacology* (2006).

Fawaz, M. V. et al. High Affinity Radiopharmaceuticals Based Upon Lansoprazole for PET Imaging of Aggregated Tau in Alzheimer's Disease and Progressive Supranuclear Palsy: Synthesis, Preclinical Evaluation, and Lead Selection. *ACS Chemical Neuroscience* 5, 718–730 (2014).

Fawcett, T. An introduction to ROC analysis. *Pattern Recognition Letters* 27, 861–874 (2006).

Fodero-Tavoletti, M. T. et al. 18F-THK523: a novel in vivo tau imaging ligand for Alzheimer's disease. *Brain* 134, 1089–1100 (2011).

Fodero-Tavoletti, M. T. et al. Assessing THK523 selectivity for tau deposits in Alzheimer's disease and non–Alzheimer's disease tauopathies. *Alzheimer's research & therapy* 6, 11 (2014).

Folstein, M. F., Folstein, S. E. & McHugh, P. R. 'Mini-mental state': a practical method for grading the cognitive state of patients for the clinician. *Journal of psychiatric research* 12, 189–198 (1975).

Fu, H. et al. Synthesis and biological evaluation of 18F-labled 2-phenylindole derivatives as PET imaging probes for β-amyloid plaques. *Bioorganic & Medicinal Chemistry* 21, 3708–3714 (2013).

Furumoto, S. et al. Recent advances in the development of amyloid imaging agents. *Current topics in medicinal chemistry* 7, 1773–1789 (2007).

Furumoto, S. et al. A 18F-Labeled BF-227 Derivative as a Potential Radioligand for Imaging Dense Amyloid Plaques by Positron Emission Tomography. *Molecular Imaging and Biology* 15, 497–506 (2013).

Gan, S. D. & Patel, K. R. Enzyme Immunoassay and Enzyme-Linked Immunosorbent Assay. *Journal of Investigative Dermatology* 133, 1–3 (2013).

Garner, R. C. & Lappin, G. Commentary: The phase 0 microdosing concept. *British Journal of Clinical Pharmacology* 61, 367–370 (2006).

Ghose, A. K. & Crippen, G. M. Atomic physicochemical parameters for three-dimensional-structure-directed quantitative structure-activity relationships. 2. Modeling dispersive and hydrophobic interactions. *Journal of chemical information and computer sciences* 27, 21–35 (1987).

Guo, Q., Brady, M. & Gunn, R. N. A Biomathematical Modeling Approach to Central Nervous System Radioligand Discovery and Development. *Journal of Nuclear Medicine* 50, 1715–1723 (2009).

Han, P. et al. A Quantitative Analysis of Brain Soluble Tau and the Tau Secretion Factor. *Journal of Neuropathology & Experimental Neurology* nlw105 (2017).

Harada, R. et al. Comparison of the binding characteristics of [18F]THK-523 and other amyloid imaging tracers to Alzheimer's disease pathology. *European Journal of Nuclear Medicine and Molecular Imaging* 40, 125–132 (2013).

Harada, R. et al. [18F]THK-5117 PET for assessing neurofibrillary pathology in Alzheimer's

disease. *European Journal of Nuclear Medicine and Molecular Imaging* 42, 1052–1061 (2015).

Harada, R. et al. 18F-THK5351: A Novel PET Radiotracer for Imaging Neurofibrillary Pathology in Alzheimer Disease. *Journal of Nuclear Medicine* 57, 208–214 (2016).

Harrison, S. T. et al. Synthesis and Evaluation of 5-Fluoro-2-aryloxazolo[5,4- b]pyridines as β-Amyloid PET Ligands and Identification of MK-3328. *ACS Medicinal Chemistry Letters* 2, 498–502 (2011).

Hartmann, T. & Schmitt, J. Lipophilicity – beyond octanol/water: a short comparison of modern technologies. *Drug Discovery Today*: Technologies 1, 431–439 (2004).

Hashimoto, H. et al. Radiosynthesis, Photoisomerization, Biodistribution, and Metabolite Analysis of 11C-PBB3 as a Clinically Useful PET Probe for Imaging of Tau Pathology. *Journal of Nuclear Medicine* 55, 1532–1538 (2014).

Hashimoto, R. et al. Quantitative analysis of neurofilament proteins in Alzheimer brain by enzyme linked immunosorbent assay system. *Psychiatry and clinical neurosciences* 53, 587–591 (1999).

Hatashita, S. et al. [18F]Flutemetamol amyloid-beta PET imaging compared with [11C]PIB across the spectrum of Alzheimer's disease. *European Journal of Nuclear Medicine and Molecular Imaging* 41, 290–300 (2014).

Heurling, K., Buckley, C., Van Laere, K., Vandenberghe, R. & Lubberink, M. Parametric imaging and quantitative analysis of the PET amyloid ligand [(18)F]flutemetamol. *Neuroimage* 121, 184–192 (2015).

Hostetler, E. D. et al. Preclinical Characterization of 18F-MK-6240, a Promising PET Tracer for In Vivo Quantification of Human Neurofibrillary Tangles. *Journal of Nuclear Medicine* 57, 1599–1606 (2016).

Ikoma, Y., Watabe, H., Shidahara, M., Naganawa, M. & Kimura, Y. PET kinetic analysis: error

consideration of quantitative analysis in dynamic studies. *Annals of Nuclear Medicine* 22, 1–11 (2008).

Ikonomovic, M. D. et al. Post-mortem correlates of in vivo PiB-PET amyloid imaging in a typical case of Alzheimer's disease. *Brain* 131, 1630–1645 (2008).

Ingelsson, M. et al. Early Aβ accumulation and progressive synaptic loss, gliosis, and tangle formation in AD brain. *Neurology* 62, 925–931 (2004).

Ishiwata, K., Kawamura, K., Yanai, K. & Hendrikse, N. H. In vivo evaluation of P-glycoprotein modulation of 8 PET radioligands used clinically. *Journal of Nuclear Medicine* 48, 81–87 (2007).

Ito, H. et al. Quantitative Analysis of Amyloid Deposition in Alzheimer Disease Using PET and the Radiotracer 11C-AZD2184. *Journal of Nuclear Medicine* 55, 932–938 (2014).

Itoh, T., Saura, Y., Tsuda, Y. & Yamada, H. Stereoselectivity and enantiomer-enantiomer interactions in the binding of ibuprofen to human serum albumin. *Chirality* 9, 643–649 (1997).

Johnson, A. E. et al. AZD2184: a radioligand for sensitive detection of β-amyloid deposits. *Journal of Neurochemistry* 108, 1177–1186 (2009).

Jonasson, M. et al. Tracer Kinetic Analysis of (S)-18F-THK5117 as a PET Tracer for Assessing Tau Pathology. *Journal of Nuclear Medicine* 57, 574–581 (2016).

Jucker, M. & Walker, L. C. Self-propagation of pathogenic protein aggregates in neurodegenerative diseases. *Nature* 501, 45–51 (2013).

Juréus, A. et al. Characterization of AZD4694, a novel fluorinated Aβ plaque neuroimaging PET radioligand: AZD4694 a new amyloid PET radioligand. *Journal of Neurochemistry* 114, 784–794 (2010).

Kalvass, J. C., Maurer, T. S. & Pollack, G. M. Use of Plasma and Brain Unbound Fractions to Assess the Extent of Brain Distribution of 34 Drugs: Comparison of Unbound Concentration

Ratios to in Vivo P-Glycoprotein Efflux Ratios. *Drug Metabolism and Disposition* 35, 660–666 (2007).

Karran, E., Mercken, M. & Strooper, B. D. The amyloid cascade hypothesis for Alzheimer's disease: an appraisal for the development of therapeutics. *Nature Reviews Drug Discovery* 10, 698–712 (2011).

Kikuchi, A., Takeda, A., Okamura, N., Tashiro, M., Hasegawa, T., Furumoto, S., Kobayashi, M., Sugeno, N., Baba, T., Miki, Y., et al. In vivo visualization of -synuclein deposition by carbon-11-labelled 2-[2-(2-dimethylaminothiazol-5-yl)ethenyl]-6-[2-(fluoro)ethoxy] benzoxazole positron emission tomography in multiple system atrophy. *Brain* 133, 1772–1778 (2010).

Kimura, Y. et al. PET Quantification of Tau Pathology in Human Brain with 11C-PBB3. *Journal of Nuclear Medicine* 56, 1359–1365 (2015).

Klaver, A. C., Patrias, L. M., Finke, J. M. & Loeffler, D. A. Specificity and sensitivity of the Abeta oligomer ELISA. *Journal of Neuroscience Methods* 195, 249–254 (2011).

Klunk, W. E. et al. Uncharged thioflavin-T derivatives bind to amyloid-beta protein with high affinity and readily enter the brain. *Life Science*. 69, 1471–1484 (2001).

Klunk, W. E. et al. The binding of 2-(4′ -methylaminophenyl) benzothiazole to postmortem brain homogenates is dominated by the amyloid component. *Journal of Neuroscience* 23, 2086–2092 (2003).

Klunk, W. E. Binding of the Positron Emission Tomography Tracer Pittsburgh Compound-B Reflects the Amount of Amyloid- in Alzheimer's Disease Brain But Not in Transgenic Mouse Brain. *Journal of Neuroscience* 25, 10598–10606 (2005).

Kopeikina, K., Hyman, B., Spires-Jones, T. Soluble forms of tau are toxic in Alzheimer's disease. *Translational Neuroscience*. 3(3): 223–233 (2012).

Kraemer, H. C. & Kupfer, D. J. Size of Treatment Effects and Their Importance to Clinical

Research and Practice. *Biological Psychiatry* 59, 990–996 (2006).

Kung, M.-P., Hou, C., Zhuang, Z.-P., Skovronsky, D. & Kung, H. F. Binding of two potential imaging agents targeting amyloid plaques in postmortem brain tissues of patients with Alzheimer's disease. *Brain Research* 1025, 98–105 (2004).

Kwong, T. C. Free drug measurements: methodology and clinical significance. *Clinica chimica acta* 151, 193–216 (1985).

Landau, S. M. et al. Amyloid PET imaging in Alzheimer's disease: a comparison of three radiotracers. *European Journal of Nuclear Medicine and Molecular Imaging* 41, 1398–1407 (2014).

Landau, S. M. et al. Measurement of Longitudinal -Amyloid Change with 18F-Florbetapir PET and Standardized Uptake Value Ratios. *Journal of Nuclear Medicine* 56, 567–574 (2015).

Lanevskij, K., Japertas, P., Didziapetris, R. & Petrauskas, A. Ionization-Specific Prediction of Blood–Brain Permeability. *Journal of Pharmaceutical Sciences* 98, 122–134 (2009).

Lee, B. C. et al. Aromatic radiofluorination and biological evaluation of 2-aryl-6-[18F]fluorobenzothiazoles as a potential positron emission tomography imaging probe for β-amyloid plaques. *Bioorganic & Medicinal Chemistry* 19, 2980–2990 (2011).

Lee, I., Yang, J., Lee, J. H. & Choe, Y. S. Synthesis and evaluation of 1-(4-[18F]fluoroethyl)-7-(4′-methyl)curcumin with improved brain permeability for β-amyloid plaque imaging. *Bioorganic & Medicinal Chemistry Letters* 21, 5765–5769 (2011).

Lee, K.-J. et al. Modulation of nonspecific binding in ultrafiltration protein binding studies. *Pharmaceutical research* 20, 1015–1021 (2003).

Leinonen, V. et al. Diagnostic effectiveness of quantitative [18 F] flutemetamol PET imaging for detection of fibrillar amyloid β using cortical biopsy histopathology as the standard of truth in subjects with idiopathic normal pressure hydrocephalus. *Acta neuropathologica*

communications 2, 46 (2014).

Lemoine, L. et al. Visualization of regional tau deposits using 3H-THK5117 in Alzheimer brain tissue. *Acta Neuropathologica Communications* 3, (2015).

Limbird, L. E. & Motulsky, H. Receptor Identification and Characterization. *Comprehensive Physiology* (1998).

Lipinski, C. A., Lombardo, F., Dominy, B. W. & Feeney, P. J. Experimental and computational approaches to estimate solubility and permeability in drug discovery and development settings. *Advanced drug delivery reviews* 23, 3–25 (1997).

Lipinski, C. A. Lead- and drug-like compounds: the rule-of-five revolution. *Drug Discovery Today: Technologies* 1, 337–341 (2004).

Liu, X., Tu, M., Kelly, R. S., Chen, C. & Smith, B. J. Development of a computational approach to predict blood-brain barrier permeability. *Drug metabolism and disposition* 32, 132–139 (2004).

Lockhart, A. et al. Evidence for the Presence of Three Distinct Binding Sites for the Thioflavin T Class of Alzheimer's Disease PET Imaging Agents on -Amyloid Peptide Fibrils. *Journal of Biological Chemistry* 280, 7677–7684 (2005).

Lockhart, S. N. et al. Dynamic PET measures of tau accumulation in cognitively normal older adults and Alzheimer's disease patients measured using [18F] THK-5351. *PLoS One* 11, e0158460 (2016).

Logan, J. et al. A strategy for removing the bias in the graphical analysis method. *Journal of Cerebral Blood Flow & Metabolism*. 21, 307–320 (2001).

Lopresti, B. J., Klunk, W. E. Mathis, C. A., Hoge, J. A., Ziolko, S. K., Lu X., Meltzer, C. C., Simplified Quantification of Pittsburgh Compound B Amyloid Imaging PET Studies: A Comparative Analysis *Journal of Nuclear Medicine*, 46:1959–1972 (2005).

Loucks, D. P., Beek, E. van & Stedinger, J. R. Water resources systems planning and management: an introduction to methods, models and applications. (*UNESCO*, 2005).

Lowe, V. J. et al. An autoradiographic evaluation of AV-1451 Tau PET in dementia. *Acta Neuropathologica Communications* 4, (2016).

Luurtsema, G. et al. Peripheral metabolism of [18F]FDDNP and cerebral uptake of its labelled metabolites. *Nuclear Medicine and Biology* 35, 869–874 (2008).

Mandula, H. Role of Site-Specific Binding to Plasma Albumin in Drug Availability to Brain. *Journal of Pharmacology and Experimental Therapeutics* 317, 667–675 (2006).

Mannhold, R., Poda, G. I., Ostermann, C. & Tetko, I. V. Calculation of Molecular Lipophilicity: State-of-the-Art and Comparison of LogP Methods on more than 96,000 Compounds. *Journal of Pharmaceutical Sciences* 98, 861–893 (2009).

Maruyama, M. et al. Imaging of Tau Pathology in a Tauopathy Mouse Model and in Alzheimer Patients Compared to Normal Controls. *Neuron* 79, 1094–1108 (2013).

Mathis, C. A. et al. A lipophilic thioflavin-T derivative for positron emission tomography (PET) imaging of amyloid in brain. *Bioorganic & medicinal chemistry letters* 12, 295–298 (2002).

Mathis, C. A. et al. Synthesis and Evaluation of 11 C-Labeled 6-Substituted 2-Arylbenzothiazoles as Amyloid Imaging Agents. *Journal of Medicinal Chemistry* 46, 2740–2754 (2003).

Matsumura, K. et al. 18 F-Labeled Phenyldiazenyl Benzothiazole for in Vivo Imaging of Neurofibrillary Tangles in Alzheimer's Disease Brains. *ACS Medicinal Chemistry Letters* 3, 58–62 (2012).

Maurer, T. S. Relationship between exposure and nonspecific binding of thirty-three central nervous systems drugs in mice. *Drug Metabolism and Disposition* 33, 175–181 (2004).

Mauri, A., Consonni, V., Pavan, M. & Todeschini, R. Dragon software: An easy approach to molecular descriptor calculations. *Match* 56, 237–248 (2006).

McGraw, K. O. & Wong, S. P. A common language effect size statistic. *Psychological Bulletin* 111, 361 (1992).

McKhann, G. M. et al. The diagnosis of dementia due to Alzheimer's disease: Recommendations from the National Institute on Aging-Alzheimer's Association workgroups on diagnostic guidelines for Alzheimer's disease. *Alzheimer's & Dementia* 7, 263–269 (2011).

Mellors, A. & McGowan, J. C. Uses of molecular volume in biochemical pharmacology. *Biochemical pharmacology* 34, 2413–2416 (1985).

Mintun, M. A., Raichle, M. E., Kilbourn, M. R., Wooten, G. F. & Welch, M. J. A quantitative model for the in vivo assessment of drug binding sites with positron emission tomography. *Annals of neurology* 15, 217–227 (1984).

Morgan, C., Colombres, M., Nuñez, M. T. & Inestrosa, N. C. Structure and function of amyloid in Alzheimer's disease. *Progress in Neurobiology* 74, 323–349 (2004).

Moriguchi, I., Hirono, S., Liu, Q., Nakagome, I. & Matsushita, Y. Simple Method of Calculating Octanol/Water Partition Coefficient. *Chemical and Pharmaceutical Bulletin*. 40, 127–130 (1992).

Mukaetova-Ladinska, E. B. et al. Tau proteins in the temporal and frontal cortices in patients with vascular dementia. *Journal of Neuropathology & Experimental Neurology*. 74, 148–157 (2015).

Nagata, K. et al. Misery perfusion with preserved vascular reactivity in Alzheimer's disease. *Annals of the New York Academy of Sciences* 826, 272–281 (1997).

Näslund, J. et al. Correlation between elevated levels of amyloid beta-peptide in the brain and cognitive decline. *JAMA* 283, 1571–1577 (2000).

Nasreddine, Z. S. et al. The Montreal Cognitive Assessment, MoCA: a brief screening tool for mild cognitive impairment. *Journal of the American Geriatrics Society* 53, 695–699 (2005).

Nelissen, N. et al. Phase 1 Study of the Pittsburgh Compound B Derivative 18F-Flutemetamol in Healthy Volunteers and Patients with Probable Alzheimer Disease. *Journal of Nuclear Medicine* 50, 1251–1259 (2009).

Nemmi, F. *et al.* Insight on AV-45 binding in white and grey matter from histogram analysis: a study on early Alzheimer's disease patients and healthy subjects. *European Journal of Nuclear Medicine and Molecular Imaging* **41,** 1408–1418 (2014).

Neumaier, B. et al. Synthesis and evaluation of 18F-fluoroethylated benzothiazole derivatives for in vivo imaging of amyloid plaques in Alzheimer's disease. *Applied Radiation and Isotopes* 68, 1066–1072 (2010).

Ni, R., Gillberg, P.-G., Bergfors, A., Marutle, A. & Nordberg, A. Amyloid tracers detect multiple binding sites in Alzheimer's disease brain tissue. *Brain* 136, 2217–2227 (2013).

Ng, K.P., Pascoal, T.A., Mathotaarachchi, S., Therriault, J., Kang, M.S., Shin, M., Guiot, M.-C., Guo, Q., Harada, R., Comley, R.A., et al. Monoamine oxidase B inhibitor, selegiline, reduces 18F-THK5351 uptake in the human brain. *Alzheimer's Research & Therapy* 9 (2017).

Nyberg, S. *et al.* Detection of amyloid in Alzheimer's disease with positron emission tomography using [11C]AZD2184. *European Journal of Nuclear Medicine and Molecular Imaging* **36,** 1859–1863 (2009).

O'Brien, R. J. & Wong, P. C. Amyloid Precursor Protein Processing and Alzheimer's Disease. *Annual Review of Neuroscience* 34, 185–204 (2011).

Okamura, N. Quinoline and Benzimidazole Derivatives: Candidate Probes for In Vivo Imaging of Tau Pathology in Alzheimer's Disease. *Journal of Neuroscience* 25, 10857–10862 (2005).

Okamura, N. et al. Novel 18F-Labeled Arylquinoline Derivatives for Noninvasive Imaging of Tau Pathology in Alzheimer Disease. *Journal of Nuclear Medicine* 54, 1420–1427 (2013).

Okamura, N. et al. Non-invasive assessment of Alzheimer's disease neurofibrillary pathology

using 18F-THK5105 PET. *Brain* 137, 1762–1771 (2014).

Ono, M. et al. Novel Benzofuran Derivatives for PET Imaging of β-Amyloid Plaques in Alzheimer's Disease Brains. *Journal of Medicinal Chemistry* 49, 2725–2730 (2006).

Ono, M. et al. Distinct binding of PET ligands PBB3 and AV-1451 to tau fibril strains in neurodegenerative tauopathies. *Brain* aww339 (2017).

Perrin, R. J., Fagan, A. M. & Holtzman, D. M. Multimodal techniques for diagnosis and prognosis of Alzheimer's disease. *Nature* 461, 916–922 (2009).

Petersen, R. C. et al. Mild cognitive impairment: clinical characterization and outcome. *Archives of neurology* 56, 303–308 (1999).

Petrauskas, A. A. & Kolovanov, E. A. ACD/Log P method description. *Perspectives in Drug Discovery and Design* 19, 99–116 (2000).

Price, J. C. et al. Kinetic modeling of amyloid binding in humans using PET imaging and Pittsburgh Compound-B. *Journal of Cerebral Blood Flow & Metabolism* 25, 1528–1547 (2005).

Qu, W. et al. Synthesis and evaluation of indolinyl- and indolylphenylacetylenes as PET imaging agents for β-amyloid plaques. *Bioorganic & Medicinal Chemistry Letters* 18, 4823–4827 (2008).

Rojo, L. E., Alzate-Morales, J., Saavedra, I. N., Davies, P. & Maccioni, R. B. Selective Interaction of Lansoprazole and Astemizole with Tau Polymers: Potential New Clinical Use in Diagnosis of Alzheimer's Disease. *Journal of Alzheimer's Disease* 19, 573–589 (2010).

Rombouts, F. J. R. et al. Discovery of N -(Pyridin-4-yl)-1,5-naphthyridin-2-amines as Potential Tau Pathology PET Tracers for Alzheimer's Disease. *Journal of Medicinal Chemistry* 60, 1272–1291 (2017).

Rowe, C. C. et al. Imaging of amyloid beta in Alzheimer's disease with 18F-BAY94-9172, a novel

PET tracer: proof of mechanism. *The Lancet Neurology* 7, 129–135 (2008).

Rutkowska, E., Pajak, K. & Jóźwiak, K. Lipophilicity--methods of determination and its role in medicinal chemistry. *Acta Poloniae Pharmaceutica* 70, 3–18 (2013).

Ryu, E. K., Choe, Y. S., Lee, K.-H., Choi, Y. & Kim, B.-T. Curcumin and Dehydrozingerone Derivatives: Synthesis, Radiolabeling, and Evaluation for β-Amyloid Plaque Imaging †. *Journal of Medicinal Chemistry* 49, 6111–6119 (2006).

Schafer, K. N., Kim, S., Matzavinos, A. & Kuret, J. Selectivity requirements for diagnostic imaging of neurofibrillary lesions in Alzheimer's disease: A simulation study. NeuroImage 60, 1724–1733 (2012).

Seneca, N. et al. Brain and whole-body imaging in nonhuman primates with [11C]MeS-IMPY, a candidate radioligand for β-amyloid plaques. *Nuclear Medicine and Biology* 34, 681–689 (2007).

Serdons, K. et al. 11C-labelled PIB analogues as potential tracer agents for in vivo imaging of amyloid β in Alzheimer's disease. *European Journal of Medicinal Chemistry* 44, 1415–1426 (2009a).

Serdons, K. et al. Synthesis of 18F-labelled 2-(4′ -fluorophenyl)-1,3-benzothiazole and evaluation as amyloid imaging agent in comparison with [11C]PIB. *Bioorganic & Medicinal Chemistry Letters* 19, 602 – 605 (2009b).

Serdons, K. et al. Synthesis and Evaluation of 18 F-Labeled 2-Phenylbenzothiazoles as Positron Emission Tomography Imaging Agents for Amyloid Plaques in Alzheimer's Disease. *Journal of Medicinal Chemistry* 52, 1428–1437 (2009c).

Serrano-Pozo, A., Frosch, M. P., Masliah, E. & Hyman, B. T. Neuropathological Alterations in Alzheimer Disease. *Cold Spring Harbor Perspectives in Medicine* 1, a006189–a006189 (2011).

Sharma, R. & Aboagye, E. Development of radiotracers for oncology - the interface with pharmacology: Radiotracer development in oncology. *British Journal of Pharmacology* 163, 1565–1585 (2011).

Shidahara, M. et al. Quantitative kinetic analysis of PET amyloid imaging agents [11C]BF227 and [18F]FACT in human brain. *Nuclear Medicine and Biology* 42, 734–744 (2015).

Shin, J., Lee, S.-Y., Kim, S.-H., Kim, Y.-B. & Cho, S.-J. Multitracer PET imaging of amyloid plaques and neurofibrillary tangles in Alzheimer's disease. *NeuroImage* 43, 236–244 (2008).

Šimundić, A.-M. Measures of diagnostic accuracy: basic definitions. *The electronic Journal of the International Federation of Clinical Chemistry and Laboratory Medicine (EJIFCC)* 19, 203 (2009).

Snellman, A. et al. Pharmacokinetics of [18F]flutemetamol in wild-type rodents and its binding to beta amyloid deposits in a mouse model of Alzheimer's disease. *European Journal of Nuclear Medicine and Molecular Imaging* 39, 1784–1795 (2012).

Sperling, R. A. et al. Toward defining the preclinical stages of Alzheimer's disease: Recommendations from the National Institute on Aging-Alzheimer's Association workgroups on diagnostic guidelines for Alzheimer's disease. *Alzheimer's & Dementia* 7, 280–292 (2011).

Steinerman, J. R. et al. Distinct pools of beta-amyloid in Alzheimer disease-affected brain: a clinicopathologic study. *Archives of neurology*. 65, 906–912 (2008).

Stelzmann, R. A., Norman Schnitzlein, H. & Reed Murtagh, F. An English translation of Alzheimer's 1907 paper,'Über eine eigenartige Erkankung der Hirnrinde'. *Clinical anatomy* 8, 429–431 (1995).

Summerfield, S. G. Improving the in Vitro Prediction of in Vivo Central Nervous System Penetration: Integrating Permeability, P-glycoprotein Efflux, and Free Fractions in Blood and Brain. *Journal of Pharmacology and Experimental Therapeutics* 316, 1282–1290 (2005).

Svedberg, M. M. et al. [11C]PIB-amyloid binding and levels of Aβ40 and Aβ42 in postmortem

brain tissue from Alzheimer patients. *Neurochemistry International* 54, 347–357 (2009).

Tago, T. et al. Structure-Activity Relationship of 2-Arylquinolines as PET Imaging Tracers for Tau Pathology in Alzheimer Disease. *Journal of Nuclear Medicine* 57, 608–614 (2016).

Tago, T. *PhD Thesis*, Graduate School of Pharmaceutical Sciences, Tohoku University, (2016).

Tournier, N. et al. Transport of Selected PET Radiotracers by Human P-Glycoprotein (ABCB1) and Breast Cancer Resistance Protein (ABCG2): An In Vitro Screening. *Journal of Nuclear Medicine* 52, 415–423 (2011).

Valk, P.E., Bailey, D.L., Townsend, D.W., Maisey, M.N., Positron Emission Tomography. *Springer-Verlag London*, London UK (2005).

van Beek, A. H. E. A., Lagro, J., Olde-Rikkert, M. G. M., Zhang, R. & Claassen, J. A. H. R. Oscillations in cerebral blood flow and cortical oxygenation in Alzheimer's disease. *Neurobiology of Aging* 33, 428.e21-428.e31 (2012).

van Berckel, B. N. M. et al. Longitudinal Amyloid Imaging Using 11C-PiB: Methodologic Considerations. *Journal of Nuclear Medicine* 54, 1570–1576 (2013).

Van de Bittner, G. C., Ricq, E. L. & Hooker, J. M. A Philosophy for CNS Radiotracer Design. *Accounts of Chemical Research* 47, 3127–3134 (2014).

Vandenberghe, R. et al. 18 F-flutemetamol amyloid imaging in Alzheimer disease and mild cognitive impairment: A phase 2 trial: 18 F-Flutemetamol Phase 2 Trial. *Annals of Neurology* 68, 319–329 (2010).

Verhoeff, N.P.L.G., Wilson, A.A., Takeshita, S., Trop, L., Hussey, D., Singh, K., Kung, H.F., Kung, M.-P., and Houle, S., In-vivo imaging of Alzheimer disease beta-amyloid with [11C]SB-13 PET. *The American Journal of Geriatric Psychiatry* 12, 584–595 (2004).

Villemagne, V. L. et al. Aβ Imaging: feasible, pertinent, and vital to progress in Alzheimer's disease. *European Journal of Nuclear Medicine and Molecular Imaging* 39, 209–219 (2012).

Villemagne, V. L. et al. In vivo evaluation of a novel tau imaging tracer for Alzheimer's disease. *European Journal of Nuclear Medicine and Molecular Imaging* 41, 816–826 (2014).

Villemagne, V. L., Fodero-Tavoletti, M. T., Masters, C. L. & Rowe, C. C. Tau imaging: early progress and future directions. *The Lancet Neurology* 14, 114–124 (2015).

Wan, H., Rehngren, M., Giordanetto, F., Bergström, F. & Tunek, A. High-Throughput Screening of Drug−Brain Tissue Binding and in Silico Prediction for Assessment of Central Nervous System Drug Delivery. *Journal of Medicinal Chemistry* 50, 4606–4615 (2007).

Wang, C. & Williams, N. S. A mass balance approach for calculation of recovery and binding enables the use of ultrafiltration as a rapid method for measurement of plasma protein binding for even highly lipophilic compounds. *Journal of Pharmaceutical and Biomedical Analysis* 75, 112–117 (2013).

Watanabe, H. et al. A dual fluorinated and iodinated radiotracer for PET and SPECT imaging of β-amyloid plaques in the brain. *Bioorganic & Medicinal Chemistry Letters* 21, 6519–6522 (2011).

Wong, D. F. et al. In Vivo Imaging of Amyloid Deposition in Alzheimer Disease Using the Radioligand 18F-AV-45 (Flobetapir F 18). *Journal of Nuclear Medicine* 51, 913–920 (2010).

Wooten, D. W. et al. Pharmacokinetic Evaluation of the Tau PET Radiotracer 18 F-T807 (18F-AV-1451) in Human Subjects. *Journal of Nuclear Medicine* 58, 484–491 (2017).

Xia, C.-F. et al. [18F]T807, a novel tau positron emission tomography imaging agent for Alzheimer's disease. *Alzheimer's & Dementia* 9, 666–676 (2013).

Yaqub, M. et al. Evaluation of Tracer Kinetic Models for Analysis of [18F]FDDNP Studies. *Molecular Imaging and Biology* 11, 322–333 (2009).

Yousefi, B. H. et al. Synthesis and Evaluation of 11 C-Labeled Imidazo[2,1- b]benzothiazoles (IBTs) as PET Tracers for Imaging β-Amyloid Plaques in Alzheimer's Disease. *Journal of*

Medicinal Chemistry 54, 949–956 (2011a).

Yousefi, B. H. et al. A Novel 18 F-Labeled Imidazo[2,1- b]benzothiazole (IBT) for High-Contrast PET Imaging of β-Amyloid Plaques. *ACS Medicinal Chemistry Letters* 2, 673–677 (2011b).

Yousefi, B. H. et al. FIBT versus florbetaben and PiB: a preclinical comparison study with amyloid-PET in transgenic mice. *European Journal of Nuclear Medicine and Molecular Imaging Research* 5, (2015a).

Yousefi, B. H. et al. Characterization and First Human Investigation of FIBT, a Novel Fluorinated Aβ Plaque Neuroimaging PET Radioligand. *ACS Chemical Neuroscience* 6, 428–437 (2015b).

Zaidi, H. & Hasegawa, B. Determination of the attenuation map in emission tomography. *Journal of Nuclear Medicine* 44, 291–315 (2003).

Zeng, F. et al. Synthesis and evaluation of two 18F-labeled imidazo[1,2-a]pyridine analogues as potential agents for imaging β-amyloid in Alzheimer's disease. *Bioorganic & Medicinal Chemistry Letters* 16, 3015–3018 (2006).

Zhang, F., Xue, J., Shao, J. & Jia, L. Compilation of 222 drugs' plasma protein binding data and guidance for study designs. *Drug Discovery Today* 17, 475–485 (2012).

Zhang, W. et al. F-18 stilbenes as PET imaging agents for detecting beta-amyloid plaques in the brain. *Journal of Medicinal Chemistry*. 48, 5980–5988 (2005a).

Zhang, W. et al. F-18 Polyethyleneglycol stilbenes as PET imaging agents targeting Aβ aggregates in the brain. *Nuclear Medicine and Biology* 32, 799–809 (2005b).

Zhang, W., Kung, M.-P., Oya, S., Hou, C. & Kung, H. F. 18F-labeled styrylpyridines as PET agents for amyloid plaque imaging. *Nuclear Medicine and Biolo*gy 34, 89–97 (2007).

Zhao, Y. H., Abraham, M. H. & Zissimos, A. M. Fast Calculation of van der Waals Volume as a Sum of Atomic and Bond Contributions and Its Application to Drug Compounds. *The Journal of Organic Chemistry* 68, 7368–7373 (2003).

Conference and Journal Papers

Journal Papers

PhD-Project related Journals

Nai, Y-H, Shidahara, M., Seki, C., Watabe, H., Biomathematical screening of amyloid PET radiotracers with clinical usefulness index. *Alzheimer's & Dementia: Translational Research & Clinical Interventions*. 2017 (Just Accepted)

Arakawa, Y.*, Nai, Y.*, Shidahara, M., Furumoto, S., Seki, C., Okamura, N., et al. Prediction of the clinical standardized uptake value ratio in amyloid PET imaging using a biomathematical modelling approach towards the efficient development of a radioligand. *Journal of Nuclear Medicine*. 2017; vol. 58 no. 8 1285-1292.
* Equal contributions

Nai, Y-H., Shidahara, M., Seki, C., Watanuki, S., Funaki, Y., Ishikawa, Y., Furumoto, S., Watabe, H., Measurement of Free Fraction in Plasma for Biomathematical Prediction of SUVR of Amyloid PET Radiotracers, *CYRIC Annual Report*. 2014-2015, VI. 6.

Other Projects

Nai, Y-H, Ose, O., Shidahara, M., Watabe, H., 137Cs Transmission Imaging and Segmented Attenuation Corrections in a Small Animal PET Scanner. *Radiological Physics and Technology*. 2017; 10(3):321–30

Sato, K., Shidahara, M., Watabe, H., Watanuki, S., Ishikawa, Y., Arakawa, Y., Nai, Y., Furumoto, S., Tashiro, M., Shoji, T., et al. Performance evaluation of the small-animal PET scanner ClairvivoPET using NEMA NU 4-2008 Standards. *Physics in Medicine and Biology* 2016;61, 696–711.

International Conference / Symposium Presentations

Oral Presentations

Nai, YH., Shidahara, M., Seki, C., Watabe, H., Feasibility of Extending Amyloid Biomathematical

Screening Methodology to Tau, *The 12th Asia Oceania Congress of Nuclear Medicine and Biology (AOCNMB)*, Yokohama, JAPAN, October 2017

Nai, YH., Shidahara, M., Seki, C., Watabe, H., Using In-silico Methods to Predict Clinical Usefulness of Amyloid Probes, *Asia Medical Device Innovation Forum 2016*, National Taiwan University, Taipei, TAIWAN, February 2016

Poster Presentations

Nai, YH., Shidahara, M., Arakawa, Y., Seki, C., Watabe, H., BiomathematicalModelling Approach Using In-Silico Data to Predict Clinical SUVR in Amyloid PET Imaging, *NeuroReceptor Mapping (NRM)*, Boston US, July 2016

Nai, YH., Shidahara, M., Seki, C., Watabe, H., Screening of 31 Amyloid PET Radiotracers with Clinical Usefulness Criterion by Biomathematical Modelling Approach using in-silico data, *NeuroReceptor Mapping (NRM)*, Boston US, July 2016

Internal Conference / Symposium Presentations

Oral Presentations

Nai, YH., Shidahara, M., Seki, C., Watabe, H., Biomathematical Screening Methodology of Amyloid PET Radiotracers based on Clinical Usefulness Criterion & In-Silico Data, *Japanese Society for Nuclear Medicine (JSNM)*, Nagoya JAPAN, November 2016

Nai, YH., Shidahara, M., Seki, C., Watabe, H., Biomathematical Screening Methodology of Amyloid PET Radiotracers based on Clinical Usefulness Criterion & In-Silico Data, Akita Seminar (秋田脳研セミナー), Akita Prefectural Cerebral Blood Vessel Research Center, Akita, JAPAN, September 2016

Nai, YH., Ose, T., Shidahara, M., Watabe, H., Comparing 3 Attenuation Correction Methods in Small Animal PET Scanner using Phantoms, Akita Seminar (秋田脳研セミナー), Akita Prefectural Cerebral Blood Vessel Research Center, Akita, JAPAN, September 2016

Nai, YH., Shidahara, M., Seki, C., Watabe, H., Using In-silico Methods to Predict Clinical Usefulness of Amyloid Probes, The 5th Nuclear Medical Image Analysis Symposium (第 5 回核

医学画像解析研究会), Tohoku University, Sendai, JAPAN, December 2015

Nai, YH., Shidahara, M., Watabe, H., *Standard Operating Procedures (SOP) for pre-clinical facility*, Japanese Society for Nuclear Medicine (JSNM), Tokyo JAPAN, November 2015

Poster Presentations

Nai, YH., Shidahara, M., Seki, C., Watabe, H., '*Comparing 3 Attenuation Correction Methods in Small Animal PET Scanner using Phantoms*', Japanese Society for Nuclear Medicine (JSNM), Nagoya JAPAN, November 2016